UNIVERSITY OF SOUTHAMPTON

SCALING AND PERFORMANCE COMPARISONS OF A
CENTRIFUGAL PUMP WITH HYDRODYNAMIC DISC SEALS
RUNNING IN WATER AND MERCURY

by

Stephanie L. Merry

DEPARTMENT OF MECHANICAL ENGINEERING

Submitted for the Degree of Doctor of Philosophy

April 1982.

SCALING AND PERFORMANCE COMPARISONS OF A
CENTRIFUGAL PUMP WITH HYDRODYNAMIC DISC SEALS
RUNNING IN WATER AND MERCURY

VOLUME 2

If you can fill the unforgiving minute
With sixty seconds' worth of distance run,
Yours is the Earth.....

                    - KIPLING.

CONTENTS : VOLUME II

NOTATION

[N.B. The following symbols are used in Chapters 1-12 and Appendices I-XVIII. In Chapter 13 and associated Appendices (XVIII and XIX) the traditional notation for thermodynamics is employed, as set out at the beginning of that Chapter, which conflicts in some cases with the definitions given below]

		Units
a	Vane height	mm
A	Area	m^2
b	Vane width	mm
c	Fluid velocity	$m.sec^{-1}$
$\dot{c}$	Fluid acceleration	$m.sec^{-2}$
C	Clearance between pump intake and sump floor	m
C_D	Drag coefficient	–
C_{EL}	End load coefficient of a HDS $[\frac{E.L.}{\frac{1}{2}\rho\omega^2R^4}]$	–
C_f	Friction coefficient	–
C_M	Torque absorption coefficient $[\frac{2M}{\rho\omega^2R^5}]$	–
C_p	HDS Pressure coefficient $[\frac{\Delta p}{\frac{1}{2}\rho\omega^2R^2}]$ (Local $C_p = \frac{P_{tap}}{\frac{1}{2}\rho\omega^2R^2}$)	–
C_v	Basic Coefficient for a Venturi Tube	–
d	Mean slot (seal clearance) diameter	mm
D	Diameter	m.
E	Velocity approach factor for a venturi tube	–
E.L.	End load	N
E_v	Nett suction energy	$J.kg^{-1}$
f	Friction factor	–
F_B	Buoyancy force	N
F_D	Drag force	N
g	Acceleration due to gravity	$m.sec^{-2}$

H	Pressure head	m. of fluid
H_r	Theoretical Euler head	m. of fluid
k	Slip factor	–
K_c	Loss coefficient at a pipe contraction	–
L	Length	m
M	Torque	N.m.
n	Rotational speed	rpm
n_s	Specific speed $\left[\dfrac{\omega Q^{\frac{1}{2}}}{(gH)^{\frac{3}{4}}}\right]$	–
N	Number of stages in a multistage HDS	–
p	Pressure	$N.m^{-2}$ (Pa)
p_v	Vapour pressure	$N.m^{-2}$ (Pa)
P_{in}	Input power	W
P_{out}	Output power	W
Q	Pump delivered flowrate	$m^3 sec^{-1}$ or $\ell.min^{-1}$
r	Droplet radius	μm
R	Radius	m
Re	Reynolds Number	–
Re_B	Bubble Reynolds Number $\left[\dfrac{2r\,c_{rel}}{\nu}\right]$	–
Re_D	Pipe Reynolds Number $\left[\dfrac{cD}{\nu}\right]$	–
Re_u	Couette Reynolds Number (formed with peripheral velocity and clearance)	–
Re_ω	Rotational Reynolds Number $\left[\dfrac{\omega R^2}{\nu}\right]$	–
$Re_{\bar{y}}$	Throughflow Reynolds Number in annular clearance	–
s	Clearance	mm
S	Suction specific speed $\left[\dfrac{NQ^{\frac{1}{2}}}{E_v^{\frac{3}{4}}}\right]$	–
t	Disc thickness	mm
T	Relative radius $\left[\dfrac{R}{R_D}\right]$	–
ΔT	Temperature increment	K
u	Peripheral velocity	$m.sec^{-1}$
V	Volume	m^3

W	Fluid velocity relative to impeller blade	$m.sec^{-1}$
We	Weber Number $[\frac{\rho c^2 L}{\sigma}]$	–
X	Relative radius of interface in a HDS $[\frac{R_i}{R_D}]$	–
$\bar{y}$	Mean axial fluid velocity	$m.sec^{-1}$
Y	Relative shaft or hub radius $[\frac{R_h}{R_D}]$	–
Z_R	Reynolds Number correction for a venturi tube	–

α	Angle between the direction of fluid velocity and the tangent to the impeller periphery	degrees
β	Blade angle	degrees
δ	Losses in a hydraulic machine	%
Δ	Specific diameter $[\frac{D(gH)^{\frac{1}{4}}}{Q^{\frac{1}{2}}}]$	–
Δ	Increment (when used in conjunction with another symbol, e.g. Δp)	–
ζ_{io}	Flow resistance coefficient at slot inlet and outlet	–
η	Efficiency	%
θ	Slot (seal clearance) flow coefficient	–
κ	Power coefficient $[\frac{P_{in}}{\rho \omega^3 D^5}]$	–
λ	Friction coefficient for a smooth walled slot	–
λ_s	Surface roughness	µm.
λ_{CLA}	Surface roughness measured on the Talysurf	µm.
μ	Dynamic viscosity	cP
ν	Kinematic viscosity	cSt
ρ	Density	$kg.m^{-3}$
σ	Surface tension	$N.m^{-1}$
$\sigma_{(n-1)}$	Sample standard deviation (statistical analysis)	–
τ	Peripheral component of shear stress	$N.m^{-2}$
ϕ	Pump flow coefficient $[\frac{Q}{\omega D^3}]$	–
ϕ_{tot}	Total flow coefficient $[\frac{Q + Q_{Leak}}{\omega D^3}]$	–
ϕ'	Flow coefficient derived from pump flowrate + upper neckring leakage	–

ψ	Pump head coefficient $[\dfrac{gH}{\omega^2 D^2}]$	–
ω	Angular velocity	$\sec^{-1}$

Subscripts

1.	Inlet conditions	N	Relating to a multistage HDS
2	Outlet conditions	N1	Relating to one stage of a multistage HDS
A	Axial flow		
c	Contraction	r	Radial component
crit	Critical	rel	Relative
dyn	Dynamic	R	At radius R
D	Disc	s	Smooth side
f	friction	sl	Slot (or clearance)
F.L.	Filter loss	ss	Single stage
h	Hub	t	Tip
hyd	Hydraulic	tap	Tapping
i	Interface	tot	Total
inc	Inception	v	Vaned side
m	Mercury	vol	Volumetric
mech	Mechanical	w	Water
		ω	Whirl component
		∞	Free stream

TERMINOLOGY

Abbreviations and terminology which occur frequently in the text (after initial definition) have been redefined below for the convenience of the reader.

Term	Definition
C.A.S.E.	Co-operative Award in Science and Engineering (jointly funded by the Science Research Council and an external body – normally an industrial concern)
CLA	Centre Line Average: measurement of surface roughness.
Clean mercury	Mercury which does not contain significant amounts of other chemicals (such as sodium), which would normally be found in "cell" mercury in the chlorine plant.
Gross absorbed power	Power absorbed by the pump, plus losses in shaft seals and bearings, in the right angle gearbox (on the water rig) and in the motor (O.L.R.)
HDS	Hydrodynamic Disc Seal.
I.D.	Internal diameter.
Nett absorbed power	Power absorbed by the pump (or pump/HDS assembly), i.e. gross absorbed power minus parasitic losses on the test rig as detailed in the definition above.
N.P.S.H.	Nett positive suction head, describing cavitation characteristics of the pump.
O.L.R.	Off-Load Rig (mercury test rig).
Standard pump	The original design of pump, fitted with upper and lower neckrings at standard clearance (0.165mm radial).
Water	When referring to pump trials in the present work, "water" indicates a 99% water/1% soluble cutting oil mixture. The temperatures are described as follows:

Cold water – at ambient room temperature ($20-27^{\circ}$C)
Warm water – at $55-57^{\circ}$C.
Hot water   – at $80-82^{\circ}$C.

LIST OF TABLES IN APPENDICES

LIST OF FIGURES
[followed by list of Figures included in Appendices]

LIST OF FIGURES IN APPENDICES

APPENDIX I

SPECIFICATIONS AND DIMENSIONS OF STANDARD PUMP

Design Duty Specifications

Nominal speed:	1,450 r.p.m.
Generated head:	5.9m (19.5 ft)
Flowrate:	$55 \ell.\text{min}^{-1}$
Gross absorbed power:	2.4kW (3.2 HP)
Specific speed (η_s):	0.22
Specific diameter (Δ):	13.0.

Pump type:	Single suction centrifugal
Impeller type:	Double shrouded
Impeller diameter:	143mm.
No. and type of vanes:	5, backward curved.
Vane inlet angle:	21°
Vane outlet angle:	33°
Vane depth:	7.0mm (inlet)
	4.8mm (outlet)
Vane width:	5.5mm (inlet)
	10.5mm (outlet)
Length of leading edge on blades:	93mm.
Impeller inlet I.D.:	57mm.
Impeller hub O.D.:	50.65mm (upper)
	69.77mm (lower)
Neckring I.D.:	50.98mm (upper)
	70.10mm (lower)
Neckring depth:	11.0mm (upper)
	12.5mm (lower)
Radial Neckring Clearance:	0.165mm (upper and lower).

APPENDIX II

CALCULATION OF THE THEORETICAL HEAD PRODUCED BY A RADIAL FLOW CENTRIFUGAL PUMP

The Euler equation may be used to calculate the theoretical head H_r which would be developed by the pump without losses:

$$H_r = \frac{1}{g}(u_2 c_{\omega 2} - u_1 c_{\omega 1}) \qquad \ldots (II.1)$$

The impeller peripheral velocity (u) is calculated directly from the pump design speed of 1450 rpm and impeller radius at inlet and outlet (see Appendix I).

At the inlet:

$$u_1 = r_1 \omega = \frac{28.5 \times 10^{-3} \times 2 \times \pi \times 1450}{60}$$

$$= 4.33 \text{ m.sec}^{-1}.$$

At the outlet:

$$u_2 = r_2 \omega = \frac{71.5 \times 10^{-3} \times 2 \times \pi \times 1450}{60}$$

$$= 10.86 \text{ m.sec}^{-1}.$$

The calculation of the whirl component of absolute fluid velocity [c_ω] is illustrated in Figure II(i).

From simple geometry at the outlet:

$$c_{\omega 2} = c_2 \cos \alpha_2 = u_2 - W_2 \cos \beta_2 \qquad \ldots \text{(II.2)}$$

and

$$c_{r2} = W_{r2} = W \sin \beta_2 . \qquad \ldots \text{(II.3)}$$

The volumetric flowrate per unit area at the rotor exit gives the radial component of the absolute fluid velocity c_{r2},

$$\text{i.e.} \quad \frac{Q}{A_2} = c_{r2}. \qquad \ldots \text{(II.4)}$$

The design flowrate [Q] is 9.17×10^{-4} $\text{m}^3.\text{sec}^{-1}$.

The depth of the vanes at the outlet is 4.8mm. There are five vanes, of width 10.5mm at the impeller circumference. Thus the cross-sectional area available to the fluid at the impeller exit is:

$$A_2 = [143\pi - 10.5 \times 5]\ 4.8 \times 10^{-6}\ \text{m}^2$$

$$= 1.90 \times 10^{-3}\ \text{m}^2$$

$$\therefore c_{r2} = \frac{9.17 \times 10^{-4}}{1.90 \times 10^{-3}}$$

$$= 0.483\ \text{m.sec}^{-1}.$$

Then from equation (II.3) with $\beta_2 = 33^{\circ}$

$$W_2 \sin 33^{\circ} = 0.483$$

$$\therefore \qquad W_2 = 0.887\text{m.sec}^{-1}.$$

Substituting in equation (II.2):

$$c_{\omega 2} = 10.86 - 0.887 \cos 33^{\circ}$$

$$= 10.12\ \text{m.sec}^{-1}.$$

To allow for deviation of the direction of fluid velocity from the vane angle, this value should be multiplied by a slip factor, say 0.8.[88]

Then:

$$c_{\omega 2} = 8.09 \ m.sec^{-1}.$$

Assuming zero prewhirl ($c_{\omega 1} = 0$), the Euler equation reduces to:

$$H_r = \frac{1}{g} u_2 c_{\omega 2} \quad .$$

Then for the pump in question:

$$H_r = \frac{1}{9.81} \times 10.86 \times 8.09$$

$$= 8.96m.$$

In practice, the pump produces a head of 5.9m at its design point, corresponding to a hydraulic efficiency of 66%.

However, for zero fluid prewhirl, applying equation (II.2) to inlet conditions with $c_{\omega 1} = 0$, we obtain:

$$u_1 = W_1 \ Cos \ \beta_1$$

i.e. $\quad 4.33 = W_1 \cos \beta_1 \quad\quad\quad \dots (II.5)$

As before, the radial component of the fluid velocity (c_{r1}) is given by the volumetric flowrate per unit area at the rotor inlet,

i.e.
$$c_{r1} = \frac{55 \times 10^{-3}}{60 \times [57\pi - 5 \times 5.5] \ 7.0 \times 10^{-6}}$$

$$= 0.864 \ m.sec^{-1}.$$

But $\quad c_{r1} = W_{r1} = W_1 \sin \beta_1$

$\therefore \quad 0.864 = W_1 \sin \beta_1 \quad . \quad\quad\quad \dots (II.6)$

Combining equations (II.5) and (II.6):

$$\frac{0.864}{4.33} = \tan \beta_1$$

$$\beta_1 = 11°17'.$$

A relative fluid inlet angle of $11°17'$ would result in high shock losses, since the vane inlet angle is $21°$. It would therefore appear that the pump has been designed for some fluid prewhirl and the simplified Euler equation cannot be applied.

For minimum shock losses at the inlet, $\beta_1 = 21°$. Then from equation (II.6):

$$W_1 \sin 21° = 0.864$$

$$W_1 = 2.41 \text{ m.sec}^{-1}.$$

Also

$$c_{\omega 1} = u_1 - w_1 \cos \beta_1 \qquad \text{... (II.2)}$$

∴

$$c_{\omega 1} = 4.33 - 2.41 \cos 21°$$

$$= 2.08 \text{ m.sec}^{-1}.$$

Multiplying by 0.8 to allow for slip, we obtain:

$$c_{\omega 1} = 1.66 \text{ m.sec}^{-1}.$$

The relevant values may now be substituted in the full Euler equation:

$$H_r = \frac{1}{g} (10.86 \times 8.09 - 4.33 \times 1.66)$$

$$= 8.22\text{m}.$$

When this theoretical value is compared with the true head produced by the pump at its design point (5.9m), the hydraulic efficiency is 72%.

Subsequent experiments with the pump running in water showed that at 1500 rpm the maximum efficiency occurs at a flow rate of $110\ell.min^{-1}$ (see Fig. 16).

At this speed;

$$u_1 = 4.48 \ m.sec^{-1}$$

$$u_2 = 11.23 \ m.sec^{-1}$$

Then applying equation (II.2) to inlet conditions with $c_{\omega_1}=0$:

$$4.48 = W_1 \cos\beta_1$$

Also, $c_{r_1} = \dfrac{Q}{A_1} = 1.73 \ m.sec^{-1}$ - (II.7)

and from equation (II.3), again for inlet conditions:

$$1.73 = W_1 \sin \beta_1 \qquad\qquad - (II.8)$$

Combining equations (II.7) and (II.8):

$$\text{Tan } \beta_1 = \frac{1.73}{4.48}$$

therefore $\beta_1 = 21^{\circ}$

which is identical to the vane inlet angle and shows that the duty point of the pump in the chlorine plant ($55\ell.min^{-1}$ at 1450rpm) is well below the true design point.

With $c_{r_2} = \dfrac{Q}{A_2} = 0.965 \ m.sec^{-1}$:

$$0.965 = W_2 \sin 33^{\circ} \qquad\qquad (II.3)$$

therefore $W_2 = 1.77 \ m.sec^{-1}$

then $c_{\omega_2} = 11.23 - 1.77 \cos 33^{\circ} \qquad\qquad (II.2)$

$$= 9.74 \ m.sec^{-1}$$

Substituting in the simplified Euler equation and allowing for slip:

$$H_r = \frac{0.8}{98.1} \times 9.74 \times 11.23 = 8.92m$$

Compared with the true head produced by the pump at this point (5.2m), this gives a hydraulic efficiency of 58%.
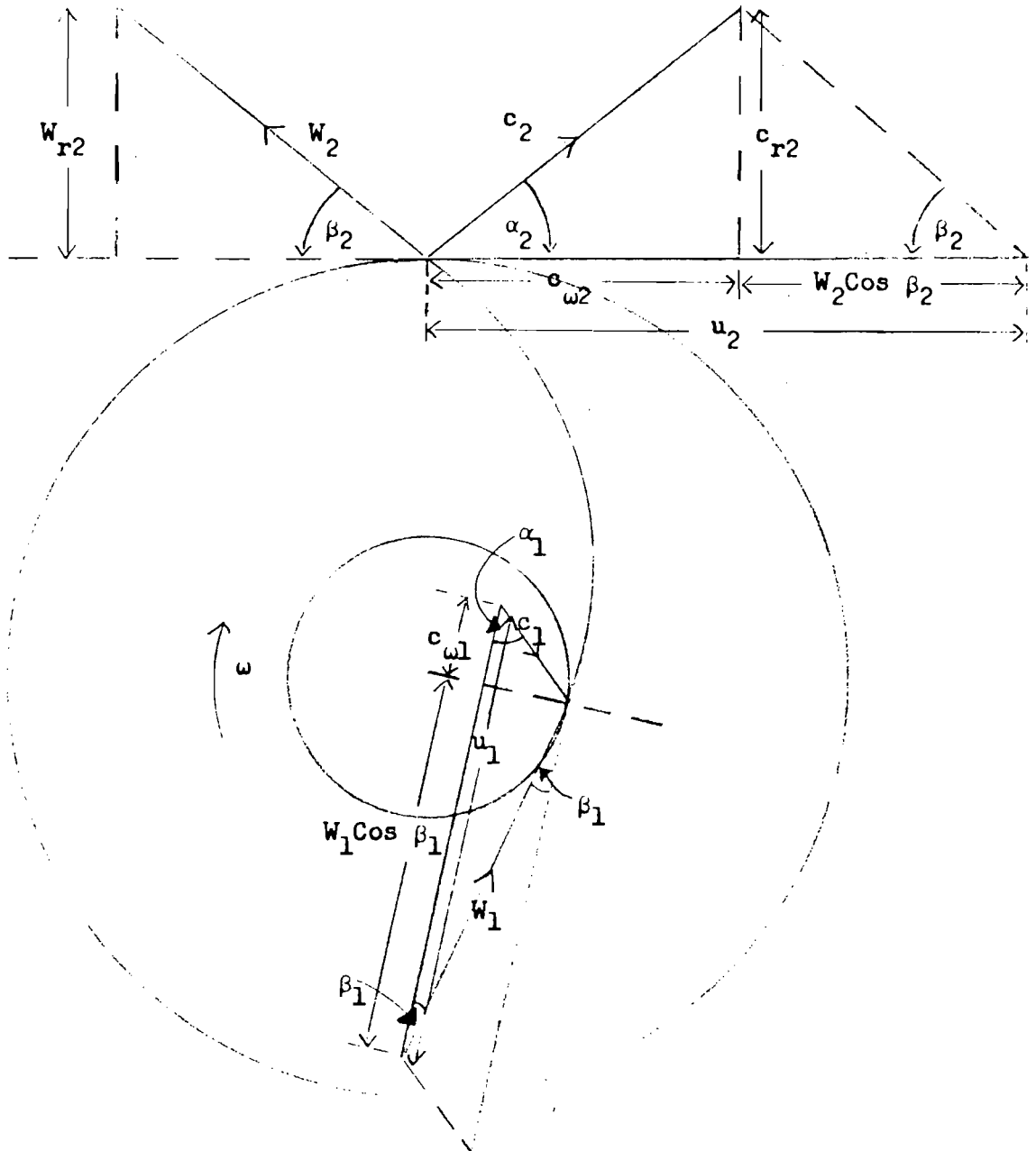
FIGURE II(i).VELOCITY DIAGRAM FOR CENTRIFUGAL PUMP IMPELLER
ENTRANCE AND EXIT.

Component	Manufacturer	Type	Maximum Rating	Range	Serial No.
Electric Motor	Newbridge Engineers	3-phase	19 kW (25HP)	–	F571709
Dynadrive Variable Slip Magnetic Coupling.	Newbridge Engineers	DXM/50	50 lb.ft at 2,600rpm	–	DXM/50/113
S.C.R. Speed Control	Newbridge Engineers	DX/C	–	Maintains speed to .2%	–
Autogard Torque Limiter	GIB Precision Ltd.	AFX P1	250 lb.in.	0–3,000 rpm.	–
Right Angle Bevel Gearbox	Neeter Drive Ltd.	Series 37	33 kW at 3,000rpm.	0–3,000 rpm.	37/2410.
Airbearing	British Aircraft Corporation, Precision Products Group.	–	{120 lb radial load 150 lb axial load	–	–
Torque Transducer	British Hovercraft Corporation	TT2/4/AD	30 lb.ft at 10,000rpm	0–15 lb.ft 0–10,000 rpm.	SE-E-12283.
Rotary Switch Valves	Drallim Industries Ltd.	1800 1 to 6 way	–	–	–
Constant Pressure Regulator	G.A. Platon Ltd.	Flostat Minor B.H.	–	–	F20486
Positive Displacement Oil Pumps	British Quadruplex Ltd.	474M	–	–	–
Motor for Oil Pumps	Power Contracts Ltd.	D.C.	93W ($\frac{1}{8}$HP)	–	–

APPENDIX III

DETAILS OF COMPONENTS AND INSTRUMENTATION ON WATER RIG

A. MECHANICAL COMPONENTS

Instrument	Manufacturer	Type	Accuracy or Resolution	Range	Serial No.
Torque Indicator	Southampton University Mechanical Engineering Electronics Dept.	Digital Readout	$\pm$ 0.01Nm resolution	0-9.99Nm	
Flowmeter	Electronic Flo-Meters Ltd.	B/1/60TC	$\pm$0.25% max. accuracy	Calibrated 27-273 $\ell.min^{-1}$	18938/E4
Flowrate Indicator	Electronic Flo-Meters Ltd.	DR1	$\pm$0.1$\ell.min^{-1}$ resolution	0-999$\ell.min^{-1}$	10862/E3
Bourdon Tube Pressure Gauge	Wallace and Tiernan	FA234	$\pm$0.5 lb.in^{-2} accuracy $\pm$0.25 lb.in^{-2} resol'n	0-500 lb.in^{-2}	I.2606
Electronic Counter (in conjunction with 60 toothed gearwheel and electronic pick-up)	Dawe Instruments Ltd.	3000AR	$\pm$1 rpm resolution	0-99,999 rpm.	12309 M
Zeatron thermister probes	G.H. Zeal Ltd.	A.	$\pm$ 0.7^{o}C accuracy		
Zeatron temperature indicator	G.H. Zeal Ltd.	10667	$\pm$ 0.5^{o}C resolution	10-80°C and 80-150°C	10667
Quartz Thermometer	Hewlett-Packard	HP2801A	Resolution $\pm$0.0001^{o}C (for temperature differences)	-80 - +250°C	1404A00864
Quartz Crystal Temperature Probes	Hewlett-Packard	2850B	$\pm$0.08^{o}C (absolute accuracy)		SN1252-4 SN1252-5

B. INSTRUMENTATION

APPENDIX IV

ACCURACY OF EXPERIMENTAL DATA

It is impossible to measure directly the true value of any variable: in other words, no measurement is without error. Thus, from any set of experimental data, we must attempt to extract the best value of the variables under consideration and to estimate the size of the associated errors. The measurement error is usually expressed in terms of two components: a random error and a systematic error.

If repeated measurements of a single variable are taken, random errors appear as scatter about the average of these measurements. This is caused by characteristics of the measuring system and/or changes in the quantity being measured. The term precision, as quantified by the standard deviation (σ) of the whole population of measurements, is used to characterise random errors. A small standard deviation indicates high precision in the data.

In addition to random errors, there are also errors that are consistently too high or too low with respect to the true value. Such errors, termed fixed or systematic, are characterised by bias. If the bias can be quantified it may be used as a correction factor to be applied to all measurements. Systematic errors can usually be minimized by instrument calibration.

In the present work, repeat measurements were only taken for the thermometric efficiency determination described in Chapter 13. The temperature rise across the pump at a given operating point was calculated as the mean value of the set of 54 ΔT measurements[73], i.e.

$$\Delta\bar{T} = \frac{1}{54} \sum \Delta T_i \qquad \ldots \text{(IV.1)}$$

The sample standard deviation is:

$$\sigma_{(n-1)} = \sqrt{\frac{1}{53} \sum (\Delta T_i - \Delta\bar{T})^2} \qquad \ldots \text{(IV.2)}$$

The 99% confidence interval for $\Delta\bar{T}$ is then given by;

$$\Delta\bar{T} \pm 2.58 \frac{\sigma_{(n-1)}}{\sqrt{54}} \qquad \ldots \text{(IV.3)}$$

Equation (IV.3) is only valid without the correction for t-distribution[73] since the number of data points (in this case 54) exceeds 30.

The accuracy of thermometric efficiency measurements depends mainly upon experimental technique and this is discussed at length in Chapter 13.4 and 13.5.

When repeat measurements are not available, which is generally the case for the pump and HDS performance trials (because of time limitations and the number of separate measurements involved), the uncertainty interval must be estimated. This is the maximum error to be reasonably associated with any measurement. The estimate is based on the resolution, sensitivity and nominal accuracy of the measuring instrument, but several other factors which might introduce random errors must also be taken into account. These include variations in controlled inputs, variations in the quantity being measured and errors caused by the experimenter, the supporting equipment and environmental conditions.

When data is presented graphically, the effect of random errors is reduced to some extent. For example, in Figure 20, the points at maximum flowrate do not coincide with the general trend of the head/flow

curve, suggesting a large random error in this measurement.

The possible sources of error and the uncertainty interval involved in the measurement of each variable on the water and mercury test rigs are discussed in detail in the following sections.

A. MEASUREMENTS ON THE WATER TEST RIG

(i) Speed

Speed was measured by an electro-magnetic pick-up in conjunction with a sixty toothed gear wheel on the drive shaft, and digitally displayed on an electronic counter, directly in rpm. With a counting period of about 4 seconds, the speed was continually monitored and any variations were immediately apparent. At speeds of 1500 rpm, and above, the Dynadrive feedback unit maintained the speed set at the beginning of a run to $\pm$2rpm. With a resolution of $\pm$1rpm on the counter, this corresponds to an accuracy of $\pm$0.2%.

When the motor was running under light load, there were wider fluctuations in speed, but the desired speed was still maintained to within $\pm$0.5% at 1000 rpm and $\pm$1% at 600 rpm.

(ii) Pressure

For the standard pump tests (see Chapter 5), pressure tappings at the elbow of the pump delivery pipe and the inlet to the upper and lower neckrings were connected via a 6-way valve to a precision Bourdon Tube gauge. The manufacturer's accuracy for this instrument is $\pm$0.5psi.

Several additional tappings were required for the HDS trials (see Chapters 11 and 12) and these were led, together with the original pump pressure tappings where necessary, via three interconnected 6-way valves to the same pressure gauge.

During experimental runs, it was noted that errors in pressure measurements could arise due to the existence of a pressure gradient in the line between the 6-way valve and the gauge, after switching from one tapping to another. This error was minimised by allowing ample time for pressure equalisation between readings and by gently tapping the gauge, then waiting for the pointer to settle again before readings were finally taken.

Leakage from one of the high pressure connections to a 6-way valve caused significant errors in the measurement of pressure distribution in the bare two-stage (I) HDS (see Figure 144). This was traced to a worn switching mechanism, which was renewed for subsequent experiments.

It is well known[28] that errors in static pressure measurement in a moving fluid may arise due to the partial sensing of dynamic pressure. Such errors are a function of the size and shape of the pressure tapping and were minimised in the present case by providing square-edged holes of 1mm diameter, as recommended in Reference [28]. No problems were encountered with blockage of these small tappings and the response time to pressure changes was negligible.

The value of the static pressure tap error is an increasing function of pipe Reynolds Number and relative tapping diameter. Therefore the error was estimated for the worst case, which is in the measurement of pump outlet pressure at 3500 rpm and maximum flowrate [$Q = 300\ell.min^{-1}$].

For: $c = 4.4\ m.sec^{-1}$

$Re_D = 1.67 \times 10^5$

$\dfrac{D_{tap}}{D} = 0.026$

published data in Reference [28] gives an error of 0.1% p_{dyn}. Since the dynamic pressure head ($\dfrac{c^2}{2g}$) is 0.98m of water, the static pressure tap error is negligible.

Therefore the main error in pressure measurements is due to the value of the manufacturer's accuracy for the Bourdon gauge (+0.5psi) in relation to the magnitude of the measured pressure. As a guide, estimated values of the maximum error for measurements on the standard pump are presented in Table IV(i). (The accuracy of the Bourdon gauge was also checked with a dead weight tester).

Table IV(i): Estimated Maximum Error in Pressure
              Measurements on the Standard pump in Water

Rotational Speed (rpm)	Generated Pressure	Neckring Inlet Pressure
3500	1.5%	2.5%
1500	6.0%	12.0%
1000	15.0%	18.0%
600	40.0%	–

For tip pressure measurements in the single and two-stage (I) HDS, the following maximum errors have been estimated:

Table IV(ii): Estimated Maximum Error for HDS Pressure
              Measurements in Water at the Disc Tip

Rotational Speed (rpm)	Single Stage HDS	Two-Stage (I) HDS	
		Upper Disc	Lower Disc
1000	20%	70%	26%
1500	8%	26%	10%
2000	5%	12%	6%
2500	2.5%	8%	3%

Errors for the two-stage (I) and (II) HDS will be similar.

In general, it is thought that the accuracy achieved in practice for pressure measurements is considerably better than indicated in Tables IV(i) and IV(ii).

(iii) Flowrate

Water flowrate was measured by turbine flowmeter and digitally displayed directly in $\ell.min^{-1}$ with a resolution of $\pm 0.1\ell.min^{-1}$. Such instruments have an attainable accuracy of $\pm 0.25\%$ for 10-100% of the flow range[84] and are relatively insensitive to viscosity changes in the metered fluid. However, the accuracy at low flowrates is not as high and accuracy throughout the range will be reduced as the bearings of the rotating impeller become worn.

In the present project, high accuracy at low flowrates is not vital, since the pump has fairly flat characteristic head and absorbed power curves in this region of operation. Even at high flowrates, when the head characteristic becomes much steeper, an error of the order of $\pm 0.5\%$ would be insignificant, particularly in relation to the errors in pressure measurement detailed above.

Inspection of the head characteristics in Figure 20 suggests a large error in pressure and/or flow measurement at high rotational speeds and maximum flowrate, since in each case these points lie to the right of the general trend of the curve. The non-dimensional head/flow curves (Figures 21-23) indicate that it is the flowrate measurement which is inaccurate. Since the effect manifests itself at a lower speed when the water temperature is raised (Figure 19) the possibility of cavitation occurring at the flowmeter has been investigated.

The pipework between the pump outlet and flowmeter consists of 57.5cm of 38mm I.D. galvanised steel pipe, followed by 113.5cm of 2.5cm I.D. stainless steel pipe, with a contraction between, and a 100 mesh water filter. The head loss due to skin friction in a length of straight pipe (ΔH_f) is given by:

$$\Delta H_f = \frac{fLc^2}{2gD} \qquad \ldots \text{(IV.4)}$$

where the friction coefficient f may be found from Moody charts[40].

For 38mm I.D. galvanised pipe, at a flowrate of $300\ell.min^{-1}$, f=0.0285 and c=4.38m.sec^{-1}

$$\Delta H_f = \frac{0.0285 \times 57.5 \times (4.38)^2}{2 \times 9.81 \times 3.8} = 0.4m.$$

For the 2.5cm I.D. stainless steel pipe, f=0.024, c=9.87m.sec^{-1}

$$\Delta H_f = \frac{0.024 \times 113.5 \times (9.87)^2}{2 \times 9.81 \times 2.5} = 6.3m.$$

The head loss at the contraction ΔH_c is given by:

$$\Delta H_c = K_c \frac{c_2^2}{2g} \qquad \ldots \text{(IV.5)}$$

The value of the constant K_c depends upon the diameters either side of the contraction. In the present case, with $\frac{D_2}{D_1} = 0.7$, $K_c = 0.23$[40]

$$\Delta H_c = \frac{0.23 \times (9.87)^2}{2 \times 9.81} = 1.1m.$$

The value of the head loss in the water filter was measured during the latter stages of the project, when a pressure tapping had been installed just upstream of the flowmeter. At 2500 rpm (the maximum rotational speed for the pump fitted with a HDS) and $227\ell.min^{-1}$ flowrate, the loss was equivalent to 4.5m of water.

Assuming that, as with other forms of pressure loss (see Equations IV.4 and IV.5):

$$\Delta H_{FL} \propto Q^2 .$$

Then, at a flowrate of $300\ell.min^{-1}$:

$$\Delta H_{FL} = 4.5 \times (\frac{300}{227})^2 = 7.8m.$$

.˙. Total losses between the pump outlet and
flowmeter = 15.6m of water.

The static lift between the pump and flowmeter is 1.7m, whilst
the dynamic head of fluid on the meter $(\frac{c^2}{2g})$ is approximately 5m. The
measured pressure head at the pump outlet corresponding to $300\ell.min^{-1}$
flowrate at 3,500 rpm is 25m (see Figure 20).

.˙. Available static pressure at the flowmeter = 25 − (15.6+1.7+5)
= 2.7m of water.

This is equivalent to $25,750Nm^{-2}$ [At $80°C$, $\rho_W = 972kg.m^{-3}$] .

Since the vapour pressure of water at $80°C = 47,400$ $N.m^{-2}$ [40] ,
cavitation will occur at the turbine flowmeter and the data points for
maximum flowrate at 3,500 rpm in hot water are inaccurate. Furthermore,
since the impeller in the meter is spinning, relative velocities at the
blade tips will be high and it is quite feasible that cavitation also
occurs at the lower water temperatures and/or flowrates.

(iv) Torque

The gross torque absorbed on the rig was measured with a transducer
manufactured by British Hovercraft Corporation and directly displayed in
Nm on a digital indicator reading to 0.01Nm. The main inaccuracy in the
measurement of nett torque absorbed by the pump lies in the uncertainty in
the value of the parasitic torque absorbed by the right angle gearbox.
During the early stages of the project, this was estimated from the graphs
in Figure IV(i). Here, the parasitic torque is shown to be extremely
temperature dependent and therefore any time lag in the system for
monitoring gearbox temperature (since the temperature probe was installed
in the case rather than right inside the box) would be reflected in a
false figure for the parasitic torque.

In an effort to reduce both the temperature dependency and absolute value of torque absorbed by the gearbox, a circulatory lubrication system was installed for the gearbox (see Chapter 4.1). Unfortunately, this modification reduced the normal running temperature of the gearbox and therefore the parasitic torque values (estimated from a new set of curves shown in Figure IV(ii)) were similar to those found with the original set-up.

The following sources of error in nett torque measurements must be considered:

(a) The parasitic torque curves in Figures IV(i) and IV(ii) were obtained by running the rig in air, without an impeller on the pump. This gives the torque absorbed by the bearings and gears under no-load conditions, which may well change when load is applied.

(b) The torque readings during parasitic torque determination involved a random error of roughly ±0.03Nm. The effect of this has been reduced by presenting the results graphically.

(c) A zero error or bias of unknown magnitude is probably present in all torque measurements. This is because the residual torque when the gearbox is at rest varies according to the position of the drive shaft, thus preventing the accurate setting of zero on the torque indicator.

The error in nett torque measurements due to the above considerations is estimated to be approximately ±0.1Nm. The corresponding error in nett power measurements for the standard pump at different speeds is tabulated overleaf.

Table IV(iii): Estimated Error in Nett Power
           Measurements for the Standard Pump
           in Water

Rotational Speed (rpm)	Error in Nett Absorbed Power
600	50%
1000	7%
1500	5%
2500	3%
3500	1.5%

The greatest problem with absorbed power measurement was
encountered during the bare HDS trials (see Chapter 11). Here the
parasitic torque constituted a major part of the gross measured
torque even at the maximum speed and therefore the associated error
in nett power absorption was high, as tabulated below.

Table IV(iv): Torque Measurements for the Bare HDS
           Trials in Water

Seal Configuration & Speed	Gross Torque (Nm)	Parasitic Torque (rpm)	Error in Nett Torque
Single stage HDS at 2000rpm	1.56	0.74	12%
Two-stage (I) HDS at 2000rpm	0.87	0.55	30%

(v) Leakage Flowrate

The measurement of leakage through the upper neckring clearance involved diverting this flow into a calibrated tank for a measured length of time, i.e. the overall error consists of components due to inaccuracies in both time and volume measurement.

Normally a leakage volume of at least 40ℓ was involved. Since the graduations on the sight glass correspond to 0.4ℓ, the accuracy of this measurement should be better than ±1%.

The time period varied with pump speed, but was always longer than one minute and sometimes as long as 4 minutes. This interval was measured with a stop-watch reading to the nearest 0.2 sec, i.e. the error due to instrument resolution was negligible. A more important source of error lies in the operator's reaction time for opening and closing the valves for diverting the fluid flow into the calibrated tank. Since this procedure arose twice for each measurement, the associated error could be as high as ±1 second.

The total error in leakage data is therefore estimated as ±1.5% at 600 rpm, increasing to ±3% at 3,500 rpm.

B. MEASUREMENTS ON THE OFF-LOAD RIG

(i) Speed

Originally no provision was made for speed measurement on the O.L.R., since the pump is keyed directly onto the extended shaft of a 3-phase induction motor, running at a nominal fixed speed of 1450 rpm. However, the motor speed is not constant, but varies with loading, and such variations were measured with a hand-held tachometer, reading to the nearest 5 rpm, applied to the top end of the shaft. However, since the speed was not continuously monitored, as in the case of the water rig, any short-term fluctuations, due for example to irregularities in the

supply voltage, might pass unnoticed. These in turn would cause errors in instantaneous pressure, power or flowrate readings.

Apart from these short-term fluctuations, the accuracy of the average speed measurements should be better than $\pm0.5\%$.

(ii) Pressure

Pressure at the pump inlet, outlet, upper neckring and lower neckring was measured on four separate diaphragm-type Bourdon gauges. The tappings to monitor pressure distribution inside the HDS were all led via a simple gate valve to another Bourdon gauge. The gauges were new and recently calibrated. They were generally chosen so that readings would fall roughly in the centre of their ranges (although this was impossible for the gauge to measure HDS pressure), as follows:

Table IV(v): Details of Bourdon Tube Pressure
Gauges on the O.L.R.

	Range of Gauge	Graduations
Pump inlet	0 - 10 psi	0.5 psi
Pump outlet	0 - 300psi	10.0 psi
Upper neckring	0 - 6 bar	0.2 bar
Lower neckring	0 - 10bar	0.2 bar
HDS	0 - 10bar	0.2 bar

Because of the high density of mercury, considerable errors will arise if corrections are not applied for the geodetic head of the gauge above the tapping point. This head was measured with a steel rule to within ±5mm. However, if the measured pressure head was less than the gauge height, the gauge did not register and this limited the measurements that could be taken at small radii in the HDS.

Bleed points were installed just below the gauges to ensure that no air was trapped in the pipe leading to the gauge, thus eliminating another source of error.

As on the water rig, errors due to partial sensing of the dynamic pressure have been minimised by providing square-edge taps of 1mm diameter. The static pressure tap error has been estimated by the method described in Section A(ii) above, for the pump outlet pressure of 3m of mercury at the maximum flowrate ($140\ell.min^{-1}$). Here, with $Re_D = 4.68 \times 10^6$ and $\frac{D_{tap}}{D} = 0.025$, data in Reference (28) gives an error of 0.95% p_{dyn}; i.e. about 4mm of mercury, or 0.1% of the measured pressure. Since the dynamic head falls rapidly with flowrate, whilst the pump outlet pressure rises, this source of error can be neglected.

Therefore, the main cause of error in pressure measurements arises through the limited resolution of the pressure gauges. It was generally possible to estimate the value of a pressure reading to about 20% of the smallest graduation on the gauge (see Table IV(v)). Probable errors for different measurements are presented in Table IV(vi).

Table IV(vi): Estimated Error in Pressure Measurements
on the O.L.R.

	% Error
Pump outlet pressure	1.5 - 3.0
Neckring inlet pressure	2.5 - 5.0
Single stage HDS tip pressure	2
Two-stage (I) HDS Upper disc	6.5
Tip Pressure Lower disc	2.5

(iii) <u>Flowrate</u>

Mercury flowrate on the O.L.R. is measured by two identical
Perspex venturi tubes on parallel branches of the hydraulic circuit.
A diagram of their geometry is presented in Figure IV(iii).

These venturis have not been calibrated experimentally,
although a calibration was carried out on a small scale model in 1974.
The experimental curve agreed with the theoretical Q/Δp curve calculated
for the model, using the formula given in B.S.1042 (which has been
reproduced for the convenience of the reader below):

$$Q_{vol} = 0.01252 \ C_v Z_R ED^2 \sqrt{\frac{\Delta H}{\rho}} \quad (m^3 h^{-1}) \qquad \ldots \ (IV.6)$$

where D = throat diameter (mm)

ΔH = pressure difference across the contraction (mm of water).

Values for C_v, Z_R and E may be found from B.S.1042.

Equation (IV.6) was therefore used by ICI personnel to produce
the conversion chart for the full sized venturis, which is presented in
Figure IV(iv), together with the points calculated by the present author
as a check.

The maximum discrepancy between the ICI conversion chart and
recently calculated data occurs at pressure differences of 200 and 250mm
of mercury. According to the present author, the flowrate should be
$2\ell.min^{-1}$ less than that indicated on the main curve.

Therefore the accuracy of flowrate measurement has been taken
as $\pm 2\ell.min^{-1}$ at $60\ell.min^{-1}$, or $\pm 3.5\%$. As with the water trials, a
high accuracy of flowrate measurement is not essential below about
$20\ell.min^{-1}$, since the pump characteristics for head and absorbed power
are very flat in this region of operation.

(iv) <u>Absorbed Power</u>

The gross input power to the O.L.R. induction motor was monitored by two Wattmeters. The resultant figure consists of power absorbed by the pump, plus power losses in the motor, seals and bearings. A correction factor for motor efficiency may be extracted from Table 6.1. for normal loads, but the efficiency for the single stage HDS trials, when the motor was overloaded, was unknown (see Appendix XV.C).

The magnitude of parasitic power losses with the standard pump was estimated as roughly 240W (see Chapter 7.3.2). A similar value was found when the two-stage (I) HDS was fitted on the pump, but the large end load caused by the single stage HDS, combined with the inefficiency of the motor on overload, increased the losses to 430W.

As a result of these uncertainties, the accuracy of nett absorbed power data is thought to be +6%.

(v) <u>Leakage Flowrate</u>

The limitations of the method for measuring neckring leakage on the O.L.R. which involved collecting small volumes (i.e. about 1ℓ) of mercury for a period of only 10 seconds, are described in detail in Chapter 7.1. The error in time measurement, caused mainly by variations in operator reaction time for diverting the leakage flow into the collecting vessel, may be as high as +0.5 seconds, i.e. +5%. An error also occurs in the measurement of fluid volume. This was carried out in a graduated cylinder, reading to the nearest 5ml., i.e. with an accuracy of +0.5%.

However, random errors in the volume collected may have arisen due to splashing of mercury both in and out of the collecting vessel. Furthermore, it is not certain whether the distribution of leakage flow between the two holes in the support tube was constant. The magnitude of the error associated with these factors has been estimated in Chapter 7.1 as +10%.

Therefore the overall accuracy of leakage flow measurements on the mercury rig is unlikely to be better than +15%.
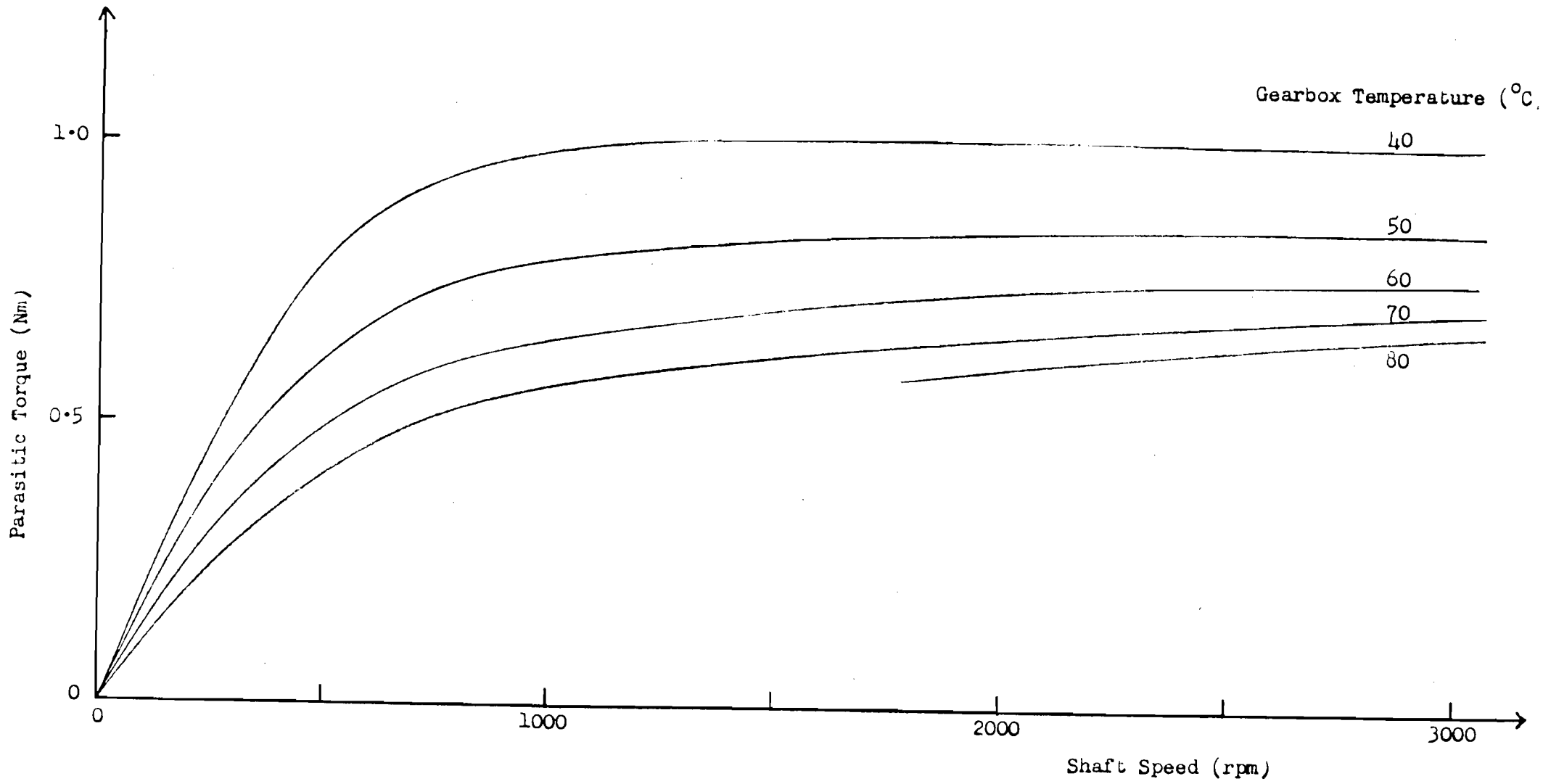
FIGURE IV (i). PARASITIC TORQUE CURVES FOR WATER RIG: GEARBOX WITH SEALED LUBRICATION SYSTEM.
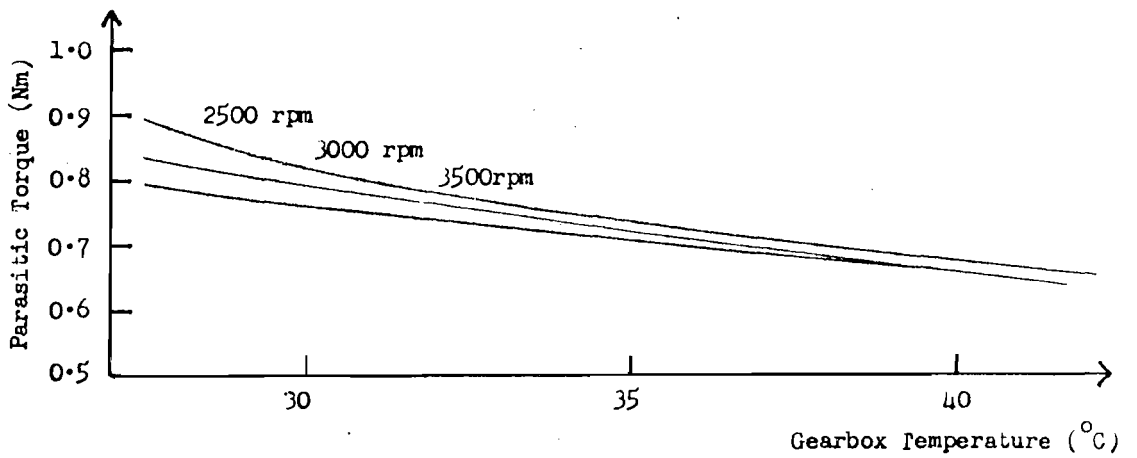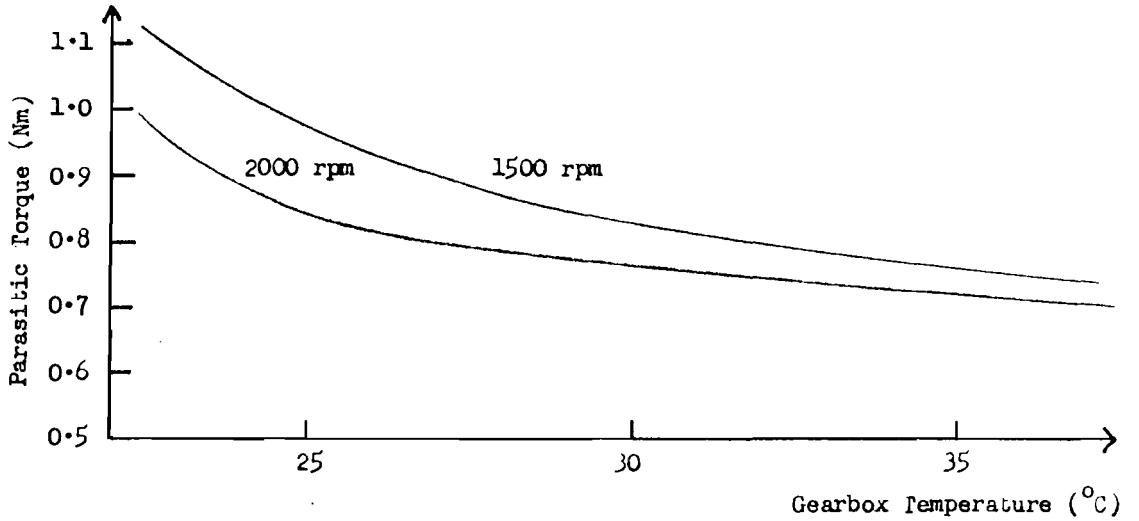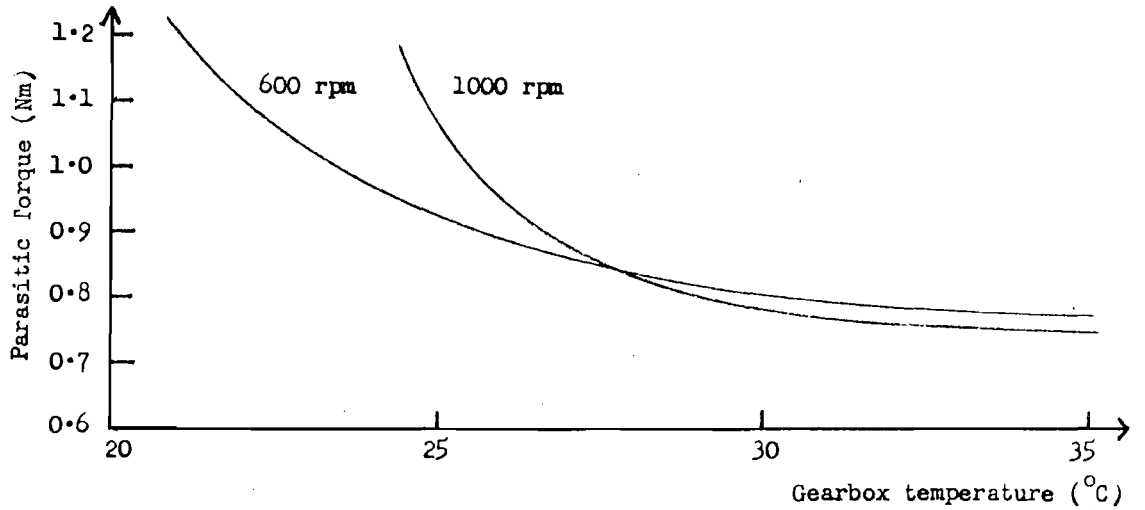
FIGURE IV(ii). PARASITIC TORQUE CURVES FOR WATER RIG: GEARBOX WITH CIRCULATORY LUBRICATION SYSTEM.
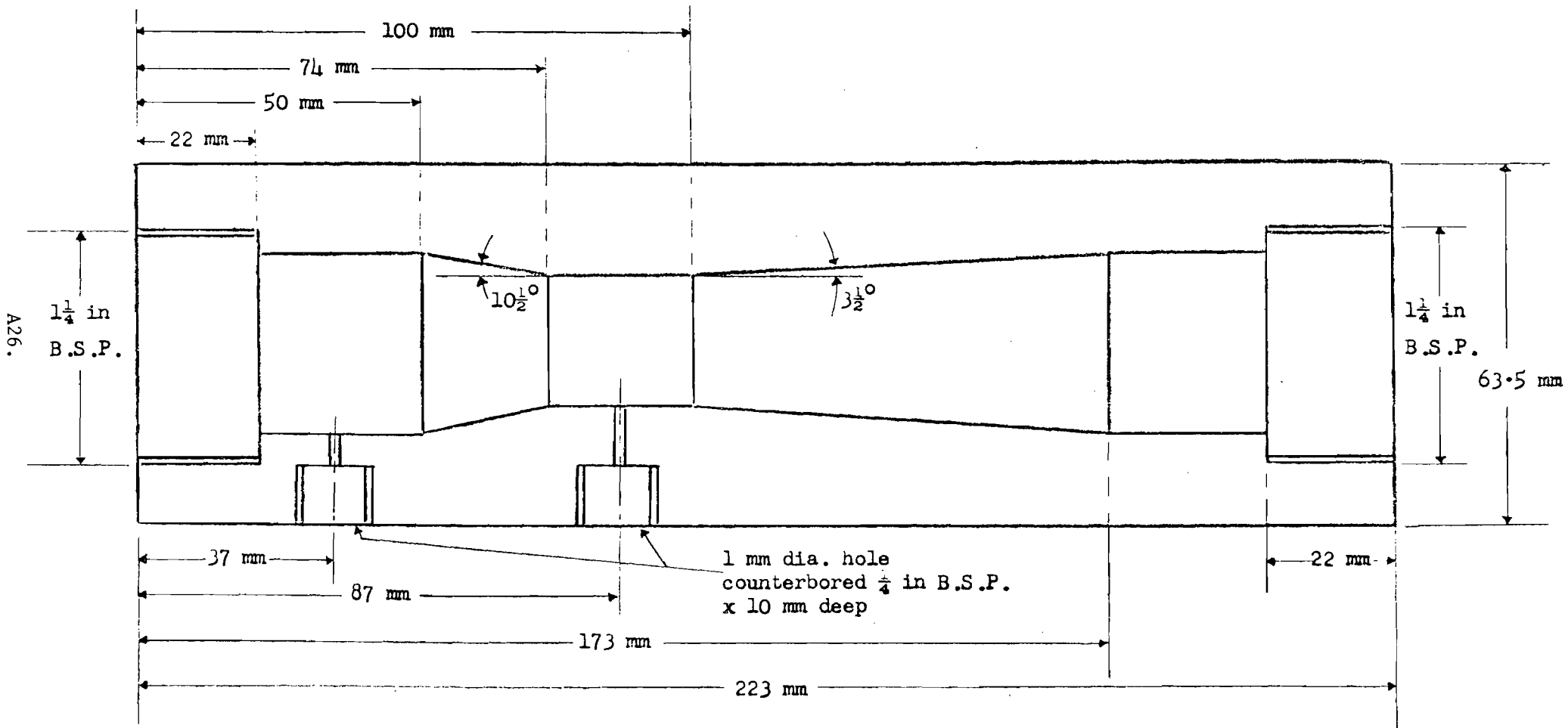
FIGURE IV(iii). GEOMETRY OF VENTURI TUBES ON THE O.L.R.

Y-axis: Mercury Flowrate (ℓ. min^{-1})

X-axis: $\triangle$ H (mm of mercury)

I.C.I. curve (March 1974)

Points calculated by the present author
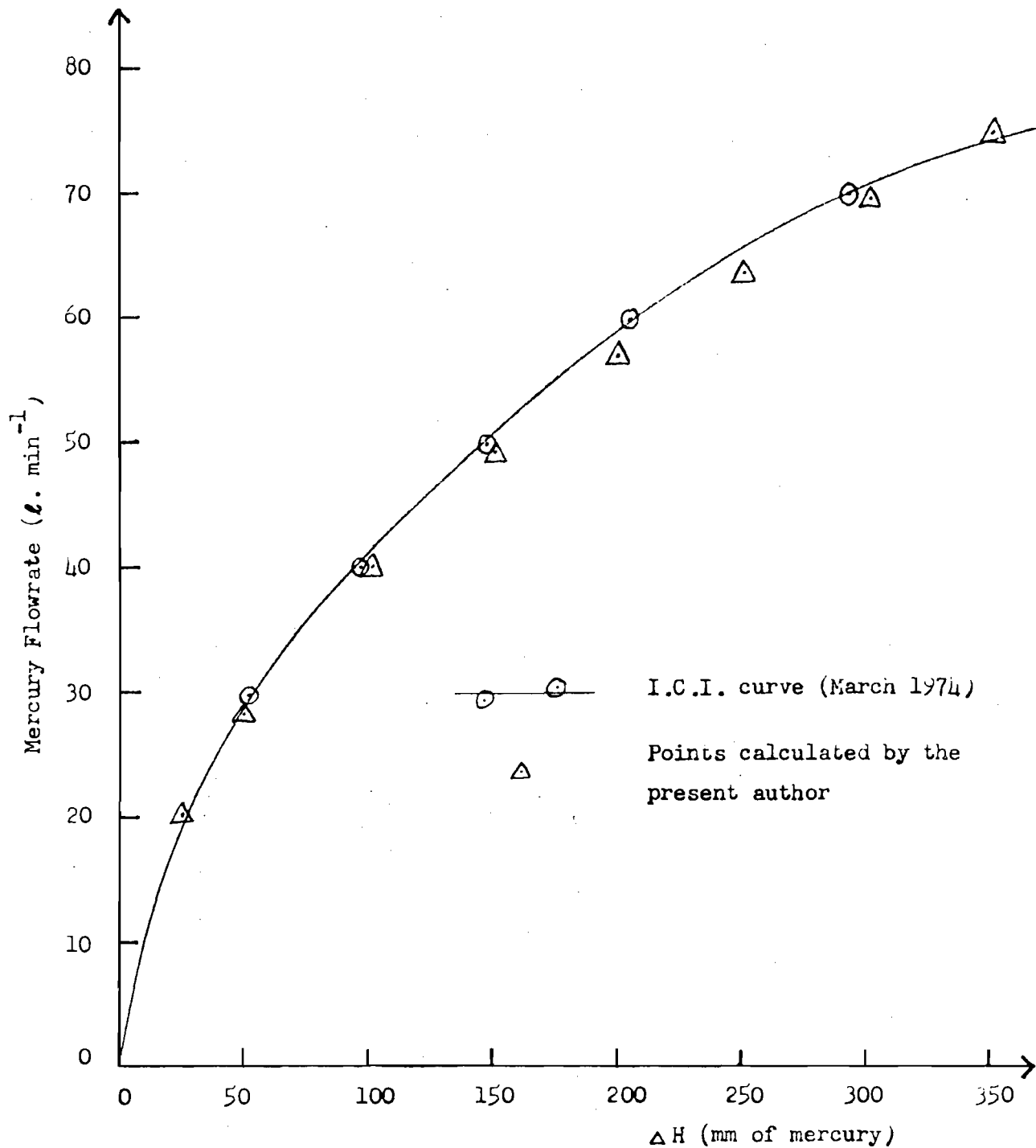
FIGURE IV(iv). CALIBRATION CURVE FOR VENTURI TUBES ON THE O.L.R.

APPENDIX V

METHODS OF SURFACE REPLICATION

Pilot tests were carried out to investigate the accuracy of the "Technovit" replicating method. This simple procedure involves the mixing of a powder and liquid in roughly the proportions 3:5. The mixture is then poured onto the surface to be replicated and allowed to set for 15 minutes. Plasticine may be used to confine the liquid within a desired area.

An attempt was made to produce 4 replicas:

(a) Inside surface of the impeller from the pump used in the present project (hereafter called impeller A) after cleaning.*

(b) Inside surface of impeller A , unprepared.

(c) Inside surface of another design of pump impeller (impeller B), after cleaning.*

(d) Inside surface of impeller B, unprepared.

*Surfaces were cleaned by brushing with a wire brush to remove rust, followed by rinsing thoroughly in acetone.

The replicas were allowed to set for somewhat longer than the recommended time (∿25 minutes). It was then found that they were extremely hard to remove and had to be chiselled free of the surface. The 2 replicas on the unprepared surface had adhered so firmly that they shattered during removal. However, since there was much loose rust impregnated on the replicas' surfaces, it was felt that they did not form a true model of the original. This was to be expected and confirms that thorough cleaning of the surface beforehand is necessary.

The most difficult replica to prise free was the one which was bounded on 2 opposite sides by the impeller vanes (rather than by

plasticine). The resin probably expands during setting and if it is totally constrained, compression stresses will be set up. A more mobile form of boundary, such as plasticine, is advisable.

The replica of the clean impeller A surface was examined on the Talysurf machine (see Chapter 8.4) which gave a CLA value of 1.9μm. The CLA of the original surface was found to be 7.0μm.

Since the Technovit replica was so inaccurate, another replica of the same surface was made using the kit supplied by Talysurf. This involves a similar routine (i.e. mixing a powder and liquid) but the quantities are pre-measured, giving sufficient resin for about two replicas. The CLA of the Talysurf replica was 7.5μm.

These preliminary tests indicated that the Technovit method is not a reliable form of surface replication, at least for the degree of roughness encountered in the present project. The Talysurf method seems superior. Therefore further tests were carried out to compare the two methods.

This time the original surfaces (of both impellers) were thoroughly cleansed by wire brushing, washing in Teepol and rinsing in acetone. Despite these efforts, it was impossible to remove all surface rust from impeller B.

Technovit and Talysurf replicas were taken from adjacent areas of each impeller. A 1% Teepol solution was used as a freeing agent for the Technovit samples, which slightly eased removal, although a chisel still had to be used. A freeing agent is supplied with the Talysurf kits, but these replicas were also difficult to remove. The rough surface provides an excellent key.

CLA measurements and surface traces were made for each replica and the corresponding original surface. In all cases, the

CLA exceeded 10μm, which is the upper limit of the Talysurf machine, thus preventing direct comparison of roughness figures. It is interesting that the previous CLA of impeller A surface was only 7.0μm; possibly the surface was more thoroughly cleaned for the present tests.

Trace Results*

(a) Runs 9 and 10 (Talysurf replica) and 1 and 2 (corresponding surface of impeller A): see Figures V(i) and V(ii).

   The main peaks and troughs appear to be of similar height, but the replicas exhibit more secondary irregularities.

(b) Runs 7 and 8 (Technovit replicas) and 3 and 4 (corresponding surface of impeller A): see Figures V(iii) and V(iv).

   The average peak-trough height appears to be less for both the replica runs than for the original surface traces.

(c) Run 11 (Technovit replica) and 5 (corresponding surface of impeller B): see Figure V(v).

   The general characteristics of both traces are similar.

(d) Run 12 (Talysurf replica) and 6 (corresponding surface of impeller B): see Figure V(vi).

   Both traces are similar. Deep troughs are more prevalent than in traces 11 and 5 (which one would expect to be similar).

Since the above tests were inconclusive, an area on top of impeller B vane, which appeared smoother, was chosen for further runs. Again CLA measurements and traces were carried out on the original and replicated surfaces.

Footnote: *The Talysurf traces are presented at the end of this Appendix. Note that the replica trace is inverted with respect to the corresponding trace of the original surface.

Results

(a)   Runs 14 (Talysurf replica) and 13 (corresponding surface of
        impeller B vane): see Figure V(vii).

Replica CLA   : 8.6μm and 7.6μm (two measurements)

Original surface CLA   : 7.6μm.

Similar type of trace overall, but again the replica exhibits
excess secondary irregularities.

(b)   Runs 16 (Technovit replica) and 15 (corresponding surface
        of impeller B vane): see Figure V(viii).

Replica CLA   : 7.6μm and 7.1μm (two measurements)

Original surface CLA   : 9.7μm.

The trace of the original surface shows that is is considerably
rougher than is indicated by the replica trace.

Conclusions

Neither of the replicating methods is 100% reliable for the
degree of surface roughness under investigation. In fact, Talysurf
recommend that their kits should only be used in the range 0.2-4.0μm
CLA.

However, the Talysurf method appears to reproduce the primary
surface irregularities more accurately than the Technovit method. It
is also quicker since no measurements of ingredients, or cleaning of
mixing vessels afterwards, have to be carried out.

In addition, these tests have shown that the surface texture
of the pump impellers is really too rough to be measured by the Talysurf
presently available. However, if the Mitronic (see Chapter 8.4) were
used (pick-up stylus consists of a 1mm radius sphere) too many of the
irregularities would be smoothed out on a trace.

More sophisticated equipment was ordered for the Talysurf,
including an average wavelength meter (to provide information regarding
the long-term waviness of surfaces) and a side-acting gauge head. The

latter would allow a longer stylus to be fitted, thereby reducing the present trace magnification by a factor of 5 or 10 and increasing the upper limit of CLA measurement to 50μm and 100μm. Unfortunately neither instrument arrived in time for the present investigations.

Run 1

Original surface
of impeller A
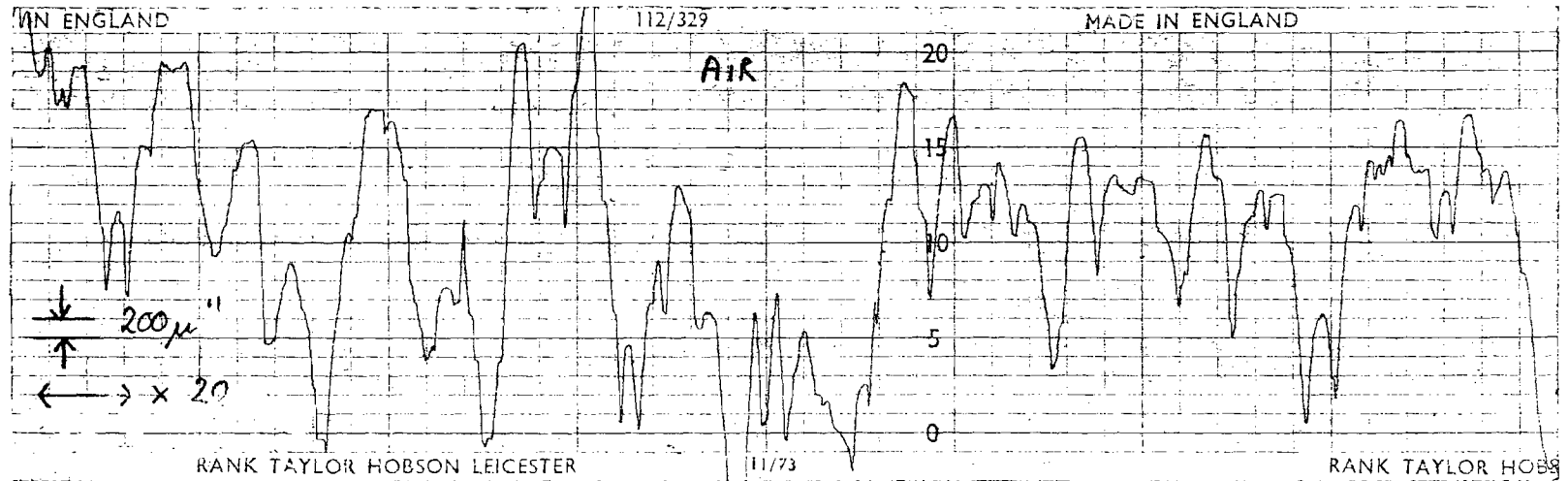
10+μm CLA

Run 9

Talysurf replica of
impeller A surface.

1J+μm CLA.
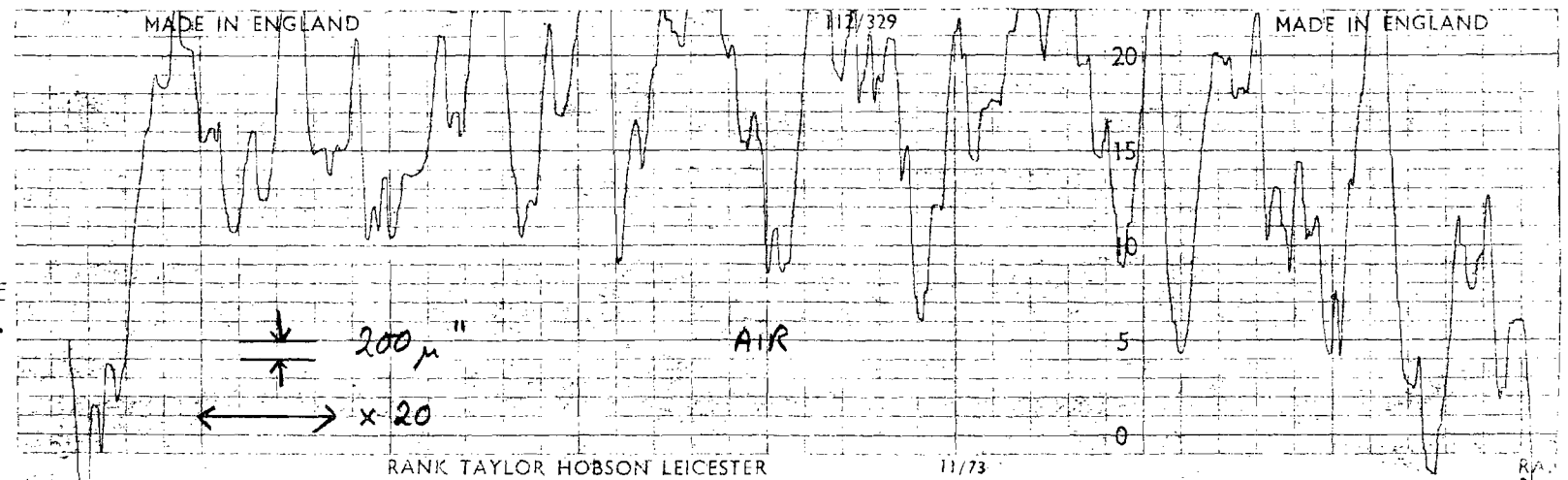
FIGURE V(i): TALYSURF TRACES OF ORIGINAL SURFACE AND OF TALYSURF SURFACE REPLICA FOR IMPELLER A.

Run 2

Original surface
of impeller A
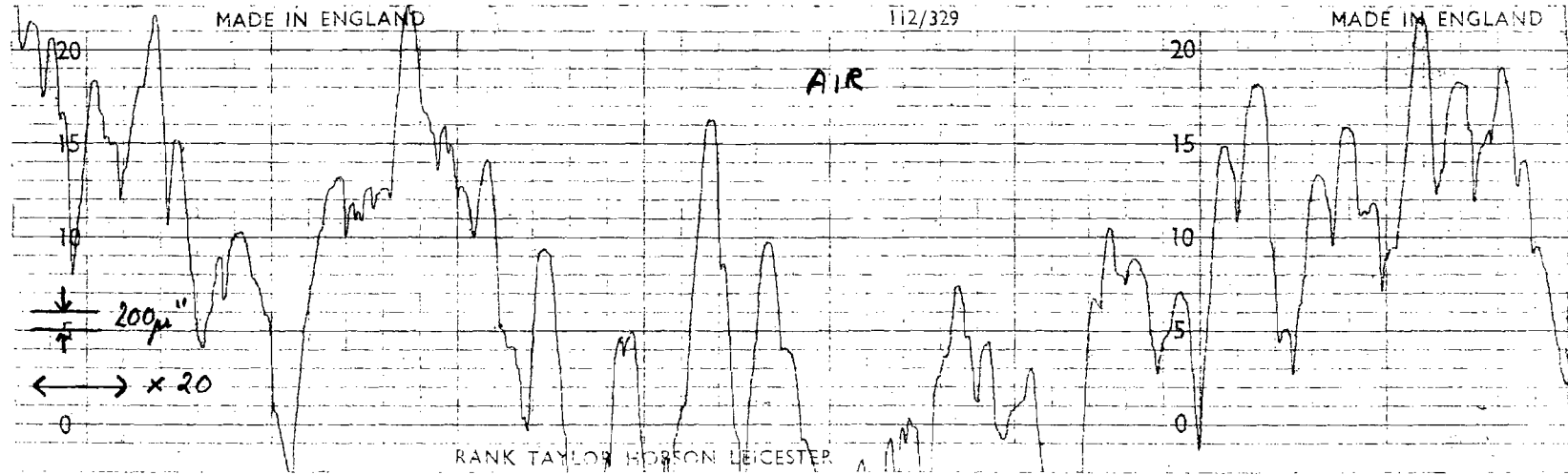
10+µm CLA

Run 10

Talysurf replica of
impeller A surface
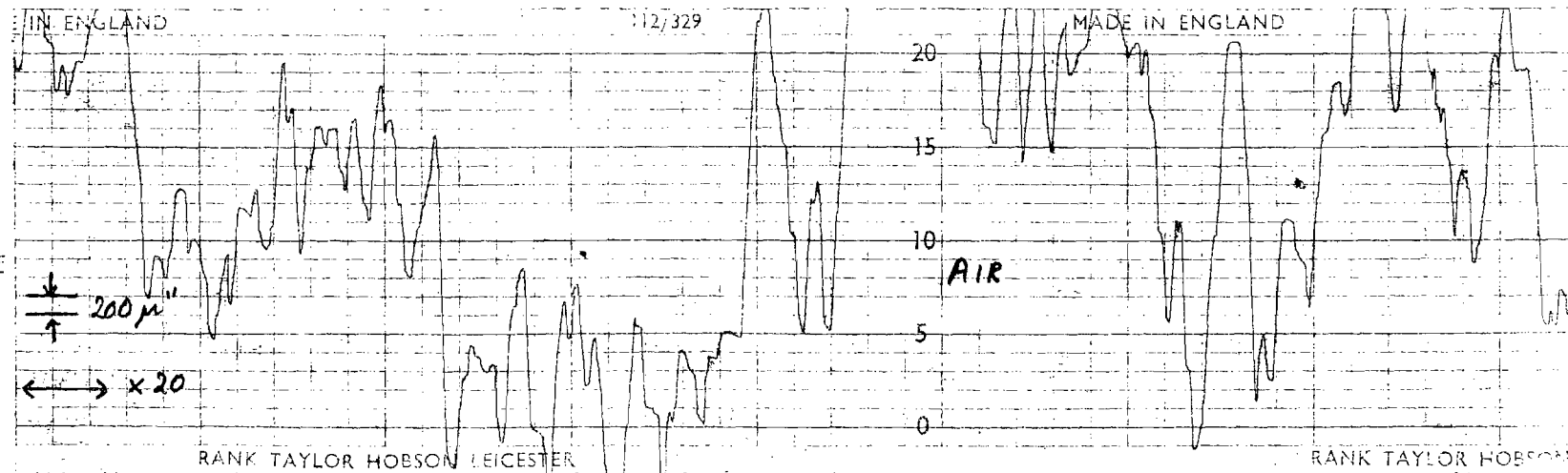
10+µm CLA.

FIGURE V(ii): TALYSURF TRACES OF ORIGINAL SURFACE AND OF TALYSURF SURFACE REPLICA FOR IMPELLER A

Run 3

Original surface
of impeller A
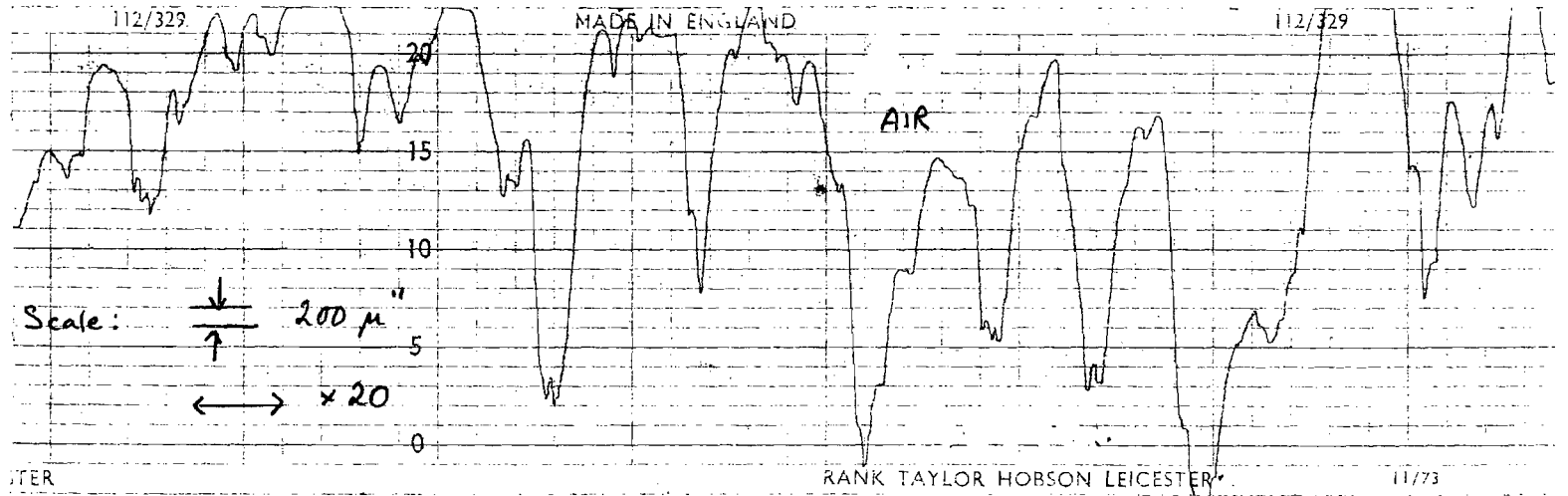
10+μm CLA

Run 7

Technovit replica of
impeller A surface

10+μm CLA
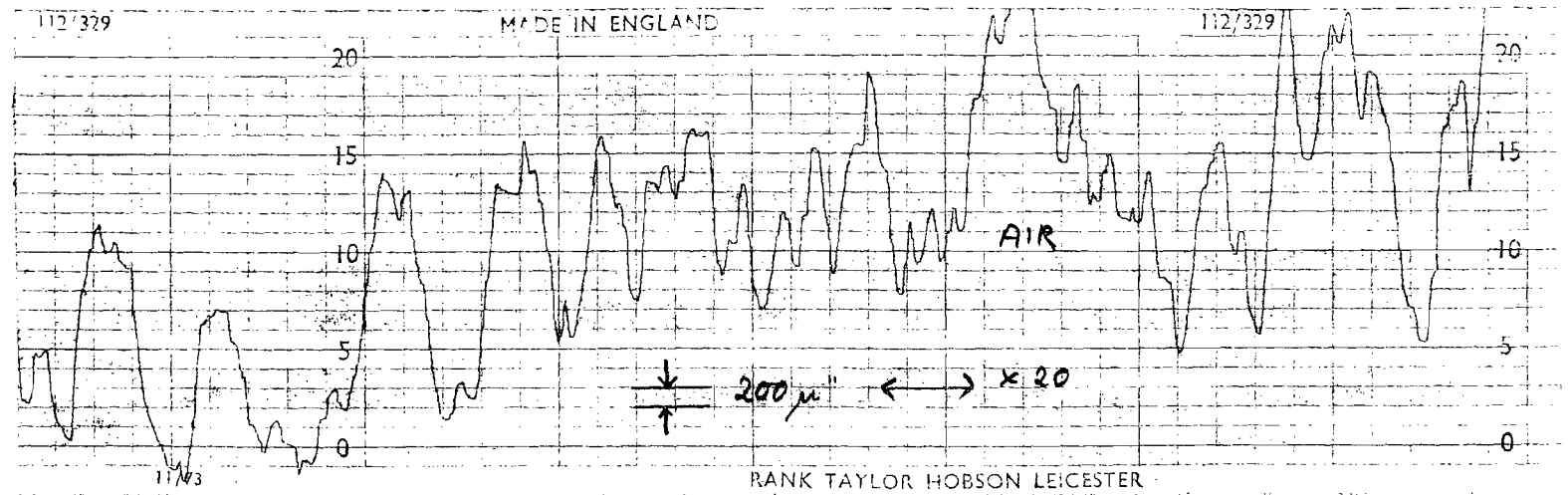
FIGURE V(iii): TALYSURF TRACES OF ORIGINAL SURFACE AND OF TECHNOVIT SURFACE REPLICA FOR IMPELLER A.

Run 4

Original surface
of impeller A

10+µm CLA
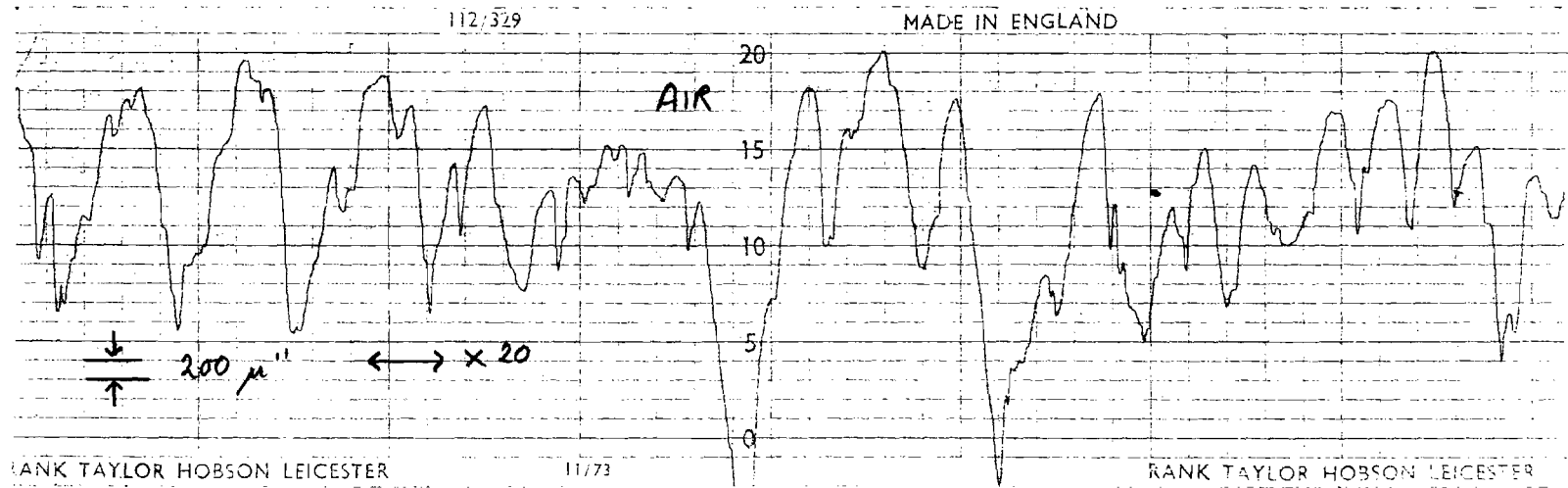
Run 8

Technovit replica
of impeller A surface

10+µm CLA
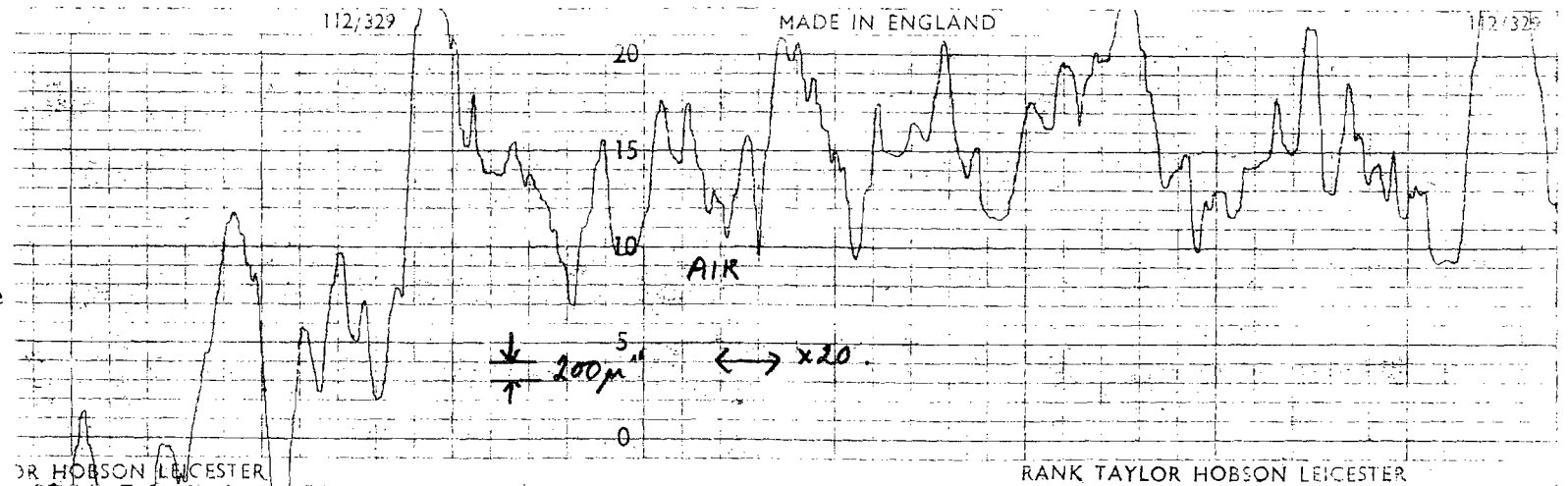
FIGURE V(iv): TALYSURF TRACES OF ORIGINAL SURFACE AND TECHNOVIT SURFACE REPLICA OF IMPELLER A

Run 5

Original surface
of impeller B.

10+µm CLA
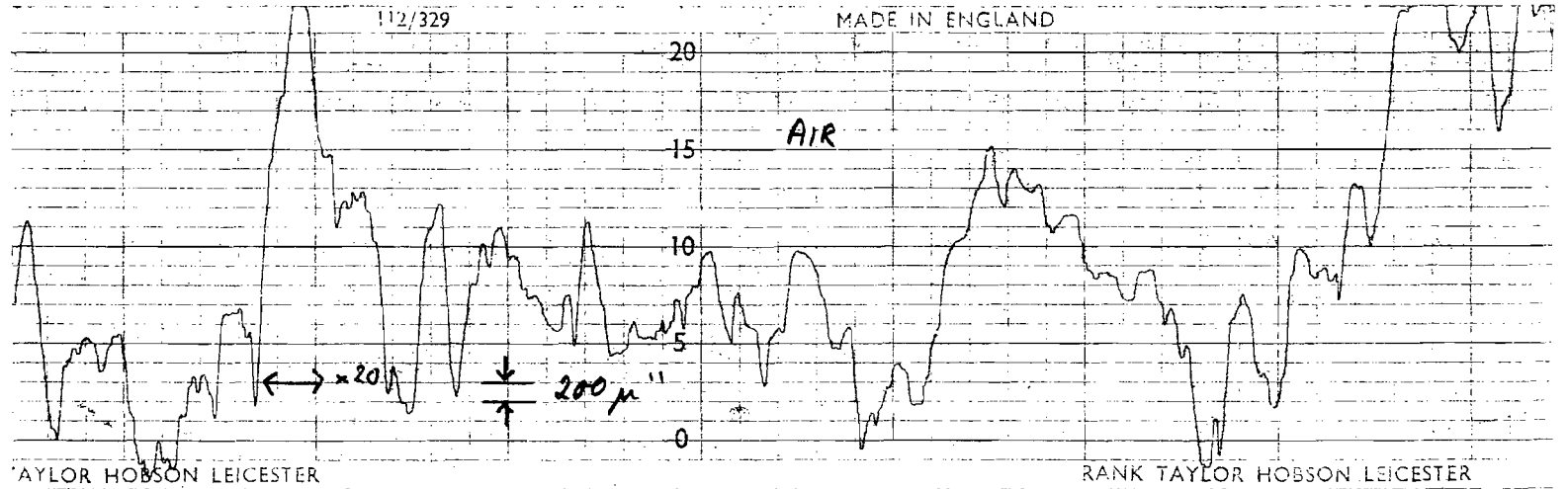
Run 11

Technovit replica of
impeller B surface

10+µm CLA.
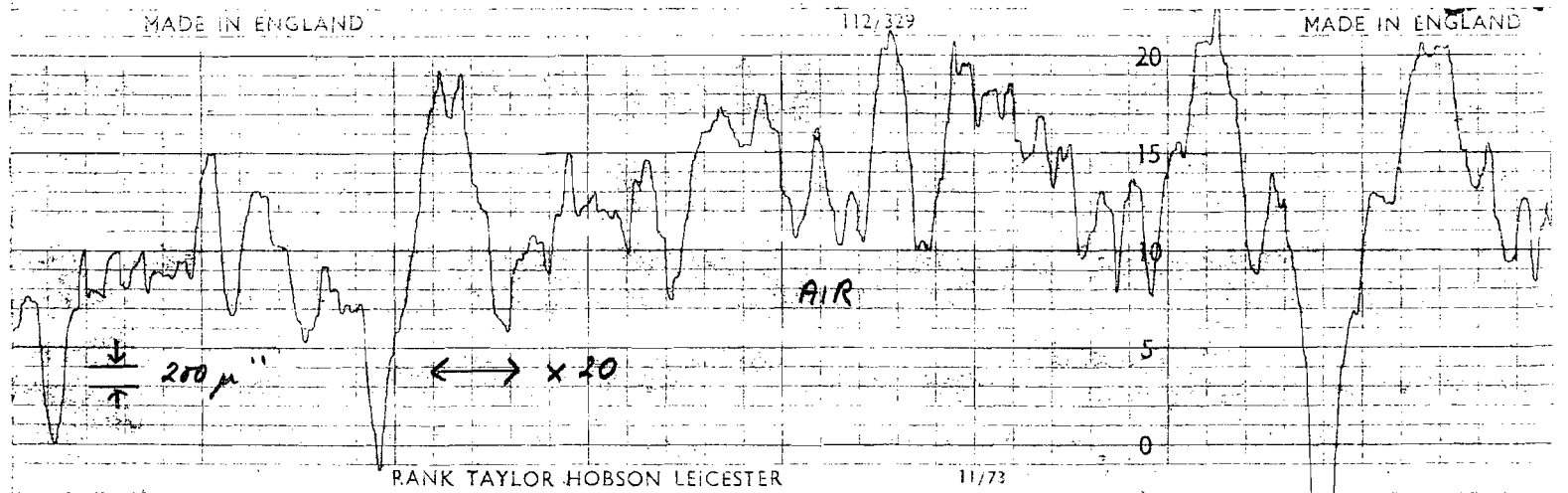
FIGURE V(v): TALYSURF TRACES OF ORIGINAL SURFACE AND OF TECHNOVIT SURFACE REPLICA FOR IMPELLER B.

Run 6

Original surface of
impeller B

10+μm CLA
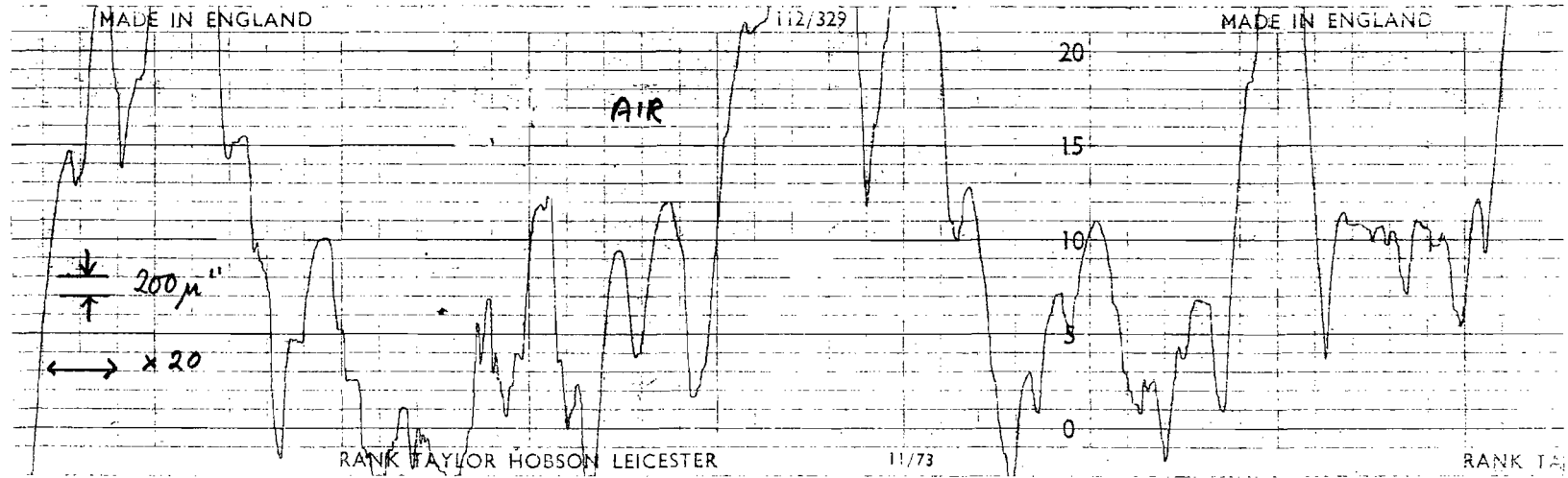
Run 12

Talysurf replica of
impeller B surface

10+μm CLA.
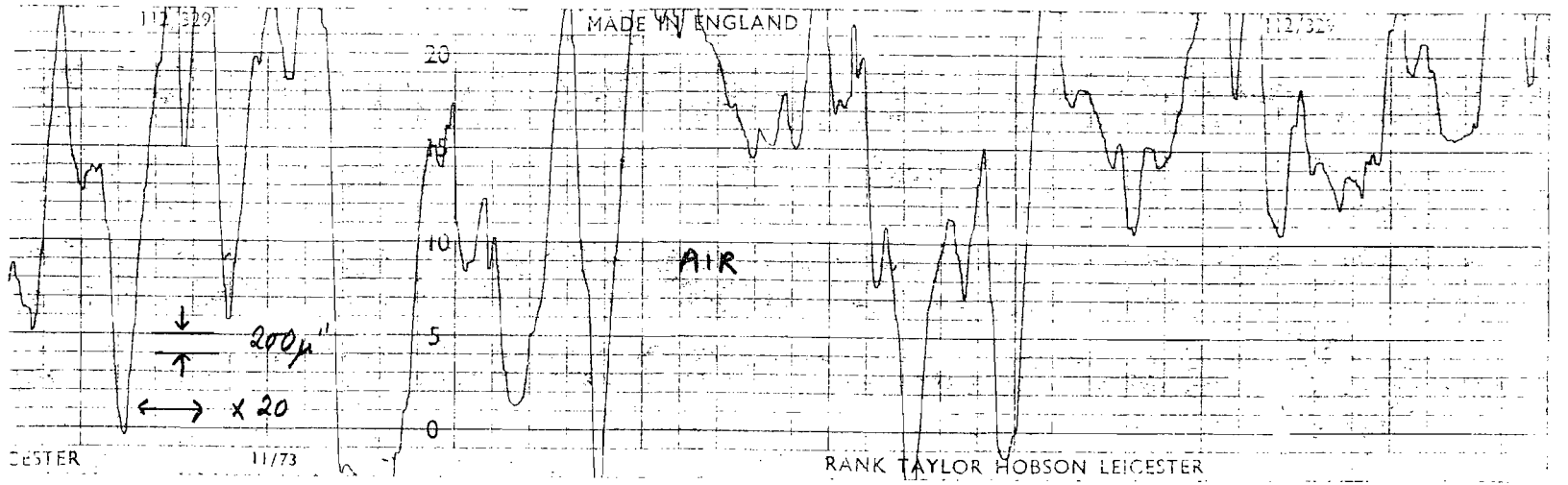
FIGURE V(vi): TALYSURF TRACES OF ORIGINAL SURFACE AND OF TALYSURF SURFACE REPLICA FOR IMPELLER B

Run 13

Original surface of
impeller B vane

7.6μm CLA
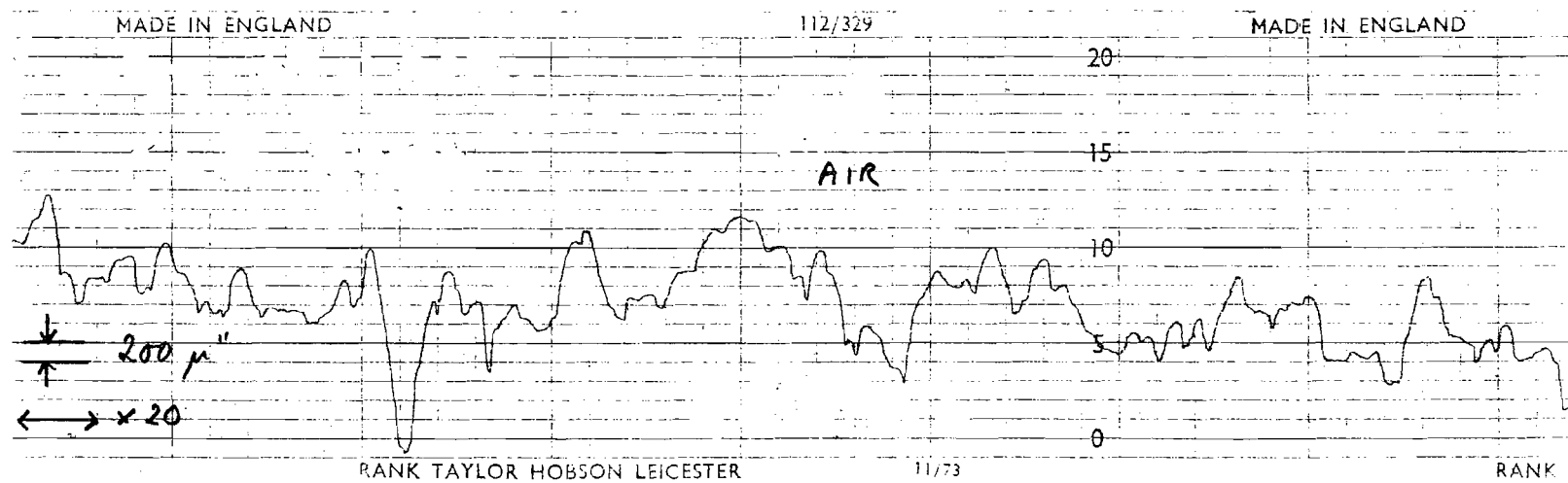
Run 14

Talysurf replica of
impeller B vane

8.6
7.6 }μm CLA
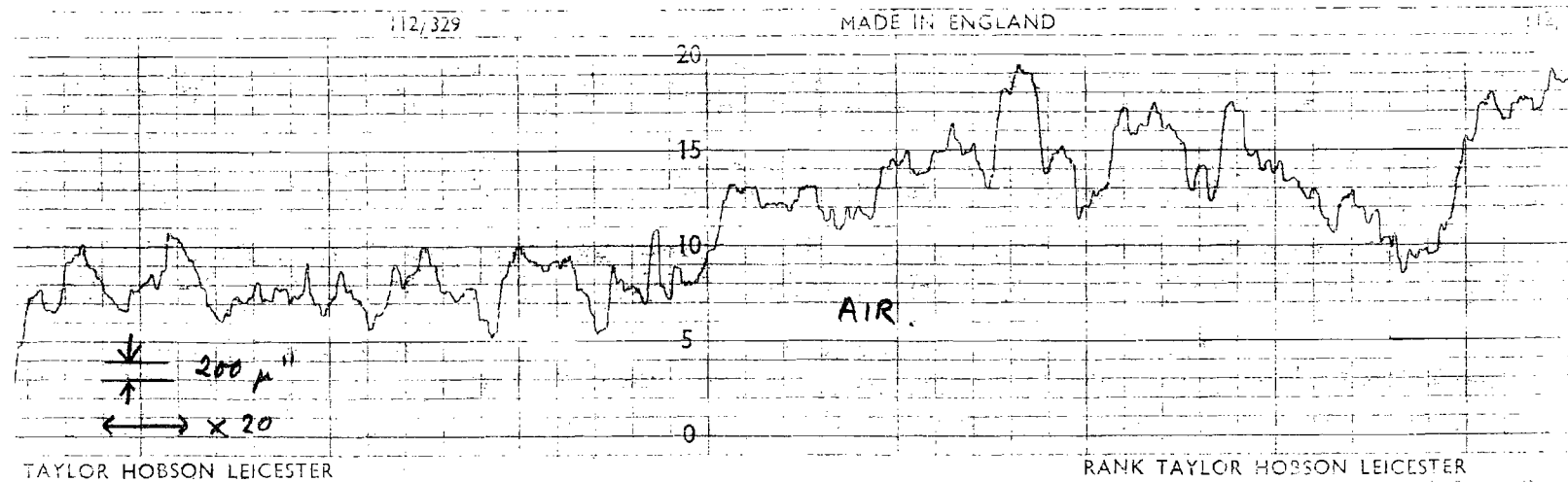
FIGURE V(vii): TALYSURF TRACES OF ORIGINAL SURFACE AND OF TALYSURF SURFACE REPLICA FOR IMPELLER B VANE.

Run 15

Original surface
of impeller B vane

9.7μm CLA
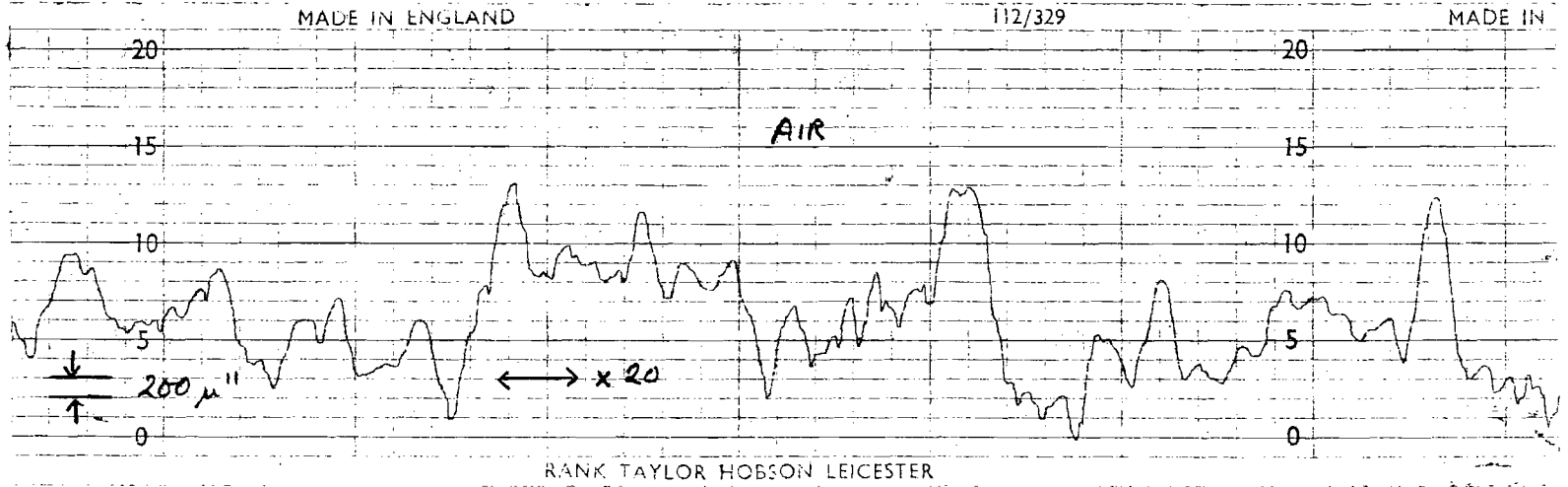
Run 16

Technovit replica of
impeller B vane.

7.6
7.1 }μm CLA
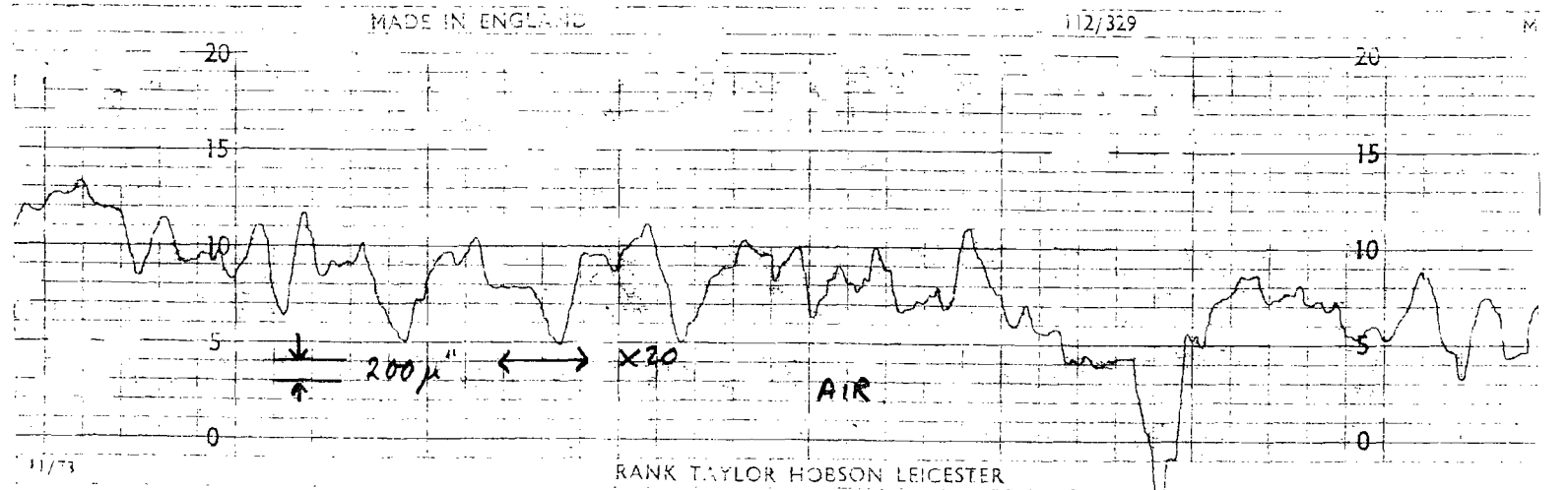
FIGURE V(viii): TALYSURF TRACES OF ORIGINAL SURFACE AND OF TECHNOVIT SURFACE REPLICA FOR IMPELLER B VANE

APPENDIX VI

NUMERICAL EXAMPLE OF CALCULATIONS FOR PREDICTING FLOWRATE THROUGH AN ANNULAR SLOT[35]

From Appendix I, the relevant pump dimensions are:

Radial neckring clearance (h):   0.165mm.

Impeller hub O.D. (D):   50.65mm.

Upper neckring length (L):   11.0mm.

$$\therefore \quad A_{sl} = \pi[50.65 + 0.165]\ 0.165\text{mm}^2$$

$$= 26.3\ \text{mm}^2.$$

To predict the upper neckring leakage rate at 1500 rpm in cold water, the following data is required:

Differential pressure head across seal (ΔH_{sl}) = 3.57m of water
(see Figure 38)

Measured upper neckring leakage rate = $8.9\ell.\text{min}^{-1}$ (see Figure 34).

$$\nu \text{ (cold water)} = 1.0 \times 10^{-6}\ \text{m}^2\text{sec}^{-1}.$$

$$\ell \text{ (cold water)} = 10^3\ \text{kg.m}^{-3}.$$

$$\text{Re}_u = \frac{2hu}{\nu}\ , \quad \text{where } u = \frac{\omega D}{2}\ .$$

$$\therefore \quad \text{Re}_u = \frac{2 \times 0.165 \times 10^{-3} \times \pi \times 50.65 \times 10^{-3} \times 1500}{1.0 \times 10^{-6} \times 60}$$

$$\approx 1,300.$$

$$Re_{\bar{y}} = \frac{2h\bar{y}}{\nu}, \quad \text{where } \bar{y} = \frac{Q_{s1}}{A_{s1}}.$$

$$\therefore \quad Re_{\bar{y}} = \frac{2 \times 0.165 \times 10^{-3} \times 8.9 \times 10^{-3}}{1.0 \times 10^{-6} \times 60 \times 26.3 \times 10^{-6}}$$

$$\approx 1,860.$$

From Figures 36a and b:

$$\lambda \approx 0.05$$

$$\zeta_{io} \approx 1.7.$$

Since

$$\theta = \frac{1}{\sqrt{(\frac{\lambda L}{2h} + \zeta_{io})}} \qquad \qquad \ldots (5.20)$$

we have

$$\theta = \frac{1}{\sqrt{(\frac{0.05 \times 11 \times 10^{-3}}{2 \times 0.165 \times 10^{-3}} + 1.7)}}$$

$$= 0.545.$$

From equation 5.19, the slot flowrate is given by:

$$Q_{s1} = \theta A_{s1} \sqrt{(2g\Delta H_{s1})}$$

Substituting the relevant values:

$$Q_{s1} = 0.545 \times 26.3 \times 10^{-6} \ (2 \times 9.81 \times 3.57)$$

$$= 0.12 \ell.sec^{-1} \text{ or } 7.2\ell.min^{-1}.$$

APPENDIX VII

CAVITATION CHARACTERISTICS OF THE PUMP

The N.P.S.H. requirements for the pump operating in water at 1450 rpm were investigated by the pump manufacturer in November 1974. Their results are reproduced in Figure 3.

The N.P.S.H. of a pump is defined by the following equation:

$$\text{N.P.S.H.} = \frac{p_1}{\rho g} + \frac{c_1^2}{2g} - \frac{p_v}{\rho g} \qquad \dots \text{(VII.1)}$$

If the inlet pressure head $(\frac{p_1}{\rho g})$ is less than the calculated value given by:

$$\text{N.P.S.H.} - \frac{c_1^2}{2g} + \frac{p_v}{\rho g}$$

then cavitation is likely to occur in the pump inlet.

The variation of mercury vapour pressure with temperature is presented in Table VII(i). It is noteworthy that at all temperatures, the absolute value of vapour pressure is very low.

TABLE VII(i)

Variation of Mercury Vapour Pressure with Temperature[62]

Temperature °C	Vapour Pressure (mm of mercury)
20	0.001201
30	0.002777
40	0.006079
50	0.01267
60	0.02524

Therefore, even in hot mercury, the vapour pressure term in equation (VII.1) $(\frac{P_v}{\rho g})$ is negligible.

In order to calculate the dynamic pressure head $(\frac{c_1^2}{2g})$, we require the value of fluid inlet velocity c_1. This is given by $\frac{Q}{A_1}$, where A_1 = impeller cross-sectional area. Since the impeller inlet diameter = 0.057m (see Appendix I),

$$A_1 \simeq \pi(0.03)^2 \simeq 2.8 \times 10^{-3} \text{ m}^2$$

Consider operation of the pump at 140ℓ.min^{-1} and 1450 rpm in cold mercury. Extrapolation of Figure 3 for the smallest seal clearance gives an N.P.S.H. requirement of 3m of water at this flowrate, which is equivalent to 0.22m of mercury.

$$c_1 = \frac{Q}{A_1} = \frac{140 \times 10^{-3}}{60 \times 2.8 \times 10^{-3}} = 0.76 \text{m.sec}^{-1}$$

$$\therefore \quad \frac{c_1^2}{2g} = 0.029.$$

Therefore, neglecting the vapour pressure term, if cavitation is to be suppressed:

$$\frac{P_1}{2g} \geqslant 0.19m.$$

Since the measured inlet pressure head fluctuated between 0.125 and 0.16m of mercury at this point of operation, cavitation must have occurred.

Although the vapour pressure term has been neglected in this calculation, it is important to note that the vapour pressure of mercury increases more than 10-fold between $20^{\circ}C$ and $50^{\circ}C$, (Table VII(i)) so cavitation will be more severe at the higher temperature.

Similar calculations for a flowrate of $119\ell.min^{-1}$ give the following results:

$$N.P.S.H. = 0.11m \text{ of mercury (from Figure 3)}$$
$$c_1 = 0.65m.sec^{-1}$$
$$\frac{c_1^2}{\rho g} = 0.02m.$$

$\therefore$ For no cavitation:

$$\frac{P_1}{\rho g} \geqslant 0.11 - 0.02 = 0.09m \text{ of mercury.}$$

Since the measured inlet pressure was 0.16m of mercury, operation at this flowrate will be cavitation free.

Data from Figure 3 has also been used to calculate the inception value of suction specific speed S_{inc} for the pump, where:

$$S_{inc} = \frac{N\ Q^{\frac{1}{2}}}{E_{V(inc)}^{\frac{3}{4}}} \qquad \ldots \text{(VII.2)}$$

$E_{V(inc)}$ is the net suction energy at cavitation inception, or NPSH x g.

S_{inc} is generally calculated for the best efficiency point, to ensure regular flow conditions at the impeller inlet. A high value of S_{inc} shows good pump design.

At 1450 rpm, the best efficiency occurs at 110 ℓ.min^{-1} (from Fig.85). NPSH = 1.4m of water (Figure 3).

$$\therefore \quad S_{inc} = \frac{\frac{2\pi \ 1450}{60} (\frac{0.110}{60})^{\frac{1}{2}}}{(1.4 \times 9.81)^{\frac{3}{4}}} = 0.91.$$

Empirical results from pumps of proven design show that $2.5 < S_{inc} < 3.5$ for good cavitation characteristics, although pumps do exist with $S_{inc} = 1.8$[77]. In comparison, the figure calculated above is exceptionally low.

At the duty flowrate, ($Q = 55$ ℓ.min^{-1}), NPSH = 0.29m of water (from Figure 3)

$$\therefore \quad S_{inc} = \frac{\frac{2\pi \ 1450}{60} (\frac{0.055}{60})^{\frac{1}{2}}}{(0.29 \times 9.81)^{\frac{3}{4}}} = 2.1.$$

This value is still very low. S_{inc} is a function of the shape of inlet flow passages, which are poorly designed in the present pump. This fact is confirmed by the calculations in Chapter 2.4, which show that fluid prewhirl is necessary to avoid high shock losses at the impeller inlet.

APPENDIX VIII

HYDRODYNAMIC SEAL DESIGN

1. Single Stage Seal

The new seals were designed in January 1978 and their manufacture was set in hand before any data was available regarding neckring pressures. The seal dimensions were therefore based on theoretical calculations of the pressure drop across the back of the impeller, as set out below:

1a) Calculated Pressure at Seal Entrance

Pump specifications at design point:

Speed:	1450 r.p.m.
Generated head:	5.9m (19.5ft) of mercury at 80°C
Flowrate:	55 ℓ.min^{-1}
Absorbed power	2.4kW (3.2 HP)
(Pump motor rating:	2.6kW)

Impeller dimensions:

Hub radius:	25.3mm	(0.995in)
Impeller tip radius:	71.5mm	(2.813in)

The pump characteristic at 1450 rpm in mercury (Figure 84) shows that the generated head at low flowrates is considerably higher than that at the design point. However, it has been assumed that some leakage of the seal could be tolerated during start-up, and the present calculations are based on the pump operating under design conditions.

Measurements of the head generated by the pump were taken outside the volute casing. Thus, since some pressure recovery will occur inside the volute, the pressure at the impeller exit will be somewhat lower. Nevertheless, a value of 5.9m of mercury has been taken for this pressure, thereby allowing a certain margin of safety.

5.9m of mercury $\simeq$ 775,600 N.m^{-2}.

(Density of mercury at 80°C - the stable operating temperature of the mercury cells - is 13.4 x 10^{3}kg.m^{-3}[37])

There will be a drop in pressure across the back of the impeller, between the impeller tip and hub, due to the rotational motion forced on the mercury by the impeller. This pressure drop (Δp) is given by:

$$\Delta p = \tfrac{1}{2}\rho_m (k\omega)^2 (R_t^2 - R_h^2) \qquad \dots \text{(VIII.1)}$$

According to Thorne and Bower[58], the slip factor k may be taken as 0.5.

Substituting the relevant values in equation (VIII.1) gives:

$$\Delta p \simeq 172,700 \text{ N.m}^{-2}.$$

Therefore, the pressure at the inlet to the hydrodynamic seal will be approximately 603,000 N.m^{-2}.

This is the nett pressure which must be generated by the disc seal for zero leakage flow to occur.

1b) Radius of HDS

Consider pressure at the disc tip (see Figure 120). The smooth surface of the disc will be completely flooded with mercury from the pump casing, entering the seal housing at the pressure calculated in

the previous section. This pressure will increase radially, due to the induced rotation of the fluid. Hence:

$$P_t = P_1 + \tfrac{1}{2}\rho_m(k_s\omega)^2 [R_D^2 - R_h^2] \qquad \ldots \text{(VIII.2)}$$

Mercury on the vaned side of the disc will form an interface with water (which covers the mercury in the pumping tank) at some radius R_i.

Thus the tip pressure is given by:

$$P_t = P_2 + \tfrac{1}{2}\rho_m(k_v\omega)^2(R_D^2 - R_i^2) + \tfrac{1}{2}\rho_w(k_v\omega)^2(R_i^2 - R_h^2) .$$

$$\ldots \text{(VIII.3)}$$

Combining equations (VIII.2) and (VIII.3), we obtain

$$\frac{P_1 - P_2}{\tfrac{1}{2}\omega^2} = \rho_m[k_v^2(R_D^2 - R_i^2) - k_s^2(R_D^2 - R_h^2)] + \rho_w k_v^2(R_i^2 - R_h^2)$$

$$\ldots \text{(VIII.4)}$$

The pressure generated by water inside the interface on the vaned side of the disc is negligible for small values of R_i. Equation (VIII.4) then reduces to the simplified, dimensionless form given in Chapter 10.1:

$$C_p \left[= \frac{P_1 - P_2}{\tfrac{1}{2}\rho_m\omega^2 R_D^2} \right] = k_v^2 (1 - X^2) - k_s^2 (1 - Y^2) \qquad \ldots \text{(10.1)}.$$

At the maximum sealing capability of the disc, $R_i = R_h$. Then:

$$\frac{P_1 - P_2}{\frac{1}{2}\rho_m \omega^2} = k_v^2(R_D^2 - R_h^2) - k_s^2(R_D^2 - R_h^2)$$

$$= (R_D^2 - R_h^2)(k_v^2 - k_s^2) \qquad \dots \text{(VIII.5)}$$

For another safety margin, we shall ignore the static pressure of water above the seal, i.e. say $p_2 = 0$.

Typical values for k_v and k_s are 0.96 and 0.46 respectively[49].

Substituting values in equation (VIII.5), we obtain:

$$R_D = 7.8\text{cm}.$$

Thus, the radius of the seal should be about 8cm.

1c) Power absorbed by HDS

The power input to the seal (P_{in}) is given by:

$$P_{in} = C_M \frac{1}{2}\rho_m \omega^3 R_D^5 \qquad \dots \text{(VIII.6)}$$

According to Reference [49] , $C_M \simeq 0.01$.

Substituting values in the above equation:

$$P_{in} \simeq 0.77 \text{ kW}.$$

At present, the pump absorbs 2.4kW at its design point. An estimated power saving of 0.2kW could be achieved by replacing the upper neckring with a 100% efficient seal (see Chapter 7.3.4). Then the total power absorbed by pump and seal would be ≃3.0kW, i.e. the present pump motors, with a rating of 2.6kW, would be inadequate to drive the pump fitted with a single stage HDS over an extended period of time and an uprated motor would be required if the seal were incorporated in pumps for the manufacturing plant.

1d) Shaft End Load

Since the radial pressure gradient is steeper on the vaned side of the disc than on the smooth side, there will be a nett end load on the disc.

The pressure (p_R) at radius R on the smooth side is given by:

$$p_R \text{(smooth)} \quad = \quad p_1 + \frac{\rho_m}{2} (k_s \omega)^2 (R^2 - R_h^2) \; . \qquad \ldots \text{(VIII.7)}$$

Thus the total end load is given by:

$$EL \text{(smooth)} \quad = \quad \int_{R_h}^{R_D} [p_1 + \frac{\rho_m}{2} (k_s \omega)^2 (R^2 - R_h^2)] \; 2\pi R \; dR \qquad \ldots \text{(VIII.8)}$$

Similarly, for the vaned side (neglecting the effect of water, since this side will be completely flooded with mercury at maximum end load conditions):

$$EL \text{(vaned)} \quad = \quad \int_{R_h}^{R_D} [p_2 + \frac{\rho_m}{2} (k_v \omega)^2 (R^2 - R_i^2)] \; 2\pi R \; dR \qquad \ldots \text{(VIII.9)}$$

The end load on the smooth side will be greater. Hence:

$$\text{Nett EL} \quad = \quad \int_{R_h}^{R_D} [p_1 + \frac{\rho_m}{2} (k_s \omega)^2 (R^2 - R_h^2)] \; 2\pi R \; dR \; -$$

$$\int_{R_h}^{R_D} [p_2 + \frac{\rho_m}{2} (k_v \omega)^2 (R^2 - R_i^2)] \; 2\pi R \; dR. \qquad \ldots \text{(VIII.10)}$$

The maximum end load occurs when $R_i = R_h$.

Also, from equation (VIII.5)

$$P_1 = P_2 + \frac{\rho_m}{2} (R_D^2 - R_h^2)(k_v^2 - k_s^2) \omega^2 .$$

Substituting these values in equation (VIII.10), integrating and simplifying we obtain:

$$EL_{(max)} = \frac{\pi \rho_m \omega^2}{4} (k_v^2 - k_s^2)(R_D^2 - R_h^2)^2 \qquad \dots \text{(VIII.11)}$$

or, in dimensionless form:

$$C_{EL_{(max)}} \left[= \frac{EL_{(max)}}{\tfrac{1}{2}\rho_m \omega^2 R_D^4} \right] = \frac{\pi}{2} (k_v^2 - k_s^2)(1 - Y^2)^2$$

$$\dots \text{(10.3)}$$

Therefore, in the present case:

$$EL_{(max)} = 5720 \text{ Newtons.}$$

This force acts upwards, i.e. in opposition to the weight of the rotating assembly.

1e) <u>HDS   Geometry</u>

i) <u>Number of Vanes</u>

Wood et al [7] found that in a HDS of ∿5.7" (145mm) diameter, 24 impeller vanes was the optimum number. Thew and Saunders [49] showed that increasing the number of vanes on a 5" (127mm) diameter HDS causes an increase in the pressure coefficient C_p and decreases the torque absorption coefficient C_M, but the number of vanes was limited to 24, to simplify fabrication.

For the specific application of sealing the mercury pump, a large number of vanes is preferable since this will reduce churning of

mercury and water within the seal housing. The maximum number compatible with simplicity of design is 16.

ii) Vane Depth

Reference [49] gives 0.06-0.08 as the most favourable ratio for vane depth:HDS tip radius, which compares well with a figure of 0.05 in reference [7]. Applied to the present case (tip radius $\simeq 80mm$) this gives a vane depth between 4.8-6.4mm, say 5.0mm.

iii) Vane Width

According to reference [49], thin vanes give higher C_p values than thick ones, but the torque coefficient C_M also rises, by about twice as much as C_p. In addition, the minimum vane section is controlled by strength considerations, particularly if the disc is to be fabricated by casting. Thus a vane width of at least 4mm is envisaged.

iv) Clearances

The effect of clearances between the HDS housing and impeller tip (S_t), vanes (s_v) and smooth face (s_s) has been investigated in Reference [49]. Tip clearances do not affect C_p, but a minimum in C_M occurs at $s_t \simeq 0.02R_D$. A vane clearance of $0.02R_D$ results in a maximum value of C_p, corresponding to a minimum in C_M.

Since pressure generated on the smooth side of the disc opposes the action of the seal, a minimum of the local pressure coefficient at the disc tip, $\dfrac{P_{tip}}{\frac{1}{2}\rho\omega^2 R_D^2}$ for variation in clearance on this side would be significant. The curves of Thew and Saunders [49] do show a minimum, but it is not well defined. For minimum torque (C_M), they show that the clearance should lie in the range 0.05-0.1R. Applied to the present case (R $\simeq 80mm$):

$$s_v = 1.6mm$$
$$s_s = 4\text{-}8mm \quad (\text{say } 6mm)$$
$$s_t = 1.6mm \quad (\text{say } 2.0mm \text{ to allow for shaft misalignment}).$$

v) <u>Vane Shape</u>

It has been shown[7,49] that optimum performance of a HDS is achieved with backward-curving vanes, but the present design will have straight vanes for ease of fabrication.

2. <u>Two-Stage HDS</u>

In order to reduce the high power consumption calculated in Section 1c, it is worthwhile using a seal consisting of two smaller discs rather than a single 8 cm disc.

To calculate the reduction in disc radius, end load and torque absorption which may be achieved with a two-stage seal, several assumptions are made [49]:

      a) C_p and C_{EL} are invariant with Reynolds Number

      b) $C_m \propto Re_\omega^{-1/m}$

      c) The stages all run full

      d) No interaction occurs between stages.

2a) <u>Radius of Equivalent Two-Stage Seal</u>

We may say that;

$$\Delta p_N = N \Delta p_{N1} \qquad \ldots \text{(VIII.12)}$$

From the assumed constancy of C_p, i.e. with $\dfrac{\Delta p}{\frac{1}{2}\rho\omega^2 R^2} = \text{constant}$

$$\left(\frac{R_N}{R_{ss}}\right)^2 = \frac{1}{N} \qquad \ldots \text{(VIII.13)}$$

for constant values of ω.

$$\therefore \quad R_N = \sqrt{\frac{R_{ss}^2}{N}} \quad .$$

For a two-stage seal in the present application:

$$R_{N=2} \simeq \underline{5.5cm}$$

Thus the radius of the seal is reduced from an unwieldy 80mm for the single stage disc, which is larger than the pump impeller itself (7cm radius), to a size which could be fitted neatly on top of the present pump casing.

2b) End Load of Equivalent Two-Stage Seal

We know that:

$$EL_N = N.EL_{N1} \qquad \ldots \text{(VIII.14)}$$

If the assumption that $C_{EL} = \dfrac{EL}{\frac{1}{2}\rho\omega^2 R^4} = $ constant is correct, then for constant values of ω:

$$\frac{EL_{ss}}{EL_{N1}} = \left[\frac{R_{ss}}{R_N}\right]^4 \qquad \ldots \text{(VIII.15)}$$

Then from equations (VIII.13) and (VIII.14):

$$\frac{EL_N}{EL_{ss}} = \frac{1}{N} \qquad \ldots \text{(VIII.16)}$$

In the present case, with $EL_{ss} = 5720$ Newtons and $N=2$

$$EL_{N=2} = 2860 \text{ Newtons.}$$

2c) Torque Absorption in Equivalent Two-Stage Seal

From the assumption that $C_M \propto Re_\omega^{-1/m}$, we may deduce that $C_M \propto R_D^{-2/m}$ (since $Re_\omega = \dfrac{\omega R_D^2}{\nu}$, with ω and ν constant).

Then from equation (VIII.6):

$$\frac{P_{in(N)}}{P_{in(ss)}} = N \left(\frac{R_N}{R_{ss}}\right)^{\frac{5m-2}{m}} \qquad \dots\text{(VIII.17)}$$

Combining equations (VIII.13) and (VIII.17), we obtain:

$$\frac{P_{in(N)}}{P_{in(ss)}} = N^{-\left(\frac{3m-2}{2m}\right)} \qquad \dots \text{ (VIII.18)}$$

According to Howard[52], values of m are likely to lie between 3 and 5. Minimum power reductions will occur for m=3, so that:

$$\frac{P_{in(N)}}{P_{in(ss)}} = N^{-7/6} \quad .$$

Applied to the present case, with P_{ss} = 0.77kW and N = 2,

$$P_{in(N-2)} = \underline{0.34 \text{ kW}} \quad .$$

This value is only 0.14kW above the estimated power saved by efficient sealing of the upper shaft (see Chapter 7.3.4) and therefore would bring the total power absorbed by the pump and seal within the rating of the existing motors (see Section 1c).

2d) Seal Geometry

The optimum geometry of the two-stage seal may be calculated from the design criteria set out in Section 1e:

Number of vanes	:	16 (straight)
Vane depth	:	4.4mm.
Vane width	:	4mm.
s_v	:	1.3mm.
s_s	:	5.5mm
s_t	:	1.3mm

3. Modified Two-Stage Seal

A two-stage seal with dimensions calculated in the preceding section was fitted to the pump and tested over a range of operating conditions (see Appendix XI). Although its performance was satis-factory at the pump duty point, the seal leaked at low pump flowrates (i.e. when the pressure at the seal entrance was increased).

Since the single stage seal did not leak at any point on the pump characteristic, it was concluded that the two designs were not equivalent and the calculation for the radius of a two-stage seal was re-assessed.

The pressure drop across one disc in the two-stage seal is assumed to be half the pressure drop across the equivalent single-stage seal, i.e. $\Delta p_{ss} = 2\Delta p_{N1}$.

If C_p is constant:

$$\frac{\Delta p_{ss}}{\frac{1}{2}\rho\omega^2 R_{ss}^2} = \frac{\frac{1}{2}\Delta p_{ss}}{\frac{1}{2}\rho\omega^2 R_{N=2}^2}$$

i.e. $$\frac{1}{2} = \left[\frac{R_{n=2}}{R_{ss}}\right]^2 \qquad \qquad \ldots \text{(VIII.13)}$$

However, this simplified equation ignores the effect of the

hub radius, which may be included in the expression as follows:

$$\frac{\Delta p_{ss}}{\frac{1}{2}\rho\omega^2[R_{ss}^2 - R_h^2]} = \frac{\frac{1}{2}\Delta p_{ss}}{\frac{1}{2}\rho\omega^2[R_{N=2}^2 - R_h^2]}$$

i.e. $\quad \frac{1}{2} = \frac{R_{N=2}^2 - R_h^2}{R_{ss}^2 - R_h^2} \quad\quad \dots \text{(VIII.19)}$

Since $R_{ss} > R_{N=2}$, the relative loss in sealing pressure due to the presence of the shaft will be greater for the two-stage seal.

With $R_h \simeq 1.5$cm, equation (VIII.19) gives:

$$R_{N=2} = 5.76\text{cm}.$$

This figure shows that the discs in the original two-stage design (5.32cm radius) are approximately 8% too small to give equivalent sealing performance to the single-stage seal.

The two-stage HDS was therefore modified by fabricating new discs of 5.9cm radius and machining out the seal casing to fit. The optimum vane width and depth, plus all clearances, remain as before (see Section 2d).

4. Final Particulars of Sealing Dics

For purposes of comparison, the dimensions (in mm) of the three designs of HDS tested have been tabulated overleaf:

Table VIII(i): Particulars of Sealing
Discs (in mm)

HDS	R	No. of Vanes	a	b	s_s	s_t	s_v	R_h	t
Single Stage	80.0	16	5.1	3.8	6.6	1.6	1.8	15	7.6
Two-Stage (I)	53.2	16	4.4	3.2	5.5	4.0*	1.3	15	7.0
Two-Stage (II)	59.4	16	4.4	3.2	5.5	1.3	1.3	15	7.0

Same dimensions for water and mercury rigs (Two-stage (II) seal tested only on water rig).

Fabrication material :   aluminium (water rig)
                         mild steel (mercury rig).

*High tip clearance on two-stage (I) seal due to an error on design drawings.

EFFECT OF THE HDS ON PUMP PERFORMANCE IN WATER

A. Seal Leakage

The single stage and two-stage (II) HDS eliminate leakage through the top shaft clearance at all points on the pump characteristic. The two-shape (I) seal leaks slightly at low flowrates (i.e. maximum inlet pressure for a given speed) but becomes 100% effective as the flowrate is increased. Table IX(i) shows that the maximum leakage rate (at shut off) is minimal compared with leakage through standard clearance neckrings (see Figures 34 and 35).

Table IX(i): Details of Seal Leakage in Cold Water:
Two-Stage HDS(I) in Pump.

Rotational Speed (rpm)	Pump Flowrate at Onset of leakage ($\ell.min^{-1}$)	Maximum Leakage Rate ($\ell.min^{-1}$)
1000	10	0.3
1500	21	0.8
2000	42	2.5
2500	80	3.4

In general, the more efficient sealing capability of the HDS as compared with the upper neckring leads to higher pressure at both upper and lower seal inlets, as shown in Figures 123-127. This will influence the leakage rate through the lower neckring, the maximum effect occurring at zero pump flowrate, where leakage is highest. Although in situ

measurements of the leakage flow were not possible, the following estimation has been made.

At zero pump flowrate, pressure at the inlet to the lower neckring on the pump fitted with the two-stage (II) HDS is 30-35% higher than in the standard pump (Figure 127). Since $Q_{leak} \propto \sqrt{\Delta p}$ across the seal (equation 5.19), the resultant increase in leakage will be less than 6% of the standard pump leakage rate. By the same argument, lower neckring leakage with the single stage HDS will not be more than 4% up on the value for the standard pump (Figures 123 and 124), whilst there should be no change in lower neckring leakage with the two-stage (I) seal (Figures 125 and 126).

The pressure pattern at both the upper and lower seal inlet varies with each design of HDS, as shown by a comparison of Figures 123-127. This is thought to be a consequence of different axial positioning of the pump impeller inside its casing. As explained in Chapter 5.3, the impeller position could not be checked in situ and changes of about ± 0.5mm (see Figure 121) each time the pump is reassembled with a new seal configuration are quite feasible.

B. Generated Head

The head/flow characteristics of the pump fitted with each design of HDS exhibit a slight speed effect when plotted in dimensionless form. Figures 128-130 show that the head values at 1000 and 1500 rpm fall below the standard pump curve at low flows and comparable performance is only attained at higher speeds.

Reasons for this breakdown of conventional head scaling laws are unclear. Although elimination of leakage through the top shaft seal may cause higher leakage rates through the lower neckring (as discussed in Section A above), any resultant influence on the pump head will be favourable (see Chapter 9). Therefore, the reduction in generated head with speed can only be attributed to secondary Reynolds Number effects.

It has previously been shown (Table 5.1) that the flow regime within the pump impeller is transitional for the majority of these tests, so that anomalous pressure losses due to skin friction cannot be discounted in the present case. The limited range of Re_ω covered by trials on the pump fitted with a HDS precludes any firm conclusions regarding such secondary losses, and a more extensive investigation (which was not possible within the time scale of this project) is recommended.

At high flows, elimination of leakage through the upper seal, and the consequent shift of the head characteristic to the right, causes an increase in outlet pressure of the pump fitted with a HDS as compared with the standard pump. The points still fall below the head/total flow characteristic (i.e. delivered flow plus leakage flow: see Chapter 5.2.1) of the standard pump, since leakage at the lower neckrings has not been checked.

C. Absorbed Power

Power consumption is a crucial factor when a new seal is designed for industrial applications. An increase in pump power requirement is to be expected with the new sealing arrangements, because shear stresses on the wall of the disc housing cause a higher torque absorption in the HDS than in the neckring. However, this will be partially offset by the improvement in pump efficiency due to leakage reduction.

Absorbed power data for the pump with single stage and two stage (I) HDS (Figures 131 and 132) scale well, except at 1000 rpm, where the accuracy of measurement is known to be poor (Appendix IV). The wider scatter on Figure 133 for the two-stage (II) HDS can be attributed to instrumentation error, since there is no systematic trend with changing speed. The torquemeter on the water test rig was in need of maintenance at this stage of the project, but funds were no longer available for the work (see Appendix XII).

If allowance is made for the uncertainty in the value of parasitic torque and the relative magnitude of error this introduces

at low test speeds, Figures 131-133 show that the conventional laws of power scaling for changes of speed can be applied to the pump fitted with a HDS, with an accuracy of $\pm5\%$.

The reduction in absorbed power that can be achieved by staging a HDS is illustrated by the comparison of data in Table IX(ii).

Table IX(ii): Effect of HDS on Pump Power Absorption
in Water

Tabulated data gives the mean increase in pump power absorption when fitted with a HDS, expressed as a percentage of the mean power absorbed by the standard pump at the same flow coefficient (from Figures 131-133).

Flow Coefficient ϕ	Pump + Single Stage HDS	Pump + Two-Stage (I) HDS	Pump + Two-Stage (II) HDS
0	70%	5%	16%
2.06×10^{-3} (duty point)	44%	6.5%	8%
5.0×10^{-3} (maximum flow)	35%	10%	16%

D. Efficiency

The efficiency characteristics of the pump with each design of HDS are presented in Figures 134-136. Scaling of data is good for the single stage seal at higher speeds (Figure 134); the disparity at 1000 rpm reflects the error in absorbed power measurement discussed in Section C above. Scaling for the two-stage (II) seal is also good (Figure 136), but the scatter on Figure 135 for the two-stage (I) HDS is wider, particularly at 1000 and 1500 rpm. The absorbed power is again uncertain at 1000 rpm, but at 1500 rpm the deviation may be due to inaccurate delivered head values, since these are unexpectedly low (see Figure 129).

The curves in Figures 134-136 peak at higher flows than in the standard pump, because of the increase in delivered head at high flow-rates with a HDS (see Section B). The best efficiency is, of course, lower than in the standard pump and these values are presented for each HDS design in Chapter 11.2.4 (Table 11.2), together with the efficiency at the duty point for pump operation in the chlorine plant.

APPENDIX X

ANALYSIS OF SINGLE STAGE HDS PERFORMANCE IN WATER

A. Sealing Performance

The radial pressure distribution across the vaned surface of the single-stage HDS in the pump is plotted for different test speeds in Figure 137. Pressures have been non-dimensionalised in the form of a local pressure coefficient $(\frac{P_{tap}}{\rho\,\omega^2 R_D^2})$, which refers to the pressure at a particular radius within the seal housing. This should not be confused with the overall pressure coefficient, which indicates the total pressure retained by the seal.

The results in Figure 137 correspond to the maximum seal inlet pressure, with the pump running at shut-off. Although the interface could not be precisely located during these tests, the close correlation of local C_p values at $R_{tap}/R_D = 0.5$ confirms that its position was similar for each speed, at a relative radius of about 0.45. The seal was not running full under these conditions and therefore is overdesigned. The design (see Appendix VIII) was based upon a theoretical value of seal inlet pressure, which was subsequently shown to be higher than the true value. Considerable power savings could be achieved by a small reduction in disc radius, and the seal would still be 100% effective.

Local C_p values in Figure 137 show a slight rise with Re_ω, particularly at the outer radius. The pressure distribution is also smoother at the higher test speeds.

The mean curve from Figure 137 is compared with the data points for radial pressure distribution in the bare single stage HDS in Figure 138. The curves are similar, but the interface in the bare seal is closer to the shaft, so that local C_p values are higher for a given relative radius. Although the curves are not quite identical, they validate the data produced in earlier work at Southampton on the HDS in a bare seal configuration[49,52,59].

The Reynolds Number effect shown in Figure 137 is less noticeable in the bare seal results, but the range of speeds covered is smaller. Local C_p values in Figure 138 near the disc tip are slightly lower at 1000 rpm, even taking the apparently wider interface radius at this speed into account.

In the absence of confirmatory pressure tappings, a similar compensatory relationship betweel local C_p and Re_ω is assumed to exist on the smooth side of the sealing disc, since no corresponding trend is found for the overall maximum C_p values, which are tabulated below.

Table X(i): Maximum C_p Values: Single Stage HDS Running in Cold Water

Rotational Speed (rpm)	Re_ω	Overall C_p	
		Bare Seal	Seal in Pump
1000	6.7×10^5	0.56	0.55
1500	1.0×10^6	0.61	0.61
1800	1.2×10^6	0.65	–
2000	1.3×10^6	–	0.58
2500	1.7×10^6	–	0.60

Random fluctuations in overall C_p can be attributed to experimental error and, particularly at 1000 rpm for the seal in the pump, where the tapping at R_{tap}/R_D did not register, small variations in interface position.

At 1800 rpm in the bare seal tests, the interface was very close to the shaft, since an increase of only 4% in the inlet pressure caused leakage. Therefore C_p = 0.65 is the maximum for this design of HDS. The data in Table X(i) confirms the conclusion drawn by Thew and Saunders[49] that C_p is invariant with Re_ω.

A C_p value of about 0.6 has been found in previous work with straight vanes, although improvements of a few percent can be achieved with the optimum backward-curved vanes[49,52].

Interface position also affects the radial pressure distribution on the vaned side of the disc as shown in Figure 139 for a representative speed of 2500 rpm. If we consider the outward radial pressure rise from the interface (which is at atmospheric pressure), the forced vortex model gives the gauge pressure at a given radius R_{tap} as:

$$P_{tap} = \tfrac{1}{2}\rho\omega^2 k_v^2 (R_{tap}^2 - R_i^2) \qquad \ldots \text{(X.1)}$$

Defining R_{tap} in terms of the disc radius, so that $\dfrac{R_{tap}}{R_D} = T$, equation (X.1) may be rewritten in the form:

$$P_{tap} = \tfrac{1}{2}\rho\omega^2 R_D^2 (T^2 - X^2) k_v^2 \qquad \ldots \text{(X.2)}$$

Then the local pressure coefficient is given by:

$$\text{Local } C_p = k_v^2 (T^2 - X^2) \qquad \ldots \text{(X.3)}$$

If k_v is constant, the curves in Figure 139 should constitute the same parabola displaced vertically by a distance $k_v^2 \Delta(X^2)$ for different values of X.

However, earlier work at Southampton[49,52,59] has shown that k_v falls at high values of X, due to a secondary circulation of fine

bubbles of air which are carried outward from the interface near the leading edge of each vane[52]. Therefore, local k_v values near the disc tip were examined in the present research. Figure 140 shows the relationship between k_v^2 (which governs overall C_p) and interface position at different speeds for the seal running in the pump. Poor control over the interface position (see Chapter 11.1) has limited the investigation for the bare seal trials to the single speed of 1500 rpm. (Figure 142a).

Despite the scatter in Figures 140 and 142a, which arises because of uncertainty in the exact interface position between pressure tappings, a decrease in k_v^2 at the disc tip with increasing X is shown. The decrease appears to be more rapid for the bare seal results, but this may be a consequence of fewer available data points.

When the HDS runs in conjunction with the pump, k_s (averaged over the disc radius) is also found to vary with interface position. Figure 141 shows a tendency for k_s^2 (which governs the parasitic pressure rise on the smooth face of the sealing disc) to increase as the interface moves outward. However, the same trend is not found in the bare seal tests (Figure 142b), which suggests that the apparent relationship between k_s^2 and X shown in Figure 141 is misleading. When the seal is fitted above the pump impeller, the interface position is controlled by altering the pump flowrate and hence both the fluid prewhirl and the symmetry of the pressure distribution at the seal inlet will change as the interface is moved. Thus k_s in Figure 141 is influenced solely by these inlet conditions and when the seal runs alone with a uniform inlet pressure and zero prewhirl, k_s remains constant for all values of X.

Average k_v values between the disc tip and interface at the minimum interface radius (i.e. maximum seal inlet pressure) show an increase with Re_ω (see Table X(ii)), which agrees with previous results

from work at Southampton[49]. k_v for the bare seal is generally a few percent higher than for the seal in the pump, probably because the interface is at a smaller radius. An average k_v value of 0.96 was chosen for the seal design (see Appendix VIII), which is endorsed at 2500 rpm, but is a little high for lower speeds.

Table X(ii): Average Values of k_v and k_s: Single Stage HDS running in Cold Water

(Data for maximum seal inlet pressure: $R_i \simeq 0.45\ R_D$)

Rotational Speed (rpm)	Re_ω	Seal in Pump			Bare Seal		
		Average k_v *	k_s(inlet →tip)	Tip Region k_v	Average k_v *	k_s(inlet →tip)	Tip Region k_v
1000	6.7×10^5	0.87**	0.38	0.98	0.90	0.43	0.91
1500	1.0×10^6	0.90	0.29	0.97	0.95	0.48	0.96
1800	1.2×10^6	–	–	–	0.95	0.46	0.95
2000	1.3×10^6	0.94	0.42	0.94	–	–	–
2500	1.7×10^6	0.96	0.46	0.98	–	–	–

* R_{tap}/R_D = 0.75→0.88 for tip region k_v and 0.5→1.02 for average k_v except ** where R_{tap}/R_D = 0.625→1.02.

Local k_v in the region of the disc tip is often higher than the average value. A similar effect has been found before, when careful pressure measurements in a single stage HDS reflected a slight rise in k_v with increasing radius[52]. The explanation lies in the secondary circulation in the seal housing, with slowly rotating fluid leaving the stationary end wall, moving axially into the sealing disc and being accelerated to a higher rotational speed (larger k_v) as it drifts outward. In comparison, the average k_v value encompasses smaller radii on the disc and also the disc tip clearance (since tip pressure is measured at the housing wall), where lower k_v is to be expected.

Although high k_v values are important for efficient operation of a HDS, further improvements in seal performance may be achieved by reducing the parasitic pressure generated on the smooth side of the sealing disc. A vaned housing has been used in earlier experiments at Southampton[49] to reduce the mean circumferential velocity of fluid, and hence the generated pressure, on the smooth side of the disc, but although this increased C_p by about 35%, the torque coefficient C_M went up by roughly 50%. Therefore, smooth housings are generally used and clearances are optimised for a minimum k_s.

Table X(ii) shows a random variation in k_s with speed for both the bare seal and the seal in the pump. Values for the bare seal lie between 0.43 and 0.48, which is close to figures obtained in previous work at Southampton, but up to 38% higher than the corresponding data for the seal/pump combination. When the HDS runs above the pump, the inlet pressure is measured at the former upper neckring tapping (see Figure 121). Pressure losses will occur at the seal inlet, so true k_s may be a few percent higher than the figures quoted in Table X(ii). Figure 122 shows that the seal inlet pressure is measured in a more acceptable position for the bare seal configuration, and therefore computed k_s data will be more accurate.

However, since the higher k_v values in the bare seal are not reflected by an improvement in overall C_p (see Table X(i)), average k_s must still be greater than the correct values for the seal in the pump. This conclusion is reasonable in the light of the preceding discussion concerning the possible effect of inlet conditions on seal performance, but requires confirmation by further trials of the seal in the pump, with a repositioned pressure tapping at the seal inlet. Unfortunately, this was not possible within the time scale of the present project.

B. Absorbed Power

The absorbed power measurements obtained during bare seal trials were unreliable as explained in Chapter 11.1. Data for the highest test speed, where error is smallest, suggests that C_M for the single stage HDS running at 2000 rpm in cold water is $0.011 \pm 12\%$.

Since direct measurements were unsatisfactory, an attempt has been made to assess the power requirements of the seal, by comparing the power characteristics of the pump with and without a HDS. For this purpose, the characteristic of the standard pump must be modified to allow for the effects of reduced leakage and removal of the upper neckring.

The power absorbed by the neckring was calculated from an extrapolation of the torque coefficient data published by Yamada[78] whose work did not extend to such small values of relative annular clearance, and also by Bilgen et al[79], whose results apply to higher Reynolds Numbers than occur for the present neckring leakage flow. Both methods indicate that the absorbed power is negligible, i.e. of the order of 1.5W at 2500 rpm.

A more important source of power absorption, which is removed when leakage through the upper seal is stemmed, lies in the rotation of the pump shaft (carrying a key and grubscrew) within the slightly pressurized leakage fluid which collects inside the cylindrical tube supporting the pump (see Figure 1). Treating the shaft as a cylinder of the same diameter rotating in infinite space filled with water, the power absorbed at 2500 rpm was calculated to be approximately 4.5W, according to a method suggested by Dorfmann[80]. The effect of the protruding shaft key and grubscrew is expected to be two or three times as large and therefore the total power absorbed by the upper neckring and rotating shaft was taken as 20W at 2500 rpm, which, in terms of the pump impeller radius, is equivalent to a power coefficient κ of 0.02×10^{-3}.

Details of the methods for calculating neckring and shaft absorbed power are presented in Appendix XIII.

To compensate for the leakage loss through the upper neckrings in the standard pump, the power coefficient (reduced by a value of 0.02×10^{-3} as explained above) was plotted against a flow coefficient ϕ' based on the nett delivered flowrate plus upper neckring leakage flowrate. The resultant curve is compared with the power characteristics of the pump with each of the new sealing arrangements in Figure 146. This correlation ignores the effect of variations in lower neckring leakage for each configuration, which is negligible for $\phi' > 1.0 \times 10^{-3}$ (see Appendix IX).

The "modified" characteristic of the standard pump now runs parallel to the curve for the pump fitted with a single stage HDS and the constant increment in power coefficient represents the power requirement of the new seal. Previous work on sealing discs of similar design[49] has shown that C_M is independent of interface position for $X < 0.65$. Therefore the mean value of the increase in κ at five equi-spaced points along the characteristic was used to calculate the power absorbed by the seal at 2000 rpm and the corresponding value of C_M. This data is presented with the bare seal results (discussed at the beginning of this section) in Table X(iii).

Table X(iii): Power absorbed by Single Stage HDS at 2000 rpm in Cold Water ($Re_\omega = 1.3 \times 10^6$)

Test Configuration	Absorbed Power (Watts)	C_M	Estimated Power
Bare seal	172	0.011	$\pm$ 12%
Seal in Pump	181	0.012	$\pm$ 3%

The greatest source of error in the indirect method of absorbed power measurement is thought to lie in the estimate of power absorbed by the rotating shaft in the standard pump, which the author acknowledges may be up to 50% inaccurate. Fortunately, this represents a small error in the final computation, as shown in the table on the previous page.

C_M is not expected to depend on the test configuration, and when the wide margin of error for the bare seal measurements are taken into account, the two values agree well. $C_M = 0.012$ is slightly higher than the figure of 0.011 found for a seal of similar design at equivalent Re_ω, but the disc radius for those experiments was about 20% smaller than the present single stage HDS.[60]

ANALYSIS OF TWO-STAGE (I) HDS PERFORMANCE IN WATER

A. Sealing Performance

The pressure distribution across the sealing discs of the initial
design of two-stage HDS (I) running in the pump is shown in Figure 143.
This seal leaked at all speeds when the pump was operating at maximum
delivered head, therefore the points on the graph represent the maximum
seal inlet pressure for no leakage (i.e. with the top housing almost full).
The results at different speeds are correlated as in Figures 137 and 138,
using a local pressure coefficient at each tapping (see Appendix X).

There will be a parasitic pressure rise between the seal inlet
and the tip of the lower disc, due to unwelcome pressure generation on
the smooth side, but this is not shown in Figure 143 as no tappings were
fitted there. The pressure falls on the vaned side of the lower disc
between the tip and the shaft, then subsequently rises across the smooth
face of the upper disc. Finally, the pressure falls on the vaned side
of this disc to C_P(local) = 0, which corresponds to the air/water interface.

Unlike the single stage seal (Figure 137), there is no sign of
speed changes affecting the pressure distribution and the small, random
scatter of points can be attributed to experimental error and/or slight
variations in interface position. The two-stage (II) HDS (described in
Appendix XII) does exhibit a Reynolds Number effect (see Figure 145) and
therefore the unusual behaviour of the two-stage (I) seal must be caused
by its wide tip clearance (see Appendix VIII, Table VIII(i)), which is
later shown to reduce tip region k_v (see Table XI(iii)).

At all speeds, the pressure distribution in Figure 143 is markedly different near the interface. This could be the result of a more ragged and frothy interface, since the two-stage seal has a relatively larger hole for the shaft in the housing wall than the single-stage version, where the pressure distribution is more uniform (Figure 137). In addition, the channels between the vanes become rather narrow near to the shaft, which also contributes to interface instability[49] and since the vane width on both versions of HDS is the same, the effect will be greater on the two-stage design with smaller discs. Unfortunately no pressure tappings are available at $R_{tap}/R_D < 0.66$ for a more detailed investigation of the region close to the shaft.

The mean curve from Figure 143 is compared with the pressure distribution in the bare two-stage (I) HDS in Figure 144. Agreement at the tapping for the lower disc tip and at all tappings on the upper disc is fair, but there is a large discrepancy at the interstage and central tapping on the lower disc. The pressure recorded here for the bare seal is thought to be too high, due to leakage from one of the other (higher pressure) tappings at the six way valve, to which they were both connected. Tappings on the upper disc were led via a separate six-way valve and would not be affected.

The data points in Figure 144 confirm the results of two-stage (I) seal tests in the pump. The pressure distribution is not altered by speed changes and there is still a marked drop in pressure near to the air/water interface.

Overall sealing pressure coefficient values on the upper and lower discs have been calculated for the seal running in the pump. No data is available for the bare seal, because of the inaccuracy of interstage pressure measurement.

Table XI(i): Maximum Sealing Pressure Coefficient Data:
Two-Stage (I) HDS in Pump Running in Cold Water

Rotational Speed (rpm)	Re_ω	C_p Lower Disc	C_p Upper Disc
1000	3.0×10^5	0.66	0.57
1500	4.4×10^5	0.62	0.53
2000	5.9×10^5	0.63	0.54
2500	7.4×10^5	0.65	0.51

The possible error in C_p on the upper disc at 1000 rpm is $\pm 15\%$, because the precision of the pressure gauge was inadequate for the small pressure increments involved. The accuracy improves with speed and therefore only the results at 1500 rpm and above will be included in the following discussion.

The lower housing of a staged seal should run full, unless some gas becomes trapped in the shaft region. This will reduce the pressure locally, and any influence on C_p for the lower disc will be favourable. Therefore C_p for the lower disc of the two-stage (I) HDS should be approximately 0.65, which is the maximum value calculated for the single stage seal running full (Table X(i)). Table XI(i) shows that this figure is only attained at 2500 rpm and C_p falls with decreasing Re_ω. This relationship, which contradicts results for a single stage HDS in both the present project (Appendix X) and in earlier work[49], may be connected with the abnormally low k_v values calculated for the two-stage (I) seal (see Table XI(ii)) and/or the relatively large interstage hole for the shaft, which hinders efficient operation of the disc at small radii. For T=0.28 (relative radius of shaft) to T=0.47 (relative radius of hole in the casing), the vane clearance(S_v) on the lower disc is effectively increased to 14mm (the distance to the smooth face of the upper disc) or $0.26R_D$. An increase in S_v is known to reduce k_v and hence C_p[49], although previous work has not encompassed such large clearances.

C_p on the upper disc is even smaller, mainly because the housing is not quite full. Table XI(i) shows a random fluctuation with speed, but whether variations in interface position conceal a more definite trend with changes in Re_ω is unclear.

The effect of interface position on seal performance, i.e. on k_v, in the tip region of the upper disc, could not be investigated due to the low precision of the pressure gauge in relation to the size of the pressure rise between the outermost tappings, even at the maximum speed. Interface position is not expected to influence any parameters on the lower disc.

Average values of k_v and k_s on both sealing discs are presented in Table XI(ii). For the bare seal, k_v on the lower disc and k_s on the upper disc have been excluded, because their calculation involves data for the interstage pressure, which is not accurately known.

Table XI(ii): Average k_v and k_s: Two-Stage (I) HDS Running in Cold Water.

(Data for maximum seal inlet pressure at zero leakage: $R_i \approx 0.5R_D$)

		Seal in Pump				Bare Seal	
		Lower Disc		Upper Disc		Lower Disc	Upper Disc
R_{tap}/R_D range for k_v and k_s		0.48→1.07	0.54→1.07	0.65→1.07	0.48→1.07	0.54→1.07	0.65→1.07
Rotational Speed(rpm)	Re_ω	k_v	k_s	k_v	k_s	k_s	k_v
1000	3.0×10^5	0.88	0.28	0.89	0.44	0.28	0.93
1500	4.4×10^5	0.89	0.41	↓	0.46	0.48	0.89
2000	5.9×10^5	0.92	0.43		0.48	0.46	0.87
2500	7.4×10^5	0.94	0.45	↓	0.48	–	–

At 1000 rpm, the pressure rise across the smooth face of the discs was so small that it could scarcely be detected by the pressure gauge and the accuracy of k_s may be worse than $\pm 50\%$. The estimated error in k_v at the same speed, due simply to the limited precision of the pressure gauge, is $\pm 15\%$ and these results are not thought to be meaningful.

When the seal runs in the pump, both k_v and k_s increase with Re_ω (except for k_v on the upper disc which remains constant), confirming previous results in the present project (see Appendix X) and earlier work [49]. k_s on the lower disc is always less than on the upper disc, which supports the hypothesis put forward in Appendix X that the former upper neckring tapping does not give a true indication of the seal inlet pressure. In the bare seal configuration, where the inlet pressure tapping is in a more acceptable position, k_s on the lower disc is closer to the accepted figure of 0.46 [49]. k_v on the upper disc of the bare seal agrees reasonably well at 1500 and 2000 rpm with data for the seal in the pump.

On both discs and in both test configurations, k_v is unexpectedly low, which may be a function of the low peripheral velocity of the small discs in this HDS design. Even at 2500 rpm, Re_ω for the two-stage (I) seal only just exceeds Re_ω at 1000 rpm in the single stage seal (compare Tables X(ii) and XI(ii)). Additional contributory factors may include the relatively wider shaft (which can reduce k_v according to Ref.49) and the large interstage hole in the seal casing, which has been discussed above. The only other geometric difference between the single stage and two-stage (I) designs is the higher value of S_t/R_D for the two-stage (I): 0.074 as compared with 0.020 for the single stage. Reference 49 indicates that tip clearance has little effect on k_v, but the range investigated did not extend to the above figure. The high tip clearance on the two-stage (I) HDS was due to an error in initial design and, in the opinion of the present author, must contribute to its poor performance.

In order to check this theory, k_v has been calculated for the shaft and tip regions of the lower disc on the seal in the pump and the results are presented in Table XI(iii).

Table XI(iii): k_v in Shaft and Tip Region of Lower Disc:
Two-Stage (I) HDS in Pump Running in Cold Water

(Data for maximum seal inlet pressure with zero leakage: $R_i \approx 0.5 R_D$)

Rotational Speed (rpm)	Shaft Region k_v $R_{tap}/R_D = 0.48 \to 0.75$	Tip Region k_v $R_{tap}/R_D = 0.75 \to 1.07$
1500	0.97	0.84
2000	1.01	0.86
2500	1.04	0.87

Air collecting at the interstage has reduced the pressure locally, causing a positive error in the calculation of shaft region k_v (which cannot exceed 1.0). Even if this error is as high as 10%, k_v near the shaft is consistently higher than at the disc tip. This is contrary to normal HDS behaviour, where k_v rises with increasing radius (see Appendix X) and the detrimental effect of a wide tip clearance is confirmed. Comparison of C_p and k_v data for the two-stage (I) and two-stage (II) seals (see Appendix XII) - where the effect of shaft radius and interstage hole will be similar - also identifies a wide tip clearance as the main cause of inferior performance in the two-stage (I) HDS.

Gas collection at the interstage region is less apparent in the two-stage (II) seal (compare Table XI(iii) and Table XII(iii)). This indicates that such behaviour is promoted by a wide tip clearance. The problem is fully discussed in Chapter 11.4 and Chapter 12.3.3.

B. Absorbed Power

Direct measurements of power absorbed by the two-stage (I) seal in the bare configuration running in cold water are particularly un-reliable, with parasitic torque accounting for more than 60% of the gross indicated torque (see Appendix IV). From the available data, C_M has been calculated as 0.010, but the error may be as high at $\pm 30\%$.

The power requirement of the HDS can be assessed more accurately by the indirect method described for the single stage seal in Appendix X. The power characteristic of the standard pump in cold water, modified for the effects of reduced leakage and removal of the upper neckring, is illustrated in Figure 146. The characteristic of the pump fitted with the two-stage (I) HDS in water runs parallel at high flowrates, but the two curves converge when $\phi' < 1.7 \times 10^{-3}$. This illustrates the reduction in disc friction with inward radial throughflow on the back of the pump impeller when the HDS starts leaking (see Appendix IX, Table IX(i)).

The constant increment in power coefficient for $\phi' > 1.7 \times 10^{-3}$ represents the power absorbed by the two-stage (I) HDS. By taking the mean value at five equispaced points along the characteristic, the power absorption has been calculated as 55 Watts at 2000 rpm in cold water, which corresponds to $C_M = 0.014$. The estimated error of $\pm 10\%$ is mainly due to uncertainties in the value of power absorbed by the rotating shaft in the standard pump (see Appendix X.B).

C_M for the single stage and two-stage (II) HDS are 15-20% lower (see Appendix X.B and XII.B). Previous work has shown that C_M increases with tip clearance for $0.02 < S_t/R_D < 0.04$, which was the maximum clearance investigated[49]. A continuation of this trend is confirmed by the high C_M value for the two-stage (I) seal ($S_t = 0.076 R_D$), although other contrib-utory factors must also be considered. A direct interdependency of C_M and Re_ω is unlikely in view of the similar C_M figures calculated for the single stage and two-stage (II) seals. However, the relative contribution of

torque absorption at the disc tip to overall C_M becomes more important at low rotational Reynolds Numbers, so that the detrimental effect of a thick disc will become more apparent here[49]. Since it has the smallest discs, the two-stage (I) HDS exhibits the least favourable b/R_D ratio of the three designs (see Appendix VIII, Table VIII(i)) and this will certainly influence the value of C_M. Relative vane height is also significant, but data published in Reference [81] indicates that any change in C_M will be negligible over the range covered by discs tested in the present project.

APPENDIX XII

ANALYSIS OF TWO-STAGE (II) HDS PERFORMANCE IN WATER

A. Sealing Performance

The relationship originally used to calculate the radius of discs
in a two-stage HDS which exhibited equivalent sealing characteristics to
the single stage design was over-simplified, since it ignored the effect
of shaft radius. The shaft becomes more important as the number of
stages is increased, not only because its radius increases in relation
to the size of the discs, but also because its presence detracts from
the performance of each additional disc.

A modified two-stage (II) HDS was fabricated during the final
stages of this project. The discs were 8% larger than in the first
version (see Appendix VIII) and the tip clearance was reduced to a more
acceptable value of $0.02R_D$. Experiments with this seal were carried out
when finance for the work had terminated, therefore it was only tested
in water with the pump, over a limited range of speeds.

The pressure distribution inside the seal housing at maximum
inlet pressure (zero pump flowrate) is shown in Figure 145. As in the
single-stage seal (Figure 137), local C_p values at the disc tips show a
slight rise with Re_ω, which is less marked in this case because of the
smaller discs. The pressure gradient on the upper disc is steeper than
on the lower, which is thought to be a similar effect to that shown in
Figures 143 and 144, where the pressure gradient increases near to the
air/water interface. Any corresponding change in pressure distribution
across the upper disc of the two-stage (II) design could not be detected,
since there is only one tapping between the interface and disc tip.

Instead it manifests itself as a sharper pressure drop in the entire region between the disc tip and this tapping. Interface instability and consequent air entrainment, which were judged in Appendix XI to be the primary cause of the change in pressure gradient near to the interface, are more likely to occur in the modified two-stage seal, where the interface lies at a wider relative radius[59].

Table XII(i): Maximum Sealing Pressure Coefficient Data:
Two-Stage (II) HDS in Pump Running in
Cold Water

Rotational Speed (rpm)	Re_ω	C_p Lower Disc	C_p Upper Disc
1500	4.4×10^5	0.65	0.38
2000	5.9×10^5	0.64	0.39
2500	7.4×10^5	0.66	0.40

C_p on the lower disc compares favourably with data for the original two-stage design (Table XI(i)), implying that the poor performance of the latter is due to its wide tip clearance rather than the relatively large hole for the shaft in the housing wall (see Appendix XI). As with the single stage seal (Table X(i)), random fluctuations in C_p (lower disc) with speed confirm that it does not vary with Re_ω[49] and at all speeds the value of C_p is close to the maximum of 0.65 found for the single stage seal in the bare configuration.

In contrast, the upper disc runs only half full, even at maximum inlet pressure from the pump, so that C_p (upper disc) is very low. If the seal were tested alone, with no constraints upon inlet pressure, slightly higher values than those shown for the two-stage (I) HDS in Table X(i) could be expected for an interface position close to the shaft.

Average k_v and k_s on both discs show an increasing trend with Re_ω (see Table XII(ii)), which corroborates the results for the single stage and two-stage (I) designs. Air entrainment at the interface leads to an overestimate of k_v on the upper disc which cannot therefore be compared with values found for the other seals, but a 3-6% increase in k_v on the lower disc over corresponding data in Table XI(ii) for the two-stage (I) HDS emphasises the advantage gained by a reduction in tip clearance. The effect on k_s for both discs is less apparent and values for the original (I) and modified (II) two-stage seals are similar.

Table XII(ii): Average k_v and k_s: Two-Stage (II) HDS
in Pump Running in Cold Water

(Data for maximum seal inlet pressure: $R_i \approx 0.8 R_D$)

		Lower Disc		Upper Disc	
R_{tap}/R_D range for k_v and k_s		0.43→1.02	0.49→1.02	0.84→1.02	0.43→1.02
Rotational Speed (rpm)	Re_ω	k_v	k_s	k_v	k_s
1500	4.4×10^5	0.95	0.41	1.04	0.46
2000	5.9×10^5	0.95	0.41	1.03	0.45
2500	7.4×10^5	0.97	0.42	1.08	0.49

k_v values on the lower disc of the two-stage (II) HDS are also higher than the figures shown in Table X(ii) for the single stage seal, which is particularly surprising in view of the comparatively low rotational Reynolds Numbers attained with smaller discs. The explanation may lie with air entrapment at the interstage region of the two-stage (II) seal, causing deceptively low pressure readings, which was also thought to produce positive errors for shaft region k_v of the two-stage (I) lower disc (see Table XI(iii)).

Table XII(iii): k_v in Shaft and Tip Region of Lower Disc:
Two-Stage (II) HDS in Pump Running in
Cold Water.

(Data for maximum seal inlet pressure: $R_i \approx 0.8R_D$)

Rotational Speed (rpm)	Re_ω	Shaft Region k_v $R_{tap}/R_D = 0.43 \rightarrow 0.67$	Tip Region k_v $R_{tap}/R_D = 0.67 \rightarrow 1.02$
1500	4.4×10^5	0.97	0.93
2000	5.9×10^5	0.94	0.95
2500	7.4×10^5	0.97	0.97

To check this theory, variations in k_v at the shaft and tip regions of the lower disc on the two-stage (II) HDS have been examined (see Table XII(iii)). There is no consistent increase in k_v between the shaft and disc perimeter, which contradicts the results for a single stage seal in the present project (Table X(ii)) and in earlier work[52]. High k_v values in the shaft region, fluctuating at random with speed, illustrate the effect of varying degrees of air entrapment in that area. The problem is found to be more severe for the two-stage (I) HDS (see Table XI(iii)), which suggests that it is encouraged by a wide tip clearance.

Tip region k_v for the two-stage (II) seal will not be affected by any air that collects near the shaft. The values in Table XII(iii) show an increasing relationship with Re_ω and fall between average k_v and tip region k_v for the single stage seal at a similar rotational Reynolds Number (Table X(ii)).

B. Absorbed Power

The two-stage (II) HDS was not run in the bare configuration, therefore its power requirement was gauged indirectly by a comparison

of the power characteristics of the pump with and without the HDS.

Figure 146 shows that the characteristic of the standard pump, modified for the effects of reduced leakage and the removal of the upper neckring as described in Appendix X, runs parallel to the curve for the pump fitted with the two-stage (II) HDS. C_M is invariant with interface position for X<0.65[49]. Therefore, the mean value of the increment in power coefficient at five equispaced points along the characteristic has been used to quantify the power absorbed by the HDS running at 2000 rpm in cold water as 71 Watts. This corresponds to C_M=0.011, with an estimated error of ±8% (due mainly to uncertainties in the power absorbed by the rotating shaft in the standard pump: see Appendix X.B). This confirms the results in Reference 60 for a single-stage seal of similar radius, although the possible error in the present case is rather high.

APPENDIX XIII

CALCULATION OF POWER ABSORBED BY THE PUMP SHAFT
AND UPPER NECKRING

A. Operation in Water

1. Shaft Power

The shaft is treated as a cylinder rotating in infinite space surrounded by water. Then:

$$\tau = C_f \; \tfrac{1}{2}\rho\omega^2 R^2 \qquad \ldots \text{(XIII.1)}$$

C_f is a function of Re_ω, as shown in Figure XIII(i), which has been redrawn from Reference [80].

The average pump shaft radius is 2.5cm, with 5cm length exposed. At 2500 rpm, $Re_\omega = 1.6 \times 10^5$, $\therefore$ $C_f = 4.0 \times 10^{-3}$ (from Figure XIII(i)).

$\therefore$ $\tau = 85.6 \; Nm^{-2}$, which gives:

$$M \; (= \pi D L \tau R) \;\; = \;\; 0.017 \; Nm.$$

$\therefore$ $P_{in} \; (=\omega M) \;\; = \;\; 4.4W.$

The shaft carries a grubscrew and projecting key, whose contribution to the gross power absorbed is estimated to be about three times that of the shaft.

$\therefore$ Gross power absorbed $\simeq$ 18W.

2. Power absorbed by Upper Neckring

The flow conditions encountered in the neckring clearance lie outside the range previously investigated in the literature. Therefore the power has been calculated twice for a representative leakage rate of $20\ell.\text{min}^{-1}$ at 2500 rpm, by extrapolating two sets of separately published data. The notation from the original papers has been changed slightly to conform with that used elsewhere in this thesis.

The following seal dimensions are required:

$$\text{Neckring length } [L] = 13.5\text{mm}$$
$$\text{Radial clearance } [h] = 0.165\text{mm}$$
$$\text{Inner hub radius } [R_h] = 25.3\text{mm}.$$

2.1 According to the method proposed by Bilgen et al[79], the moment coefficient for an annular slot with no through flow $[C_{M_{sl}}]$ is a function of the Couette Reynolds Number $[\text{Re}_u = \frac{\omega R_h h}{\nu}]$* and the slot clearance ratio $[\frac{h}{R_h}]$: see Figure XIII(ii). C_{MA}, which is the moment coefficient with axial throughflow, may then be found from Figure XIII(iii), which shows the relationship between $C_{MA}/C_{M_{sl}}$** and $\bar{y}/u$, (the ratio of throughflow and peripheral velocities).

In the present case:

$$\text{Re}_u = 1094$$
$$\frac{h}{R_h} = 0.0065 \qquad \therefore \ (\frac{h}{R_h})^{-0.1} = 1.65.$$

From Figure XIII(ii), $C_{M_{sl}}(\frac{h}{R_h})^{-0.1} = 0.013.$

$$\therefore \quad C_{M_{sl}} = 7.88 \times 10^{-3} .$$

---

* The definition of Re_u given by Bilgen et al [79] differs from that used elsewhere in this thesis (see Figure 36) by a factor of 2.

** The definition of C_M for an annular slot is: $C_M = \dfrac{M}{\frac{1}{2}\rho\omega^2 R^4 L}$, which also differ from that given in the notation at the beginning of this thesis.

Also: $u(= \omega R_h)$ =   6.63 m.sec^{-1}

          $\bar{y}(= \dfrac{Q_{s1}}{A_{s1}})$ =   12.66 m.sec^{-1}.

$\therefore$ $\bar{y}/u$ = 1.91, which is outside the range covered in Figure XIII(iii). By extrapolation:

$$C_{MA}/C_{M_{s1}} = 0.8. \qquad \therefore C_{MA} = 6.3 \times 10^{-3}.$$

Then M $[= C_{MA} \tfrac{1}{2} \pi \rho \omega^2 R_h^4 L]$ = 3.7 $\times 10^{-3}$ Nm.

$\therefore$ $\underline{P_{in} = 0.97 W}$

2.2   The torque coefficient in an annular slot $[C_f]$ has been investigated by Yamada[78] for a range of gap widths and axial and throughflow Reynolds Numbers.

In the present case:

$$Re_u = 1094 \text{ (see above)}$$
$$Re_{\bar{y}} [= \dfrac{\bar{y}h}{\nu}]* = 2165$$
$$h/R_h = 0.0065 \text{ (see above)}.$$

The smallest clearance ratio covered by Yamada's work is h/R_h = 0.0136 (see Figure XIII(iv)). By extrapolating the general trend of increasing C_f with decreasing clearance ratio for a given value of Re_u and $Re_{\bar{y}}$ shown by other gap geometries in Reference [78], a representative value of C_f = 0.002 has been chosen for the present calculations.

Then M $[= C_f 2\pi\rho\omega^2 R_h^4 L]$ = 4.75 $\times 10^{-3}$ Nm.

[Note that by definition, C_f differs from C_{MA} in the preceding section by

---

*The definition of $Re_{\bar{y}}$ given by Yamada[78] differs from that used elsewhere in this thesis (see Figure 36) by a factor of 2.

a factor of 4].

$$\therefore \quad \underline{P_{in} \quad = \quad 1.25 \ W} \ .$$

Agreement between the two figures for power absorbed by the upper neckring at 2500 rpm in water, calculated by separate methods, is reasonable.

The total power absorbed by the shaft (see Section A) and neckring has been rounded up to 20W at 2500 rpm. This corresponds to a power coefficient (κ), derived from the pump impeller diameter (0.143m) of 0.02×10^{-3}.

B. Operation in Mercury

1. Shaft Power

The shaft diameter on the O.L.R. is irregular and mercury which has leaked through the top neckring rises a considerable distance up the shaft before it can escape through holes in the pump support tube (see Figure 1). Therefore the shaft has been divided into three sections, which are each treated as a cylinder rotating in infinite space surrounded by mercury.

For the top section [R = 3.75cm, L = 1.6cm] :

$$Re_{\omega} \ = \ 1.8 \times 10^{6} \ [\text{at 1450 rpm}]$$
$$\therefore \quad C_{f} \ = \ 2.5 \times 10^{-3} \ [\text{from Figure XIII(i)}]$$
$$\tau \ = \ 547 \ Nm^{-2}$$
$$M \ = \ 0.077 \ Nm.$$

For the central section [R = 1.5cm, L = 2.0cm] :

$$Re_\omega = 1.7 \times 10^5$$
$$C_f = 6.3 \times 10^{-3}$$
$$\tau = 221 \text{ Nm}^{-2}$$
$$M = 0.0063 \text{ Nm.}$$

This section also carries a projecting key, whose contribution to the total torque is estimated as twice that of the shaft section itself.

∴ Gross torque (shaft section + key) = 0.019 Nm.

For the lower hub section [R = 2.54cm, L = 1.8cm] :

$$Re_\omega = 8.3 \times 10^5$$
$$C_f = 2.8 \times 10^{-3}$$
$$\tau = 272 \text{ Nm}^{-2}$$
$$M = 0.021 \text{ Nm.}$$

∴ Total torque absorbed by shaft = 0.117 Nm

$$\underline{P_{in} = 17.8 \text{ W}}$$

When a HDS is fitted on the pump, so that mercury leakage through the upper seal is stemmed, the rotating shaft will be surrounded by water (which covers all exposed mercury surfaces on the O.L.R). The length of exposed shaft differs for the single and two-stage HDS configurations, but the major contribution to total power absorption will be at the upper section, where the radius is largest.

For this top section in water [R = 3.75cm, L = 1.6 cm] :

$$Re_\omega = 2.1 \times 10^5$$
$$C_f = 3.8 \times 10^{-3}$$

$$\tau = 62 \text{ Nm}^{-2}$$

$$\therefore \frac{\tau_w}{\tau_m} = \frac{62}{547} = 0.11.$$

Thus the power absorbed by the shaft when a HDS is fitted on the pump is about 10% of the power absorbed by the shaft of the pump fitted with neckrings. This is less than 0.1% of the total measured torque and has therefore been neglected.

2. Power absorbed by Upper Neckring

2.1   Following the procedure used in Reference[79] :

$$Re_u = 5566 \quad \text{(for the upper neckring in mercury at 1450 rpm).}$$

Then, from Figure XIII(ii):

$$C_M \left(\frac{h}{R_h}\right)^{-0.1} = 0.01, \text{ with } h/R_h = 0.0065.$$

$$\therefore \quad C_{M_{s1}} = 6 \times 10^{-3}.$$

Also
$$u = 1.22 \text{ m.sec}^{-1}$$
$$\bar{y} = 7.4 \text{ m.sec}^{-1} \quad [\text{Maximum leakage} = 13.5 \ell.\text{min}^{-1}] \ .$$

$$\therefore \quad \bar{y}/u = 6.04, \text{ which again is outside the range of}$$
$$\text{Figure XIII(iii).}$$

By extrapolation, $C_{MA}/C_{M_{s1}} \simeq 0.85.$

Then $M = 13.9 \times 10^{-3}$ Nm.

$$\therefore \quad \underline{P_{in} = 2.1 \text{ W}} \ .$$

2.2   According to the method suggested by Yamada[78],

$$Re_u = 5566$$
$$Re_{\bar{y}} = 1.2 \times 10^4 \ .$$

Although the clearance ratio (h/R_h) is lower than the minimum value examined by Yamada, for $Re_u \simeq 5,000$, C_f remains remarkably constant at 0.0012 for larger clearances [See Figure XIII(iv)].

Then $M = 12.9 \times 10^{-3}$ Nm.

∴. $\underline{P_{in} = 1.95 \text{ W}}$

The total power absorbed by the shaft and upper neckring when the standard pump runs in mercury at 1450 rpm has been rounded up to 20W. This figure corresponds to a power coefficient (κ) of 0.007×10^{-3}, derived from the pump impeller diameter of 0.143m.

Laminar flow

$C_f = \frac{4}{R}$

Turbulent flow

$\frac{1}{\sqrt{C_f}} = -0\cdot6 + 4\cdot07 \log Re_\omega \sqrt{C_f}$
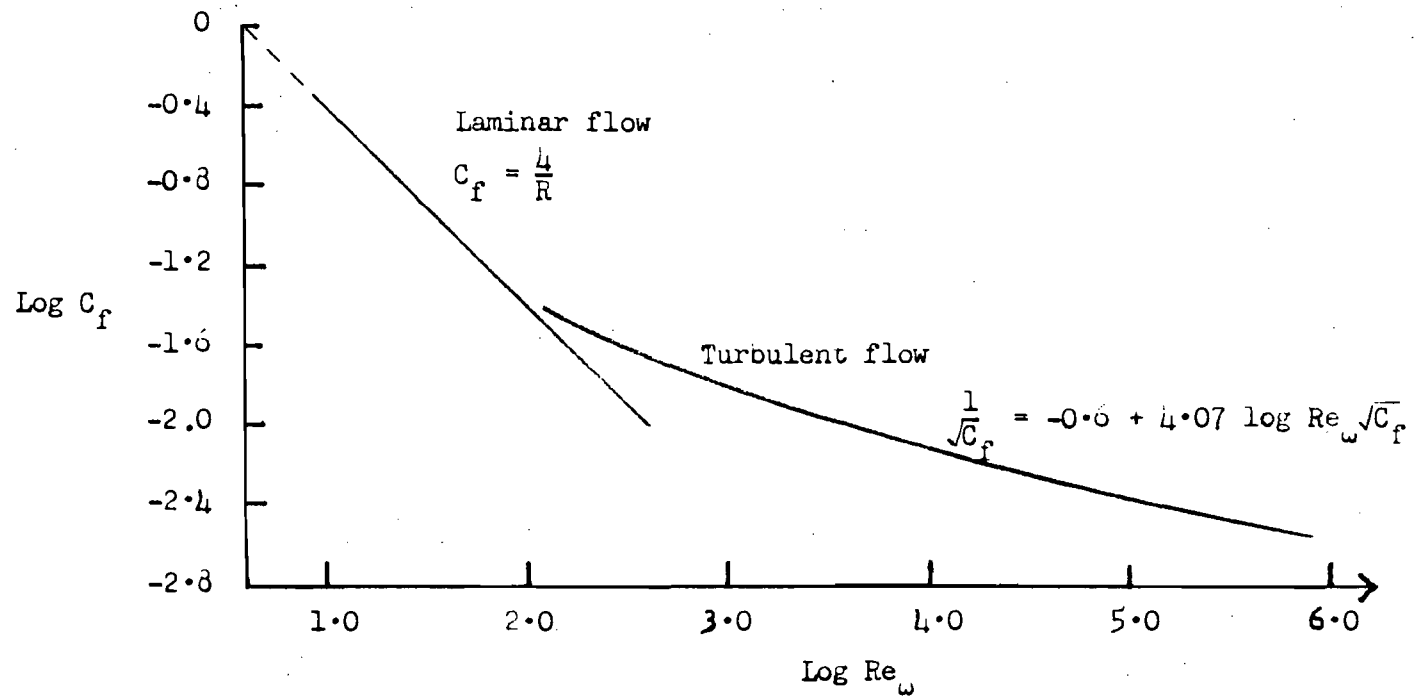
FIGURE XIII(i). COEFFICIENT OF FRICTION FOR THE SMOOTH SURFACE OF A ROTATING CYLINDER AS A FUNCTION OF REYNOLDS NO.[80]

A94.
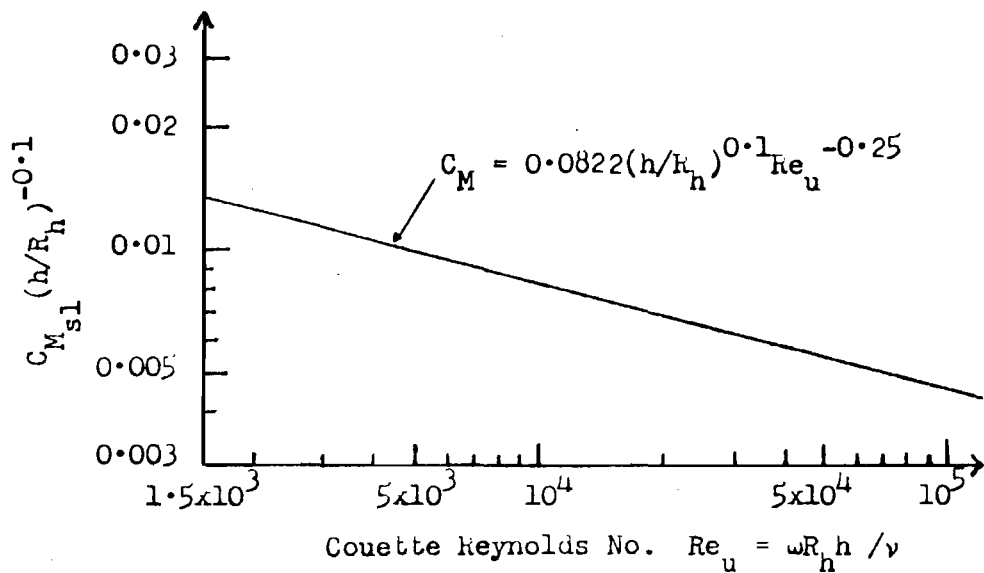
FIGURE XIII(ii). MOMENT COEFFICIENT OF COAXIAL CYLINDERS
VERSUS COUETTE REYNOLDS NUMBER.
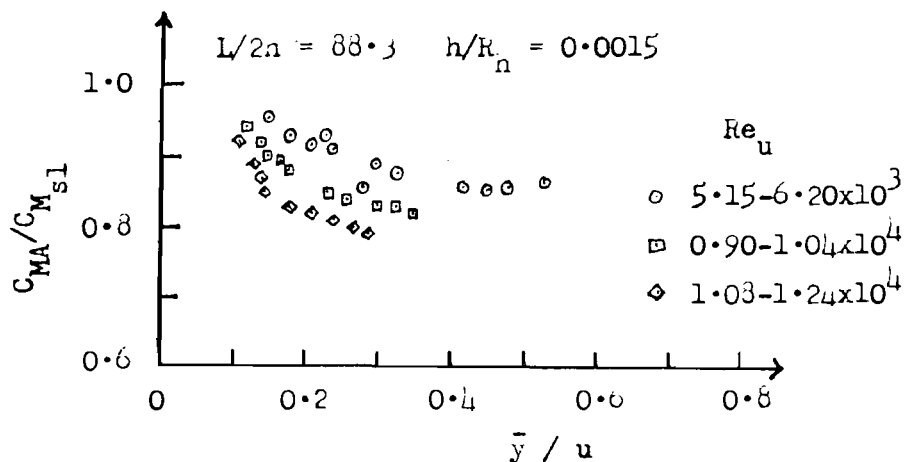
FIGURE XIII(iii). MOMENT COEFFICIENT RATIO VERSUS VELOCITY
RATIO FOR COAXIAL CYLINDERS.
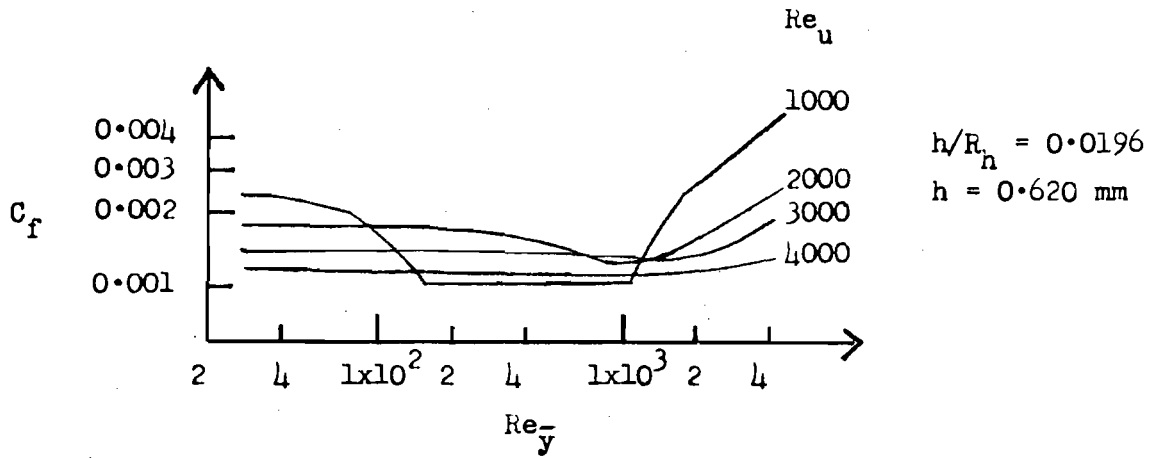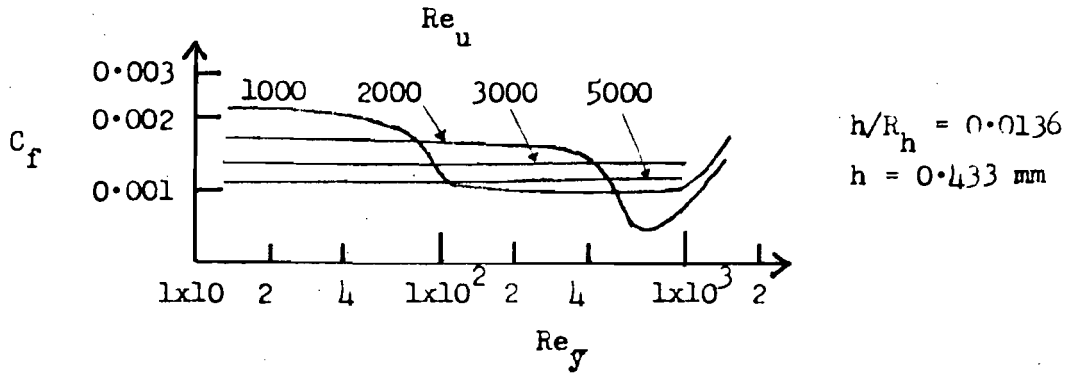
FIGURE XIII (iv). RELATIONSHIP BETWEEN C_f AND $Re_{\bar{y}}$ FOR VARIOUS Re_u.[78]

APPENDIX XIV

COMPARISON OF DRAG AND BUOYANCY FORCES ON ENTRAINED DROPLETS IN A HDS

A. Single Stage HDS in Mercury

1. Consider an interface radius of 6cm (X=0.75). Corresponding rotational speed = 1420 rpm (motor running on overload). The interface will be unstable because of its wide relative radius[59], facilitating the entrainment of water droplets. There is a maximum size of droplet for which the drag force exerted by the radial outflow of mercury in the HDS exceeds the buoyancy force due to the different densities of the two fluids.

The buoyancy force (F_B) is given by Equation (12.3):

$$F_B = \Delta \rho \, \frac{4}{3} \, \pi \, r^3 \, \dot{c}_r$$

where $\Delta \rho = 12.6 \times 10^3$ for water drops in mercury, r = droplet radius and $\dot{c}_r$ = radial acceleration of droplets = $(k_v \omega)^2 R_i$.

∴ For a droplet of 0.5μm diameter:

$$F_B = 12.6 \times 10^3 \times \frac{4}{3} \pi 2.5^3 \times 10^{-21} (0.94 \times \frac{2 \pi 1420}{60})^2 \times 0.06$$

$$= 9.7 \times 10^{-13} \text{ N} .$$

For a droplet of 0.6μm diameter:

$$F_B = 1.7 \times 10^{-12} \text{ N.}$$

The drag force (F_D) is given by equation (12.4):

$$F_D = \pi r^2 C_D (c_{rel})^2$$

where C_D is a function of Reynolds Number (Re_B), based on droplet size[82,83] [see Figure XIV(i)], and c_{rel} = radial velocity of mercury flow relative to water droplets $\simeq$ 10% tangential velocity ($k_v \omega R_i$).

$$\therefore c_{rel} = \frac{1}{10} \frac{2 \pi 1420}{60} \times 0.06 \times 0.96 = 0.84 \text{ m.sec}^{-1}.$$

For a droplet of 0.5μm diameter:

$$Re_B = \frac{c_{rel} \times 2r}{\nu_m} = 3.7. \qquad \therefore C_D = 9 \text{ (from Figure XIV(i)).}$$

$$\therefore \quad F_D = \pi 2.5^2 \times 10^{-14} \times 9 \times 0.84^2$$

$$= \underline{1.2 \times 10^{-12} \text{ N.}}$$

For a droplet of 0.6μm diameter:

$$Re_B = 4.4 \qquad \therefore C_D = 7.5.$$

$$\therefore \quad \underline{F_D = 1.5 \times 10^{-12} \text{ N.}}$$

Therefore the buoyancy force exceeds the drag force for any droplets larger than 0.6μm diameter, and these will move inwards, back to the interface. However, when the droplet size is reduced below this value, the drag force increases rapidly, due to the logarithmic relationship between C_D and Re_B (see Figure XIV(i)) and drops may be carried outward to the disc tip.

2.   Consider the situation where water droplets have been swept across the disc tip and coalesce to form a pool of water surrounding the shaft on the smooth side of the disc. If this pool is to disperse, droplets of water must be formed at the mercury/water interface and be swept back out to the disc tip by the radial outflow of mercury.

Taking a representative radius of 4cm for the interface (X=0.5):

$$C_{rel} = \frac{1}{10} \ \frac{2 \pi \, 1420}{60} \ x \ 0.04 \ x \ 0.46 = 0.27 \ m.sec^{-1}.$$

For a droplet of 0.7μm diameter:

$$F_B = 12.6 \ x \ 10^3 \ x \ \frac{4}{3} \pi 3.5^3 \ x \ 10^{-21} (0.46 \ x \ \frac{2 \pi \, 1420}{60})^2 \ x \ 0.04$$

$$= \underline{4.3 \ x \ 10^{-13} \ N} \ .$$

$Re_B = 1.7 \qquad \therefore \ C_D = 17.$

$$F_D = \pi \, 3.5^2 \ x \ 10^{-14} \ x \ 17 \ x \ 0.27^2$$

$$= \underline{4.8 \ x \ 10^{-13} \ N}$$

For a droplet of 0.8μm diameter:

$$\underline{F_B = 6.4 \ x \ 10^{-13}}$$

$Re_B = 1.9 \qquad \therefore \ C_D = 15 \ .$

$$\underline{F_D = 5.5 \ x \ 10^{-13}}$$

Therefore the maximum size of water droplet that could be swept back out to the disc tip is 0.7μm diameter, and water collecting near the shaft will be slow to disperse.

B. Two-Stage (I) HDS in Mercury

Consider an interface radius of 37mm (X=0.7), i.e between the two innermost pressure tappings on the upper disc. Rotational speed = 1450 rpm. Water bubbles will be entrained at the unstable interface.

For a droplet of 0.5μm diameter:

$$F_B = 12.6 \times 10^3 \times \frac{4}{3} \pi 2.5^3 \times 10^{-21} \left(\frac{0.94 \times 2 \pi 1450}{60}\right)^2 \times 0.037.$$

$$= \underline{6.2 \times 10^{-13} \text{ N}} \; .$$

$$C_{rel} \simeq 0.53 \text{m.sec}^{-1}$$

$$Re_B = 2.3 \qquad \therefore C_D = 13.$$

$$\therefore \quad F_D = \pi 1.5^2 \times 20 \times 0.53^2$$

$$= \underline{7.2 \times 10^{-13} \text{ N}}$$

For a droplet of 0.6μm diameter:

$$\underline{F_B = 1.1 \times 10^{-12} \text{ N}}$$

$$Re_B = 2.8 \qquad \therefore C_D = 11.$$

$$\therefore \quad \underline{F_D = 1.0 \times 10^{-12} \text{ N}}$$

Therefore entrained water droplets of <0.6μm diameter will be swept out from the interface to the disc tip, and eventually will collect at the interstage region of the two-stage seal.

C. Two-Stage (I) HDS in Water

Consider similar operating conditions to the above example for mercury, i.e. R_i = 37mm and n = 1450 rpm. Air bubbles will be entrained at the interface with water.

For an air bubble 5μm diameter:

$$F_B = 997 \times \frac{4}{3} \pi \, 2.5^3 \times 10^{-18} \left(\frac{0.94 \times 2 \pi \, 1450}{60}\right)^2 \times 0.037$$

$$= 4.9 \times 10^{-11} \text{ N}$$

$$Re_B = 2.7 \qquad \therefore \quad C_D = 11.5.$$

$$\therefore F_D = \pi \, 2.5^2 \times 10^{-12} \times 11.5 \times 0.53^2$$

$$= 6.3 \times 10^{-11} \text{ N.}$$

For a bubble 6μm diameter:

$$F_B = 8.5 \times 10^{-11} \text{ N}$$

$$Re_B = 3.18 \qquad \therefore \quad C_D = 10.$$

$$\therefore F_D = 7.9 \times 10^{-11} \text{ N}$$

These calculations show that water bubbles which are swept out from the interface to the disc tip when the two-stage HDS runs in water may be up to 10x larger than the water droplets which reach the disc tip when the seal runs in mercury.

Data extracted from Reference (82 and 83)

Stokes Law

$C_D = 24/Re_B$
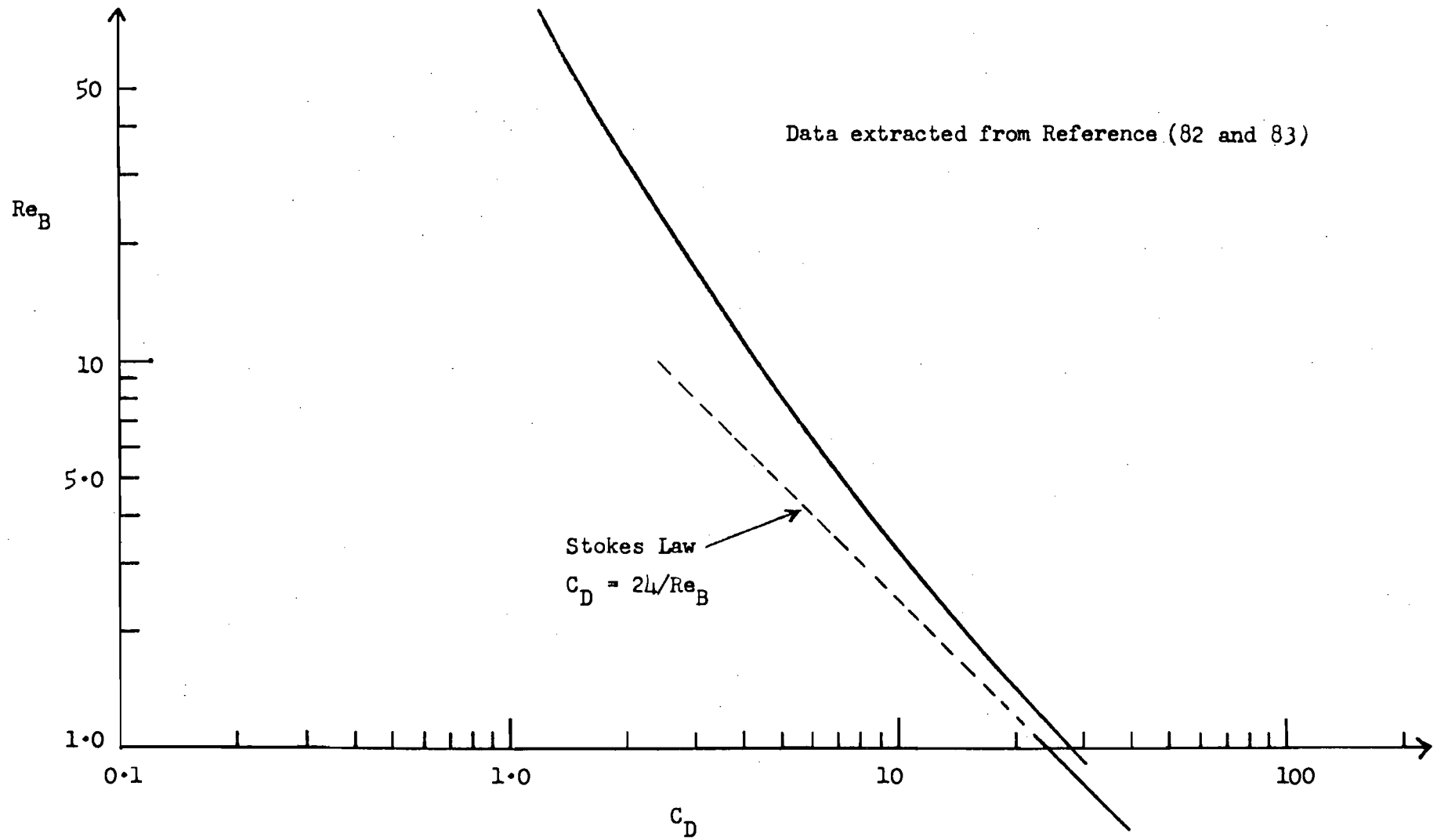
FIGURE XIV(i). RELATIONSHIP BETWEEN DRAG COEFFICIENT AND REYNOLDS NUMBER FOR SPHERICAL BUBBLES.

EFFECT OF THE HDS ON PUMP PERFORMANCE IN MERCURY

A. Seal Leakage

The single stage HDS eliminates leakage through the top shaft clearance at all points on the pump characteristic in mercury. The two-stage (I) HDS leaks slightly at pump shut off, but not at the duty point of $55\ell.min^{-1}$ at 1450 rpm. The maximum measured leakage rate is $0.2\ell.min^{-1}$ and leakage ceases at a pump flowrate of $10\ell.min^{-1}$, which is a slight improvement over the performance in water (see Table IX(i)).

The variation of pressure at the upper and lower seal inlets with pump flowrate is similar for the two designs of HDS running in mercury (see Figures 147 and 148). Pressure at the lower neckring is some 36% higher than in the standard pump at zero flow and hence a 6% faster leakage rate would also be expected (Equation (5.19)). The pressure differential becomes smaller as the pump flowrate increases and at the duty flowrate leakage through the bottom seal should not exceed that in the standard pump by more than 4%. The rapid fall in pressure at the inlet to the HDS and lower neckring at maximum flowrate is related to the concomitant drop in pump delivered head, shown in Figures 149 and 150. Reasons for this are fully discussed in the following section.

B. Generated Head

Changes in the dimensionless head/flow characteristic of the pump in mercury when the upper neckring is replaced by either design of HDS are minimal for $\phi < 2.6 \times 10^{-3}$ (see Figures 149 and 150). At very

low flows, the head curve is flatter than that of the standard pump. Similar behaviour was noted when the pump fitted with a HDS was tested in water (Figures 128-130) and it is probable that this represents a part of the characteristic which cannot be achieved in the standard pump because of the high leakage rate with neckrings.

At high mercury flows, the head characteristic of the pump with the new sealing arrangements falls below that of the standard pump, which is inconsistent with the behaviour in water. Here the head characteristic is shifted to the right (and therefore above that of the standard pump: see Figures 128-130) because of the lower leakage rate with a HDS.

Modifications on the Q.L.R. to accommodate a HDS are thought to have enhanced the likelihood of water entrainment through the pump inlet (see Chapter 12.1). The lower density of a mercury/water mixture will reduce the pressure generated by the pump and will also reduce the pressure differential across the venturi flowmeter. Therefore the experimental data for both head and flowrate will be affected.

Since the head characteristics of the standard pump in water and mercury are similar at high flowrates (Figure 86), the water content of the mercury in the present tests has been calculated on the assumption that the head characteristic of pump fitted with a HDS will also coincide with the water curve at high flows. The "mercury/water" data points have been replotted in Figures 149 and 150, showing that the water content increases from about 2% at the duty flowrate ($\phi = 2.06 \times 10^{-3}$) to more than 30% at maximum flows.

Water ingestion through the pump inlet alone is insufficient to explain such a high apparent water content. Cavitation would have a similar adverse effect on the head characteristic and this is known to occur in the standard pump at maximum flows (see Chapter 7.2.1 and Appendix VII). The suction specific speed of the pump is only 0.9 (see

Appendix VII), an exceptionally low value indicative of poor
cavitation performance, and cavitation on the O.L.R. will also be
promoted by the presence of water in the mercury, because water has
a higher vapour pressure. The distinctive sound of cavitation was
detected for the pump fitted with both designs of HDS running at
maximum flowrate, but the inception point will occur much earlier on
the characteristic. Since the consequences of water ingestion and
cavitation on the pump generated head are indistinguishable, a flow
coefficient of 4.0×10^{-3} is suggested as the maximum for which the
characteristics in Figures 149 and 150 represent cavitation-free
performance.

The rapid fall in pump head when $\phi < 4.0 \times 10^{-3}$ is reflected
by a drop in pressure at the inlet to the HDS (see Figures 147 and
148). The mercury/water interface must therefore move outward on the vaned
side of the sealing disc and will become unstable when the relative radius
X exceeds 0.8[59]. This situation facilitates the entrainment of water
droplets at the interface (see Chapter 12.3.3) which may easily reach
the disc tip, because of its proximity. Previous research using dye
injection techniques[59] demonstrated instantaneous mixing of fluid
between the smooth and vaned surfaces at the tip of a HDS. Therefore,
many of the water droplets will be carried across the tip to the smooth
side of the disc, whence they will be swept towards the shaft by
buoyancy forces.

Water which collects in the shaft region on the smooth side of
the sealing disc(s) is unlikely to be swept away, since the inward
buoyancy forces exceed the drag forces exerted by the radial outflow of
mercury at a representative radius of 4cm, or halfway across the single
stage sealing disc for any water droplets larger than 0.6μm diameter
(see Appendix XIV). A detailed discussion of the problem of water entrain-
ment and collection near the shaft may be found in Chapter 12.3.3.

The low density of water compared with mercury reduces the
parasitic pressure rise across the smooth face of the disc(s) and the
mercury/water interface on the vaned side must move further out.
Eventually, the interface becomes totally unstable and the seal breaks
down, so that water (which covers the mercury pool in the tank and
fills the space around the drive shaft above the HDS: see Figure 1) is
pumped by the pressure rise across the vaned surface of the sealing
disc(s) into the pump volute. Here it mixes with fluid from the pump
impeller and passes out through the delivery pipe.

The seal breakdown is clearly indicated by a sudden decrease
in the pressure rise across the smooth side of the sealing disc(s),
when they become flooded with low density water rather than mercury.
The experimental points where water is flowing in through the HDS
have been marked in Figures 149 and 150.

C. Absorbed Power

The dimensionless absorbed power characteristics of the pump
fitted with a HDS running in mercury are presented in Figures 151 (single
stage seal) and 152 (two-stage seal). Curve A in each Figure, which
represents the power characteristics if the pumping liquid were 100%
mercury, is thought to be inaccurate and the experimental data has been
corrected for water content (as estimated from Figures 149 and 150) and
replotted to give Curve B. High flowrate points, where water was pumped
through the seal, have been disregarded.

The pump motor was running on overload at high flowrates,
particularly with the single stage HDS, where it overheated and eventually
cut out. The motor efficiency is gradually reduced with overload and the
time lag for recovery is apparent from the slight hysteresis effect
exhibited by the data points in Figures 151 and 152. Power measurements
for increasing flowrate are thought to be more accurate.

The power characteristic of the pump and single stage HDS, corrected for water content in the mercury (Curve B in Figure 151), runs above and almost parallel to Curve C, which is the corresponding characteristic in water. The extra power requirement in mercury is ascribed to parasitic power losses, which will be greater than for the standard pump tests on the O.L.R. (see Chapter 7.3.2). The single stage HDS generates a high end load (Appendix VIII), which must be absorbed by the thrust bearings, and in addition, the efficiency of the motor is progressively reduced at overload. No precise information is available concerning the motor efficiency under these conditions, therefore the full load efficiency (see Table 6.1) was used to compute the nett power absorbed by the pump and HDS from the gross input power data. Consequently, the parasitic power consumption increases with pump flowrate. The average parasitic power coefficient is 0.15×10^{-3}, as compared with 0.085×10^{-3} for the standard pump on the O.L.R. (Chapter 7.3.2).

Figure 151 clearly demonstrates that the single stage HDS is unsuitable for the pump operating in mercury if it is to be driven by the present motor. Even at zero flow, the motor rating of 2.6kW is exceeded: the gross input power (including motor losses) is 2.8kW or 8% overload.

The two-stage(I) HDS is more acceptable (see Figure 152). At the duty flowrate of $55\ell.\text{min}^{-1}$, the measured input power (including motor losses) is 2.5kW and therefore the existing motors would be adequate to drive the pump fitted with this design of seal.

The power characteristic of the pump with two-stage(I) HDS and corrected for water content in mercury (Curve B in Figure 152) runs parallel to the characteristic in water (Curve C) for $\phi = (1.6-3.5) \times 10^{-3}$. The average difference in power coefficient is 0.08×10^{-3}, which is remarkably close to the parasitic power coefficient of 0.085×10^{-3} estimated for the standard pump on the O.L.R. in Chapter 7.3.2. This

suggests that variations in Reynolds Number due to changes in fluid viscosity do not affect the power coefficient of the HDS.

At low flows ($\phi < 1.6 \times 10^{-3}$) the power characteristics of the pump with two-stage (I) HDS (Curve A) and of the standard pump (Curve C) diverge. This is surprising since the opposite effect was found in water, where leakage of the HDS at low flows reduced C_{MD} across the back of the pump impeller and the two curves converged (see Figure 132). The explanation may lie in a slight rub on the lower neckring with the two-stage HDS in mercury, caused by a difference in the assembled geometry of the pump with the new seal (see Appendix IX, Section A), coupled with the asymmetric pressure distribution which is known to exist in the pump volute at low flowrates (Chapter 5.1).

Power requirements of the pump fitted with the single and two-stage(I) HDS are compared in the Table below:

Table XV(i): Effect of HDS on Pump Power Absorption
in Mercury.

Tabulated data gives the mean increase in power absorbed by the pump fitted with a HDS, expressed as a percentage of the mean power absorbed by the standard pump at the same flow coefficient (from Figures 151-152).

Flow Coefficient	Pump + Single-stage HDS	Pump + Two-stage(I) HDS
0	60%	22%
2.06×10^{-3} (duty point)	48%	6%
3.5×10^{-3} (maximum for which seal was operating correctly)	47%	7.5%

Since the power coefficient for a HDS is not affected by changes in Re_ω, it is possible to scale up data from the two-stage (II) HDS trials in water, in order to predict the power requirement of the pump fitted with this seal running in mercury.

From Figure 146, at its normal operating point ($\phi = 2.06 \times 10^{-3}$) the power coefficient for the pump fitted with the two-stage (II) HDS is 0.02×10^{-3} higher than that of the pump with the two-stage (I) seal. This is equivalent to an increase in absorbed power in mercury of:

$$\Delta P_{in} = 0.02 \times \left(\frac{2\pi 1460}{60}\right)^3 \times 0.143^5 \times 13.6 = 58W$$

Added to the gross (measured) input power to the motor when driving the pump fitted with the two-stage (I) HDS (see above), this gives a gross power requirement of 2.56kW. Therefore, the existing motor would also be adequate to drive the pump fitted with the two-stage (II) HDS.

D. Efficiency

The efficiency characteristics of the pump with the new sealing arrangements are presented in Figures 153 (single stage HDS) and 154 (two-stage (I) HDS). The characteristics which have been corrected for water content in the mercury (Curve B in both Figures) are still rising at the last data point before the seal breaks down and pumps water from above into the pump volute, so maximum efficiency is not achieved.

The overall efficiency is lower than for the standard pump, but the difference with the two-stage HDS is small. Pump efficiency data with a HDS and with neckrings is compared in Chapter 12.2.4, Table 12.1.

ANALYSIS OF SINGLE STAGE HDS PERFORMANCE IN MERCURY

A. Sealing Performance: Comparison with Water

The radial pressure distribution across the vaned surface of the single stage HDS fitted in the pump running at shut-off (i.e. maximum seal inlet pressure) in mercury is compared with the mean curve for water in Figure 155. Unlike the Reynolds Number effect displayed for speed changes in water (see Figure 137), there is no sign of the higher Reynolds Number flow regime in mercury affecting the pressure gradient and seal performance in the two fluids correlates well. The superficial scatter of mercury data points was also evident for water results at comparable speeds. A slightly lower local pressure coefficient at small radii in mercury may be due to water entrainment and a consequent density gradient in the vicinity of the interface. Similar behaviour is observed for a two-stage HDS running in water, when air entrainment causes unexpectedly low pressure readings close to the interface (see Figures 143-145).

Water entrainment at the mercury/water interface is reflected by a slight rise in tip region k_v (calculated from experimental pressure measurements) as the interface moves outwards: see Figure 156a. Calculations of k_v based on radial pressure differences are only accurate for fluid of a constant density and in this case, there is a radial density gradient. Generally, k_v for a HDS is acknowledged to fall as the interface moves outward[49,52,59], as confirmed by the single stage HDS performance in water (see Figure 140). Figure 156a suggests that the mercury/water interface on the vaned surface of the sealing disc is less

stable than the water/air interface which forms when the HDS runs in water. Pressure measurements indicate that water entrainment in mercury occurs more readily than air entrainment in water, although this can only be confirmed by visual inspection (see Chapter 11.6.1). Reasons for the variation of interface stability in the two systems are fully discussed in Chapter 12.3.3.

The relationship between average values of k_s and interface position is shown in Figure 156b, which confirms the results for water (Figure 141). This increase in k_s with interface radius is attributed to changes in the asymmetry of the seal inlet pressure and fluid preswirl as the pump flowrate varies: see Appendix X.A.

Table 12.2, which has been partially reproduced below as Table XVI(i) for the convenience of the reader, lists the main performance parameters for the single stage HDS running in conjunction with the pump in water and mercury.

Table XVI(i): Comparison of Performance Parameters in Water and Mercury: Single Stage HDS in Pump

(Data for maximum seal inlet pressure: $R_i \approx 0.45 R_D$)

	Water		Mercury
Rotational speed (rpm)	1500	2500	1440
Re_ω	1.0×10^6	1.7×10^6	8.5×10^6
C_p (max)	0.61	0.60	0.60
Average k_v.	0.90	0.96	0.93
Average k_s.	0.29	0.46	0.33

Maximum C_p in mercury compares well with values in water, which corroborates the conclusion drawn from tests at different speeds in water, that C_p is invariant with Re_ω (see Appendix X).

k_v in the high Reynolds Number mercury flow is lower than the maximum value for water. In earlier studies on water, using an interface radius of $0.65R_D$[49], k_v was found to increase with Reynolds Number up to $Re_\omega \simeq 1.5 \times 10^6$, and then decrease again. This is verified by the present results, which also apply to a relatively wide interface position at $0.5R_D$. (Note that for an interface closer to the shaft, k_v would be expected to increase with Re_ω and then remain constant at its maximum value).

k_s in mercury is also much lower than the value for water at 2500 rpm. (The figure of 0.29 at 1500 rpm in water is exceptionally low in relation to data at other speeds: see Table X(ii)). On the smooth side of the sealing disc, rotational motion is passed on to the fluid solely by viscous drag, which will be less effective in a low viscosity fluid such as mercury. Previous research has not encompassed such high Reynolds Numbers, but Reference [49] suggests that k_s for a similar disc may fall when $Re_\omega > 1.8 \times 10^6$. A low value of k_s improves the performance of a HDS and in the present case compensates for the relatively low k_v in mercury discussed above.

At maximum pump flowrate, where the seal is malfunctioning and pumping water from above, k_s increases to 0.49. This confirms data from Reference [57], where radial fluid inflow in a HDS combined with a labyrinth seal was shown to increase the value of k_s.

B. Absorbed Power

No facilities were provided by ICI for testing the HDS alone in mercury, therefore an attempt has been made to estimate the power requirements of the seal by comparing the power characteristics of the pump with and without the HDS. This procedure has already been described in Appendix X. The power characteristic of the standard pump must be modified to allow for the effects of reduced leakage and removal of the upper neckring.

Published data by Yamada[78] and Bilgen et al[79] require extrapolation to cover the operating range of the mercury pump, but both methods of calculating the power absorbed by the upper neckring give a figure of about 2 Watts at 1450 rpm. Power absorbed by the pump shaft rotating in the cavity of the cylindrical pump support tube filled with mercury (see Figure 1) has been estimated at 18W by treating the shaft as a series of coaxial cylinders of different radii[80]. Total power absorbed by the shaft and neckrings is therefore 20W, corresponding to a power coefficient κ of 0.007×10^{-3}, based on the pump impeller radius.

The power coefficient of the standard pump, reduced by this amount, has been plotted against ϕ', which is the flow coefficient derived from the nett pump delivered flow plus upper neckring leakage. The curve is compared with the power characteristic of the pump fitted with the single and two-stage (I) HDS, corrected for water content in the mercury (i.e. curve B in Figures 151 and 152) in Figure 158.

The correlation ignores the effect of variations between lower neckring leakage rate in the standard pump and the pump with a HDS. When $\phi' > 1.5 \times 10^{-3}$ ($Q > 40\ell.min^{-1}$), the increase in leakage with a HDS due to the higher pressure at the bottom seal inlet (Figures 147 and 148) will be less than 4% of the total flow (see Appendix XV). The maximum resultant error in the estimated value of C_M for the HDS will be +1%, decreasing at higher flows.

When mercury leakage through the upper seal is stemmed, the shaft will rotate in water rather than mercury. Power absorption by the shaft is directly proportional to the density of the surrounding fluid (see Appendix XIII) and will therefore be approximately 1/13.6 of the power absorbed in mercury, or less than 1.5W. This contribution to the total power absorbed by the pump with the new sealing arrangements (which always exceeds 2.2kW - see Figures 151 and 152) is negligible.

The power characteristic of the pump fitted with the single stage HDS diverges from the "modified" characteristic of the standard pump in Figure 158, because of the fall in motor efficiency when it is overloaded at high pump flowrates (see Appendix XV). Therefore, the power absorbed by the seal itself has been calculated from the increase in κ as compared with the standard pump at $\phi=1.5\times10^{-3}$, which is the lowest flowrate where the effect of variations in lower neckring leakage rate can be discounted, (see above). The resultant figure of $0.012\pm11\%$ for C_M in mercury is identical to the value in water (Table 11.3), although there is a wider margin of error because of the uncertainty in the value of parasitic torque when the pump/single stage HDS assembly runs on the O.L.R.(see Appendix XV.C).

APPENDIX XVII

ANALYSIS OF TWO-STAGE (I) HDS PERFORMANCE IN MERCURY

A. Sealing Performance: Comparison with Water

The radial pressure distribution in the two-stage (I) HDS fitted on the pump running in mercury at the maximum seal inlet pressure (i.e. minimum pump flowrate) for no leakage is presented in Figure 157. The mean curve for water (from Figure 143) has been included for comparison.

Correlation between the water and mercury results is good, except for the single tapping on the upper disc at $R_{tap}/R_D = 0.96$. The same point is an outlyer for all values of seal inlet pressure, which suggests that the tapping may have been incorrectly positioned and lies at a wider radius than specified on the design drawings. As explained in Section 12.3, the main drawback of testing different (although nominally identical) seal assemblies in water and mercury is that geometric similarity - including the positioning of pressure tappings - cannot be guaranteed.

The coincidence of the mercury data points with the mean water curve was anticipated, in view of the absence of any Reynolds Number effect for speed changes when this seal runs in water (see Figure 143).

The change in pressure distribution close to the interface on the upper disc, caused by a radial density gradient because of air entrainment in water (Appendix XI) is also present when the HDS runs in mercury. Several geometry factors of the two-stage (I) seal contribute

to interface instability (and hence air or water entrainment), such as a relatively larger hole for the shaft in the housing wall than for the single stage seal, and relatively narrower channels between the vanes. In addition, water entrainment in mercury has been shown by the single stage seal trials to occur more readily than air entrainment in water (see Appendix XVI).

The main parameters governing the performance of the two-stage (I) HDS running in conjunction with the pump in water and mercury are listed in Table 12.3, which is partly reproduced below as Table XVII(i) for the convenience of the reader.

Table XVII(i): Comparison of Performance Parameters in Water and Mercury: Two-Stage (I) HDS in Pump

(Data for maximum seal inlet pressure with no leakage: $R_i \approx 0.5 \, R_D$)

		Water		Mercury
Rotational Speed (rpm)		1500	2500	1460
Re_{ω}		4.4×10^5	7.4×10^5	3.8×10^6
Lower disc	C_p	0.62	0.65	0.68
	Av. k_v	0.89	0.94	0.92
	Av. k_s	0.41	0.45	0.35
Upper disc	C_p	0.53	0.51	0.57
	Av. k_v	0.89	0.89	0.89
	Av. k_s	0.46	0.48	0.42

C_p on both discs is higher in mercury than in water. On the upper disc, this may be due to a comparatively low k_s value (discussed below), combined with the beneficial effect of pressure generated by water inside the interface. On the lower disc, a high C_p value in mercury follows the rising trend with Reynolds Number that was found in water, although

C_p=0.68 is exceptionally high in comparison with other results from the present and previous research[49,52] on a single stage HDS. C_p is not expected to vary with Re_ω (see Appendix X and XII for data from the single stage and two-stage (II) HDS in water) and this unusual behaviour of the two-stage (I) seal is attributed in Appendix XI to its wide tip clearance.

k_s data in Table XVII(i) confirms the single stage HDS results, which showed that the value in mercury is lower than in water. As previously discussed in Appendix XVI, this is a type of Reynolds Number effect, caused by the low kinematic viscosity of mercury.

Poor figures for k_v on the upper disc in water are verified by the mercury results. Without the favourable effect of fluid entrainment at the interface (i.e. air in water and water in mercury) the values would be even smaller. On the lower disc, k_v was shown to be an increasing function of Re_ω in water (Table XI(ii)) but the trend is not continued in mercury. The reason becomes apparent when the variation in k_v between the shaft and tip regions of the lower disc is examined for the two fluids: see Table XVII(ii).

Table XVII(ii): Variation of k_v between the Shaft and Tip Regions of the Lower Disc: Two-Stage (I) HDS in Pump

(Data for maximum seal inlet pressure with no leakage: $R_i \approx 0.5\ R_D$)

Test Fluid	Rotational Speed (rpm)	Re_ω	Shaft region k_v R_{tap}/R_D=0.48→0.75	Tip region k_v R_{tap}/R_D=0.75→1.07
Water	1500	4.4×10^5	0.97	0.84
Water	2500	7.4×10^5	1.04	.0.87
Mercury	1460	3.8×10^6	0.98	0.89

Although k_v in the tip region is greatest for the high Reynolds Number mercury flow, air collecting near the shaft in water leads to deceptively

high k_v in this region (as previously discussed in Appendix XI). The effect of water entrapment in mercury is less pronounced and therefore average k_v across the whole disc is lower than for water.

B. Absorbed Power

The power characteristic of the pump fitted with the two-stage (I) HDS and running in mercury is compared with the characteristic of the standard pump, modified for the effects of reduced leakage and removal of the upper neckring (see Appendix XVI.B) in Figure 158. The power coefficient for the seal itself has been calculated from the difference in κ at five equi-spaced points along the characteristic for $\phi > 1.5 \times 10^{-3}$. By omitting low flowrates, errors due to a suspected lower neckring rub (Appendix XV.C) have been excluded, in addition to the problem of variations in lower neckring leakage rate (Appendix XV.A).

According to this analysis, C_M for the two-stage (I) HDS in mercury is 0.013±10%, which compares well with a value of 0.014±10% found for water (see Appendix XI.B).

NUMERICAL EXAMPLES OF EFFICIENCY DETERMINATION
FROM THERMOMETRIC MEASUREMENTS

[See Chapter 13.1 for Notation]

A. Calculation for Water

Physical properties of water at $20^{\circ}C$ and 1 atm absolute
pressure[62,76]:

Heat capacity (C_p) = 4,182 J $(kgK)^{-1}$

Coefficient of thermal expansion $(\frac{1}{V}[\frac{\partial V}{\partial T}])$ = 206.78×10^{-6} K^{-1}

Isothermal compressibility $(\frac{1}{V}[\frac{\partial V}{\partial p}])$ = 45×10^{-11} N^{-1}

Specific volume $(V = \frac{1}{\rho})$ = 1.00×10^{-3} $m^3 kg^{-1}$

Dynamic viscosity (μ) = 1.002 cP

Thermal conductivity (k) = 0.6 $W(mK)^{-1}$

Measured parameters:

Pump speed = 2000 rpm

Pump flowrate = $149.8\ell.min^{-1}$

Gauge pressure at pump inlet = 2940 Pa (1.04 bar absolute)

Gauge pressure at pump outlet = 93190 Pa (1.95 bar absolute)

ΔT_m (corrected for zero error) = 0.0182 $\pm$ 0.0007 K.

Temperature rise of bulk fluid = 7×10^{-4} $K.sec^{-1}$

Difference in geodetic level of T_1 and T_2 probes = 0.53m.

(i) Recovery Factor

Since the temperature of a moving fluid is being measured with a
stationary probe, the indicated temperature (T_M) will be higher than the
true, free-stream temperature (T) (see Chapter 13.5(d)). The difference
is a function of the dynamic temperature $(\frac{c^2}{2gC_p})$ as follows:

$$T_M = T + \frac{c^2}{2gC_p} R_f \qquad \ldots (13.17)$$

where $\quad R_f = KS + (1 - k)r \qquad \ldots (XVIII.1)$

is the overall recovery factor for a given fluid and thermometer probe geometry[74].

The first term on the right hand side of equation (XVIII.1) accounts for fluid stagnation effects at the probe. The pressure coefficient K is a function of the probe/conduit configuration and may be determined by averaging measured or calculated values of K_θ (the local pressure coefficient at a given point on the probe surface) at different points around the probe, i.e. $K = \frac{1}{\pi} \int_0^\theta K_\theta d\theta$. At $\theta=0$ (the leading edge of the probe), K=1 and from Equation (XVIII.1) the temperature rise is due entirely to stagnation effects.

The stagnation coefficient S is a property of the fluid, since:

$$S = \frac{T}{V} \left(\frac{\partial V}{\partial T}\right)_p \qquad \ldots (XVIII.2)$$

The second term on the right hand side of Equation XVIII.1 accounts for frictional heating, which predominates in liquid flows. The frictional recovery factor (r) is also a property of the fluid, since:

$$r = Pr^n \qquad \ldots (XVIII.3)$$

n, which varies with Reynolds Number and probe:pipe diameter ratio, may be determined experimentally.

It has been estimated that the available cross-sectional area for water flow at the T_1 measurement station is more than 40 times greater than the pipe cross-sectional area at T_2, so the effect of fluid inlet velocity and corresponding dynamic temperature on ΔT_M will be negligible.

The recovery factor for T_2 has been calculated from the empirical data in Reference [74] as follows:

For a 9.5mm ($\frac{3}{8}$") probe in a 38mm ($1\frac{1}{2}$") pipe:

$$K = -1.05$$
$$n = 0.18.$$

For water at $20^O C$:

$$Pr = \frac{\mu C_p}{k} = \frac{1.002 \times 10^{-3} \times 4182}{0.6} \simeq 7.0$$

$$S = \frac{T}{V}\left(\frac{\partial V}{\partial T}\right)_p = 293 \times 206.78 \times 10^{-6} = 0.0605.$$

Then, from Equation (XVIII.1):

$$R_f = -1.05 \times 0.0605 + 2.05 \times 7^{0.18}$$
$$= 2.97.$$

The mean fluid velocity at T_2 is given by:

$$\bar{c}_2 = \frac{Q}{A} = \frac{149.8 \times 10^{-3}}{60 \times 1.14 \times 10^{-3}} = 2.19 \text{ m.sec}^{-1}$$

and the corresponding dynamic temperature is:

$$T_{D2} = \frac{2.19^2}{2 \times 9.81 \times 4182} = 5.9 \times 10^{-5} \text{ K.}$$

This value of T_{D2} is based on the mean velocity $\bar{c}$ rather than the true, free-stream velocity c_∞. The coefficient of velocity distribution ($k_{\bar{c}}$) which is a function of pipe friction and pipe Reynolds Number, may be used as a correction factor to obtain the true dynamic temperature (T'_{D2}).

From Reference [74]:

$$k_{\bar{c}} = 1.18$$
$$T'_{D2} = 7.0 \times 10^{-5} \text{ K.}$$

Finally, from Equation (13.17):

$$T_{M2} = T_2 + 7.0 \times 10^{-5} \times 2.97 \text{ K.}$$

$$\therefore \quad \Delta T = T_2 - T_1 = 0.0180 \text{ K.}$$

(ii) Heat Capacity of Pump Assembly and Pipework

Total weight of pump assembly and pipework between inlet and $T_2 \approx 25\text{kg}$.

$$C_p \text{(mild steel)} = 460 \text{ J}(\text{kg.K})^{-1}$$

Heating rate of bulk fluid and pump assembly = 7×10^{-4} K.sec^{-1}.

For the pump and pipework, the total heat requirement
is $25 \times 460 \times 7 \times 10^{-4} = 8.05 \text{J.sec}^{-1}$.

This is equal to the enthalpy drop of the water as it passes between the T_1 and T_2 measurement stations. The consequent fall in fluid temperature ΔT_{HC} is given by:

$$\Delta h = \frac{Q}{V} C_p \Delta T_{HC} \qquad \ldots \text{(XVIII.4)}$$

$$\therefore \Delta T_{HC} = \frac{8.05 \times 10^{-3} \times 60}{149.8 \times 10^{-3} \times 4182} = 7.7 \times 10^{-4} \text{ K.}$$

The true temperature increment across the pump is then given by:

$$\Delta T_{corr} = \Delta T + \Delta T_{HC}$$

$$\text{ie} \quad \Delta T_{corr} = 0.0188 \text{ K}$$

(iii) <u>Calculation of the Separate Terms in Equation (13.12)</u>

The hydraulic efficiency of the pump may be found from the following equation:

$$\eta = \frac{P_2 V_{2'} - P_1 V_1 - E_{CT_1} - P_2 (\frac{\partial V}{\partial T})_p (T_2 - T_1) + \frac{1}{2}(c_{2'}^2 - c_1^2) + g(Z_2 - Z_1)}{\bar{C}_p(T_2 - T_1) - T_1 \alpha + P_2 V_2 - P_1 V_1 - E_{CT_1} - P_2 (\frac{\partial V}{\partial T})_p (T_2 - T_1) + \frac{1}{2}(c_2^2 - c_1^2) + g(Z_2 - Z_1)}$$

$$\dots (13.12)$$

Each term will be examined separately, to assess its relative importance.

(a)   Since water is virtually incompressible, we may say that

$$P_2 V_{2'} - P_1 V_1 \simeq P_2 V_2 - P_1 V_1 \simeq V_1(P_2 - P_1)$$

$$V_1(P_2 - P_1) = 10^{-3} \times 90250 = \underline{90.25 \text{ J.kg}^{-1}}$$

(b) $E_{CT_1} = \int_{P_1}^{P_2} P [\frac{\partial V}{\partial p}]_T \, dp = [\frac{p^2}{2} [\frac{\partial V}{\partial p}]_T]_{P_1}^{P_2}$ where P_2 and P_1 are absolute pressures

$$\therefore \quad E_{CT_1} = \frac{10^{-3} \times 45 \times 10^{-11}}{2} (1.95^2 - 1.04^2) \times 10^{10}$$

$$= \underline{6.1 \times 10^{-3} \text{ J.kg}^{-1}}$$

(c) $P_2 (\frac{\partial V}{\partial T})_p (T_2 - T_1) = 1.95 \times 10^5 \times 10^{-3} \times 206.78 \times 10^{-6} \times 0.0188$

$$= \underline{7.5 \times 10^{-4} \text{ J.kg}^{-1}}$$

(d) $\frac{1}{2}(c_{2'}^2 - c_1^2) = \frac{1}{2}(c_2^2 - c_1^2) = \frac{1}{2}(2.19^2 - 0.05^2) = \underline{2.40 \text{ J.kg}^{-1}}$

(e) $g(Z_2 - Z_1) = 9.81 \times 0.53 = \underline{5.23 \text{ J.kg}^{-1}}$

(f) $\bar{C}_p(T_2-T_1)$ = 4,182 x 0.0188 = $\underline{78.62 \text{ J.kg}^{-1}}$

(g) $T_1\alpha$ = $T_1 \displaystyle\int_{P_1}^{P_2} [\frac{\partial V}{\partial T}]_p \, dp$ = $T_1[\frac{\partial V}{\partial T}] \, (p_2-p_1)$

$\therefore \, T_1\alpha$ = 293 x 10^{-3} x 206.78 x 10^{-6} x 90250 = $\underline{5.47 \text{ J.kg}^{-1}}$

It is apparent that the isothermal compressibility and thermal expansion terms ((b) and (c) above) are negligible. This is expected since we are dealing with a fluid of large bulk modulus and a relatively small pressure rise, whilst the temperature rise is minute.

Equation (13.12) then reduces to:

$$\eta = \frac{V_1(p_2-p_1) + \tfrac{1}{2}(c_2^2-c_1^2) + g(Z_2-Z_1)}{\bar{C}_p(T_2-T_1) - T_1\alpha + V_1(p_2-p_1) + \tfrac{1}{2}(c_2^2-c_1^2) + g(Z_2-Z_1)}$$

$$\ldots \text{(XVIII.5)}$$

Inserting the appropriate data:

$$\eta = \frac{90.25 + 2.40 + 5.23}{78.62 - 5.47 + 90.25 + 2.40 + 5.23} = \frac{97.88}{171.03} = \underline{\underline{57.2\%}}$$

B. Calculation for Mercury

Physical properties of mercury at 20°C and 1 atm. absolute pressure[62,76] :

Heat capacity (C_p) = 139.2 J $(\text{kg.K})^{-1}$

Coefficient of thermal expansion $(\frac{1}{V}[\frac{\partial V}{\partial T}])$ = 182 x 10^{-6} K^{-1}

Isothermal compressibility $(\frac{1}{V}[\frac{\partial V}{\partial p}])$ = 3.881 x 10^{-6} bar^{-1}

Specific volume ($V = \frac{1}{\rho}$) = $\frac{1}{13.6 \times 10^3}$ m^3kg^{-1}

Dynamic viscosity (μ) = 1.55 cP

Thermal conductivity (k) = 8.7 W $(\text{mK})^{-1}$

Measured parameters:

Pump speed = 1450 rpm

Pump flowrate = $102\ell.\text{min}^{-1}$

Gauge pressure at pump inlet = 0.106 bar (1.12 bar absolute)

Gauge pressure at pump outlet = 6.922 bar (7.94 bar absolute)

ΔT_M(corrected for zero error) = 0.243 $\pm$0.003 K.

Temperature rise of bulk fluid = 2.3×10^{-3} K.sec^{-1}

Difference in geodetic level of T_1 and T_2 probes = 1.0m.

(i) Recovery Factor

From the following considerations, the recovery factor effect in mercury may be neglected.

$$R_f = KS + (1-K)r \qquad \qquad \dots \text{(XVIII.1)}$$

Since the temperature probe and outlet pipe geometry is identical to that in water,

$$K = -1.05$$

and for mercury at 20$^{\text{o}}$C:

$$S = \frac{T}{V}\left(\frac{\partial V}{\partial T}\right)_p = 293 \times 182 \times 10^{-6} = 0.0533$$

$$Pr = \frac{\mu C_p}{k} = \frac{1.55 \times 10^{-3} \times 139.2}{8.7} = 0.025.$$

The frictional recovery factor (r) is given by Pr^n. There is no published data for values of n in mercury, but frictional heating effects will be small in this low viscosity fluid, and will be removed from the vicinity of the probe by the high thermal conductivity.

If the exponent n is ignored in Equation (XVIII.1):

$$R_f = -1.05 \times 0.0533 + 2.05 \times 0.025$$
$$= 0.11.$$

Also $\quad \bar{c}_2 = \frac{Q}{A} = \frac{102 \times 10^{-3}}{60 \times 1.14 \times 10^{-3}} = 1.49 \text{ m.sec}^{-1}$,

and the corresponding dynamic temperature is:

$$T_{D2} = \frac{1.49^2}{2 \times 9.81 \times 139.2} = 8.1 \times 10^{-4} \text{ K.}$$

Since the kinamatic viscosity of mercury is exceptionally low, the mean velocity ($\bar{c}$) and free stream velicity (c_∞) are almost identical and no correction for free stream dynamic temperature is necessary, i.e.

$$T'_{D2} = 8.1 \times 10^{-4} \text{ K.}$$

Then, from equation (13.17):

$$T_{M2} = T_2 + 8.1 \times 0.11 \times 10^{-4} = T_2 + 8.9 \times 10^{-5} \text{ K.}$$

The correction for recovery factor (8.9×10^{-5}K) is negligible in relation to the measured temperature rise across the pump (0.243K). Since $102\ell.\text{min}^{-1}$ is the maximum flowrate for which the pump efficiency was computed [due to the errors introduced by a high water content in the mercury (see Chapter 12.2.2)], the correction will be even smaller at other flowrates and may safely be ignored.

(ii) Heat Capacity of Pump Assembly, Pipework and Pump Sump

    Total weight of pump and pipework between inlet
    and T_2 $\simeq$ 25 kg.
    Total weight of sump (calculated from design drawings)
        $\simeq$ 49 kg.
    C_p (mild steel) = 460 J $(\text{kg.K})^{-1}$
    Heating rate of bulk fluid and surrounding hardware
        = 2.3×10^{-3} K.sec^{-1}.
    For the pump, pipework and sump, the total heat
    requirement is $74 \times 460 \times 2.3 \times 10^{-3}$
        = 78.3 J.sec^{-1}.

This is equal to the enthalpy drop of the mercury as it passes from the T_1 to the T_2 measurement stations. The consequent fall in fluid temperature ΔT_{HC} is given by Equation (XVIII.4).

$$\therefore \Delta T_{HC} = \frac{78.3 \times 60}{13.6 \times 10^3 \times 139.2 \times 102 \times 10^{-3}} = 0.0243 \text{ K.}$$

Then $\quad \Delta T_{corr} = \Delta T + \Delta T_{HC}$

$$= 0.267 \text{ K}$$

(iii) <u>Calculation of the Separate Terms in Equation (13.12)</u>

As for water (see Section A(iii) of this Appendix), each term in the efficiency equation will be examined separately to assess its relative importance.

(a) $V_1(p_2-p_1) = \dfrac{1}{13.6 \times 10^3} \times 6.816 \times 10^5 = \underline{50.12 \text{ J.kg}^{-1}}$

(b) $E_{CT_1} = \dfrac{3.881 \times 10^{-6}}{2 \times 13.6 \times 10^3}(7.94^2 - 1.12^2) = \underline{8.8 \times 10^{-3} \text{ J.kg}^{-1}}$

(c) $p_2\left(\dfrac{\partial V}{\partial T}\right)_p(T_2-T_1) = \dfrac{7.94 \times 10^5 \times 182 \times 10^{-6} \times 0.267}{13.6 \times 10^3} = \underline{2.8 \times 10^{-3} \text{J.kg}^{-1}}$

(d) $\frac{1}{2}(c_2^2-c_1^2) = \frac{1}{2}(1.49^2 - 0.15^2) = \underline{1.10 \text{ J.kg}^{-1}}$

(e) $g(Z_2-Z_1) = \underline{9.81 \text{ J.kg}^{-1}}$

(f) $\bar{C}_p(T_2-T_1) = 139.2 \times 0.267 = \underline{37.17 \text{ J.kg}^{-1}}$

(g) $T_1\alpha = 293 \times \dfrac{182 \times 10^{-6}}{13.6 \times 10^3} \times 6.816 \times 10^5 = \underline{2.67 \text{ J.kg}^{-1}}$

Again is is apparent that the isothermal compressibility and thermal expansion terms ((b) and (c) above) can be neglected in relation to the magnitude of the remaining terms. Therefore, Equation (XVIII.5) may be used.

Inserting the appropriate data:

$$\eta = \frac{50.12 + 1.10 + 9.81}{37.17 - 2.67 + 50.12 + 1.10 + 9.81} = \frac{61.03}{95.53} = 63.9\%$$

At flowrates higher than $50 \ell.min^{-1}$, water is entrained in the mercury at the pump inlet (see Chapter 12.2.2). The pump efficiency has therefore been recalculated for a 85% mercury/15% water mixture (the water content was extracted from Figure 150) as follows:

$$\bar{C}_p = 0.15 \times 4182 + 0.85 \times 139.2 = 745.6 \; J.(kg.K)^{-1}$$

$$\therefore \Delta T_{HC} = \frac{78.3 \times 60}{102 \times 10^{-3} \times 745.6 \times (0.15 + 0.85 \times 13.6) \times 10^3} = 5.3 \times 10^{-3} K$$

$$\therefore \Delta T_{corr} = 0.248 \; K$$

(f) $\bar{C}_p(T_2-T_1) = 745.6 \times 0.248 = \underline{185.12 \; J.kg^{-1}}$

(g) $T_1\bar{\alpha} = 293 \times [\frac{0.15 \times 206.78}{10^3} + \frac{0.85 \times 182}{13.6 \times 10^3}] \times 10^{-6} \times 6.816 \times 10^5$

$\qquad = \underline{8.47 \; J.kg^{-1}}$

The remaining terms in Equation (XVIII.5) remain unchanged.

$$\therefore \eta = \frac{61.03}{185.12 - 8.47 + 61.03} = 25.7\%$$

ESTIMATION OF HEAT LOSSES FOR ΔT MEASUREMENTS ON THE O.L.R.

[See Chapter 13.1 for Notation]

A. Heat Transfer from the Mercury Flow

The process of heat loss from mercury (flowing in a conduit) to the surrounding environment (water or air) involves the initial transfer of heat between mercury and the pipe.

Heat transfer in liquid metals has been studied by Lyon[84], who suggests the following expression for fully developed turbulent flow in a circular pipe of constant wall temperature:

$$\frac{\lambda D}{k} = 5 + 0.025 \, Re^{0.8} Pr^{0.8} \qquad \ldots \text{(XIX.1)}$$

Applied to the pump outlet pipe on the O.L.R. (D=38mm) for a typical flowrate of $60\ell.min^{-1}$, this gives:

$$\frac{\lambda \times 0.038}{8.7} = 5 + 0.025 [\frac{10^{-3} \times 0.038 \times 4}{\pi \, 0.038^2 \times 1.14 \times 10^{-7}}]^{0.8} [\frac{139.2 \times 1.55 \times 10^{-3}}{8.7}]^{0.8}$$

$$= 5 + 0.025 \times 23700 \times 0.052$$

$$\therefore \quad \lambda = 8180$$

This high value of heat transfer coefficient confirms that the overall process of heat loss to the surrounding air or water is not rate controlled by heat exchange between the mercury and pipework.

B. Heat Transfer by Forced Air Convection

The O.L.R. is fitted with an extraction hood. The mean air velocity across components of the test rig is estimated to be 5m.sec^{-1} and the following calculations are based on a typical temperature difference between the mercury in the pipework and the surrounding air of 4°C. The following physical properties of air at 20°C are required:

Kinematic viscosity (ν)	=	15 cSt
Dynamic viscosity (μ)	=	1.8×10^{-2} cP
Thermal conductivity (k)	=	2.6×10^{-2} W $(\text{mK})^{-1}$
Heat capacity (C_p)	=	1.005×10^{3}

(i) Cooling of Mercury in Delivery Tube

The expression for heat transfer by forced convection of a gas flowing across a circular pipe is[85]:

$$\frac{\lambda D}{k} = b(\text{Re})^{n} \qquad \qquad \dots \text{(XIX.2)}$$

where $\text{Re} = \dfrac{Dc_{\infty}}{\nu}$ and the values of b and n may be extracted from Table XIX.1, which contains data from Reference [86].

For the 50mm O.D. pump delivery pipe on the O.L.R.:

$$\text{Re} = \frac{.05 \times 5}{15 \times 10^{-6}} \simeq 17,000$$

Also n = 0.618 and b = 0.174.

$$\therefore \quad \frac{\lambda 0.05}{2.6 \times 10^{-2}} = 0.174 \, (17 \times 10^{3})^{0.618}$$

$$\therefore \quad \lambda = 37.2.$$

Table XIX.(i): Constants for Use in Equation
(XIX.2) [86]

Re$_D$	n	b
1-4	0.330	0.891
4-40	0.385	0.821
40-4000	0.466	0.615
4000-4000	0.618	0.174
40000-250000	0.805	0.0239

Then the heat flowrate may be found from:

$$q = \lambda A \Delta'T \qquad \ldots \text{(XIX.3)}$$

where A is the area available for heat transfer.

Since 0.6m of pipe is exposed to the air between the pump tank
and T_2 measuring point, with $\Delta'T = 4$

$$q = 37.2 \times \pi \times 0.05 \times 0.6 \times 4$$
$$= \underline{14 \text{J.sec}^{-1}}$$

(ii) Cooling of Mercury in Sump

The section of the sump into which the return flow of mercury
is channelled (next to the delivery pipe, see Figure 82) is treated as
a circular pipe of 127mm radius and 144mm length.

$$Re = \frac{0.127 \times 2 \times 5}{1.5 \times 10^{-5}} \simeq 85,000.$$

From Table XIX(i) $n=0.805$, $b=0.0239$.

Substituting in Equation (XIX.2):

$$\frac{\lambda 0.127 \times 2}{2.6 \times 10^{-2}} = 0.0239 \times (85,000)^{0.805}$$

$$\lambda = 22.7.$$

From equation (XIX.3), with mercury flowing only down one side of the sump section (i.e. half the available area):

$$q = 22.7 \times \pi \times 0.127 \times 0.144 \times 4$$

$$= \underline{5.2 \text{ J.sec}^{-1}}$$

Heat is also lost from the base of the sump, which may be treated as a flat plate. For the longest dimension across the plate:

$$Re = \frac{0.356 \times 5}{1.5 \times 10^{-5}} \simeq 1.2 \times 10^5$$

Since $Re < 5 \times 10^5$, the boundary layer in air will be laminar and the following expression for heat transfer applies[85]:

$$\frac{\lambda L}{k} = 0.664 \, Re^{\frac{1}{2}} \, Pr^{1/3} \qquad \ldots \text{(XIX.4)}$$

$$Pr = \frac{1.8 \times 10^{-5} \times 1005}{2.6 \times 10^{-2}} \simeq 0.70$$

$$\therefore \qquad \lambda = \frac{0.664 \times 2.6 \times 10^{-2}}{0.356} \times (1.2 \times 10^5)^{\frac{1}{2}} \times (0.70)^{1/3}$$

$$= 14.9.$$

Area of sump base $= 0.074 \text{ m}^2$

$\therefore$ From equation (XIX.3):

$$q = 14.9 \times 0.074 \times 4$$

$$= \underline{4.4 \text{ J.sec}^{-1}}$$

C. Heat Transfer to Cooling Water

The lower 0.4m of the pump delivery pipe is submerged in the cooling water above the mercury pool in the pump tank. The water was fed into the tank at about $1\ell.sec^{-1}$ and the water velocity was about 8.5×10^{-3} $m.sec^{-1}$ (calculated from the vertical cross-sectional area available to the water flow). The following calculations are based on a typical temperature difference between the mercury and water of $2^{o}C$.

For cooling by liquid flows, an extra term to account for the effect of Prandtl Number must be added to equation (XIX.2) as follows[85]:

$$\frac{\lambda D}{k} = b(Re)^n 1.1Pr^{1/3} \qquad \ldots \text{(XIX.5)}$$

For water flow across the delivery pipe:

$$Re = \frac{0.05 \times 8.5 \times 10^{-3}}{10^{-6}} \simeq 430$$

$$Pr = \frac{4182 \times 1.002 \times 10^{-3}}{0.6} \simeq 7$$

[The physical properties of water are listed at the beginning of Appendix XVIII

From Table XIX(i):

n=0.466, b=0.615.

$$\therefore \frac{\lambda 0.05}{0.6} = 0.615 \times (430)^{0.466}(7)^{1/3}$$

$$\therefore \qquad \lambda = 262.$$

With 0.4m length of vertical pipe and 0.1m of horizontal pipe at the pump outlet, we obtain from Equation (XIX.5):

$$q = 262 \times 0.5 \times \pi \times 0.05 \times 2$$
$$= 41 \text{ J.sec}^{-1}$$

Consider also the heat lost to water flowing round the pump body, which constitutes a cylinder of 0.235m diameter.

$$Re \simeq 2000$$

From Table XIX(i):

$$n = 0.466, \quad b = 0.615.$$

$$\therefore \quad \frac{\lambda 0.235}{0.6} = 0.615 \times (2000)^{0.466} \times 1.1(7)^{1/3} \quad \text{(Equation (XIX.5))}$$

$$\lambda = 114.$$

Suppose the upper 3cm of the pump were surrounded by water, so that

$$A = 0.254 \pi \times 0.03 \text{ m}^2.$$

Then, from equation (XIX.3):

$$q = 5.5 \text{ J.sec}^{-1}$$

D. Consequent Error in ΔT Measurement

The total heat loss from the mercury flowing between the T_1 and T_2 measurement stations by the processes considered above is roughly 70J.sec^{-1}. For a typical mercury flowrate of $60\ell.\text{min}^{-1}$, we may calculate the associated error $\delta(\Delta T_M)$ in ΔT_M. The enthalpy drop of the mercury due to this heat loss in passing from T_1 to T_2 is:

$$\Delta h = \frac{Q}{V} C_p \delta(\Delta T_M)$$

$$\therefore \quad 70 = 10^{-3} \times 13.6 \times 10^3 \times 139.2 \ \delta(\Delta T_M)$$

$$\delta(\Delta T_M) = 0.037 \text{ K}$$

Shaft Casing

Proposed path of
seal leakage flow

Shaft

Upper Neckring

Pressure tapping

Pump Casing

Impeller

Fluid Outlet

Pressure tapping

Lower Neckring

Fluid Inlet
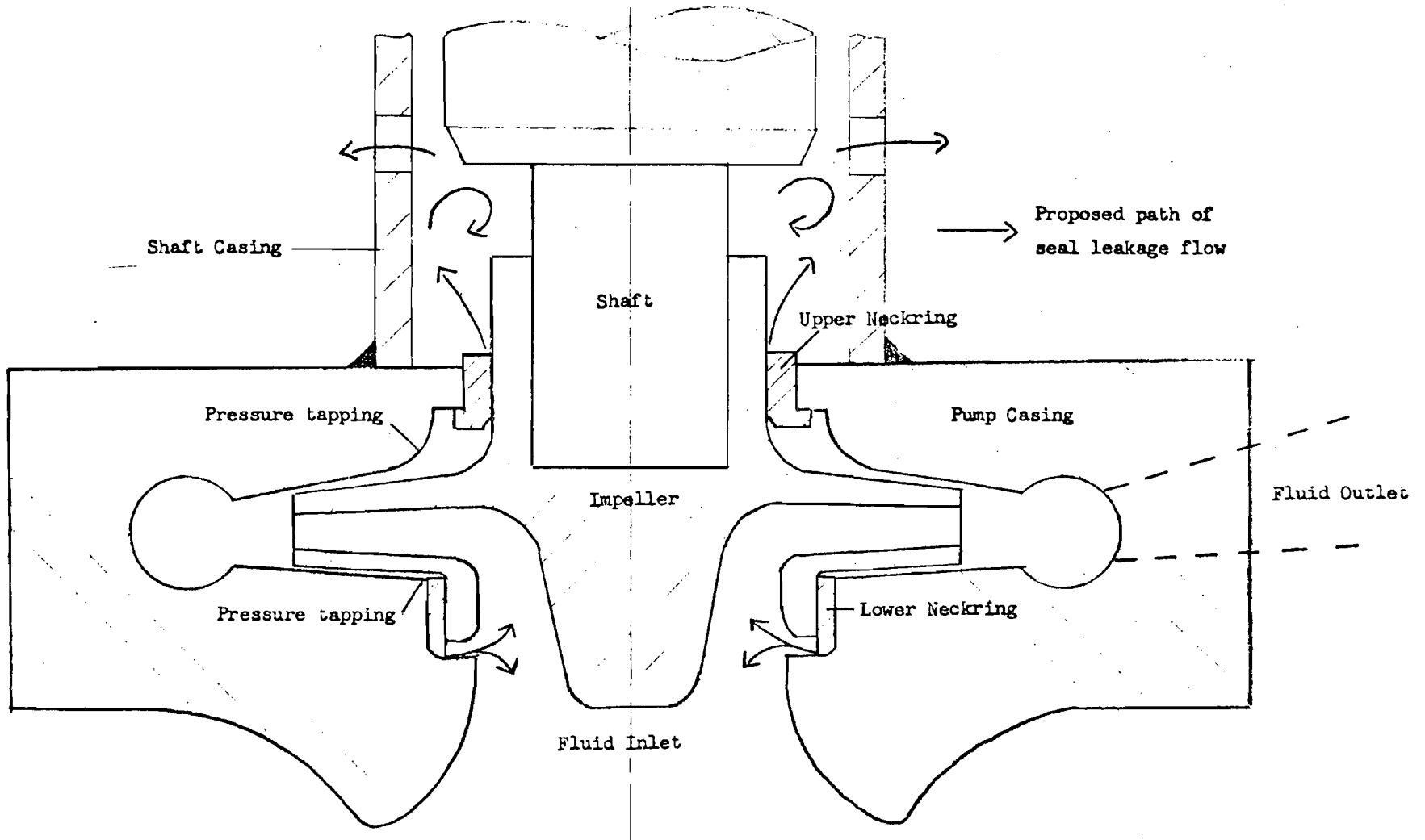
FIGURE 1.   STANDARD PUMP ASSEMBLY.

Specific Speed n_s (y-axis)

Specific Diameter Δ (x-axis)

Balje[6c]

Cordier[6]

Daily[6a]

Sabersky and Acosta[6b]

Mercury pump at duty point
(55 ℓ.min^{-1} at 1450 rpm)
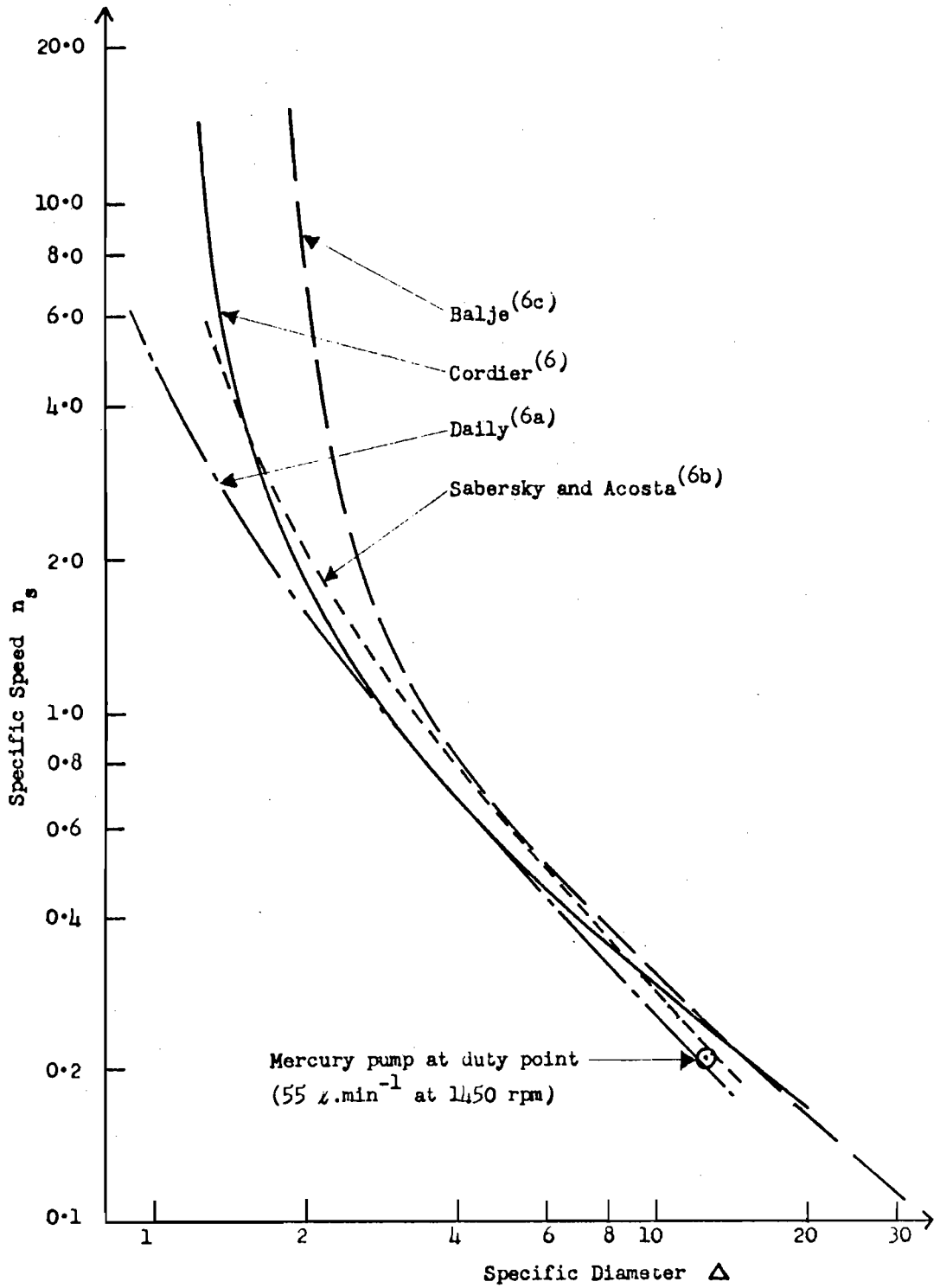
FIGURE 2. CORRELATION OF SPECIFIC SPEED AND SPECIFIC DIAMETER
FOR EFFICIENT TURBO-MACHINES[6].
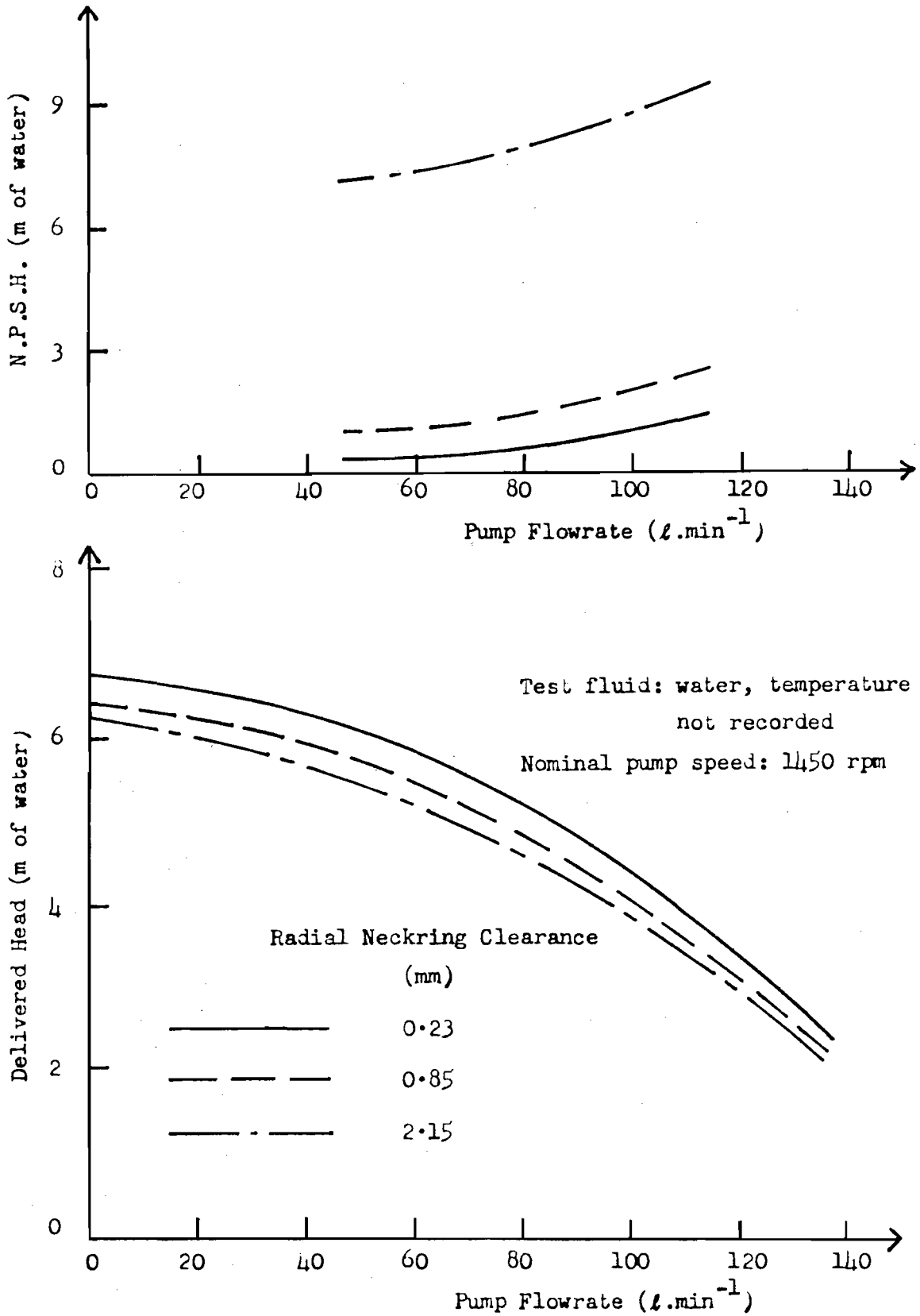
FIGURE 3. EFFECT OF INCREASED NECKRING CLEARANCE ON PUMP PERFORMANCE.
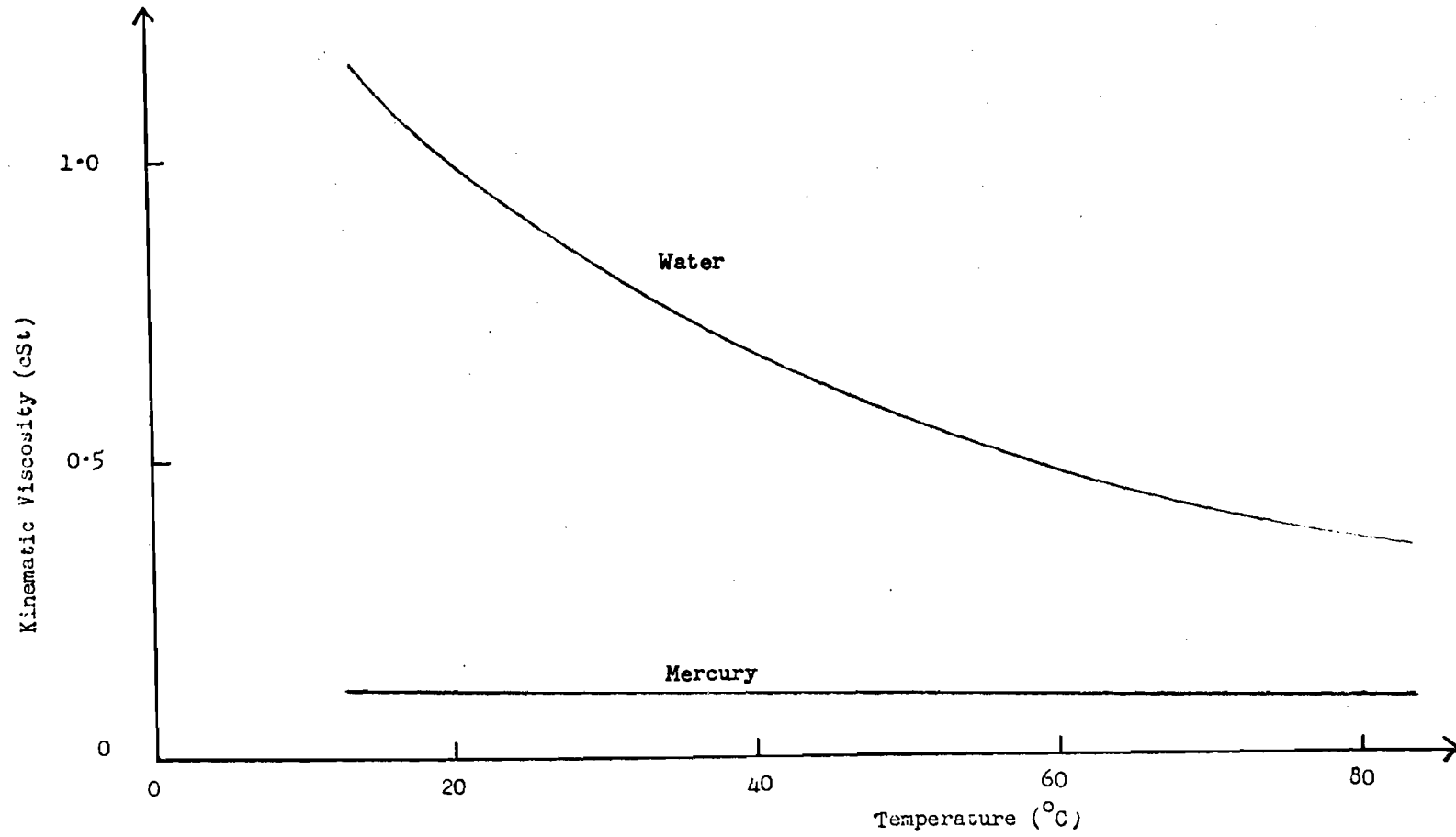
FIGURE 4. VARIATION IN KINEMATIC VISCOSITY OF MERCURY[37,38] AND WATER[40] WITH TEMPERATURE.
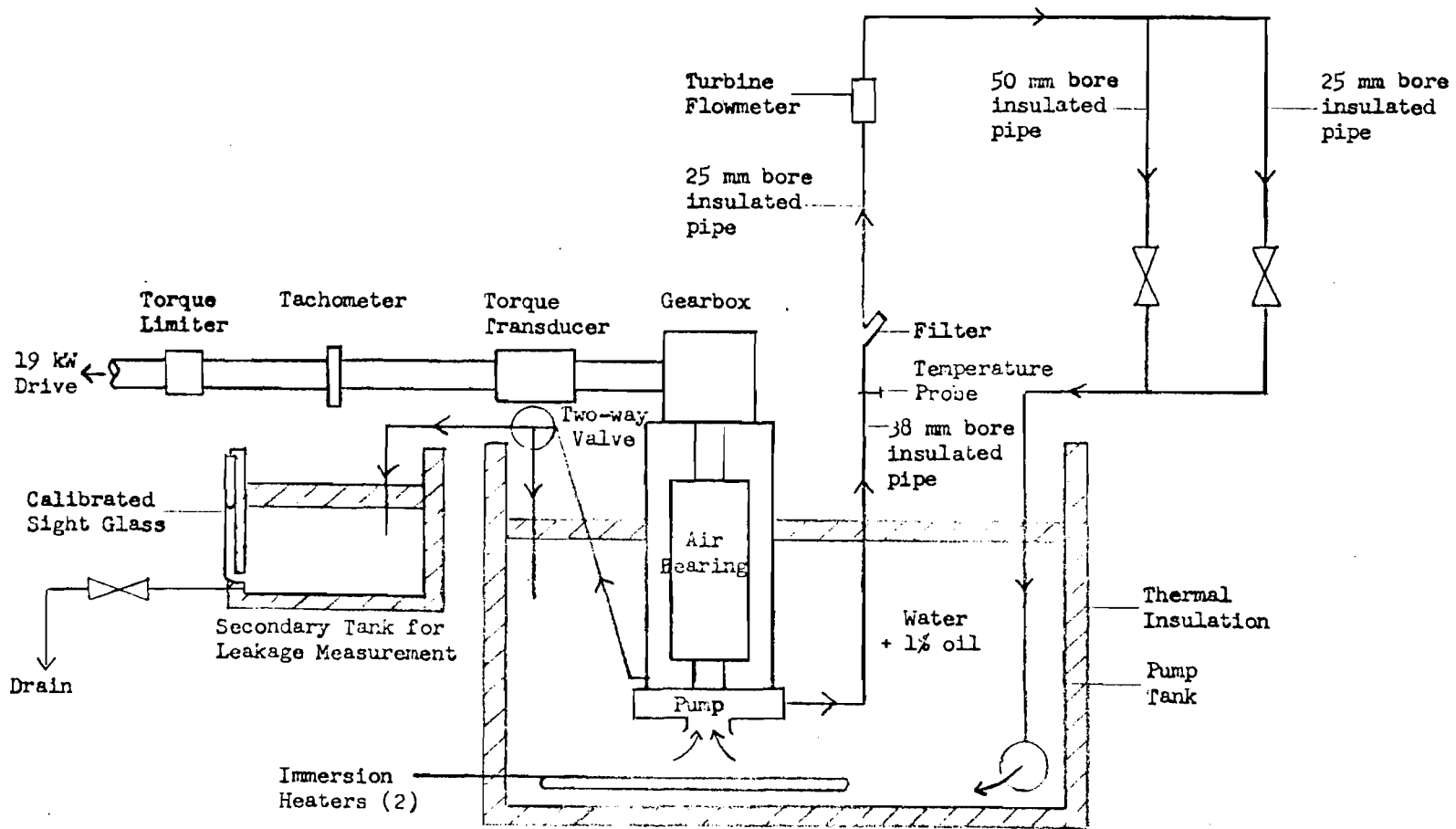
FIGURE 5.   DIAGRAM OF WATER TEST RIG.
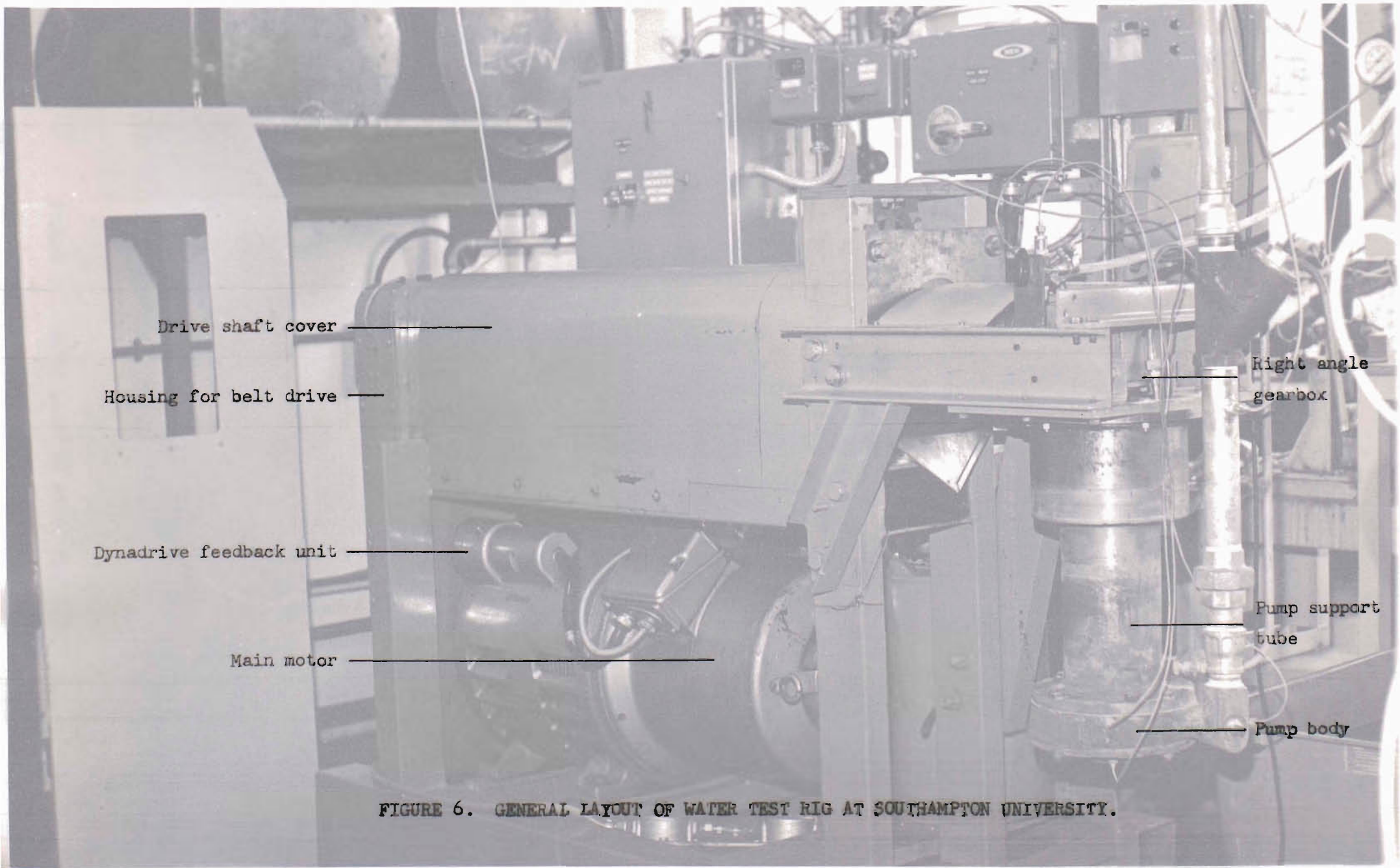
Drive shaft cover

Housing for belt drive

Dynadrive feedback unit

Main motor

Right angle gearbox

Pump support tube

Pump body

FIGURE 6. GENERAL LAYOUT OF WATER TEST RIG AT SOUTHAMPTON UNIVERSITY.

Bearing lubricant control

Motor speed control

Speed counter

Torque limiter   Drive shaft   Torque transducer
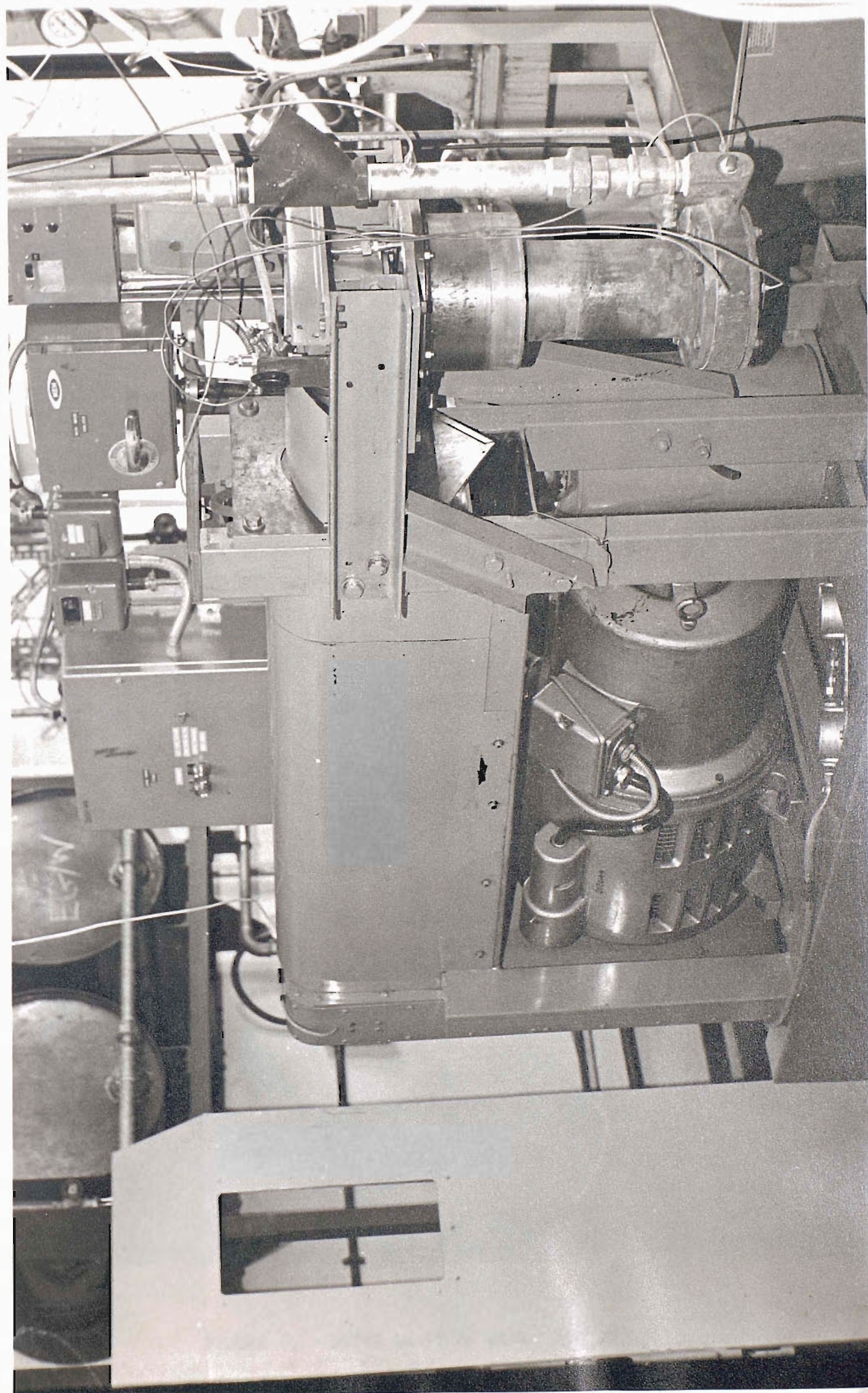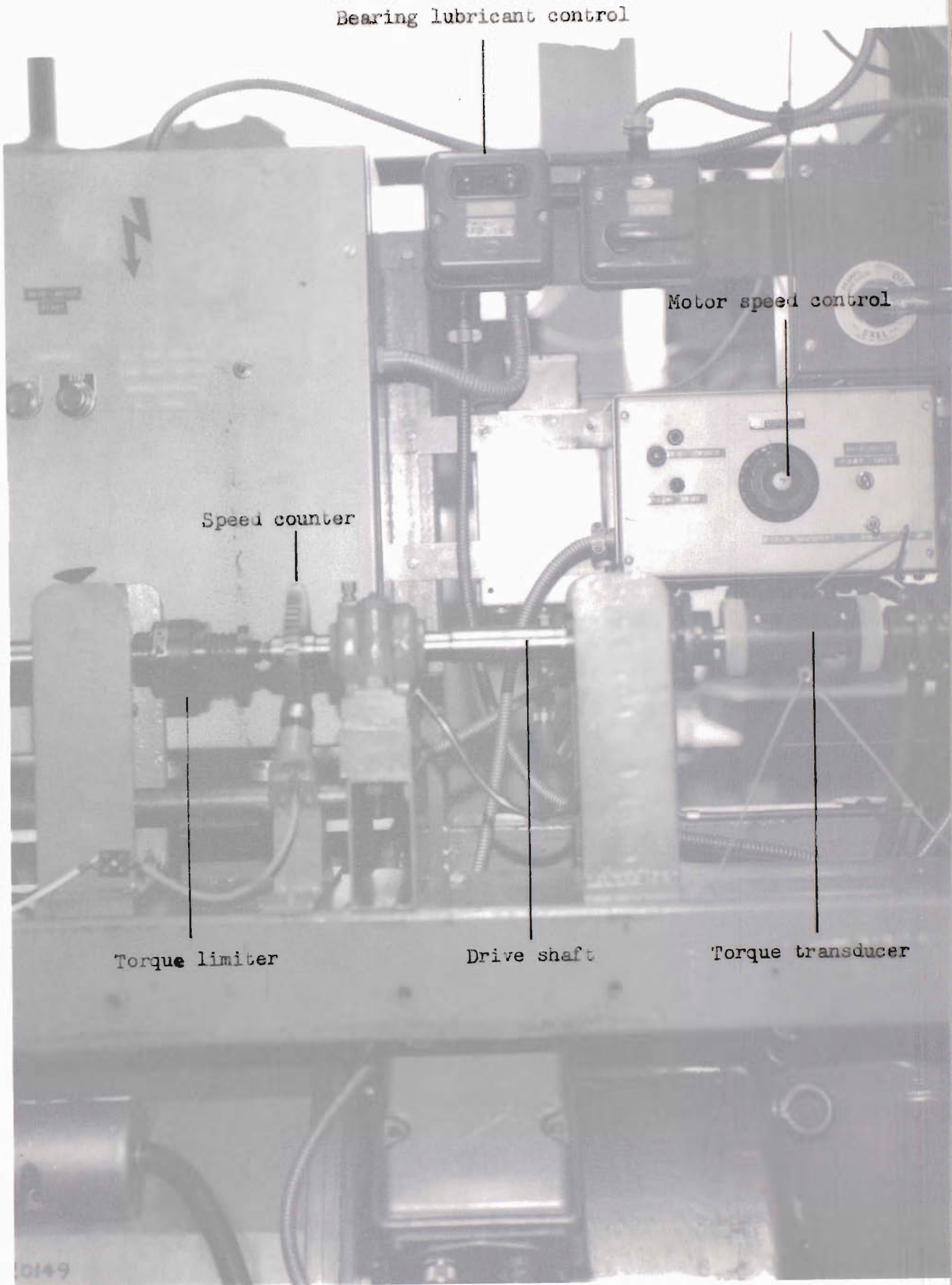
FIGURE 7.   DRIVE SHAFT OF WATER TEST RIG.
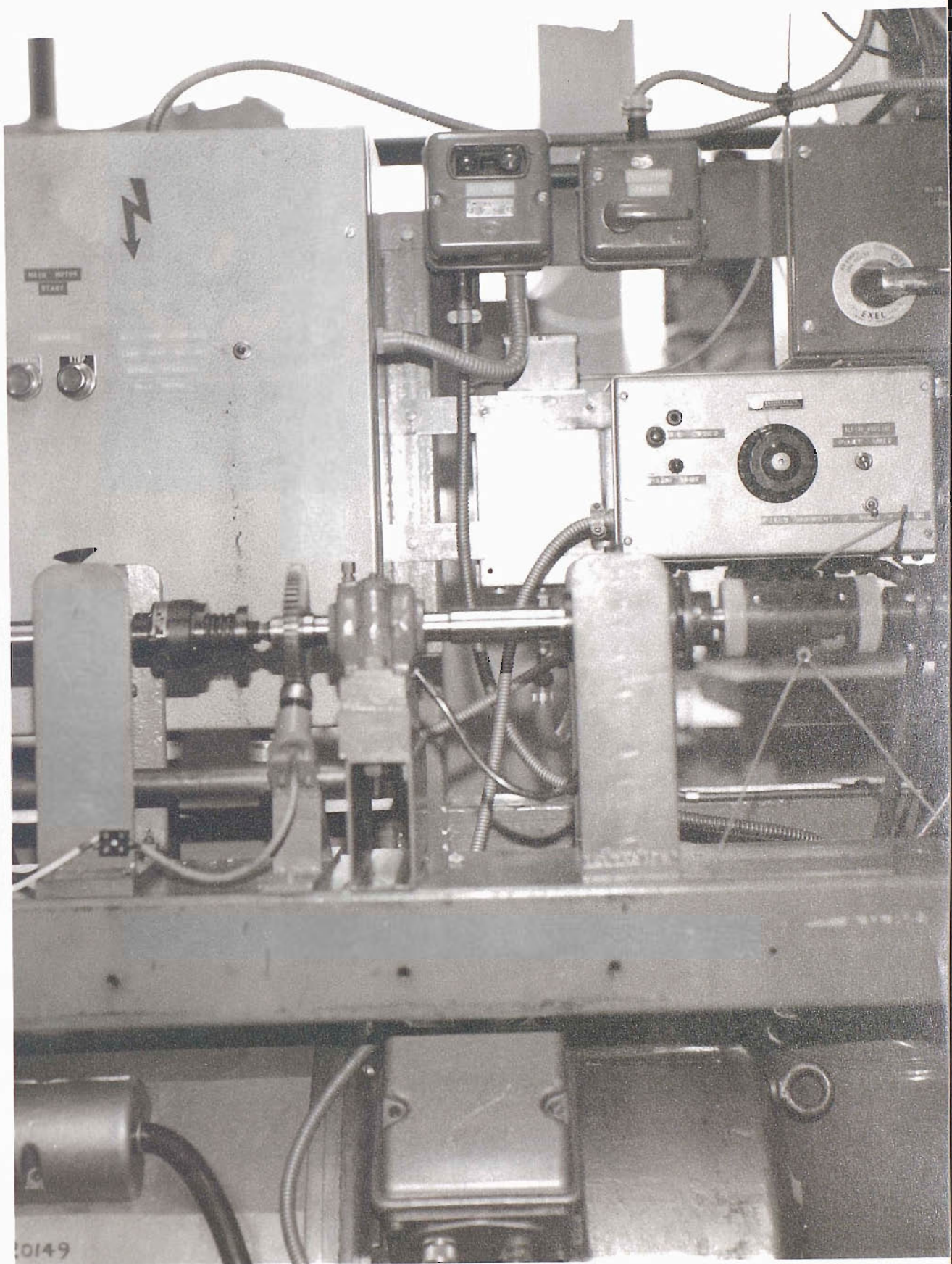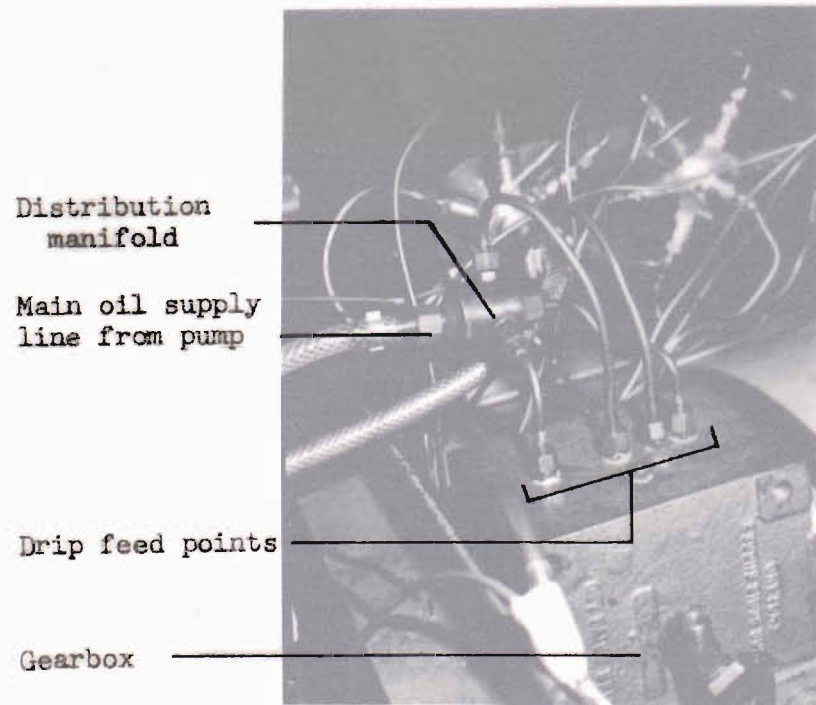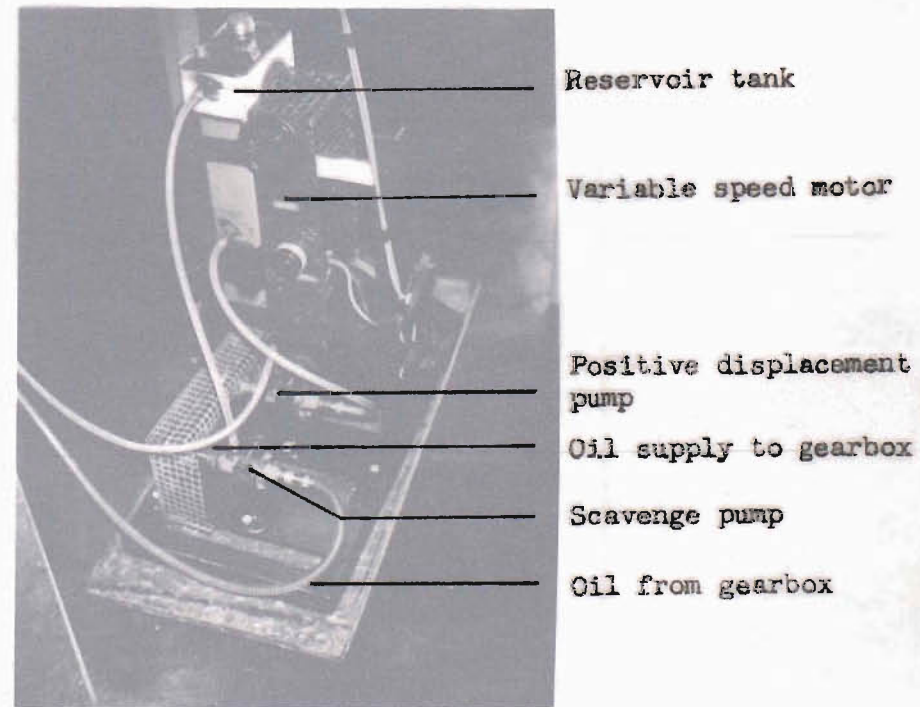
MAIN MOTOR
START

20149

Distribution
  manifold

Main oil supply
line from pump

Drip feed points

Gearbox

3A.   GEARBOX TAPPINGS FOR OIL DRIP FEED.
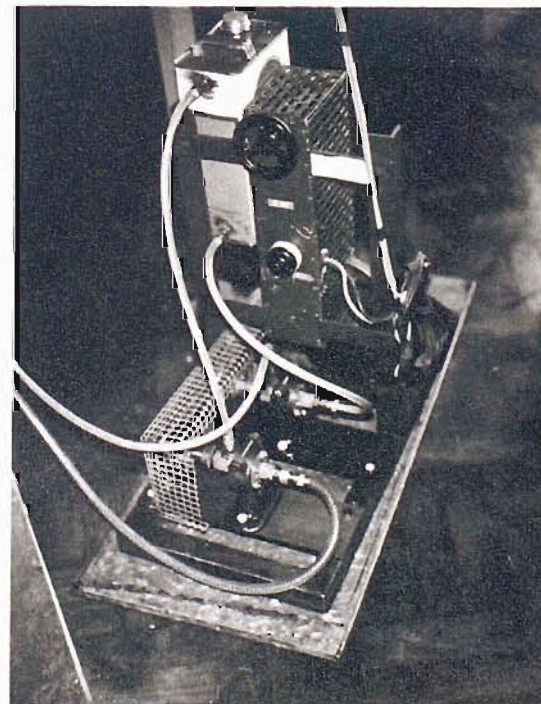
Reservoir tank

Variable speed motor

Positive displacement
pump

Oil supply to gearbox

Scavenge pump

Oil from gearbox

8B.   OIL PUMPING SYSTEM.

FIGURE 8.   CIRCULATORY OIL SYSTEM FOR WATER TEST RIG GEAR BOX.

8A. GEARBOX TAPPINGS FOR OIL DRIP FEED.

8B. OIL PUMPING SYSTEM.

FIGURE 8.   CIRCULATORY OIL SYSTEM FOR WATER TEST RIG GEAR BOX.

Flow control valves
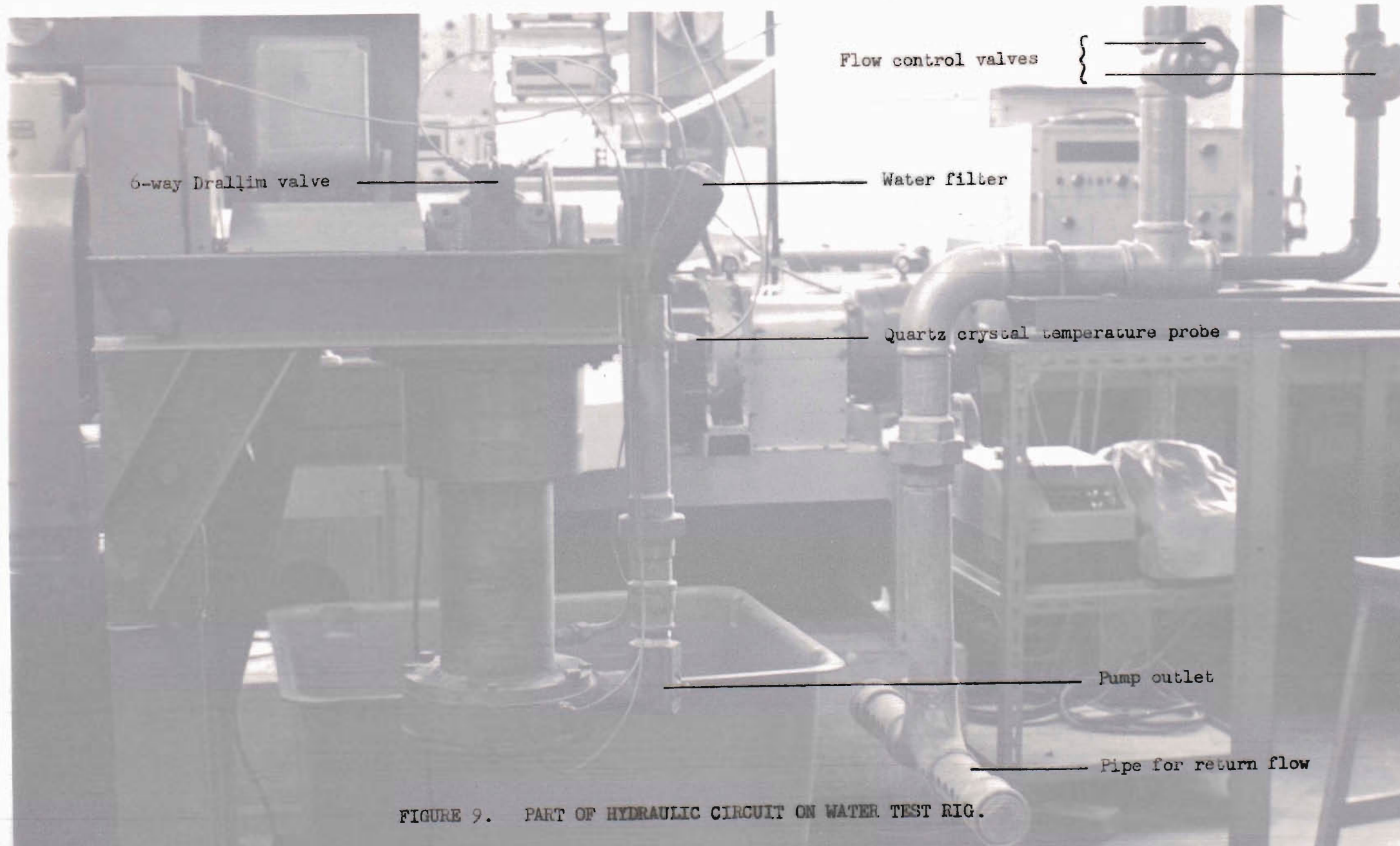
6-way Drallim valve

Water filter

Quartz crystal temperature probe

Pump outlet

Pipe for return flow

FIGURE 9. PART OF HYDRAULIC CIRCUIT ON WATER TEST RIG.
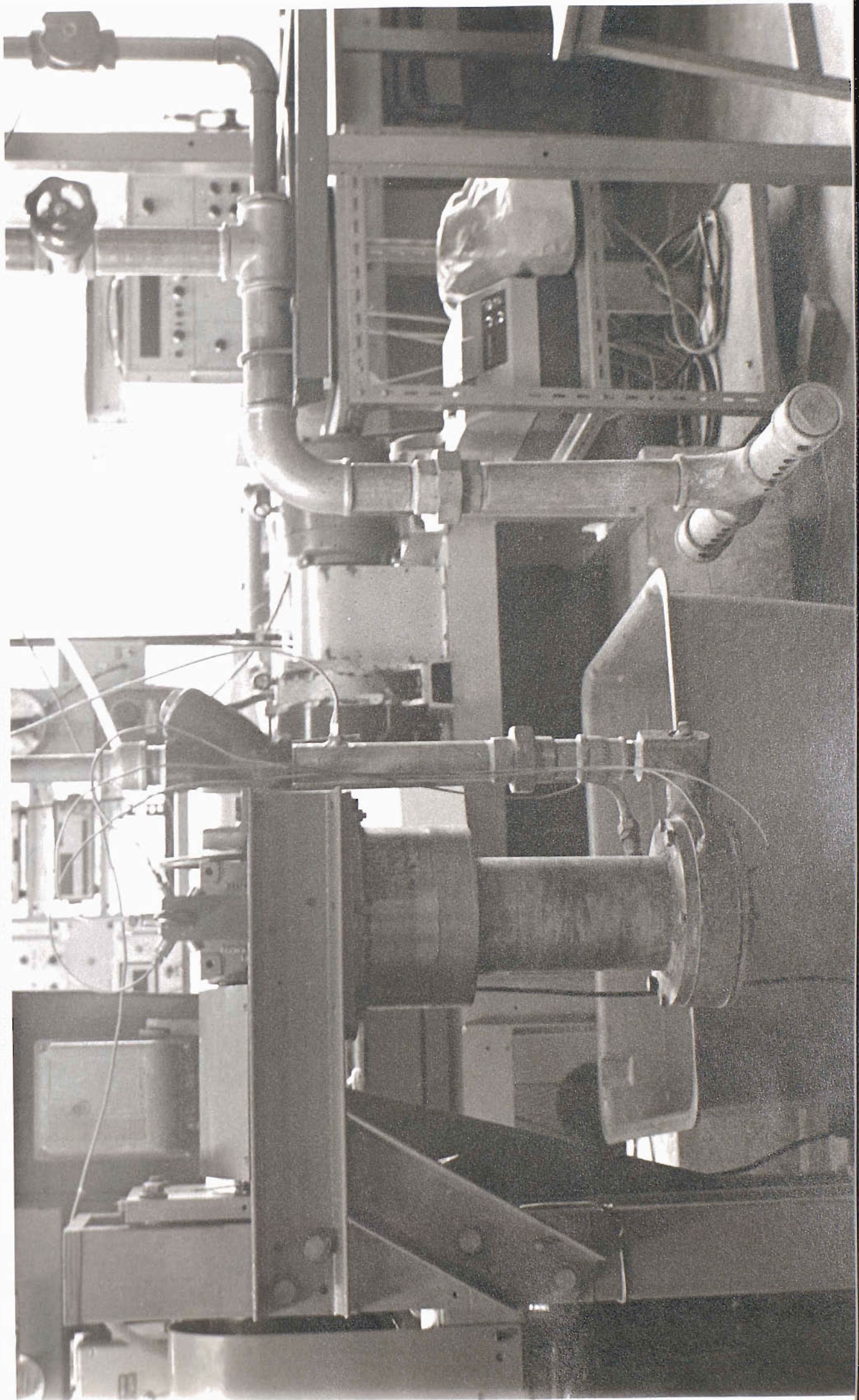
Control handle for both
two-way valves

Two-way valves {

Return pipes to main tank {

Secondary calibrated tank

Pipes for leakage flow
from upper neckring {

Overflow pipe

Main pump tank

FIGURE 10. SECONDARY TANK AND HYRAULIC CIRCUIT
FOR SEAL LEAKAGE MEASUREMENTS.

Pipes to secondary tank
for leakage flow

Upper seal casing

Lower seal casing

Pump body

Tappings to monitor radial
pressure distribution in HDS
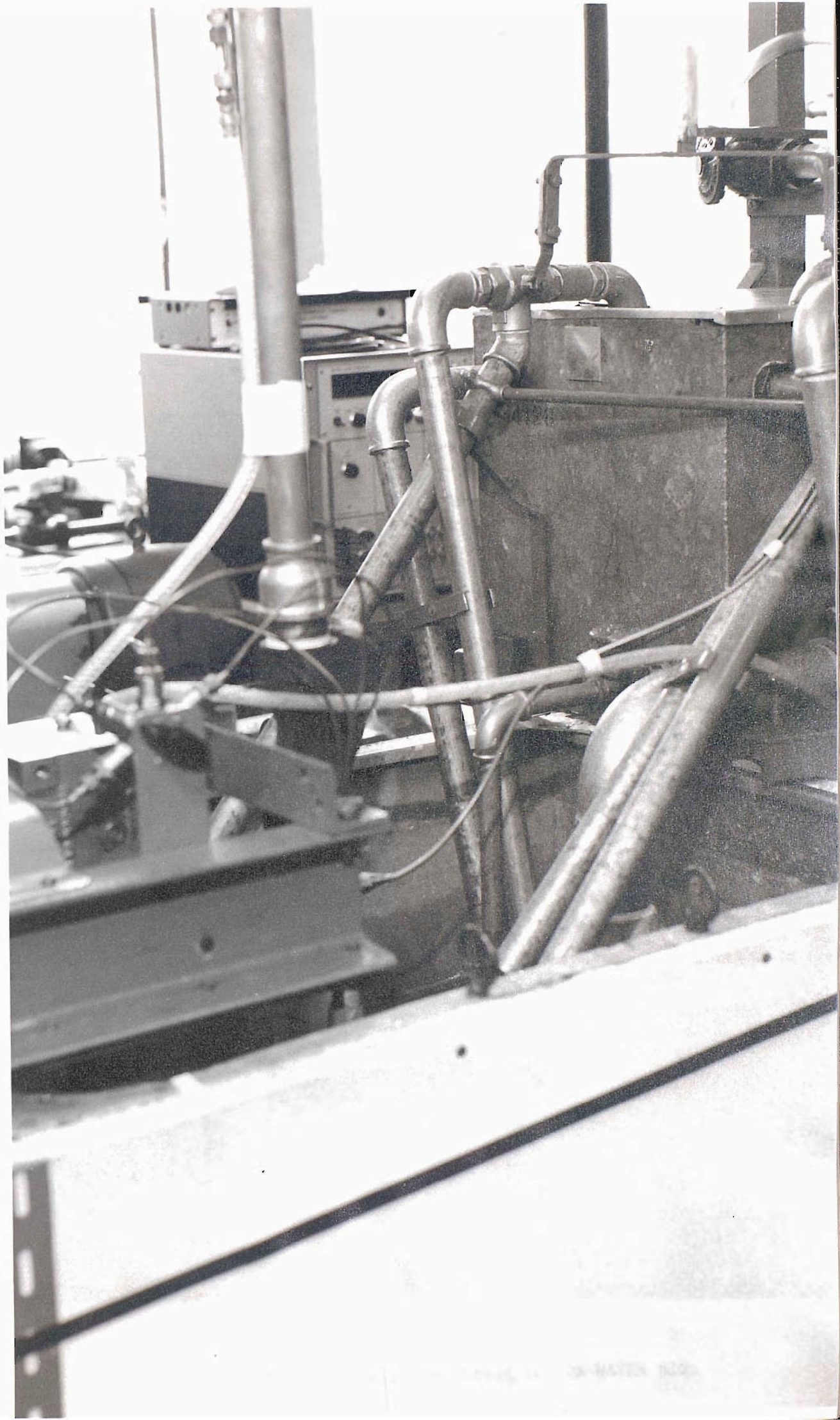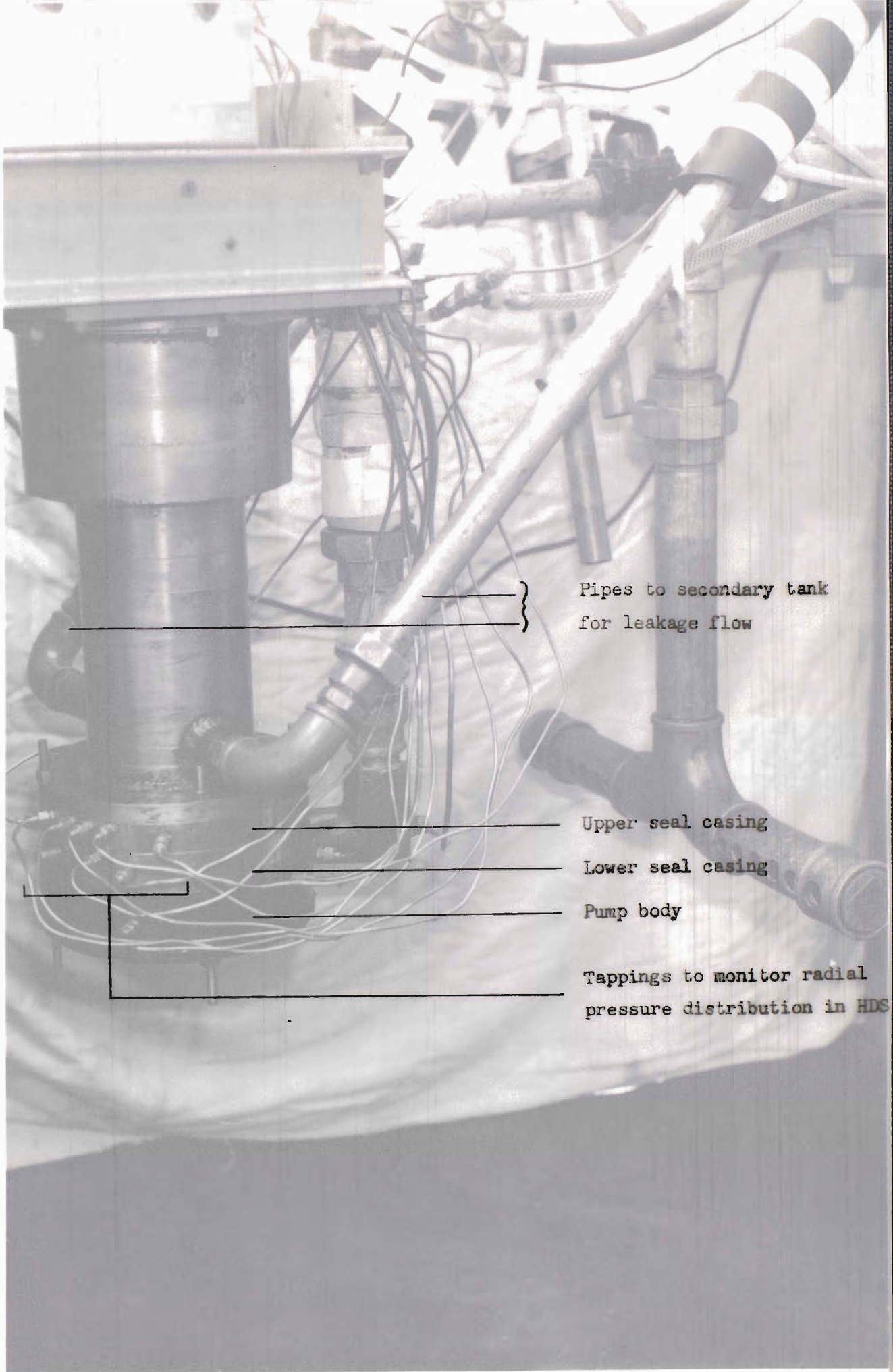
FIGURE 11. PUMP FITTED WITH TWO-STAGE HDS ON WATER RIG.

Two-stage HDS

Seal inlet pressure tapping

Cylindrical block replacing pump

Pressurized water supply
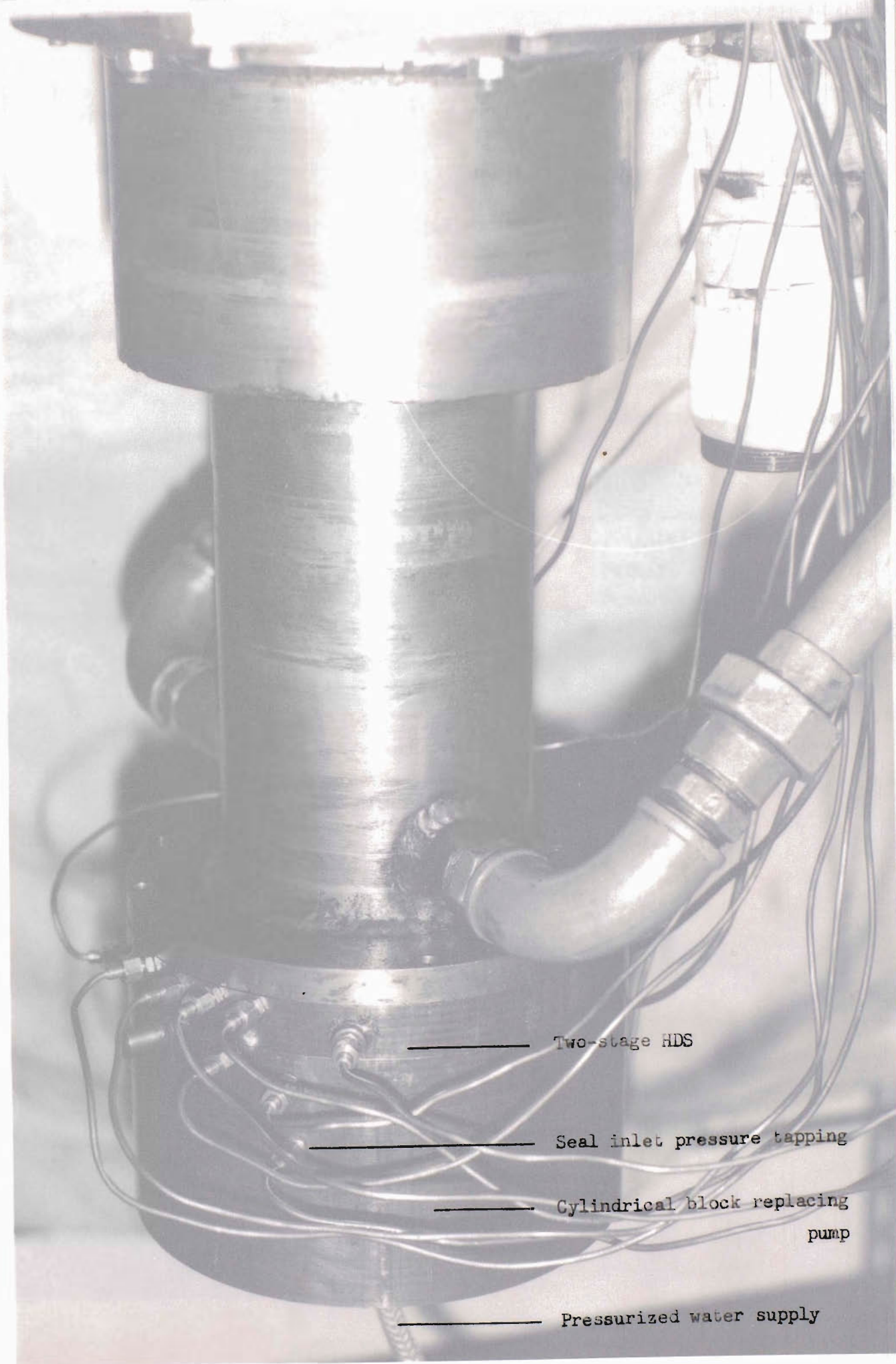
FIGURE 12. RIG ASSEMBLY FOR BARE SEAL TRIALS IN WATER.

D.V.M. (ref volts)

Flowmeter Display

Thermister Display (gearbox temperature)

Digital Counter (shaft speed)

Torque Display

Quartz Crystal Thermometer Display (water temperature)

U.V. Recorder (not used)

Amplifier (not used)

Pressure Gauge
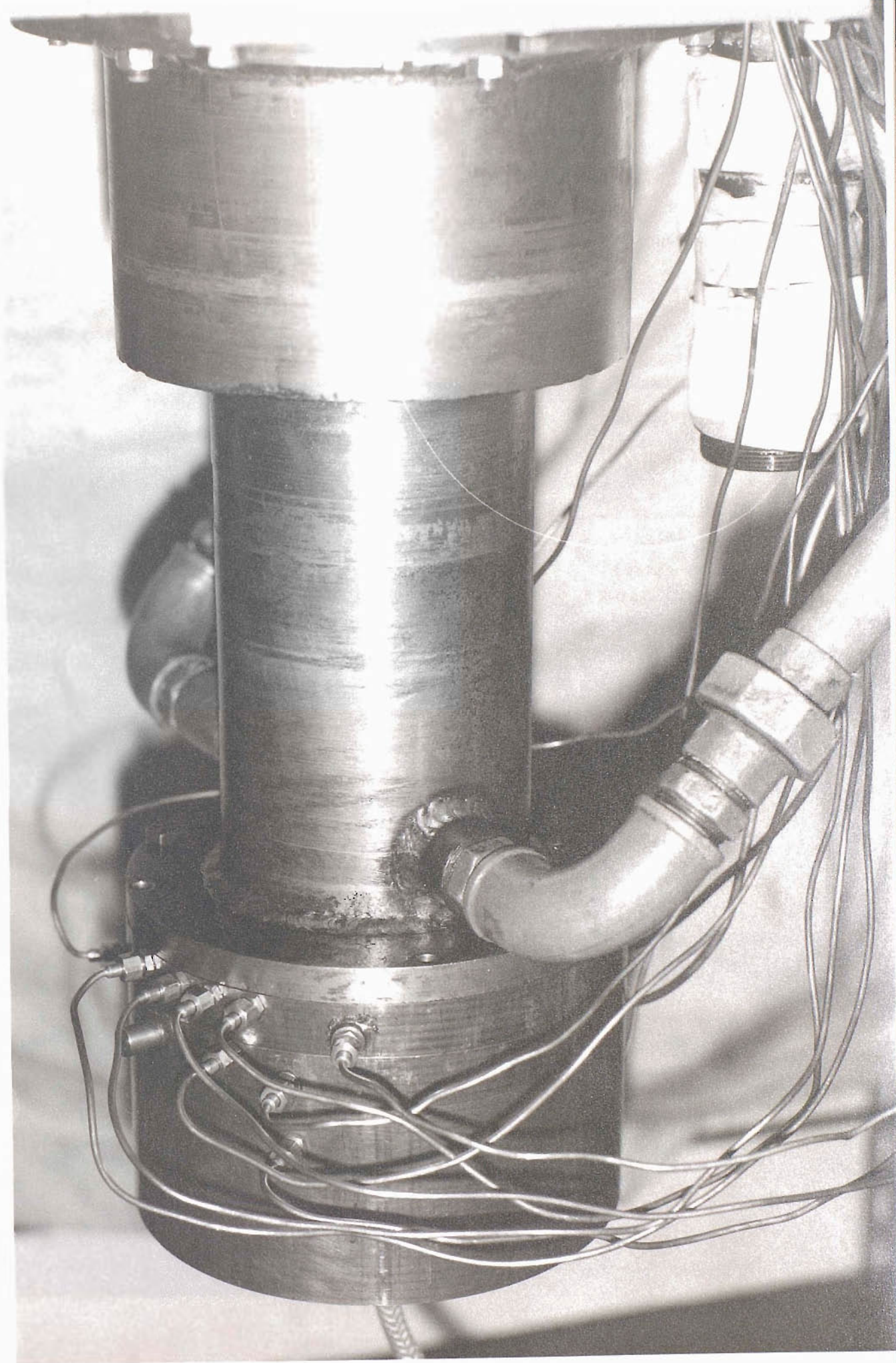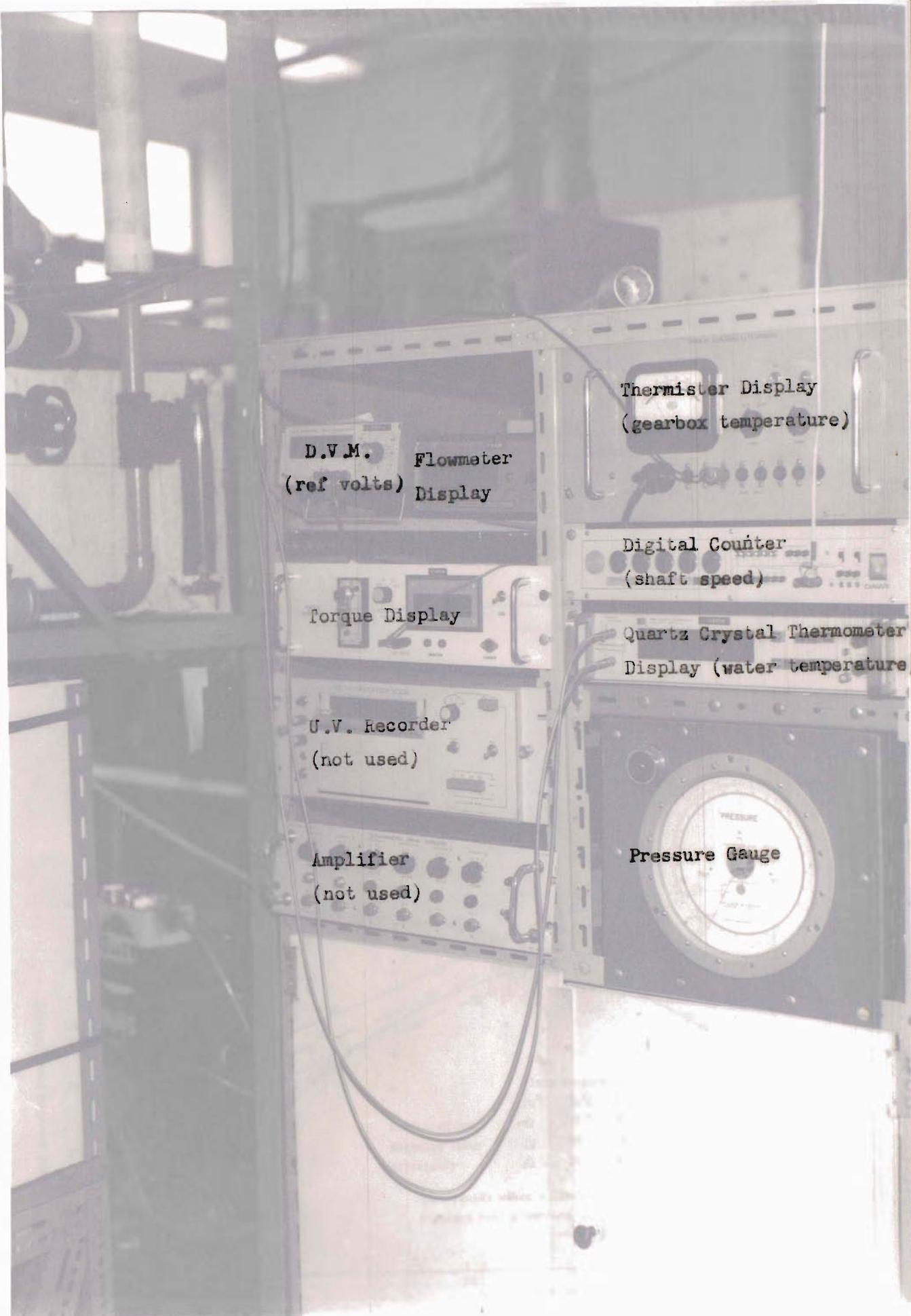
FIGURE 13.   INSTRUMENT PANEL FOR WATER TEST RIG.

Fluid Temperature

⊙	28°C	Test Fluid: water + 1% oil
⊕	56°C	Standard seal clearance
●	82°C	
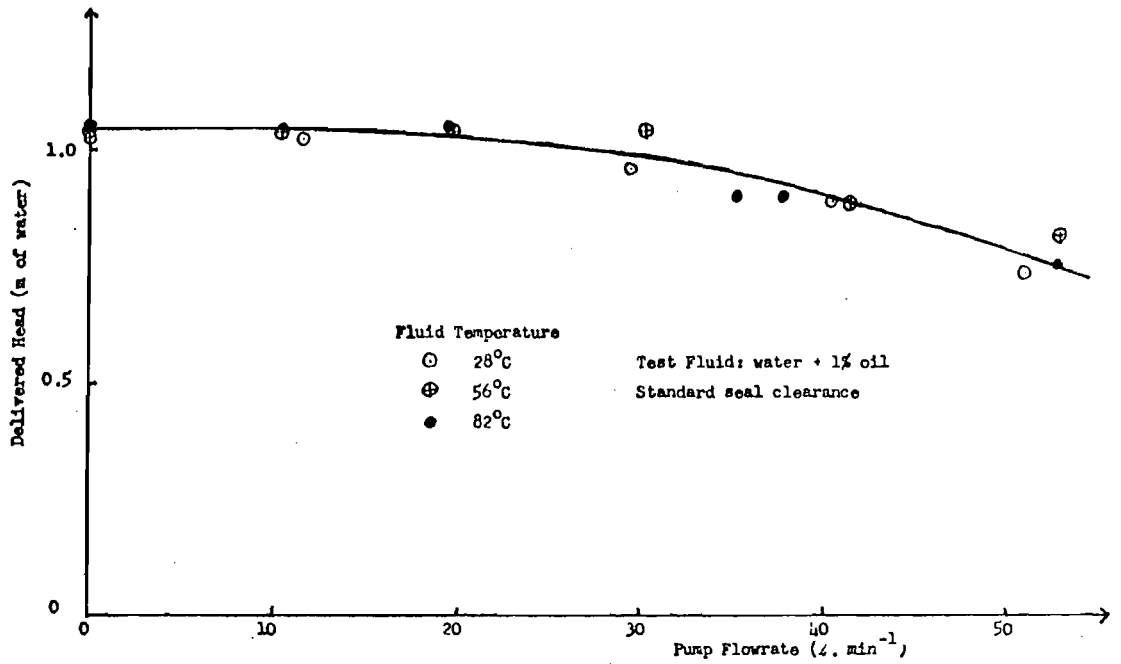
FIGURE 14.   PUMP HEAD CHARACTERISTIC AT 600 RPM IN WATER.

Fluid Temperature

	20°C	56°C	81°C
Delivered Head	⊙	⊕	●
Absorbed Power	☐	⊞	■
Efficiency	△	▲	▲

Test fluid: water + 1% oil

Standard seal cloarance
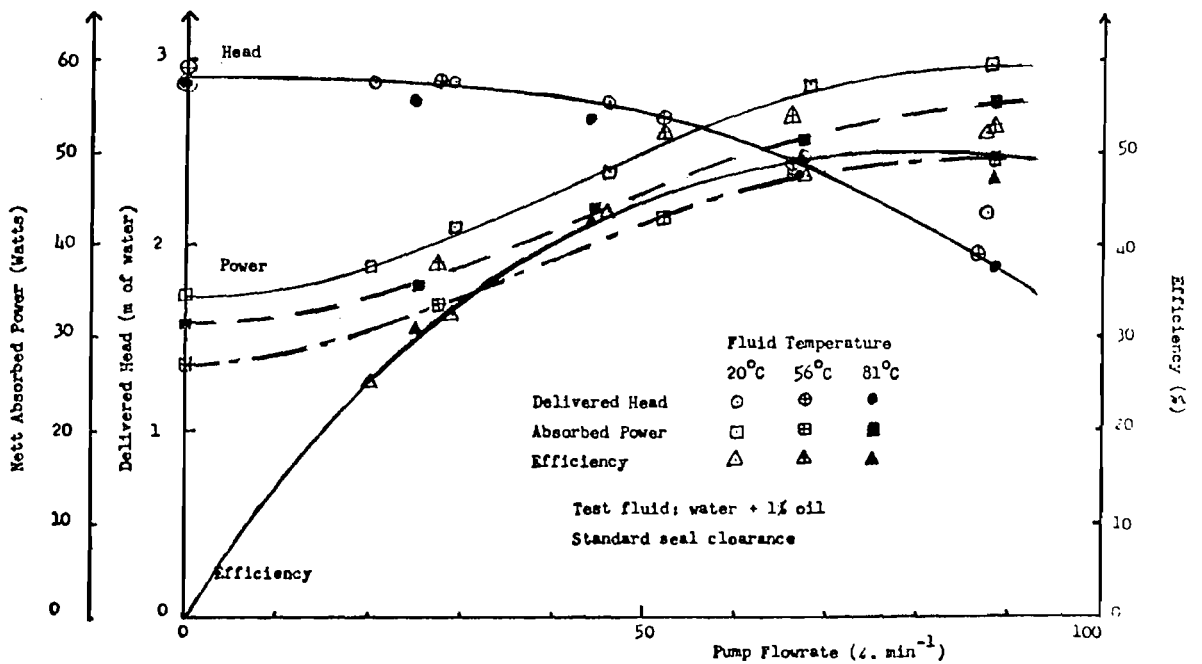
FIGURE 15.   PUMP CHARACTERISTICS AT 1000 RPM IN WATER.
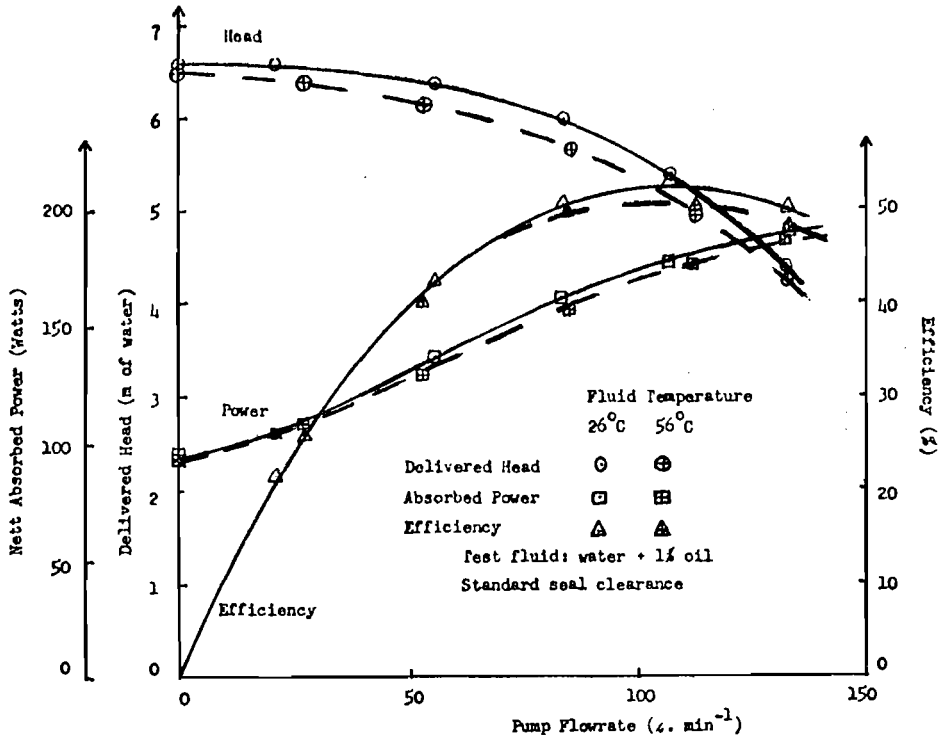
FIGURE 16.   PUMP CHARACTERISTICS AT 1500 RPM IN WATER.
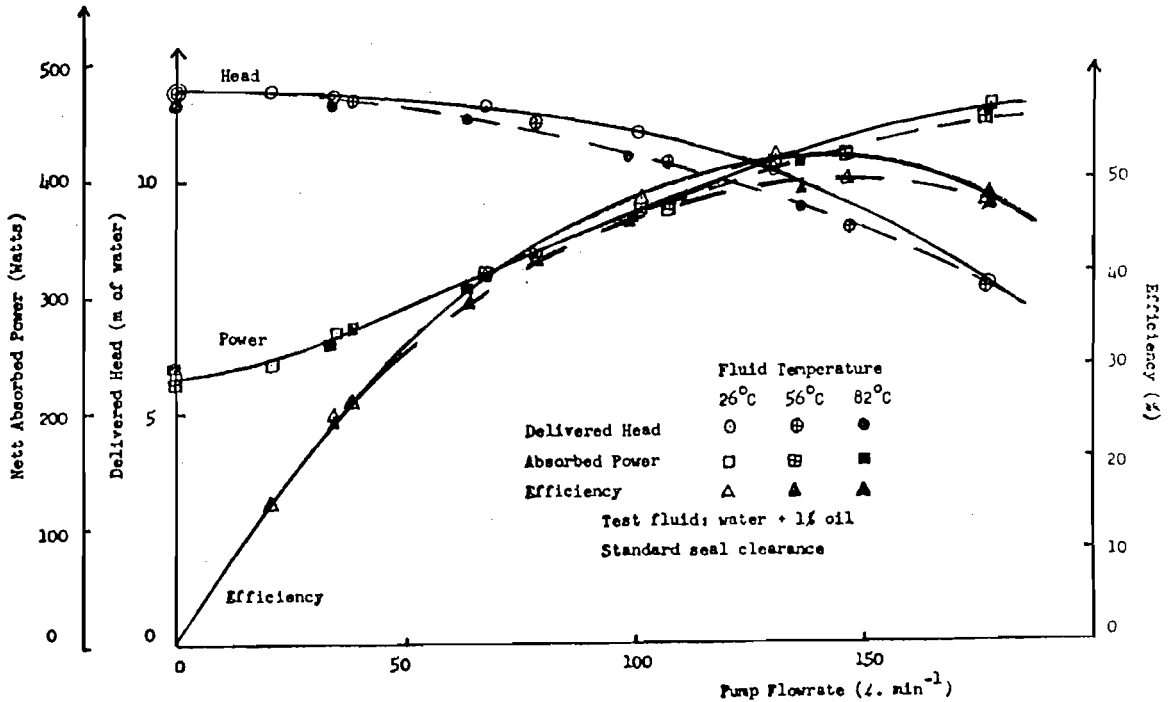
FIGURE 17.   PUMP CHARACTERISTICS AT 2000 RPM IN WATER.
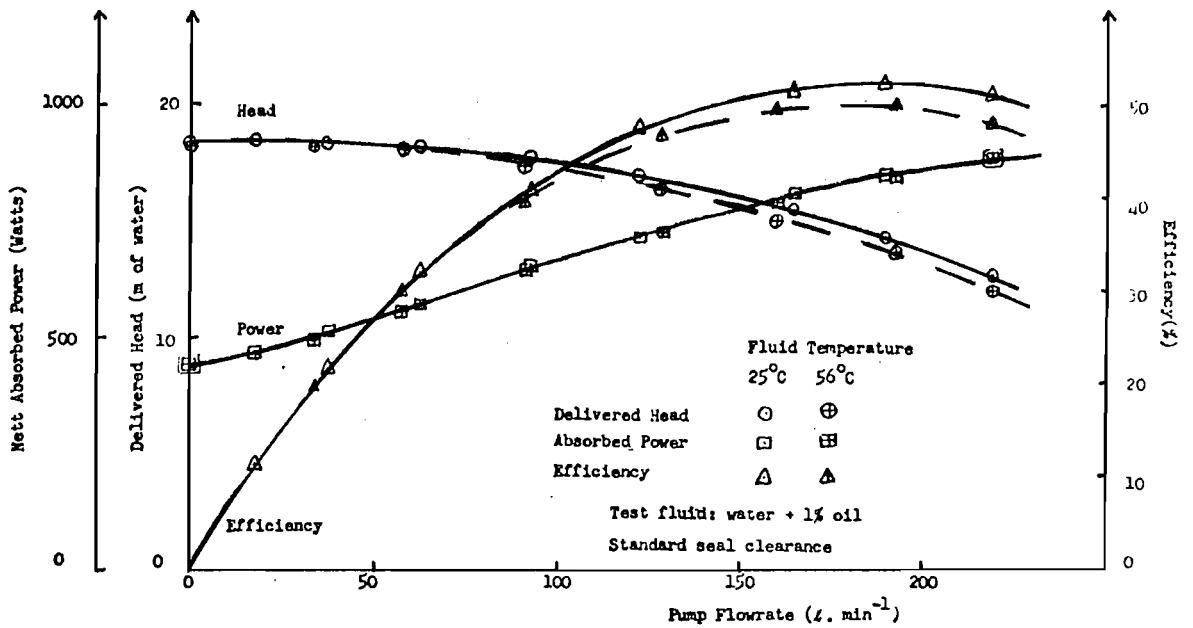
FIGURE 18. PUMP CHARACTERISTICS AT 2500 RPM IN WATER
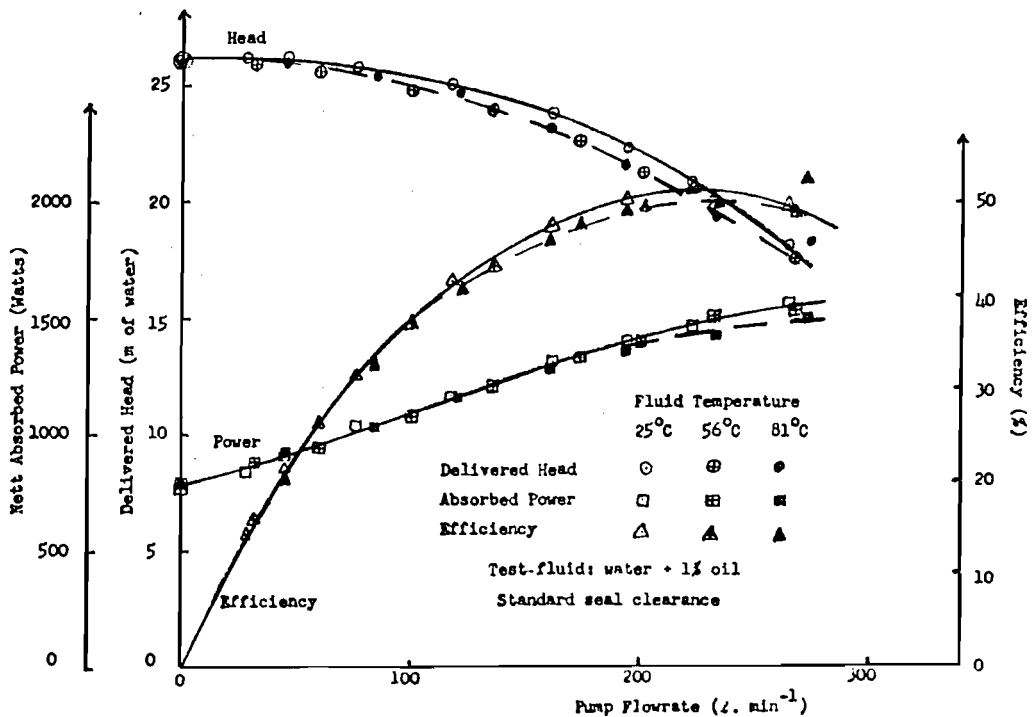
FIGURE 19. PUMP CHARACTERISTICS AT 3000 RPM IN WATER.
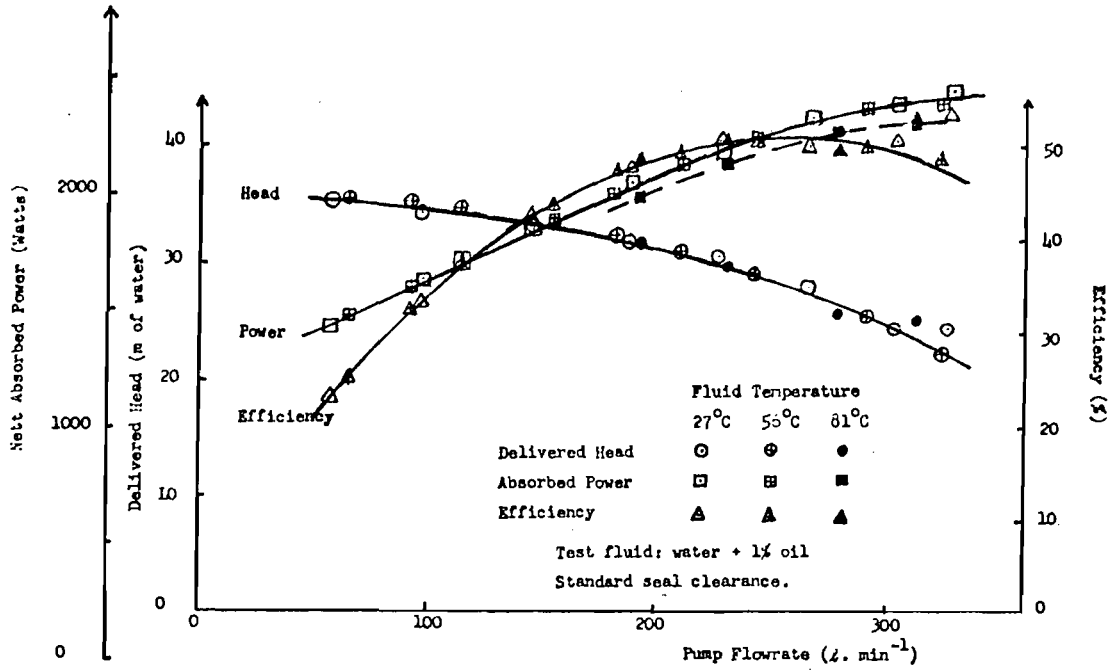
FIGURE 20.   PUMP CHARACTERISTICS AT 3500 RPM IN WATER.
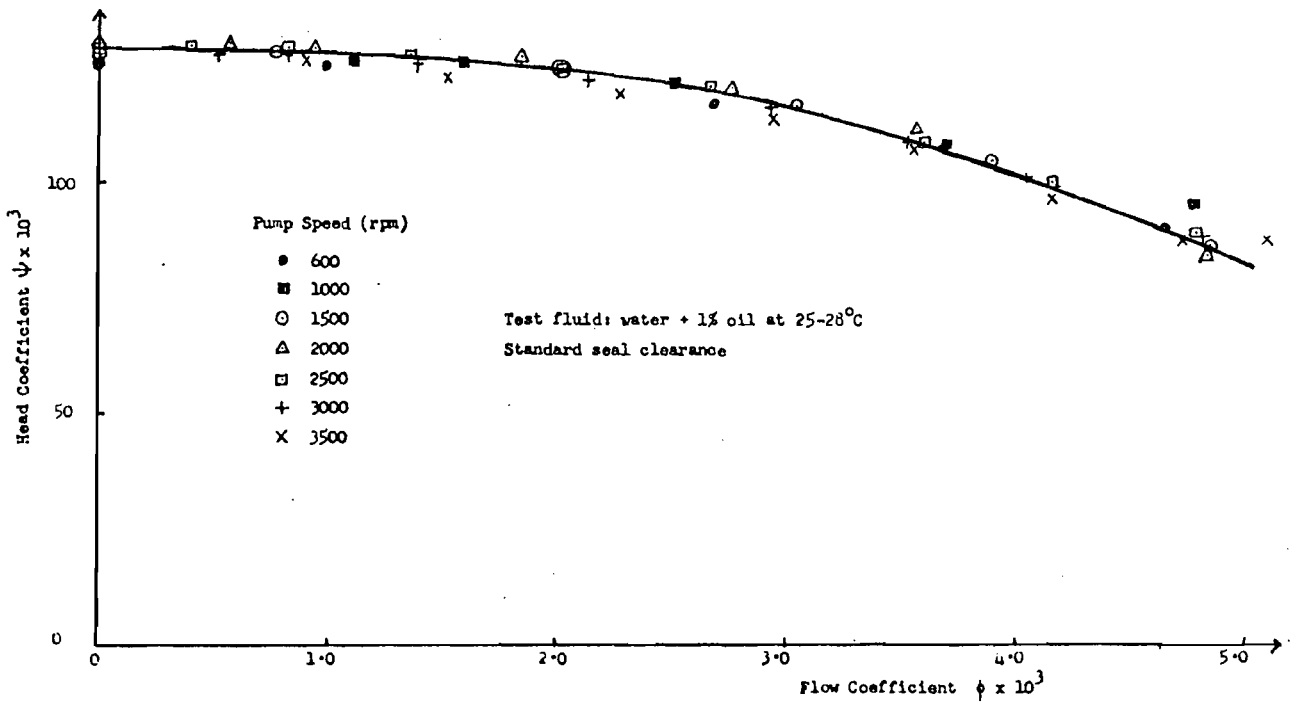
FIGURE 21.   DIMENSIONLESS HEAD / FLOW CHARACTERISTIC IN COLD WATER.
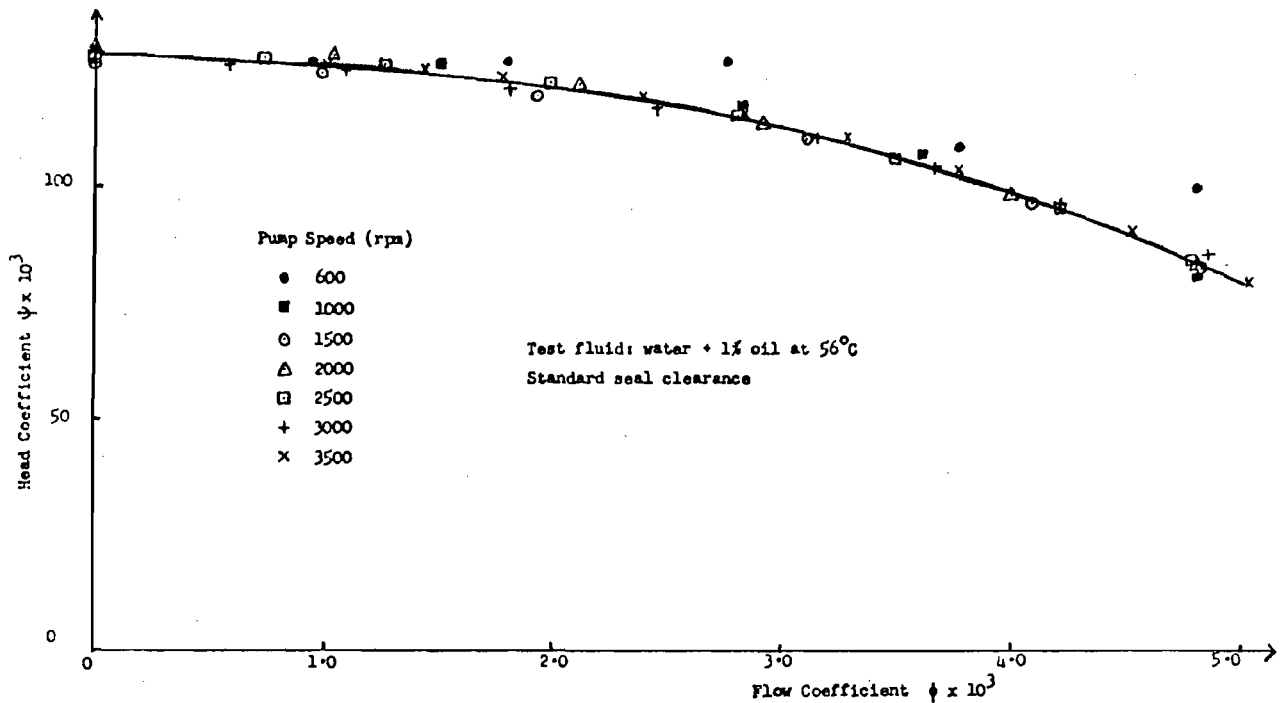
FIGURE 22.   DIMENSIONLESS HEAD / FLOW CHARACTERISTIC IN WARM WATER.
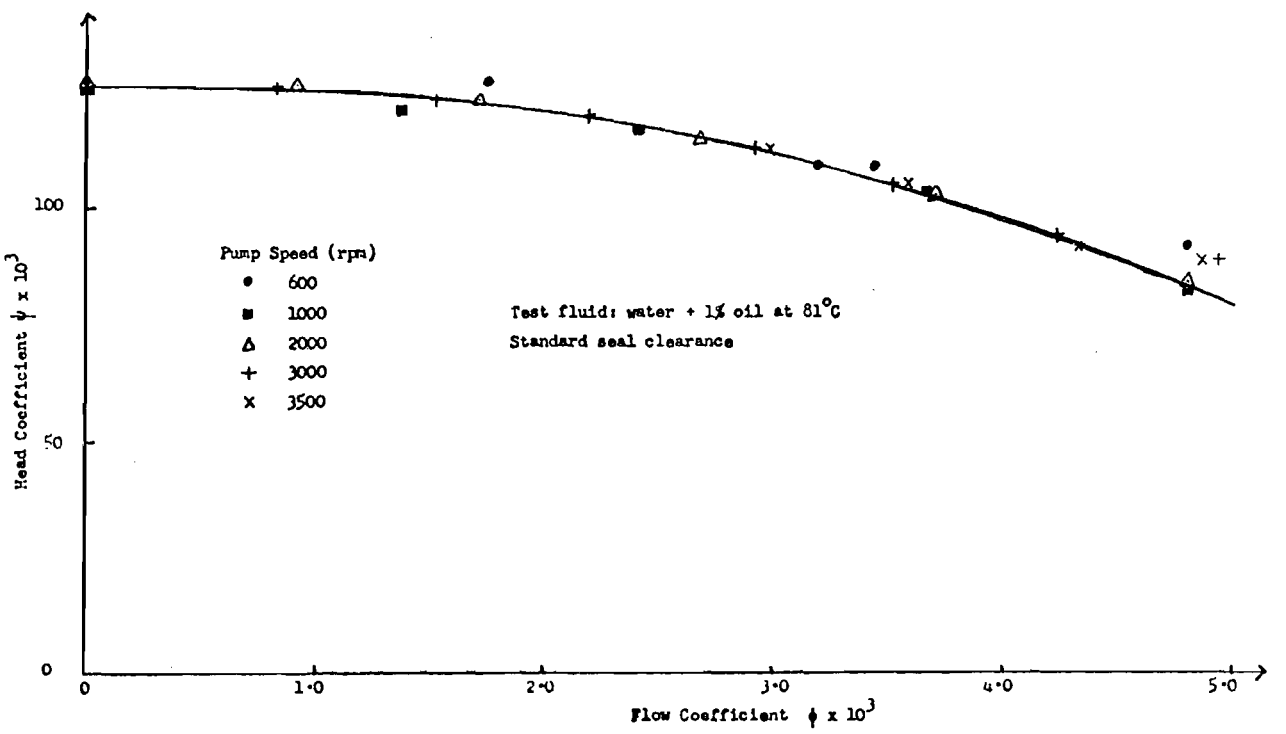
FIGURE 23.   DIMENSIONLESS HEAD / FLOW CHARACTERISTIC IN HOT WATER
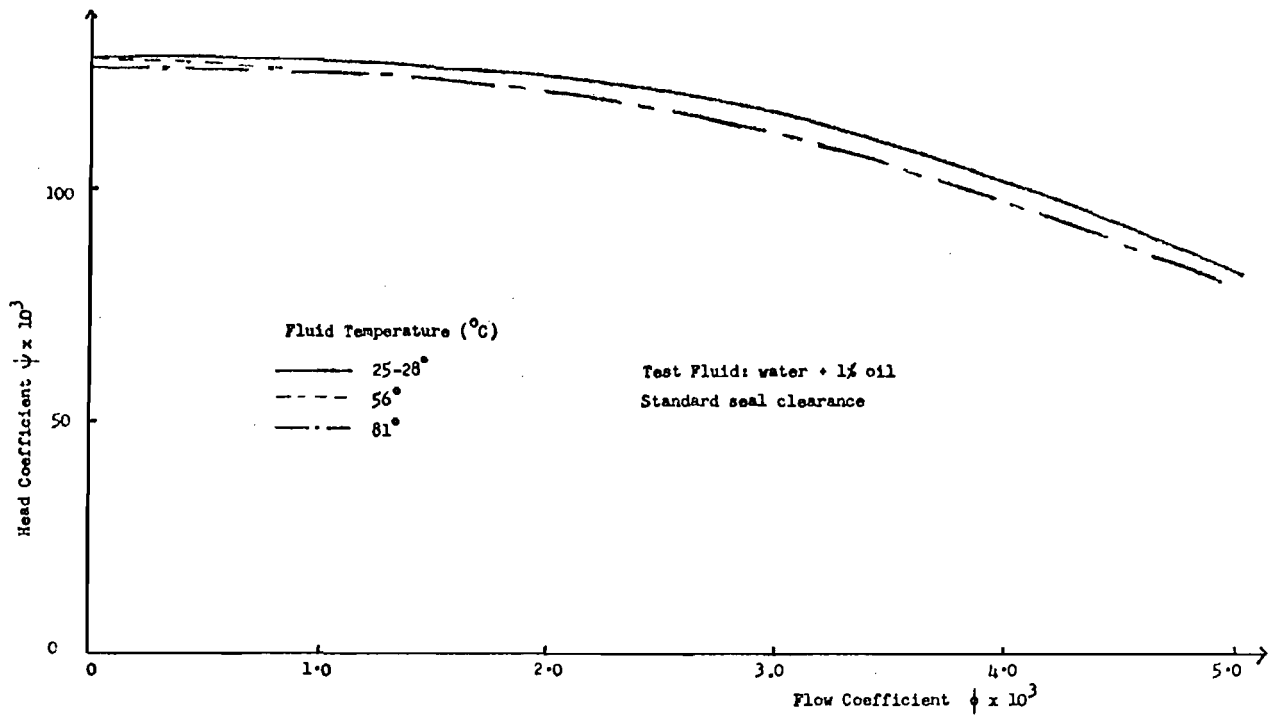
FIGURE 24a.   THE EFFECT OF WATER TEMPERATURE ON DIMENSIONLESS HEAD / FLOW CHARACTERISTIC.
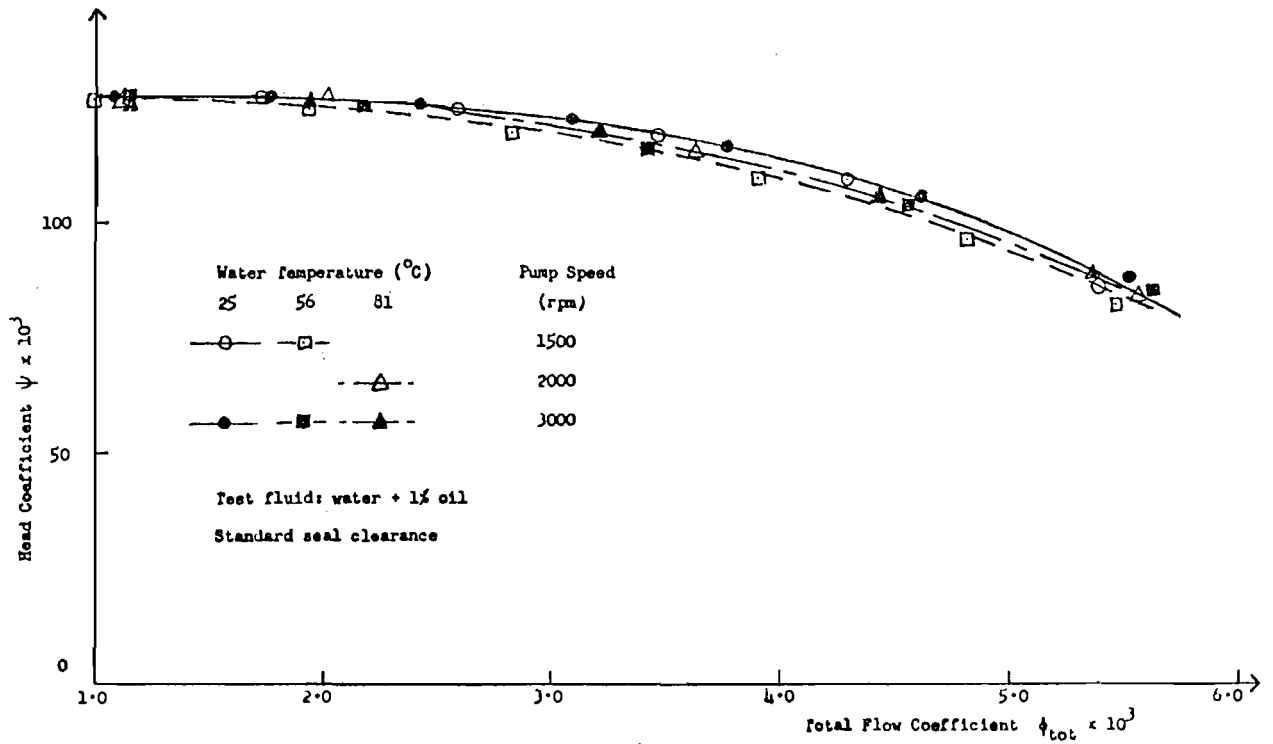
FIGURE 24b.   EFFECT OF WATER TEMPERATURE ON DIMENSIONLESS HEAD / TOTAL FLOW CHARACTERISTIC.
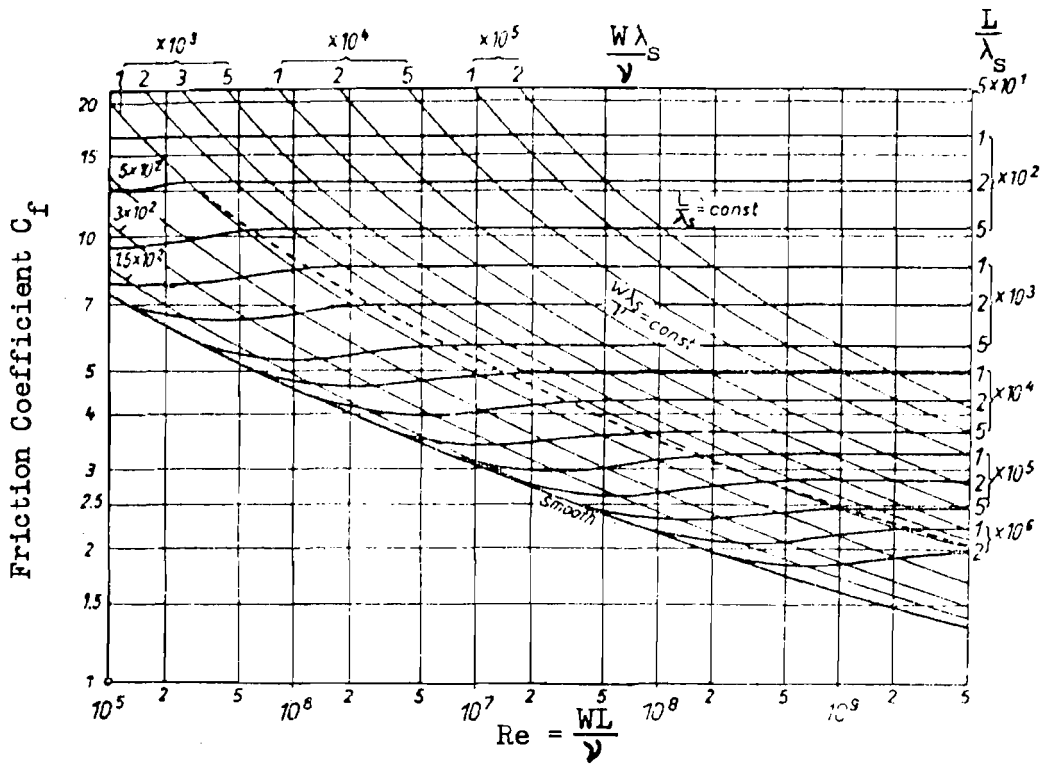
(a) Flat Plate at Zero Incidence[19]
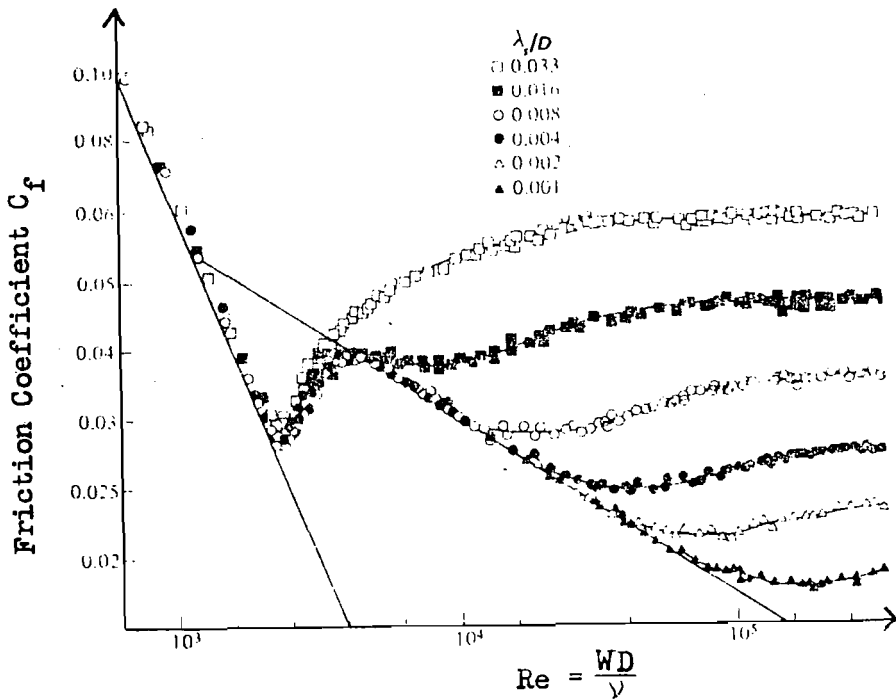
(b) Artificially Sand-Roughened Pipes[23]

FIGURE 25. VARIATION OF FRICTION COEFFICIENT WITH REYNOLDS NO.
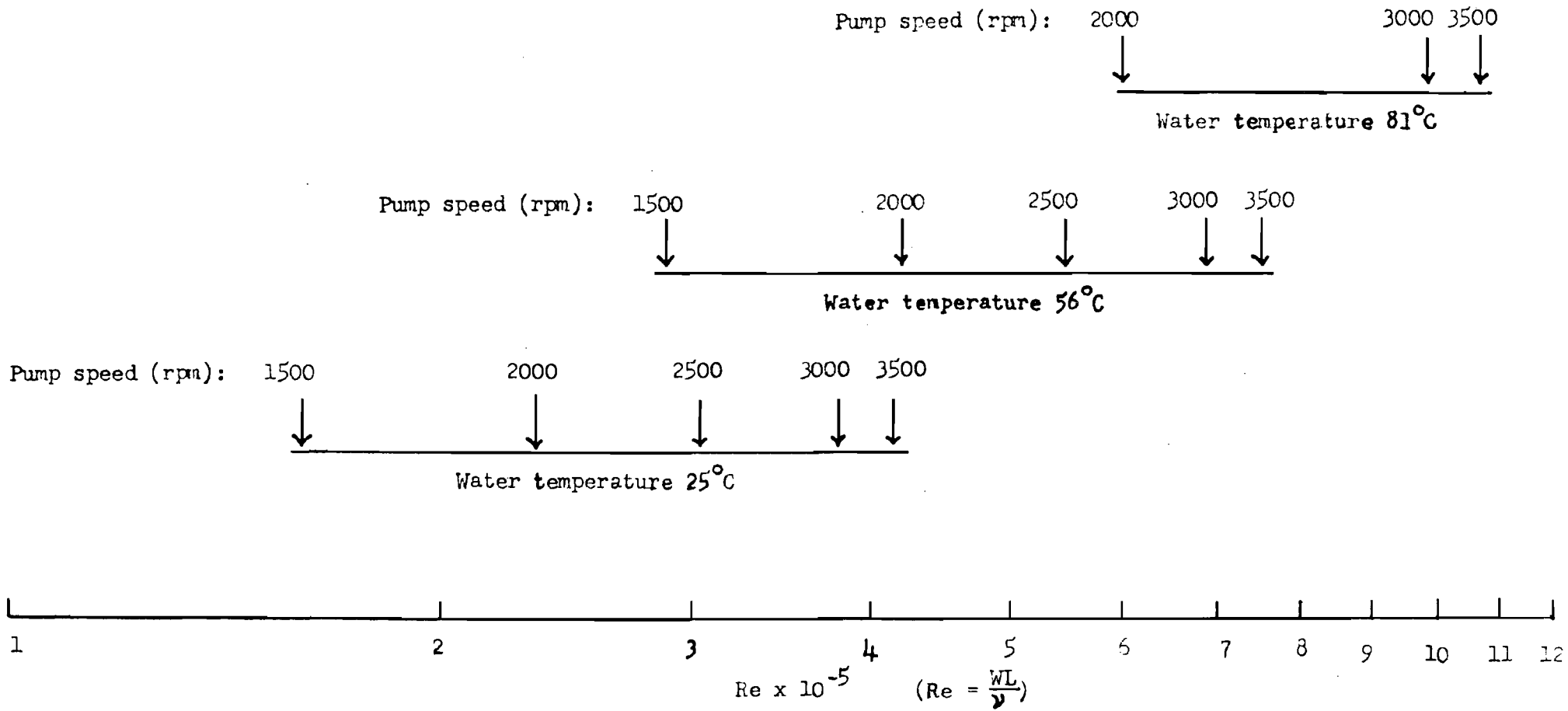
FIGURE 26.   RANGE OF THROUGHFLOW REYNOLDS NO COVERED BY PUMP TESTS IN WATER.
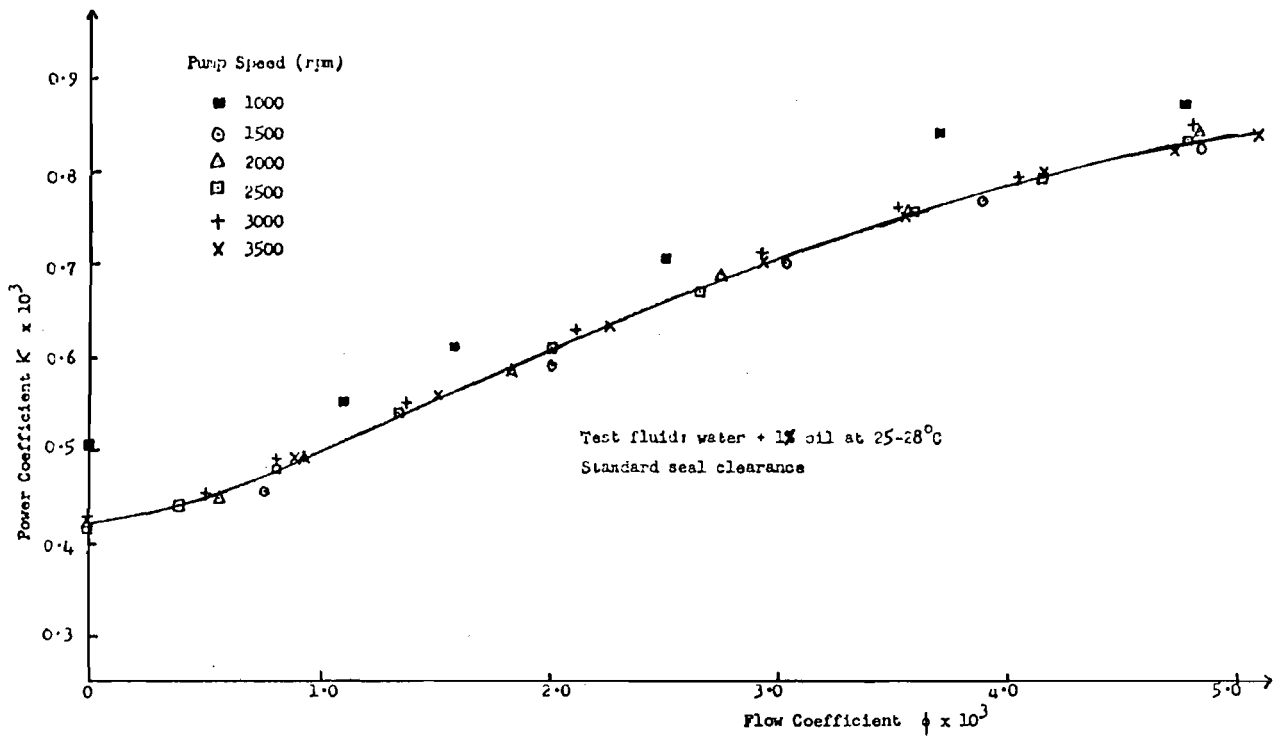
FIGURE 27.   DIMENSIONLESS POWER / FLOW CHARACTERISTIC IN COLD WATER.
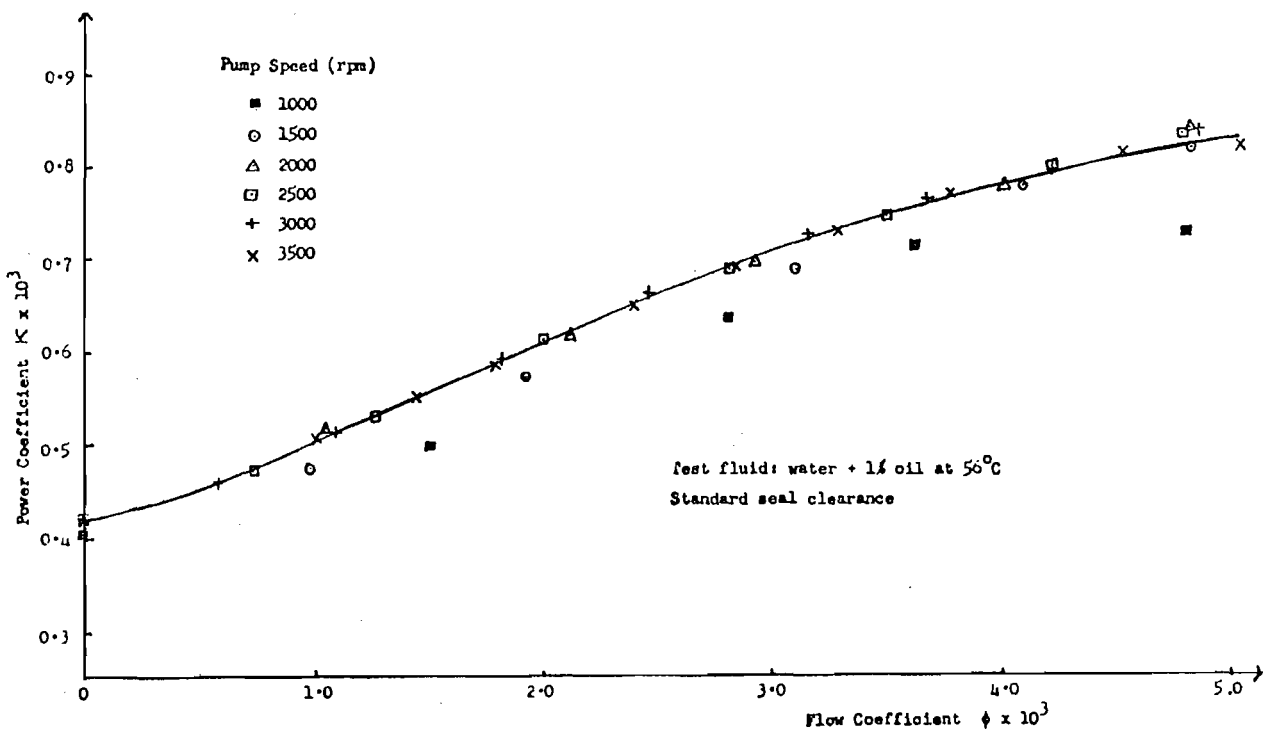
FIGURE 28.   DIMENSIONLESS POWER / FLOW CHARACTERISTIC IN WARM WATER.
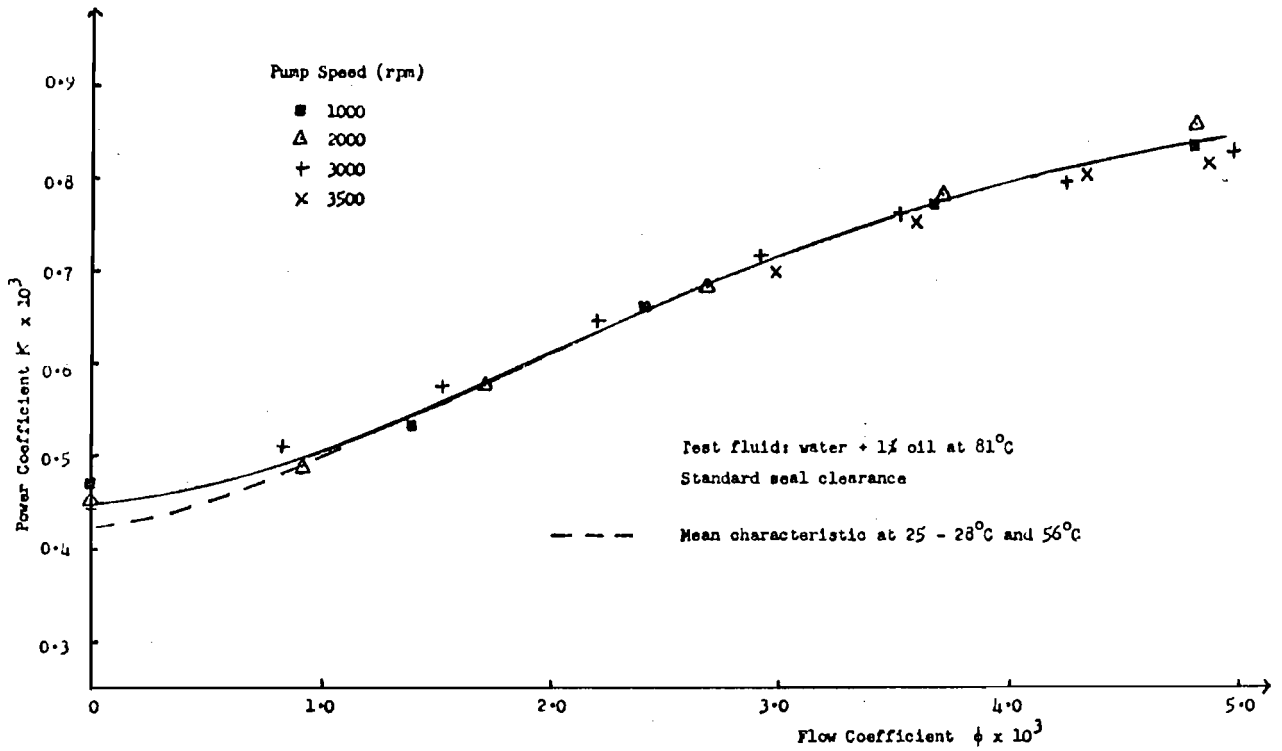
FIGURE 29.   DIMENSIONLESS POWER / FLOW CHARACTERISTIC IN HOT WATER.
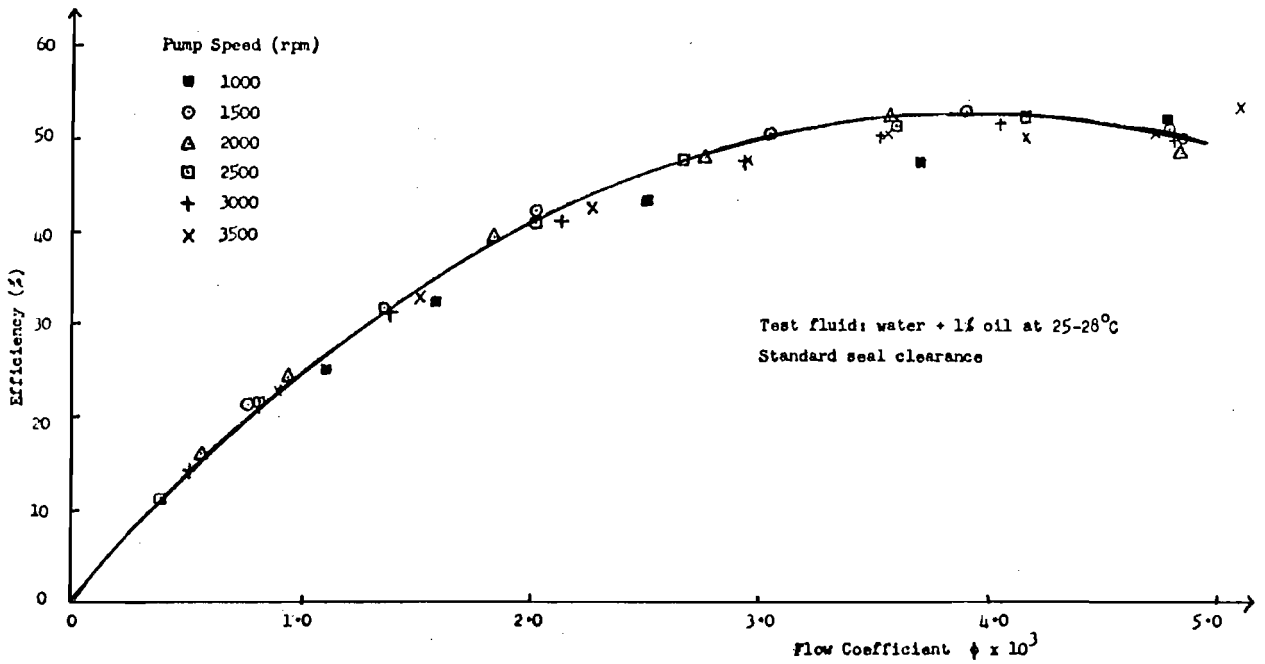
FIGURE 30.   DIMENSIONLESS EFFICIENCY / FLOW CHARACTERISTIC IN COLD WATER.
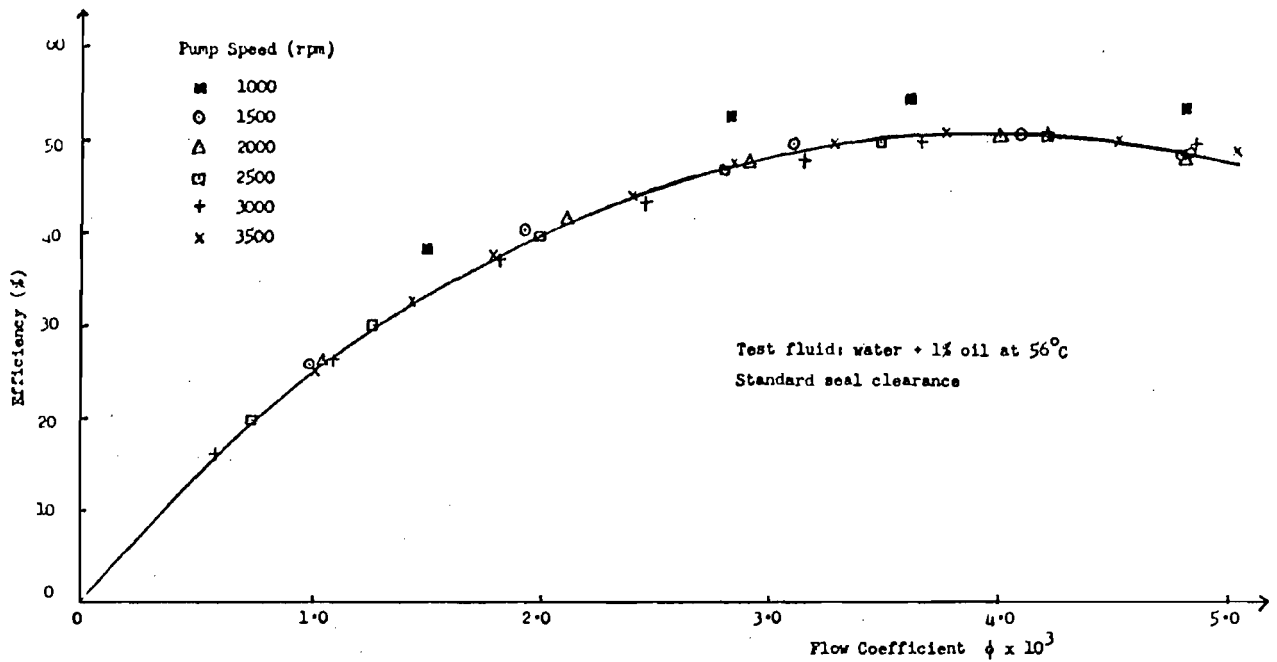
FIGURE 31.   DIMENSIONLESS EFFICIENCY / FLOW CHARACTERISTIC IN WARM WATER.
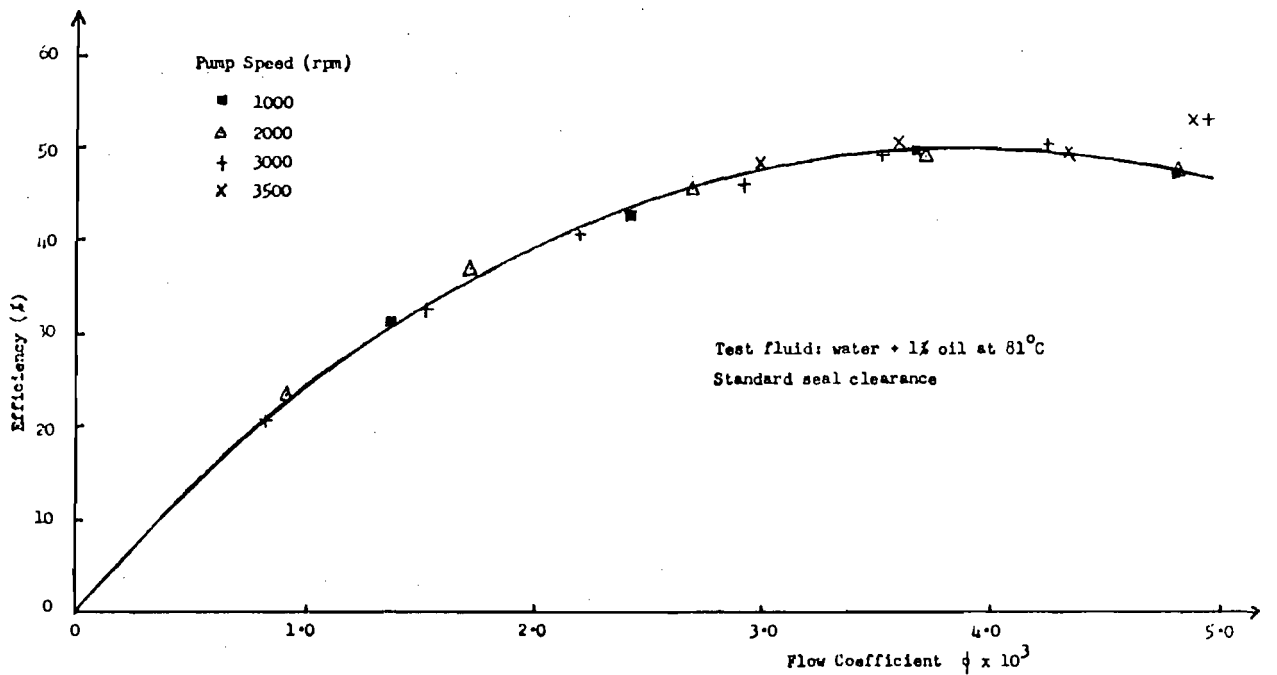
FIGURE 32.   DIMENSIONLESS EFFICIENCY / FLOW CHARACTERISTIC IN HOT WATER.
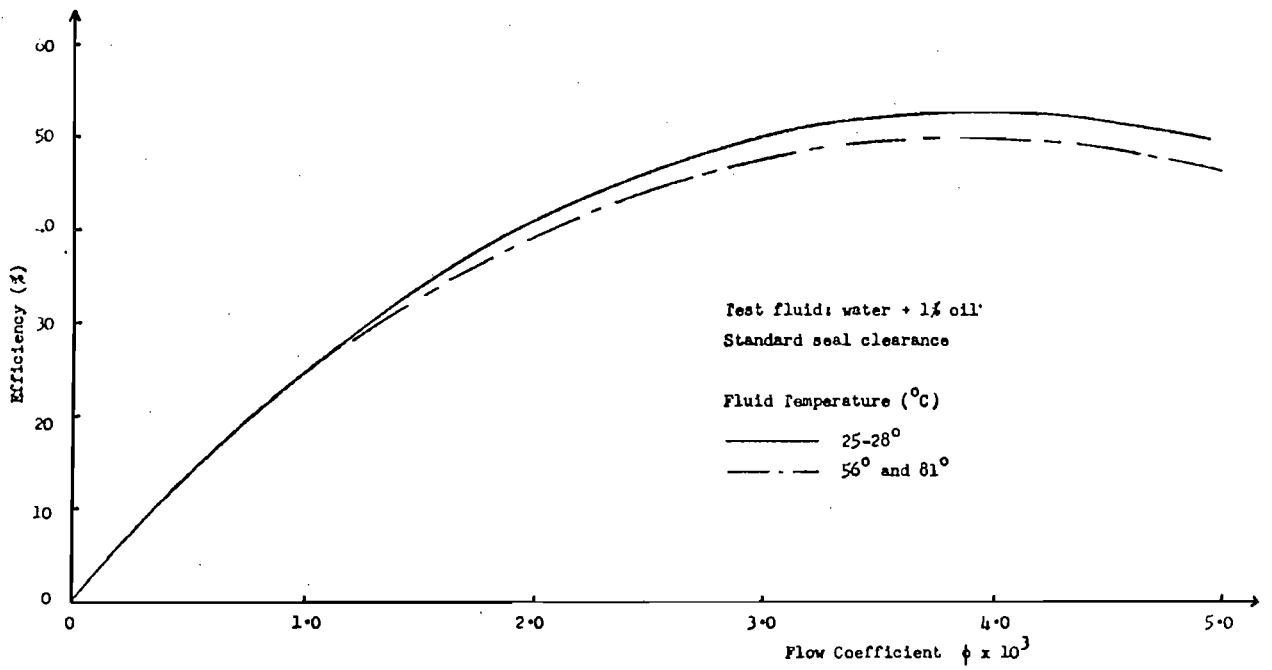
FIGURE 33.   THE EFFECT OF WATER TEMPERATURE ON DIMENSIONLESS EFFICIENCY / FLOW CHARACTERISTIC.
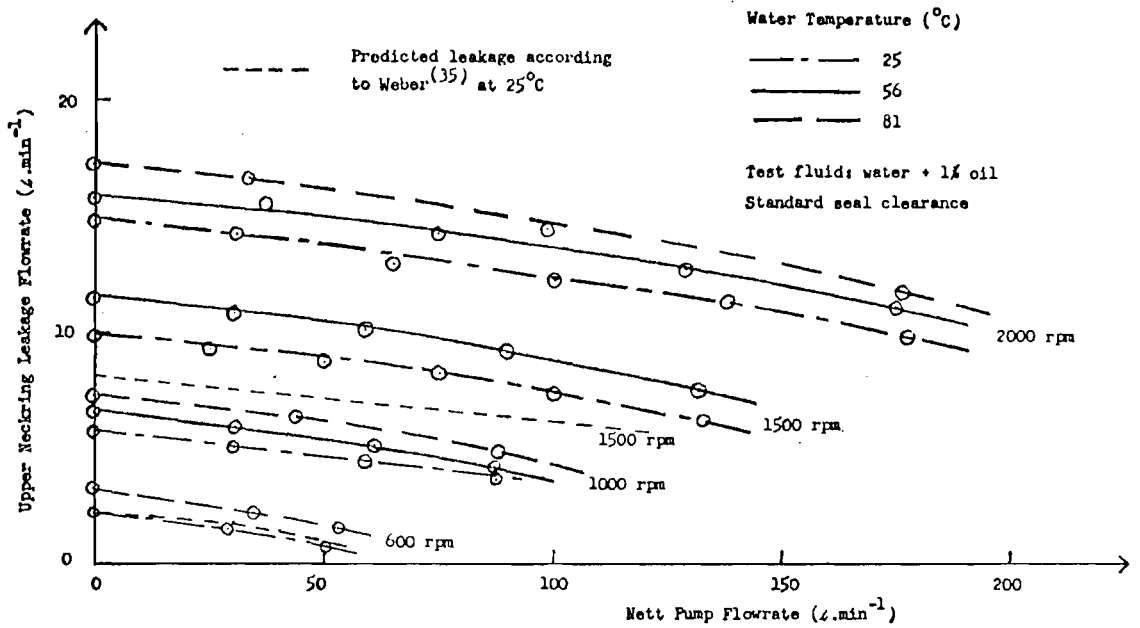
FIGURE 34. UPPER NECKRING LEAKAGE AS A FUNCTION OF NETT PUMP FLOWRATE IN WATER (600 - 2000 RPM).
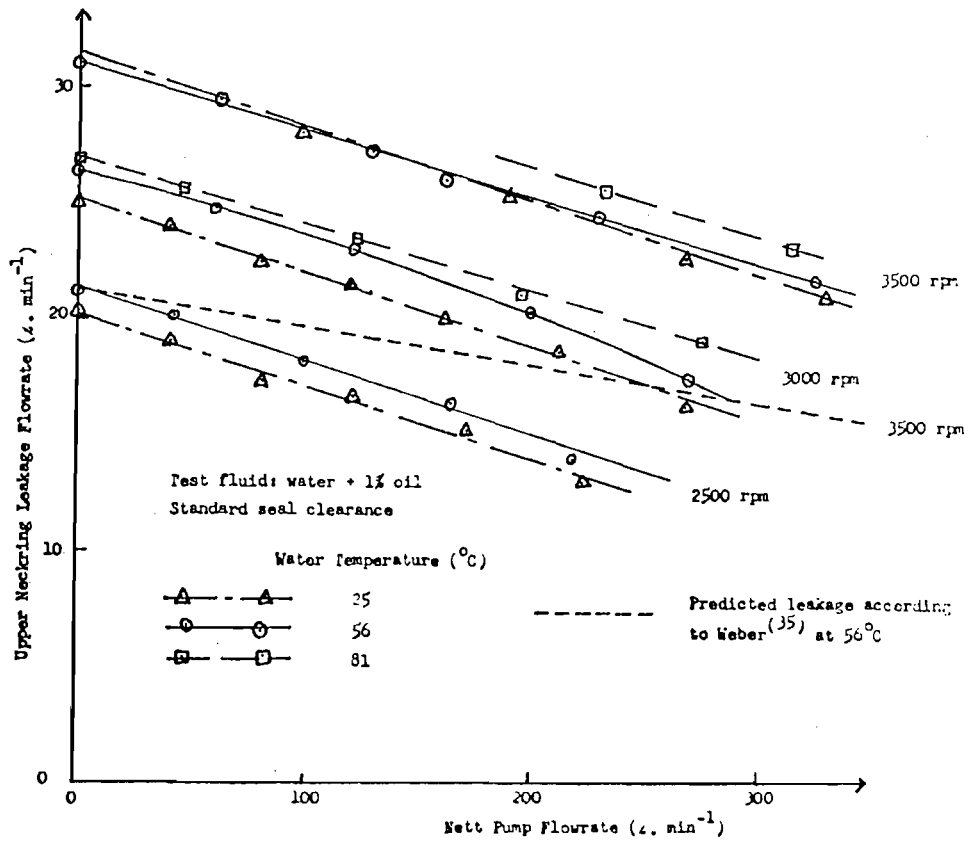
FIGURE 35. UPPER NECKRING LEAKAGE AS A FUNCTION OF NETT PUMP FLOWRATE IN WATER (2500 - 3500 RPM).
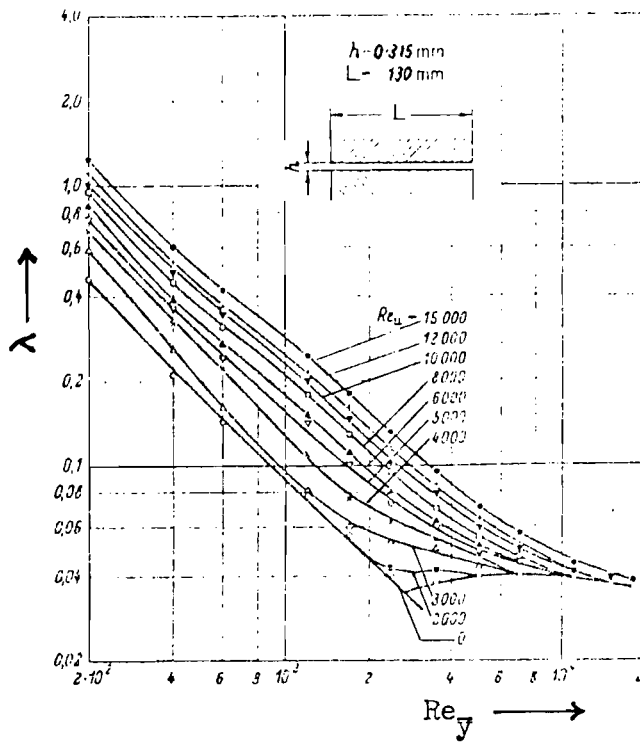
FIGURE 36a. VARIATION OF SLOT FRICTION COEFFICIENT (λ) WITH
THROUGHFLOW AND ROTATIONAL REYNOLDS NOS ($Re_{\bar{y}}$ and Re_u)[35].
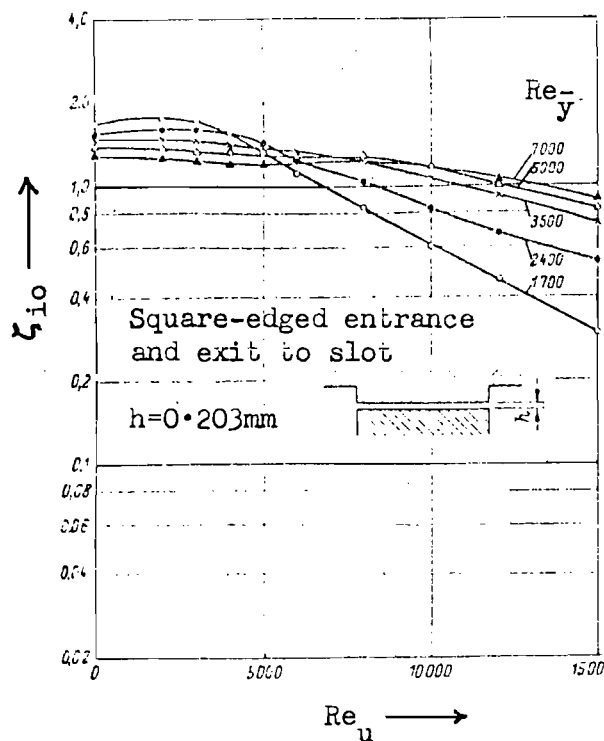
FIGURE 36b. VARIATION OF SLOT INLET AND OUTLET RESISTANCE COEFFICIENT (ζ_{io})
WITH THROUGHFLOW AND ROTATIONAL REYNOLDS NOS ($Re_{\bar{y}}$ and Re_u).
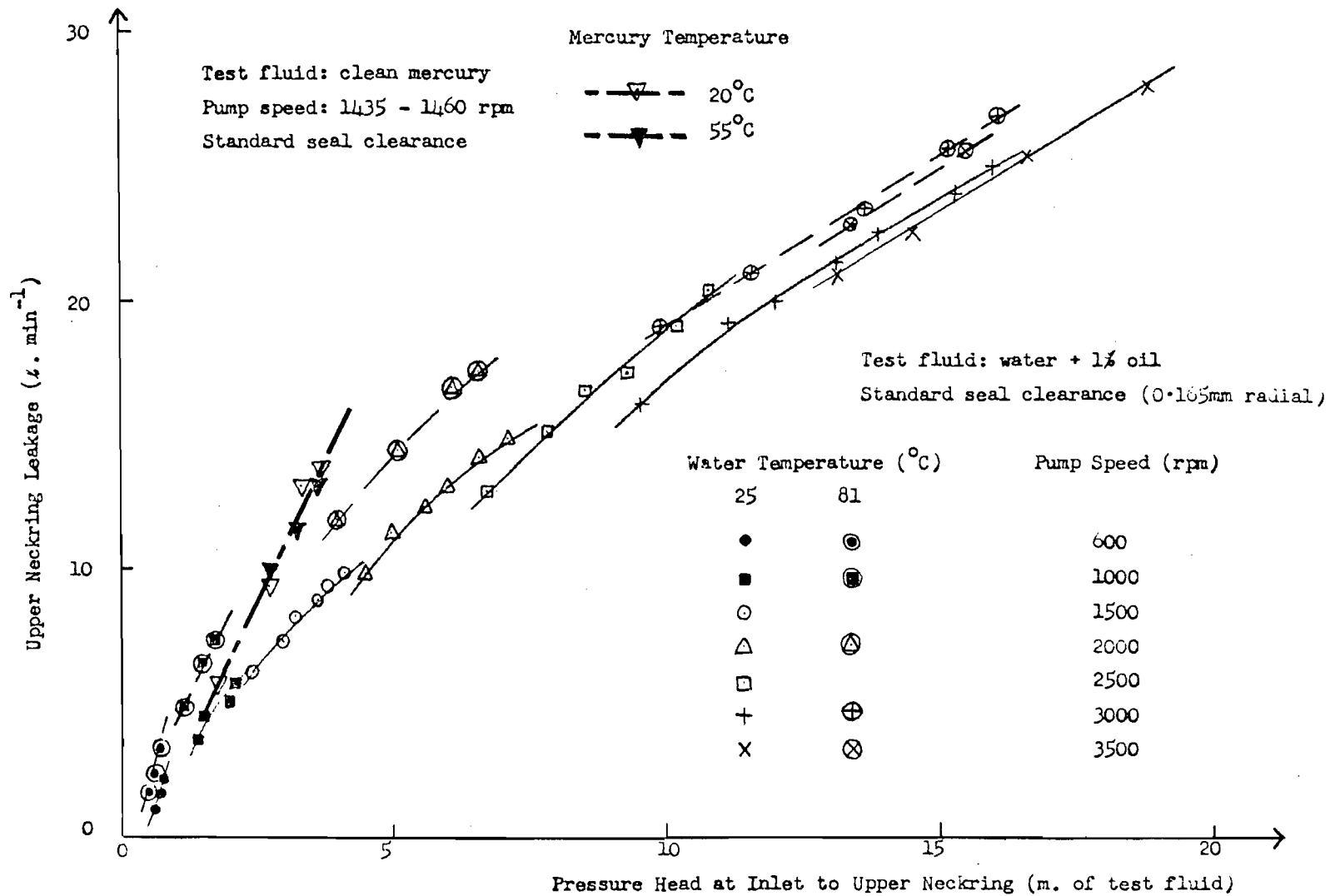
FIGURE 37.   VARIATION IN LEAKAGE RATE WITH PRESSURE AND SPEED.
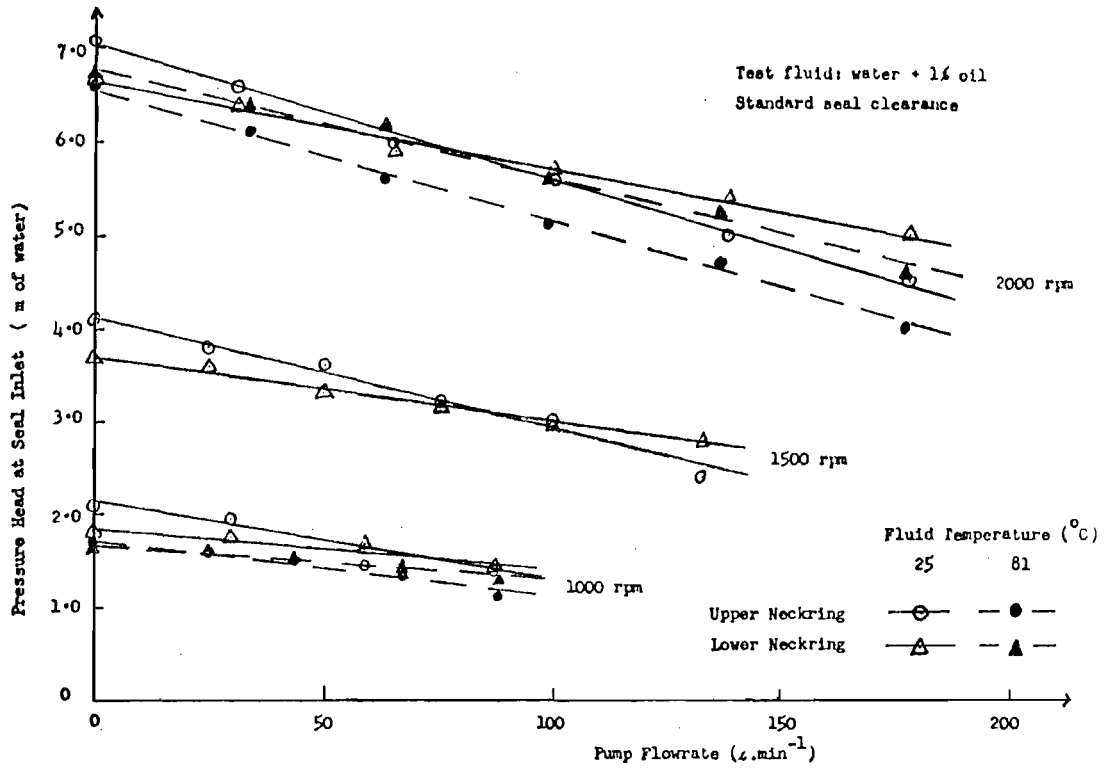
FIGURE 38. SEAL INLET PRESSURE AS A FUNCTION OF PUMP FLOWRATE IN WATER (1000 - 2000 RPM) .
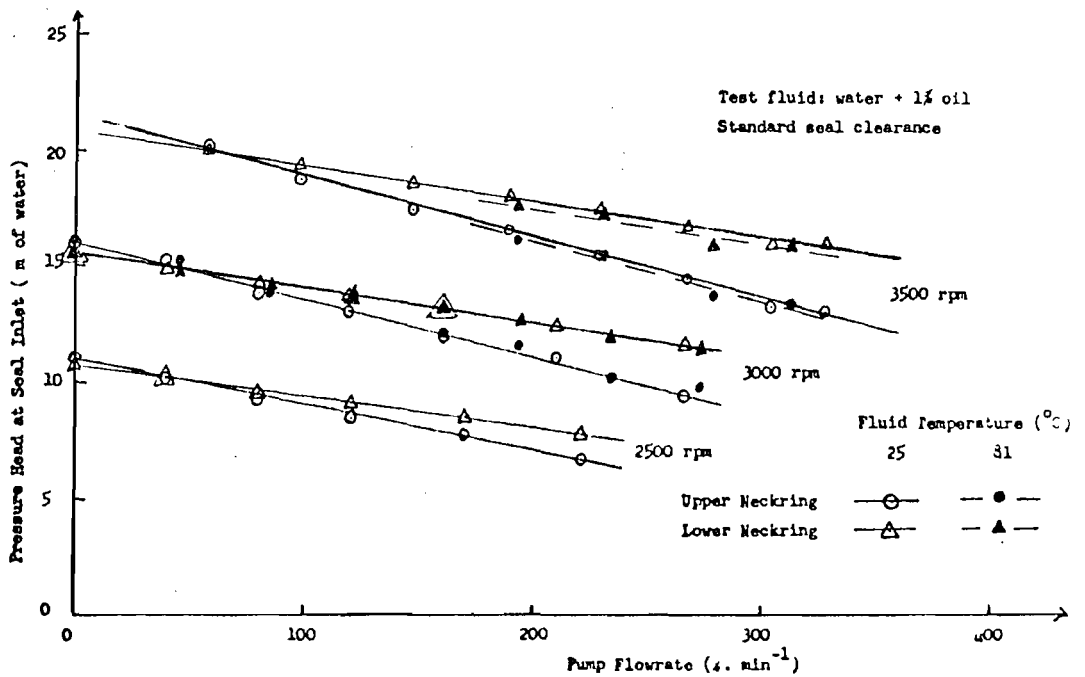
FIGURE 39. SEAL INLET PRESSURE AS A FUNCTION OF PUMP FLOWRATE IN WATER (2500 - 3500 RPM) .
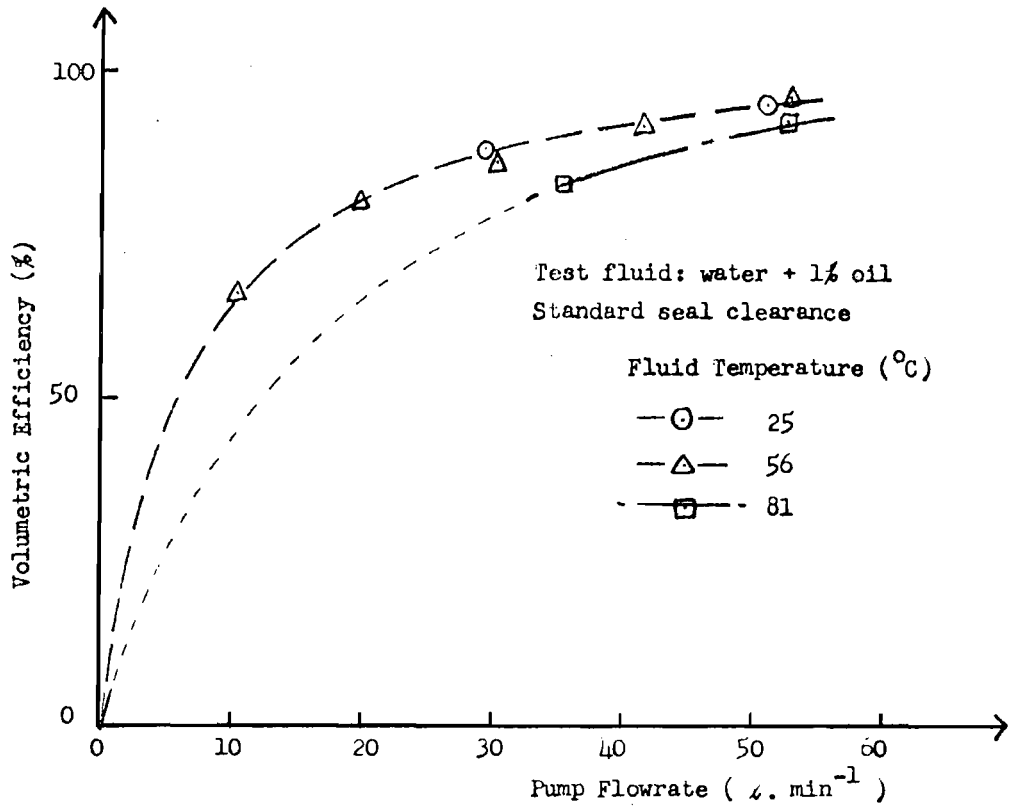
FIGURE 40.   VOLUMETRIC EFFICIENCY CURVES AT 600 RPM IN WATER.
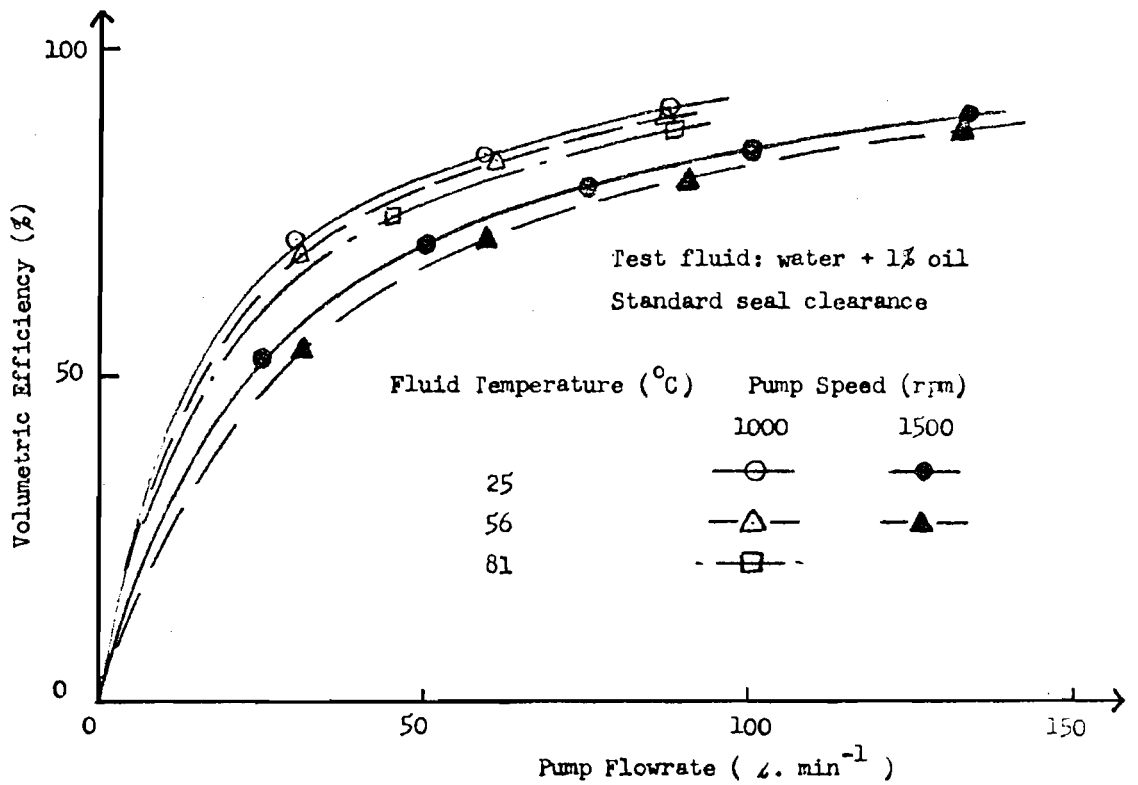
FIGURE 41.   VOLUMETRIC EFFICIENCY CURVES AT 1000 AND 1500 RPM IN WATER
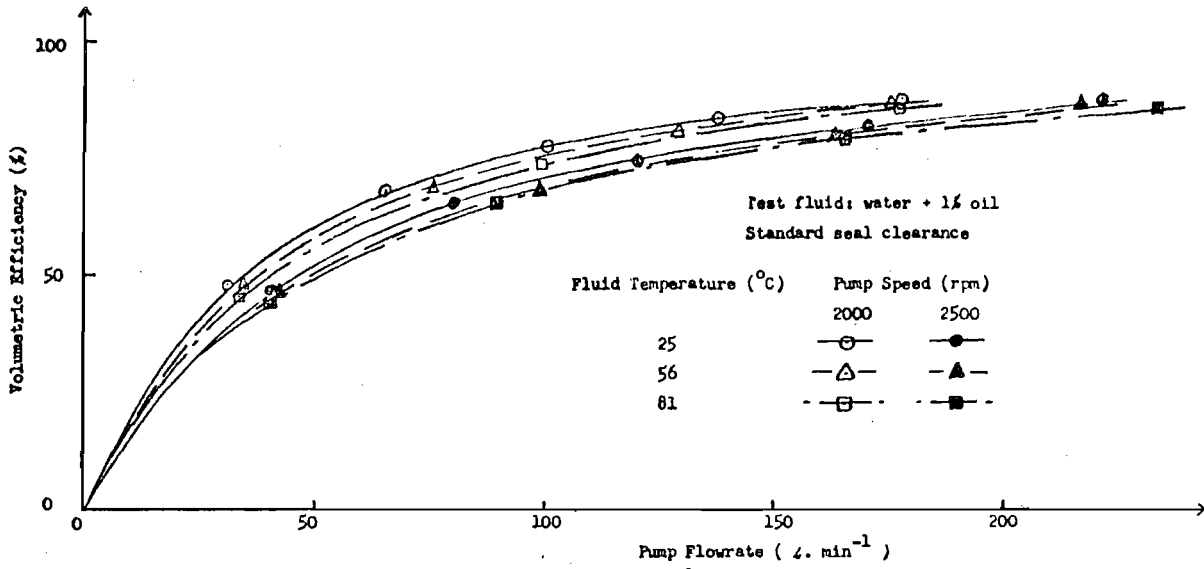
FIGURE 42.   VOLUMETRIC EFFICIENCY CURVES AT 2000 AND 2500 RPM IN WATER.
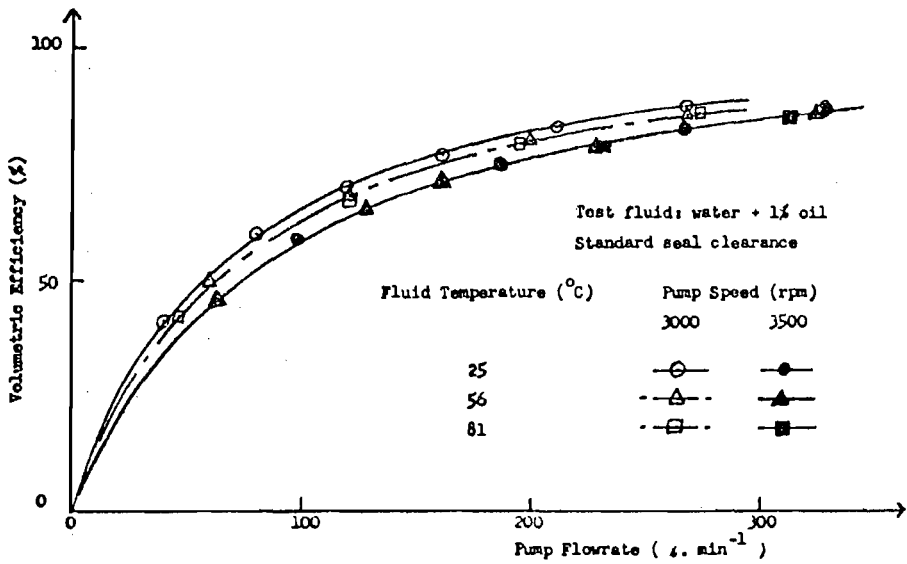
FIGURE 43.   VOLUMETRIC EFFICIENCY CURVES AT 3000 AND 3500 RPM IN WATER.

Test fluid: water + 1% oil at 25°C
Standard seal clearance
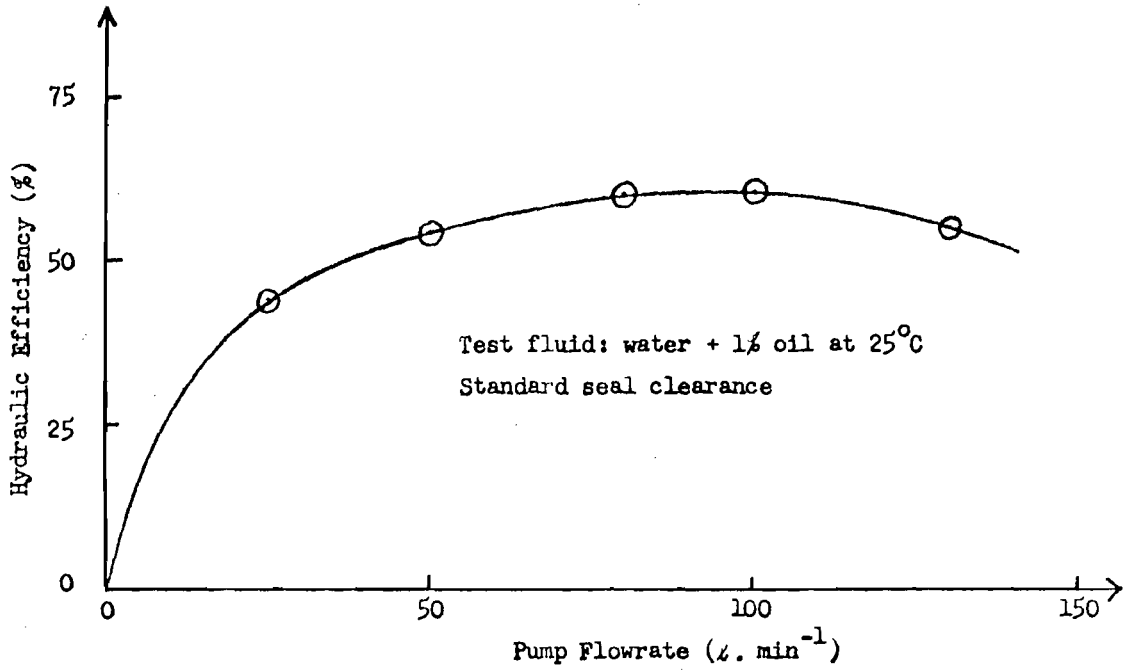
FIGURE 44.   HYDRAULIC EFFICIENCY CURVE AT 1500 RPM IN COLD WATER.

Test fluid: water + 1% oil at 25°C
Standard seal clearance
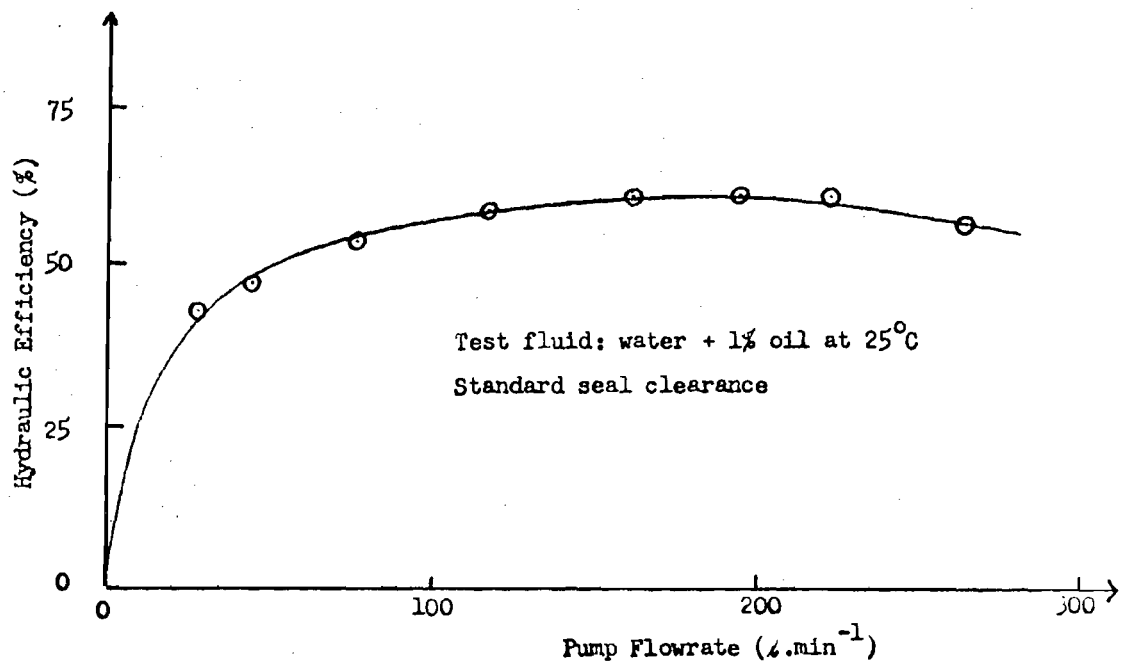
FIGURE 45.   HYDRAULIC EFFICIENCY CURVE AT 3000 RPM IN COLD WATER.
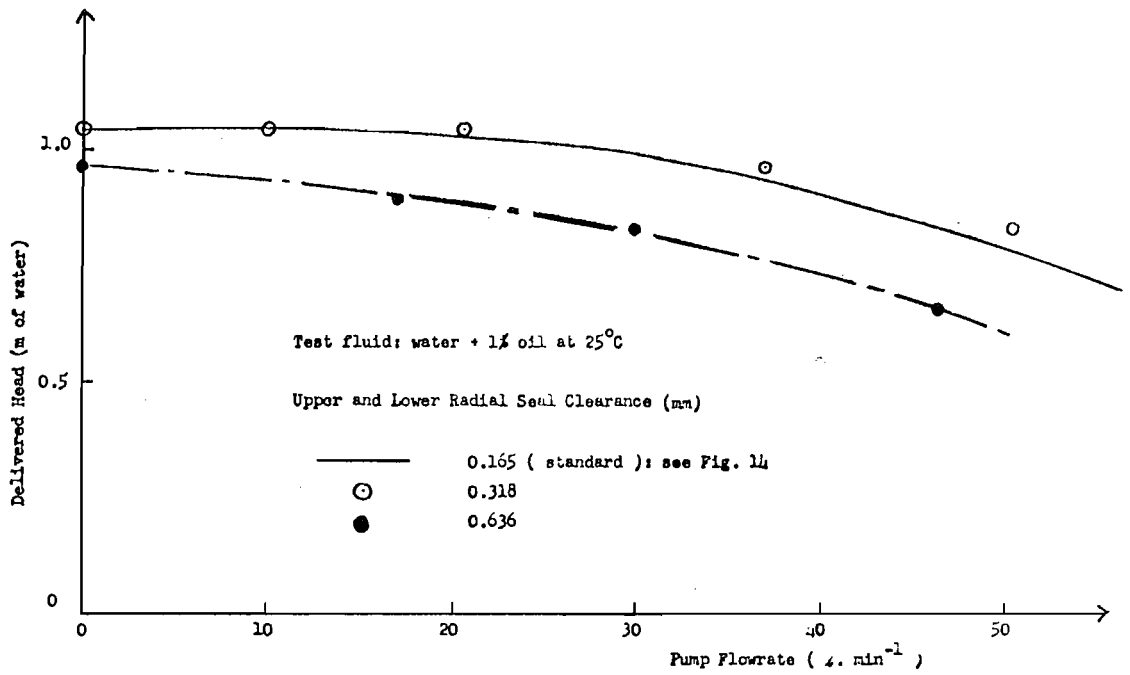
FIGURE 46.   EFFECT OF INCREASED SEAL CLEARANCE ON PUMP HEAD CHARACTERISTIC AT 600 RPM IN COLD WATER.
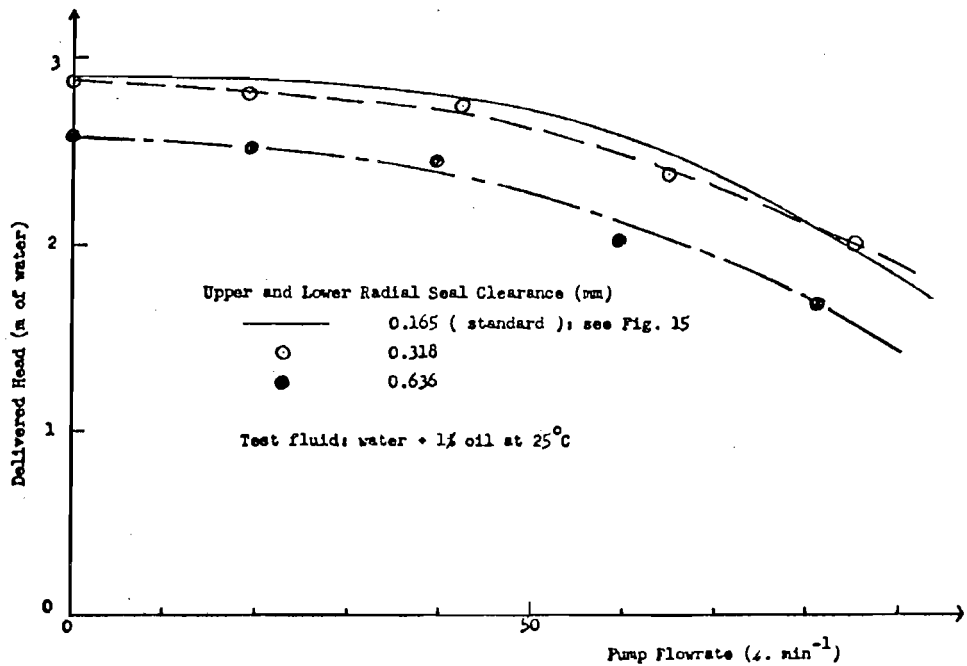
FIGURE 47.   EFFECT OF INCREASED SEAL CLEARANCE ON PUMP HEAD CHARACTERISTIC AT 1000 RPM IN COLD WATER.
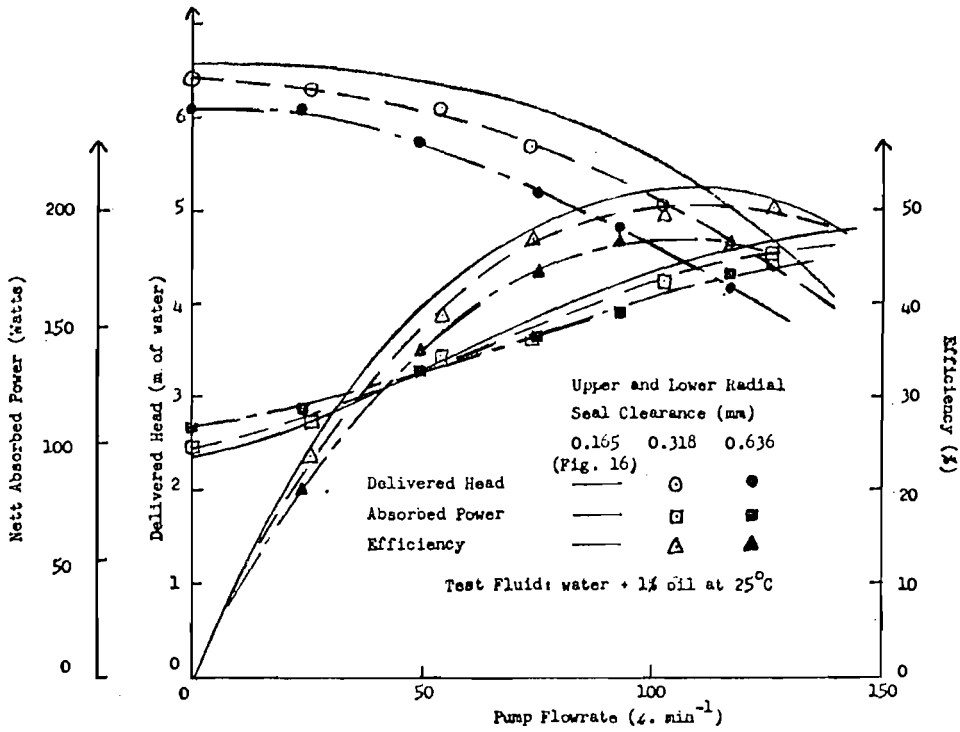
FIGURE 48.   EFFECT OF INCREASED SEAL CLEARANCE ON PUMP CHARACTERISTICS AT 1500 RPM IN COLD WATER.
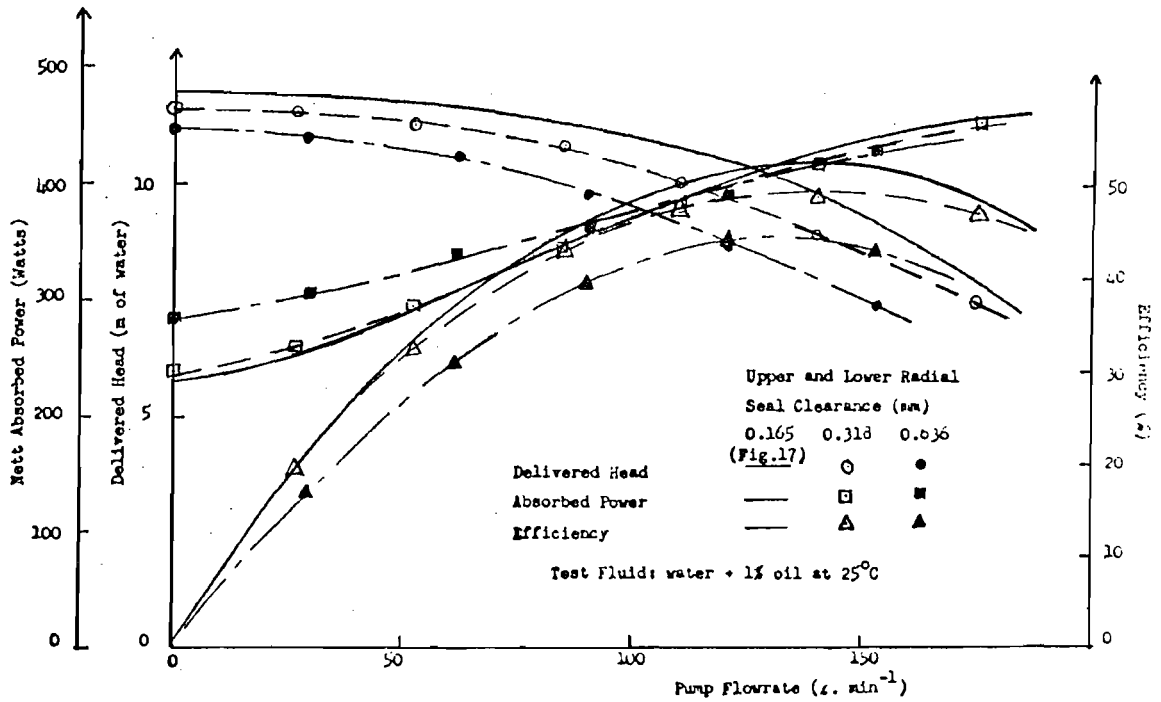
FIGURE 49.   EFFECT OF INCREASED SEAL CLEARANCE ON PUMP CHARACTERISTICS AT 2000 RPM IN COLD WATER.
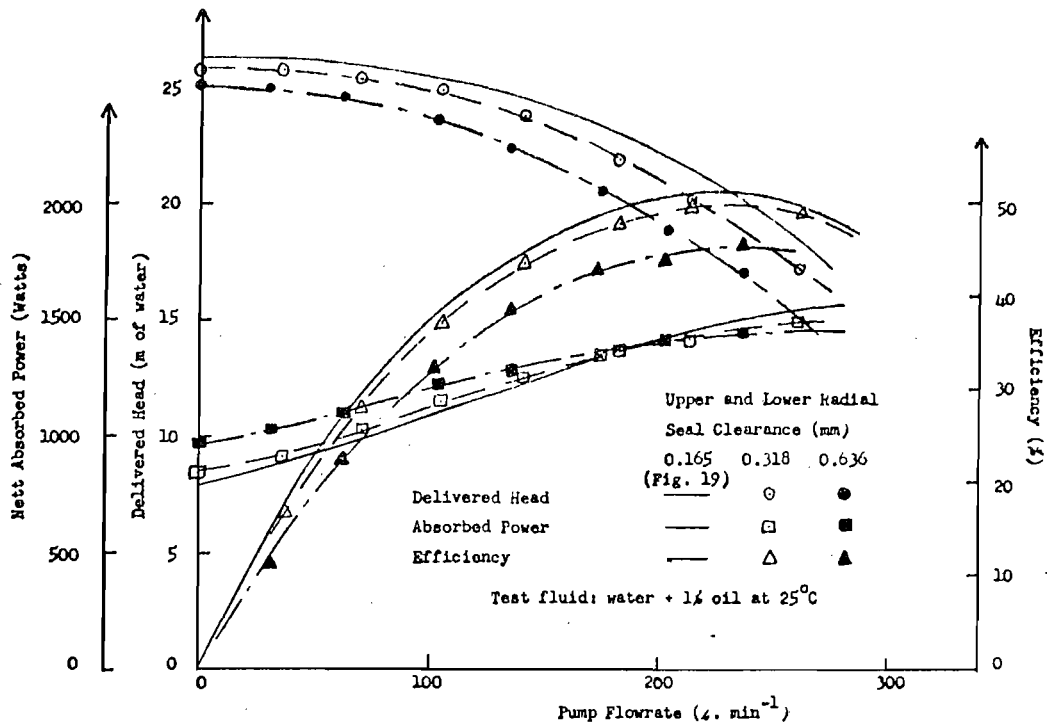
FIGURE 50.   EFFECT OF INCREASED SEAL CLEARANCE ON PUMP CHARACTERISTICS AT 3000 RPM IN COLD WATER.
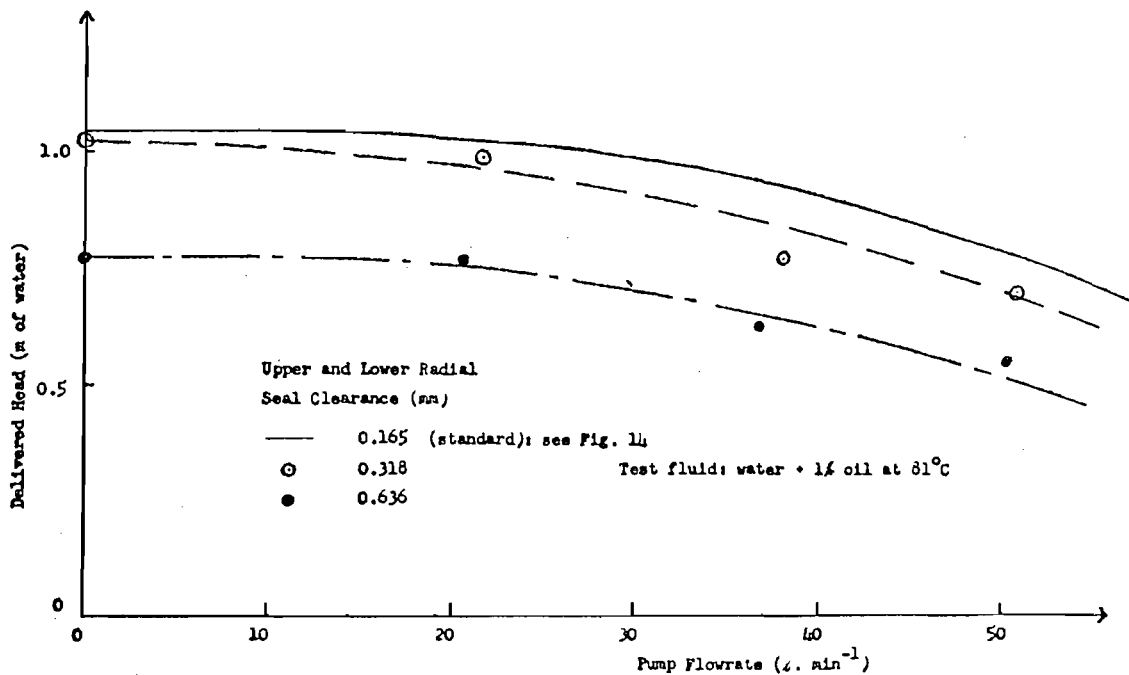
FIGURE 51.   EFFECT OF INCREASED SEAL CLEARANCE ON PUMP HEAD CHARACTERISTIC AT 600 RPM IN HOT WATER.
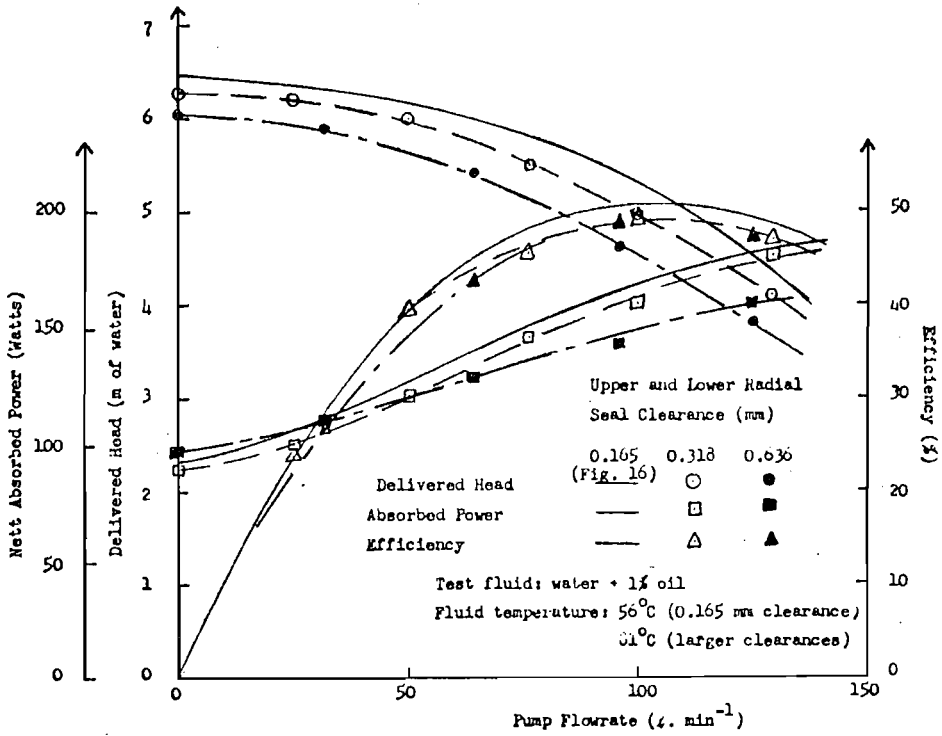
FIGURE 52. EFFECT OF INCREASED SEAL CLEARANCE ON PUMP CHARACTERISTICS AT 1500 RPM IN HOT WATER.
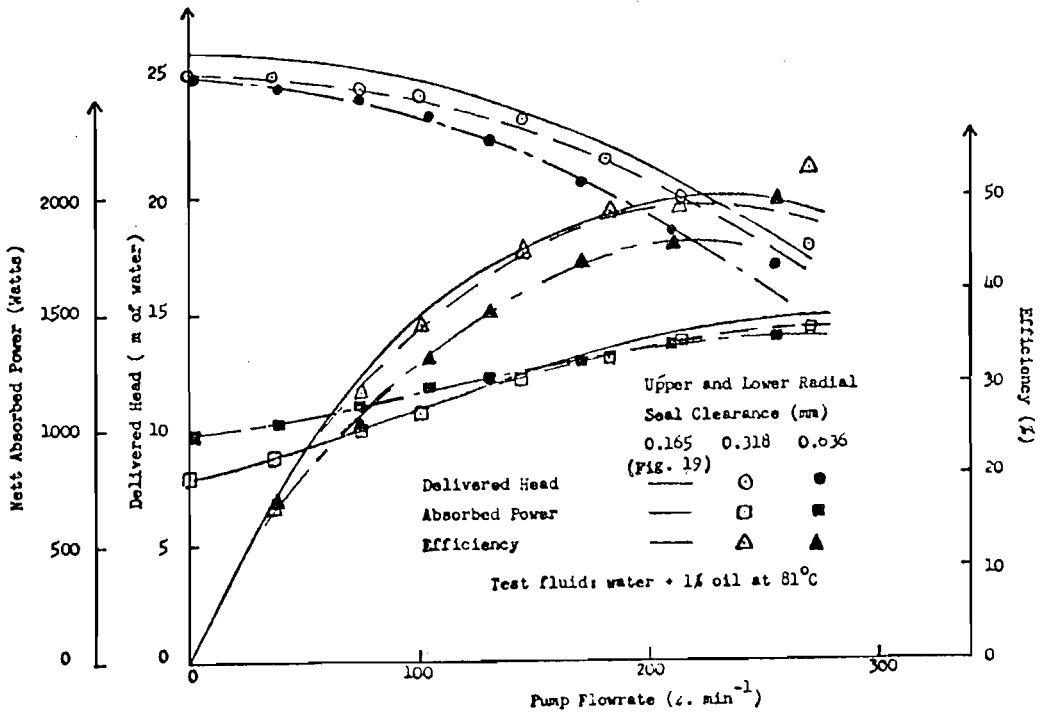
FIGURE 53. EFFECT OF INCREASED SEAL CLEARANCE ON PUMP CHARACTERISTICS AT 3000 RPM IN HOT WATER.

Figure 54 (top chart):

Head Coefficient $\psi \times 10^3$

100

50

0

Pump Speed (rpm) | Upper and Lower Radial Seal Clearance (mm)
0·318 | 0·636

600 | ▽ | ▼
1000 | ▢ | ◼
1500 | ◎ | ●
2000 | △ | ▲
3000 | + | ✕

0·318 mm

0·636 mm

——— Smoothed curve for standard seal clearance (0·165 mm) ; see Fig. 21

Test fluid: water + 1% oil at 25°C

Flow Coefficient $\phi \times 10^3$

0   1.0   2·0   3·0   4·0   5·0
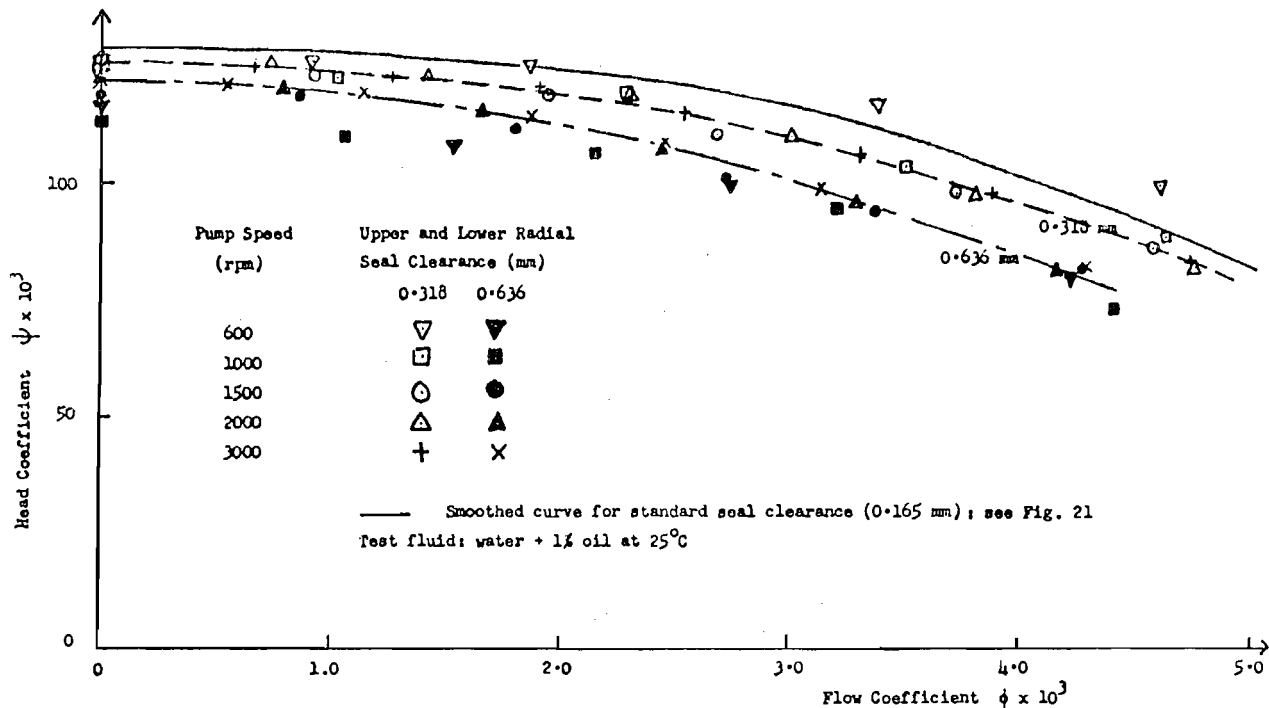
FIGURE 54.   EFFECT OF INCREASED SEAL CLEARANCE ON DIMENSIONLESS HEAD / FLOW CHARACTERISTIC IN COLD WATER.

Figure 55 (bottom chart):

Head Coefficient $\psi \times 10^3$

100

50

0

Pump Speed (rpm) | Upper and Lower Radial Seal Clearance (mm)
0·318 | 0·636

600 | ▽ | ▼
1500 | ◎ | ●
3000 | + | ✕

Test fluid: water + 1% oil at 81°C

——— Smoothed curve for standard seal clearance (0·165 mm) : see Fig. 23

Scatter band for 0·318 mm seal clearance

Scatter band for 0·636 mm seal clearance

Flow Coefficient $\phi \times 10^3$

0   1·0   2·0   3·0   4·0   5·0
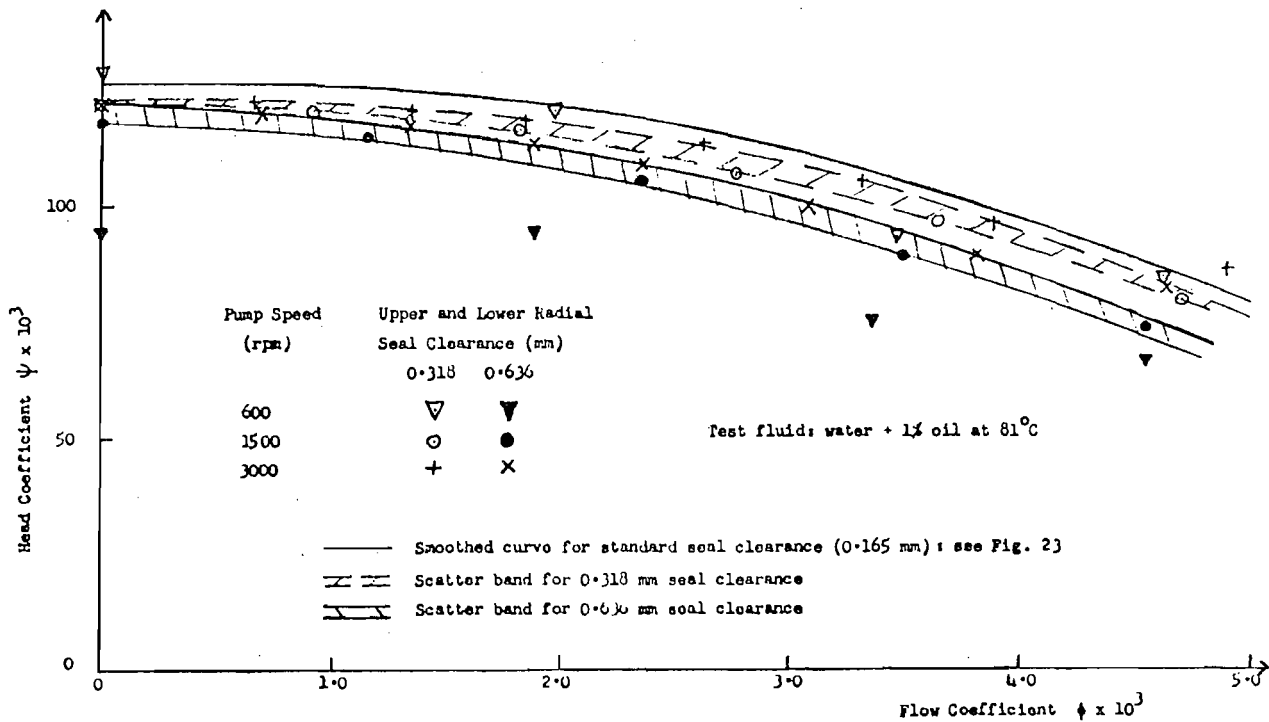
FIGURE 55.   EFFECT OF INCREASED SEAL CLEARANCE ON DIMENSIONLESS HEAD / FLOW CHARACTERISTIC IN HOT WATER.
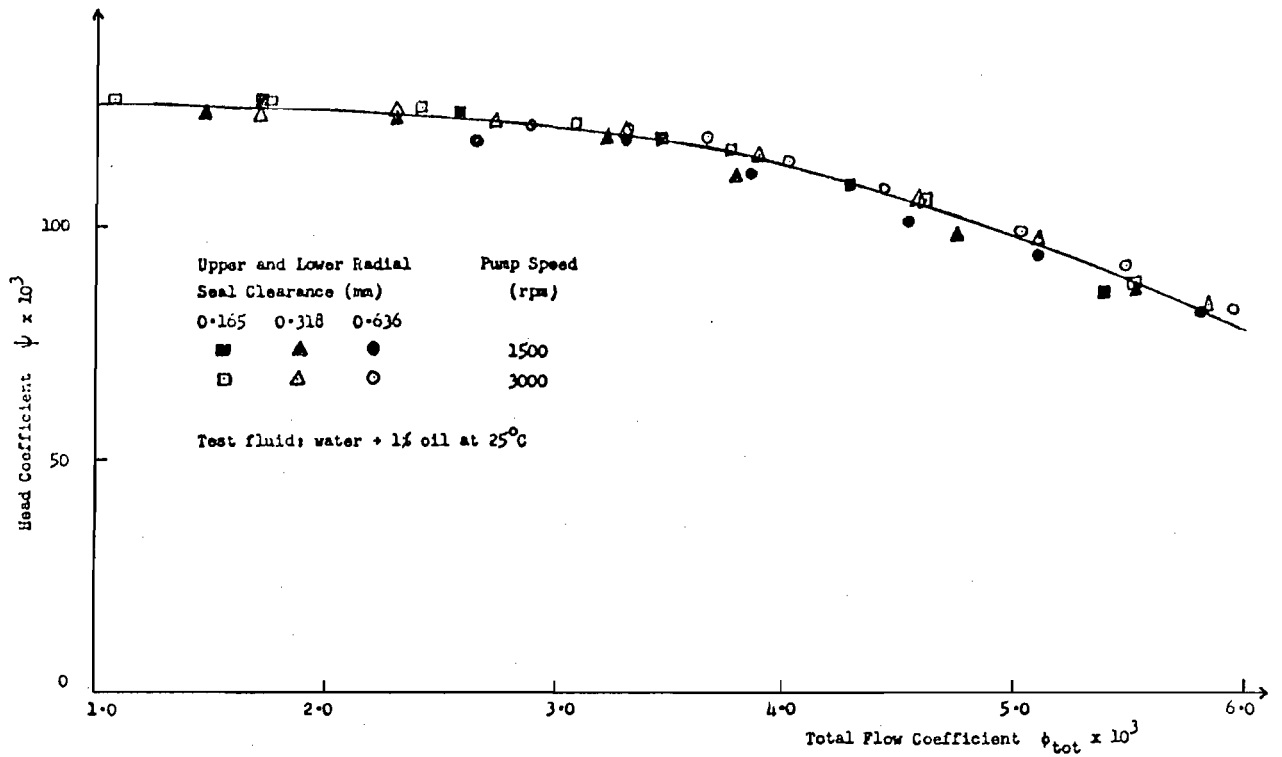
FIGURE 56.   DIMENSIONLESS HEAD / TOTAL FLOW CHARACTERISTIC IN COLD WATER.
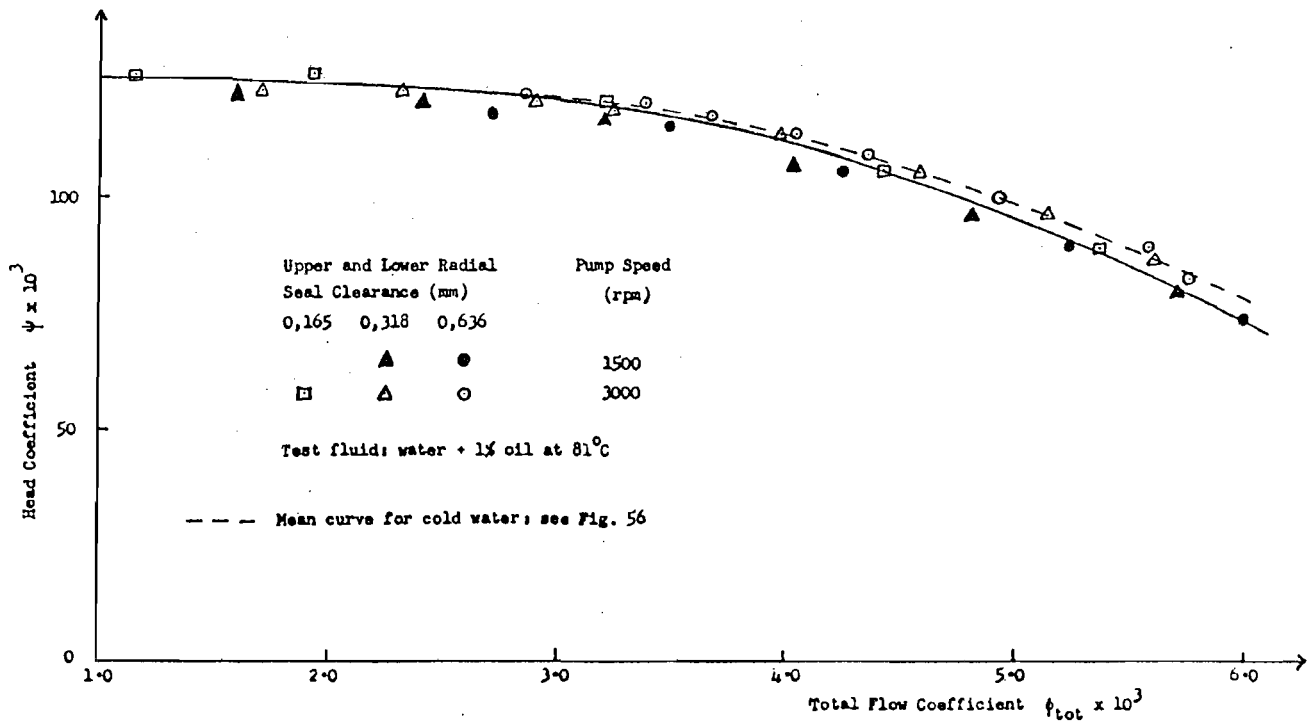
FIGURE 57.   DIMENSIONLESS HEAD / TOTAL FLOW CHARACTERISTIC IN HOT WATER.
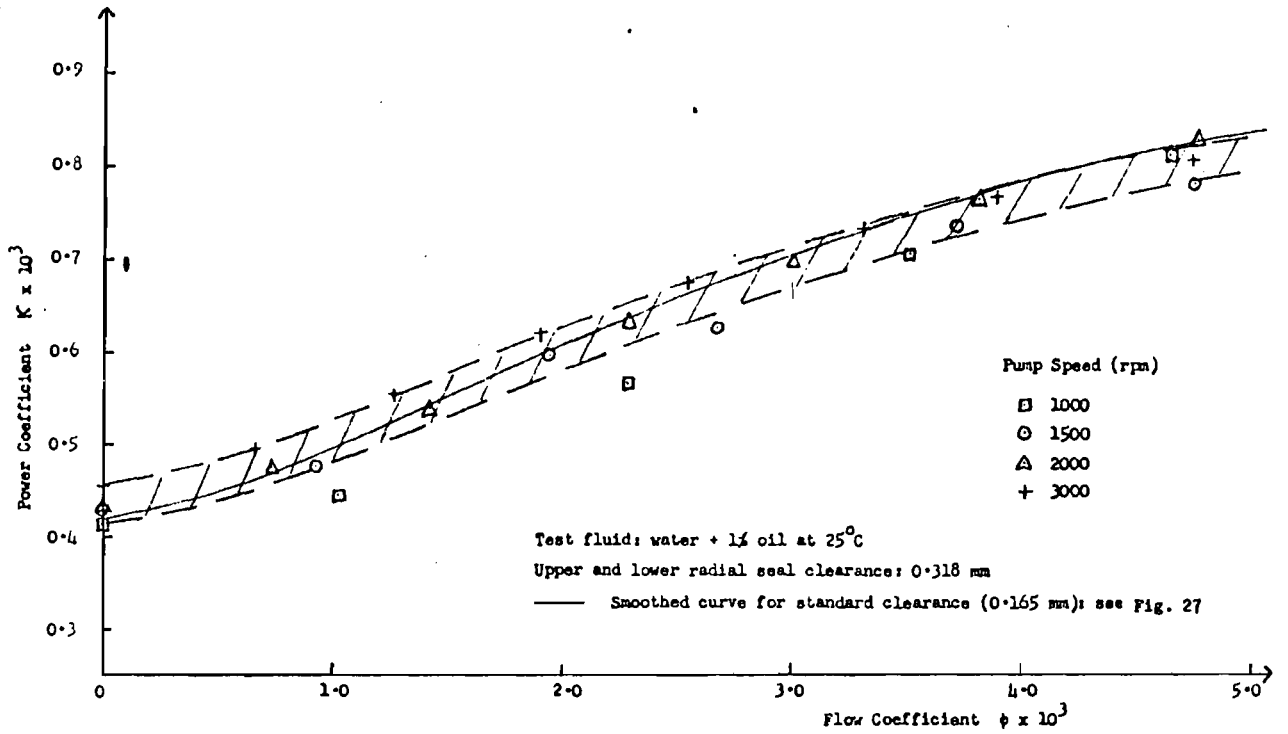
FIGURE 58.   EFFECT OF INCREASED SEAL CLEARANCE ON DIMENSIONLESS POWER / FLOW CHARACTERISTIC IN COLD WATER (0·318 MM CLEARANCE).
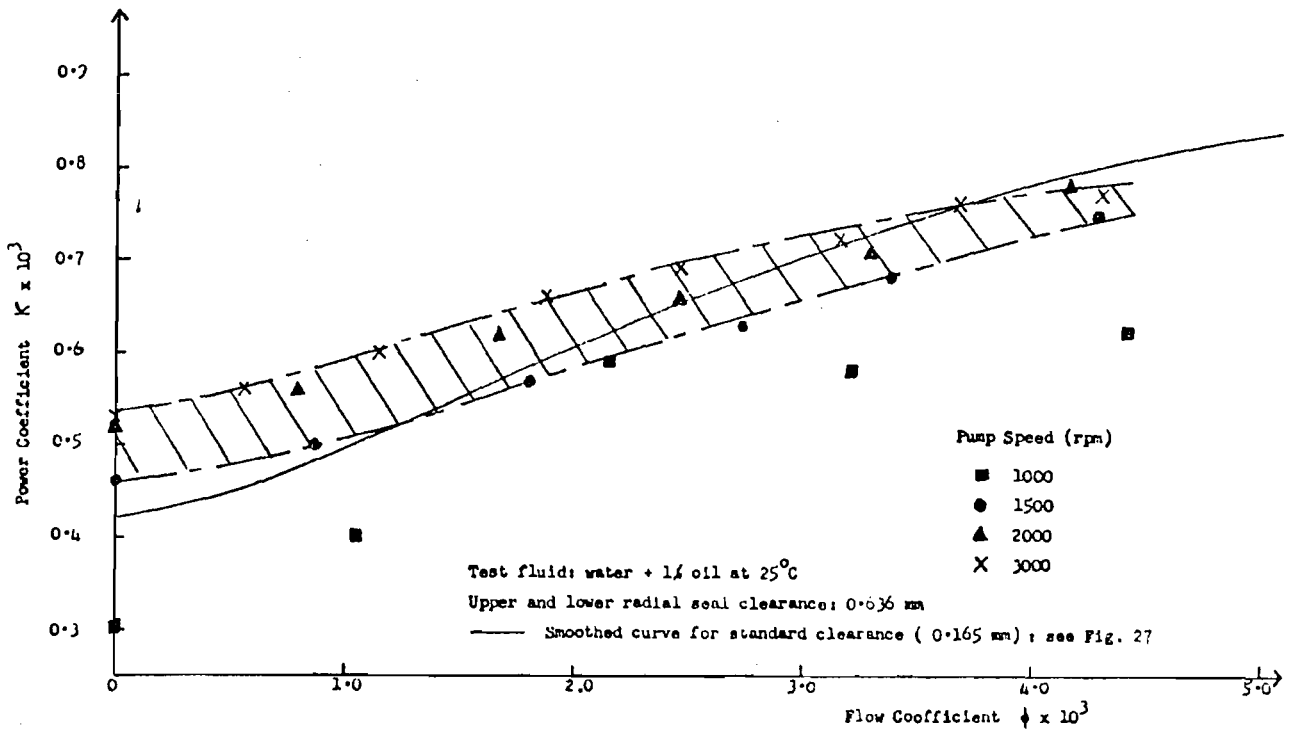
FIGURE 59.   EFFECT OF INCREASED SEAL CLEARANCE ON DIMENSIONLESS POWER / FLOW CHARACTERISTIC IN COLD WATER (0·636 MM CLEARANCE).
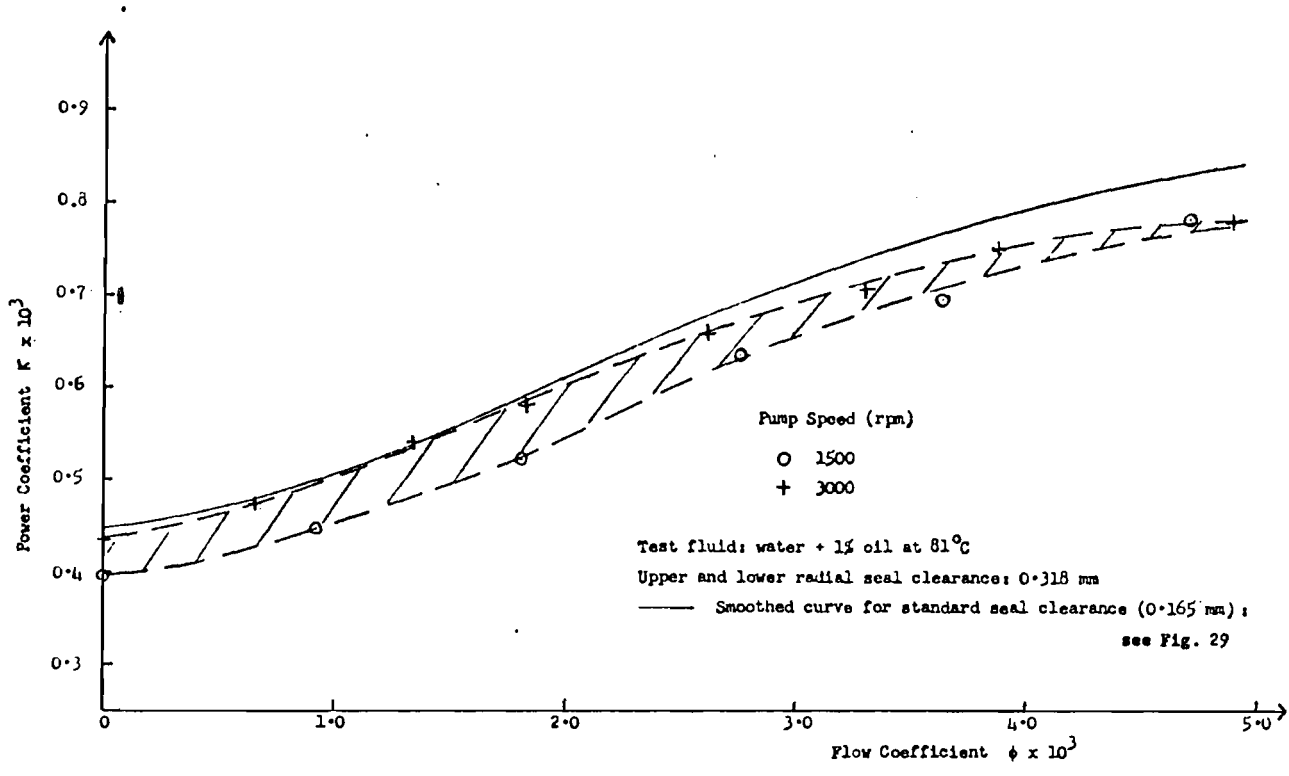
FIGURE 60.   EFFECT OF INCREASED SEAL CLEARANCE ON DIMENSIONLESS POWER / FLOW CHARACTERISTIC IN HOT WATER (0·318 MM CLEARANCE).
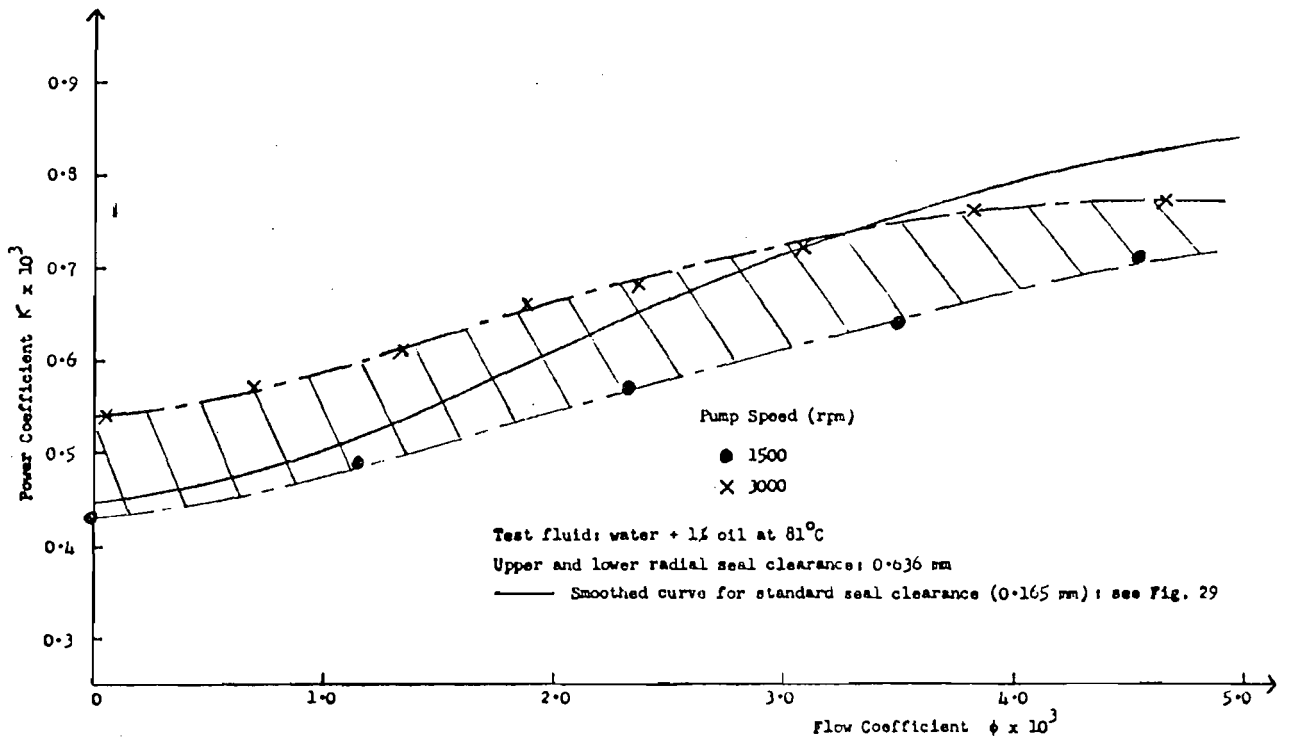
FIGURE 61.   EFFECT OF INCREASED SEAL CLEARANCE ON DIMENSIONLESS POWER / FLOW CHARACTERISTIC IN HOT WATER (0·636 MM CLEARANCE).
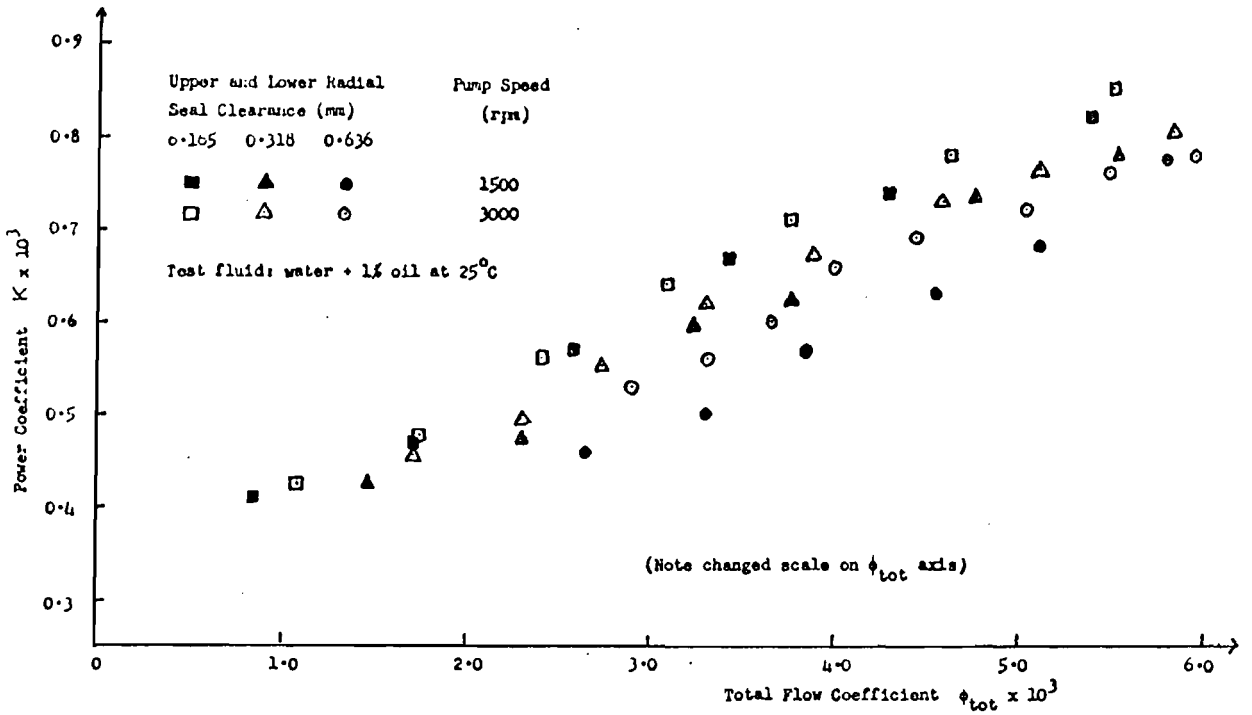
FIGURE 62.　DIMENSIONLESS POWER / TOTAL FLOW CHARACTERISTIC IN COLD WATER.
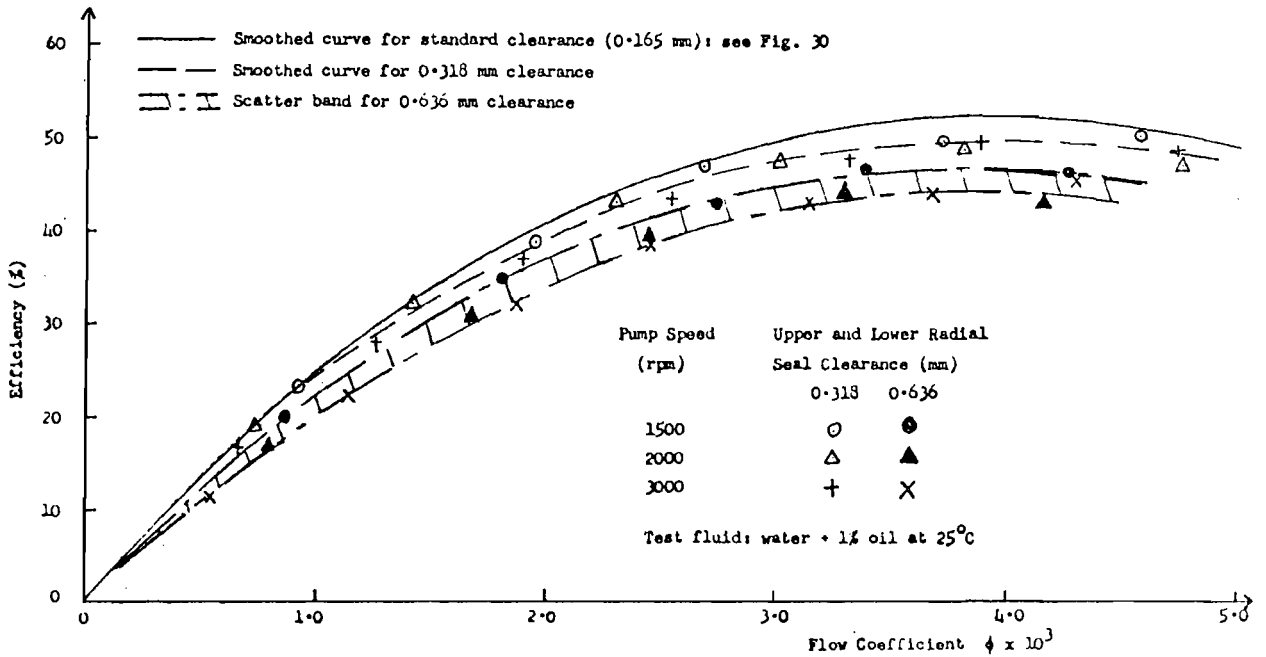
FIGURE 63.　EFFECT OF INCREASED SEAL CLEARANCE ON DIMENSIONLESS EFFICIENCY / FLOW CHARACTERISTIC IN COLD WATER
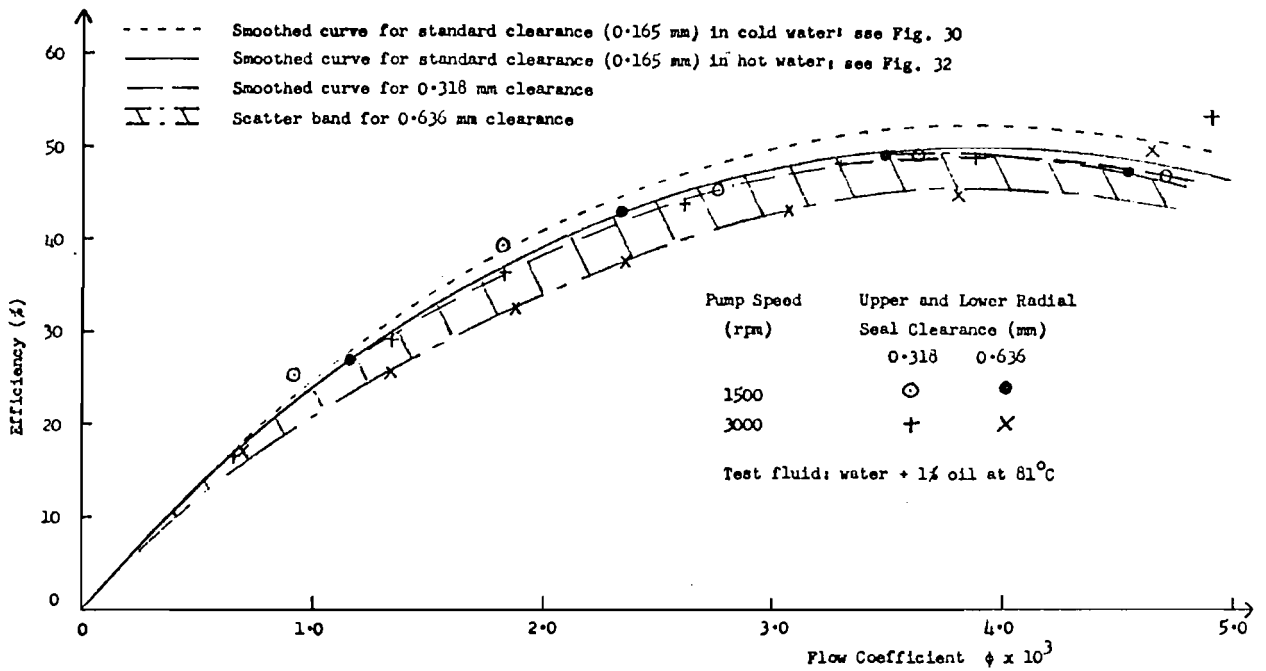
FIGURE 64. EFFECT OF INCREASED SEAL CLEARANCE ON DIMENSIONLESS EFFICIENCY / FLOW CHARACTERISTIC IN HOT WATER.
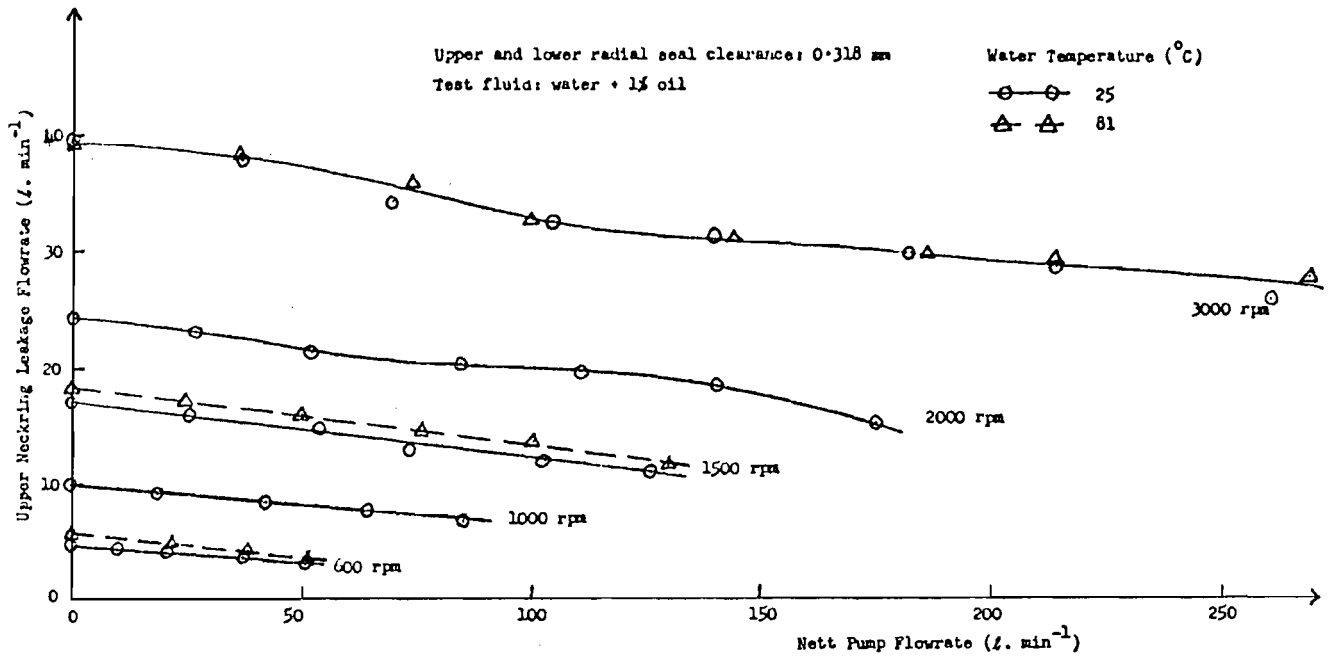
FIGURE 65. UPPER NECKRING LEAKAGE AS A FUNCTION OF NETT PUMP FLOWRATE IN WATER (0.318 MM SEAL CLEARANCE).
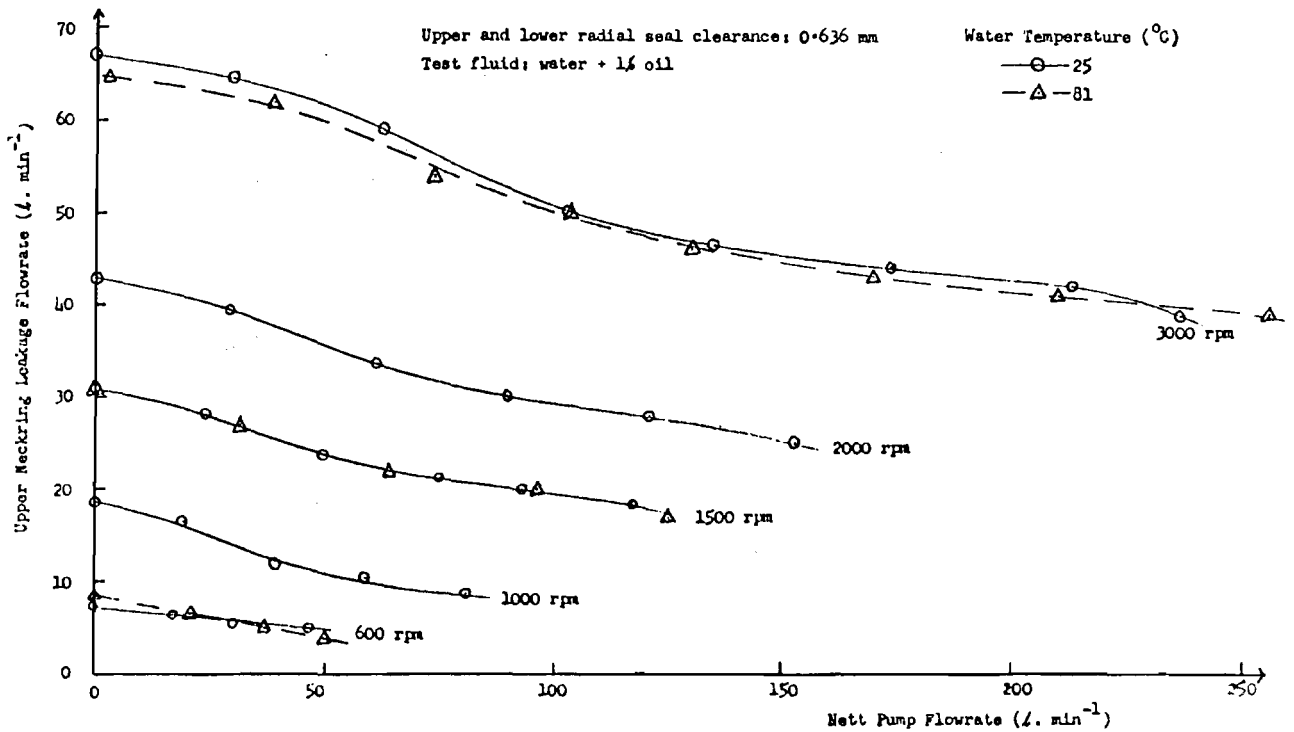
FIGURE 66. UPPER NECKRING LEAKAGE AS A FUNCTION OF NETT PUMP FLOWRATE IN WATER (0.636 MM SEAL CLEARANCE).
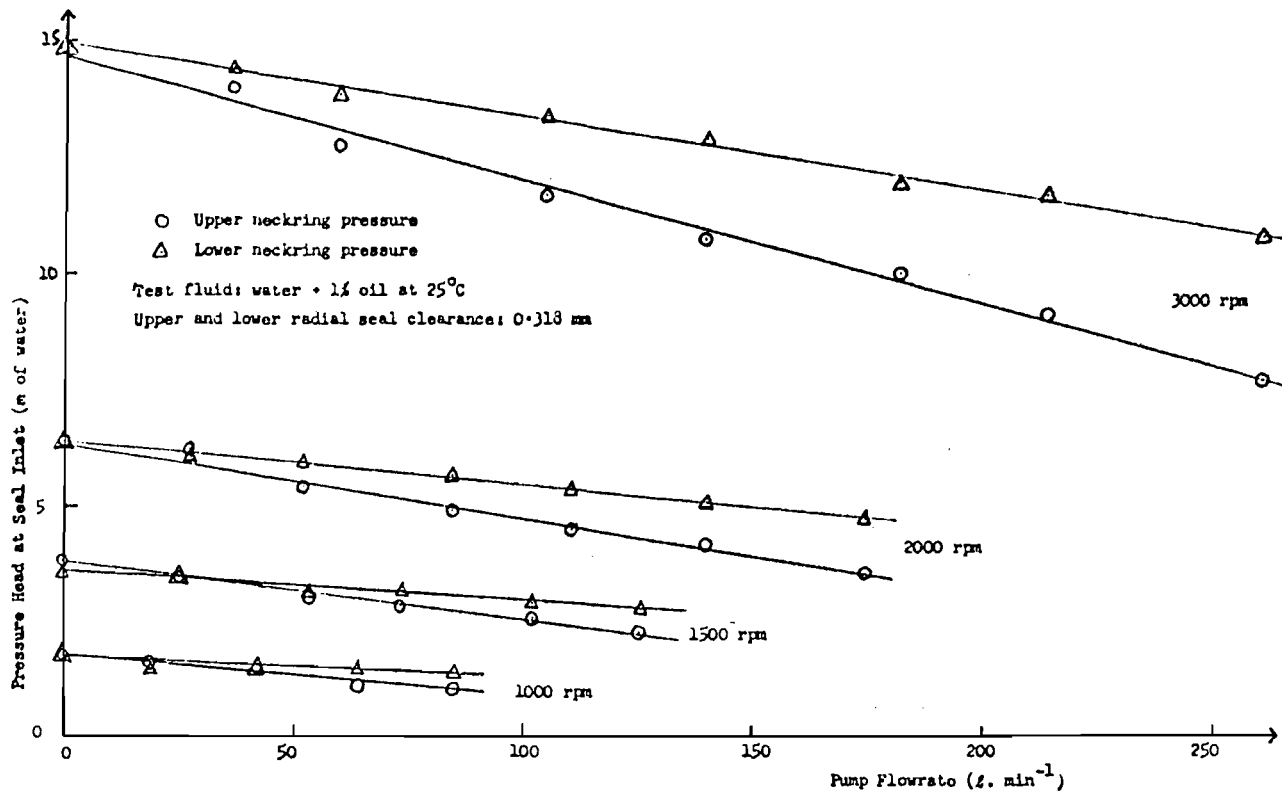
FIGURE 67. SEAL INLET PRESSURE AS A FUNCTION OF PUMP FLOWRATE IN COLD WATER (0·318 MM SEAL CLEARANCE).
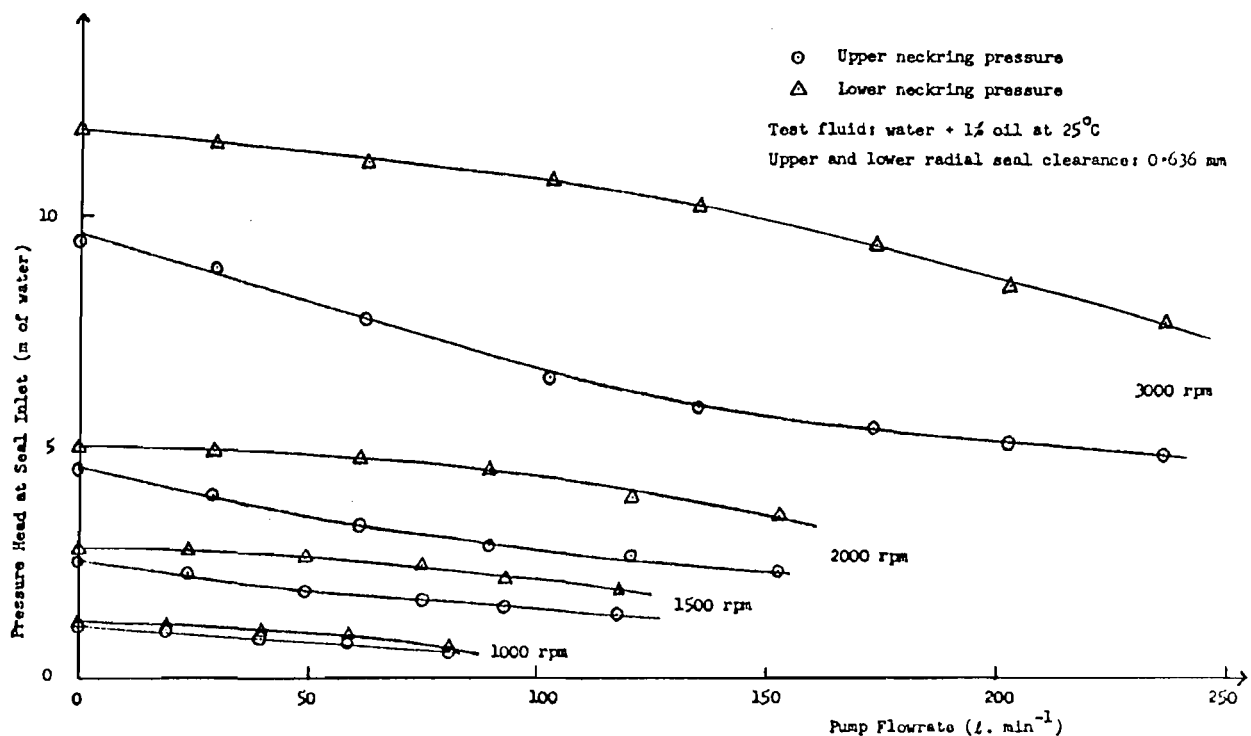
FIGURE 68. SEAL INLET PRESSURE AS A FUNCTION OF PUMP FLOWRATE IN COLD WATER (0·636 MM SEAL CLEARANCE).
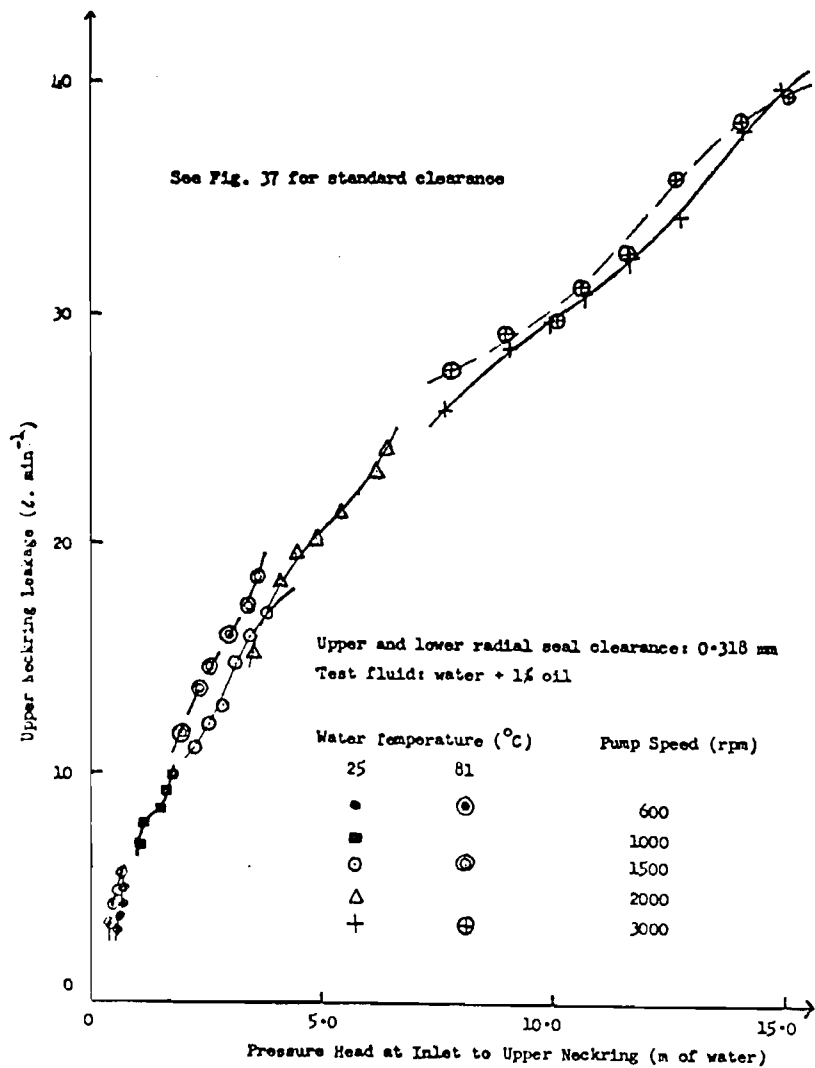
FIGURE 69. VARIATION IN LEAKAGE RATE WITH DIFFERENTIAL PRESSURE ACROSS UPPER NECKRING
(0·318 MM SEAL CLEARANCE).
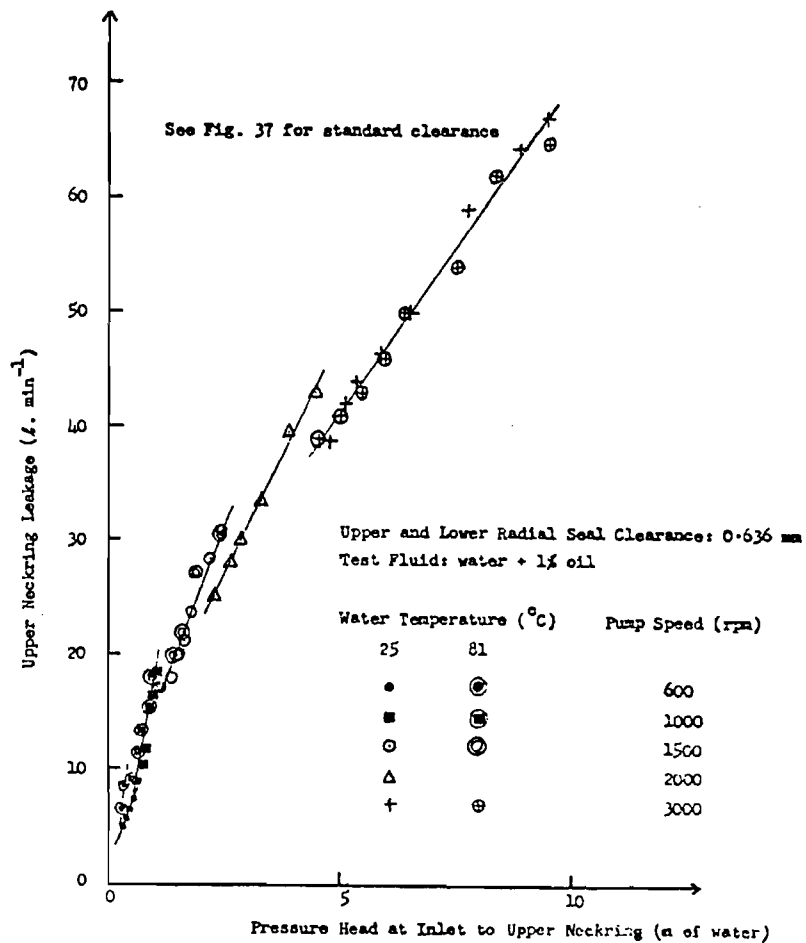
FIGURE 70. VARIATION IN LEAKAGE RATE WITH DIFFERENTIAL PRESSURE ACROSS UPPER NECKRING
(0·636 MM SEAL CLEARANCE)
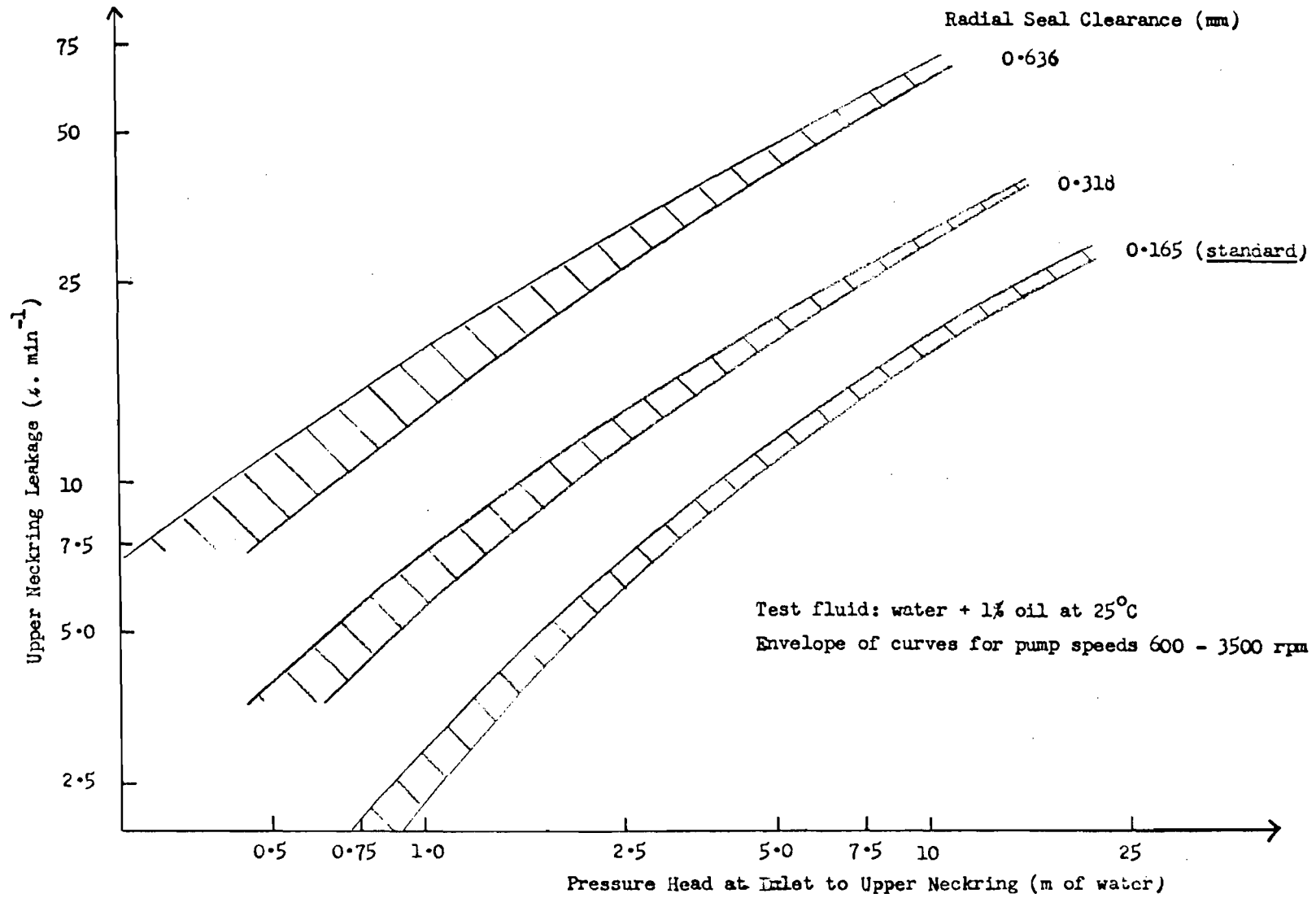
FIGURE 71. EFFECT OF CLEARANCE ON NECKRING LEAKAGE.
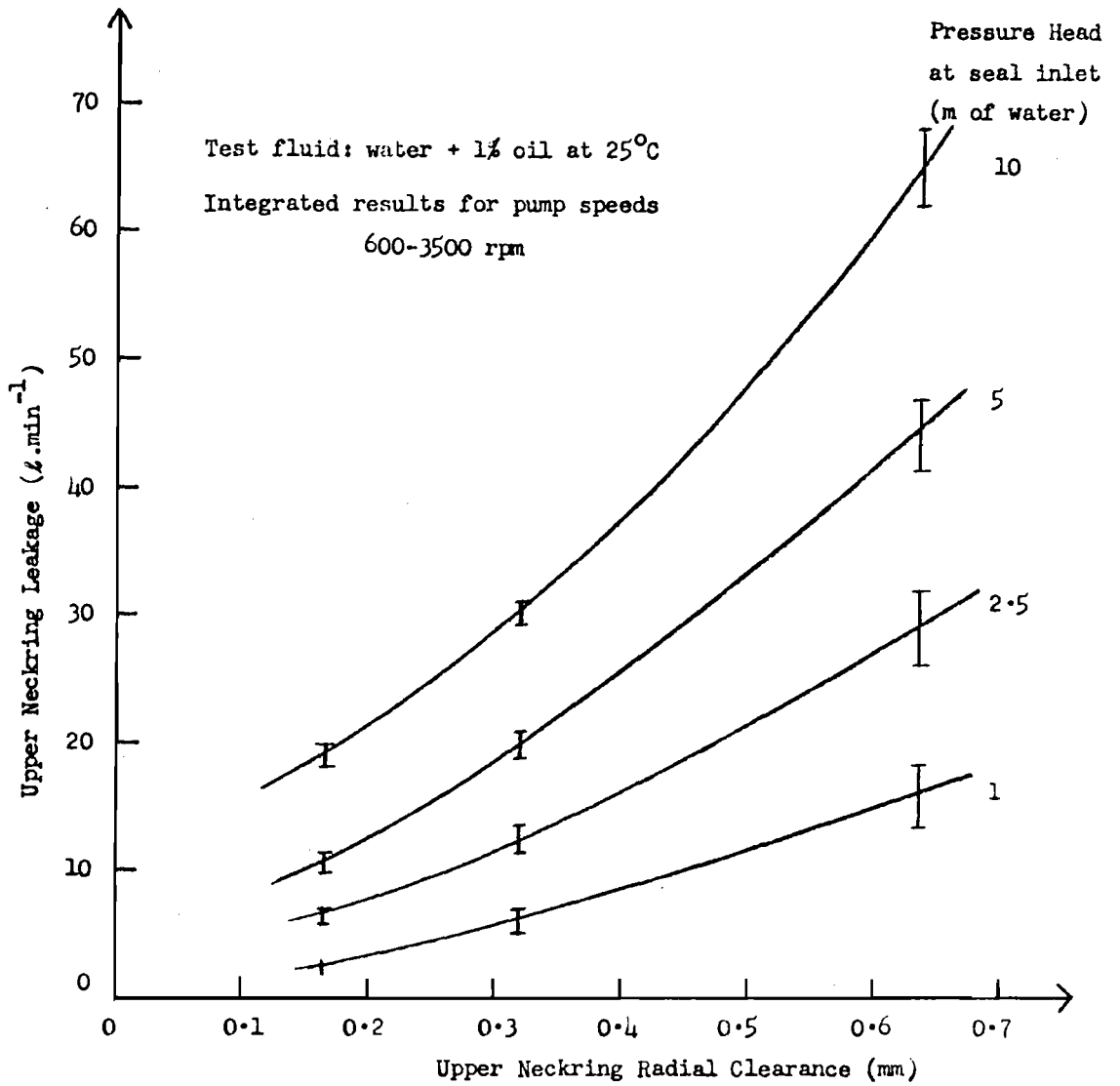
FIGURE 72. VARIATION OF LEAKAGE WITH SEAL CLEARANCE AND PRESSURE.
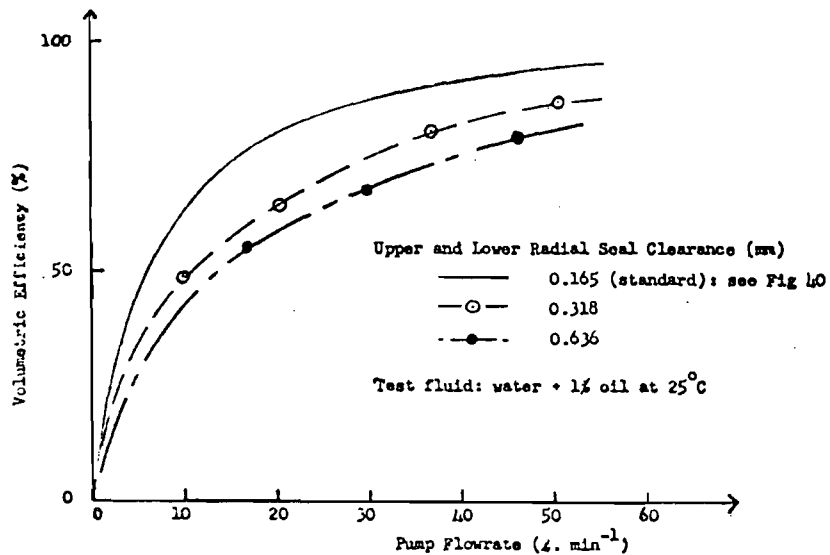
FIGURE 73. EFFECT OF INCREASED SEAL CLEARANCE ON VOLUMETRIC EFFICIENCY
AT 600 RPM IN COLD WATER.
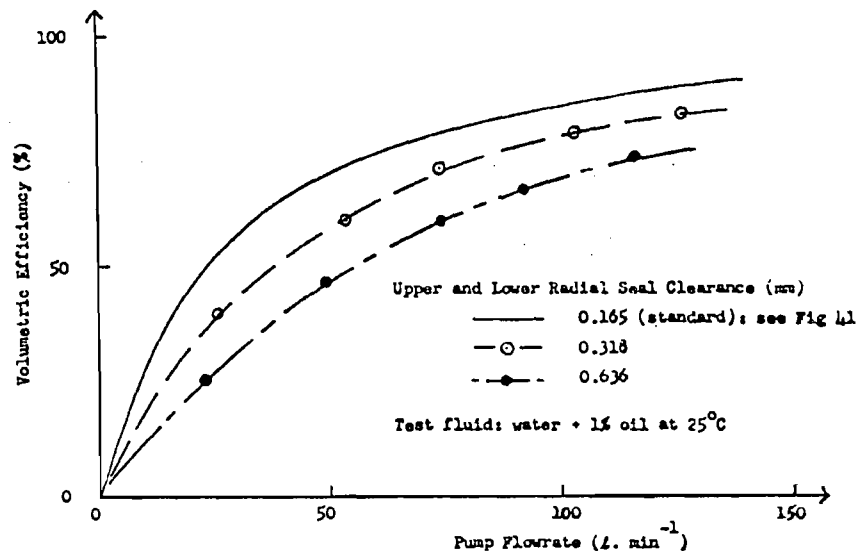
FIGURE 75. EFFECT OF INCREASED SEAL CLEARANCE ON VOLUMETRIC EFFICIENCY
AT 1500 RPM IN COLD WATER.
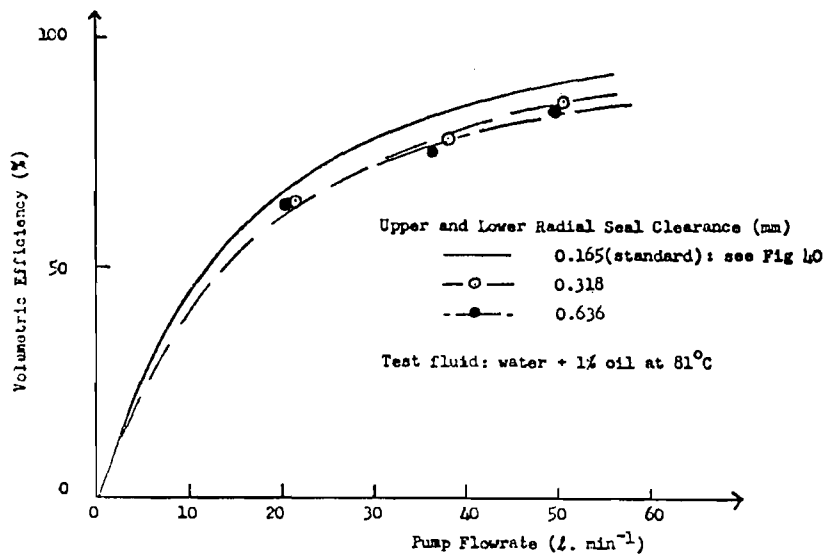
FIGURE 74. EFFECT OF INCREASED SEAL CLEARANCE ON VOLUMETRIC EFFICIENCY
AT 600 RPM IN HOT WATER.
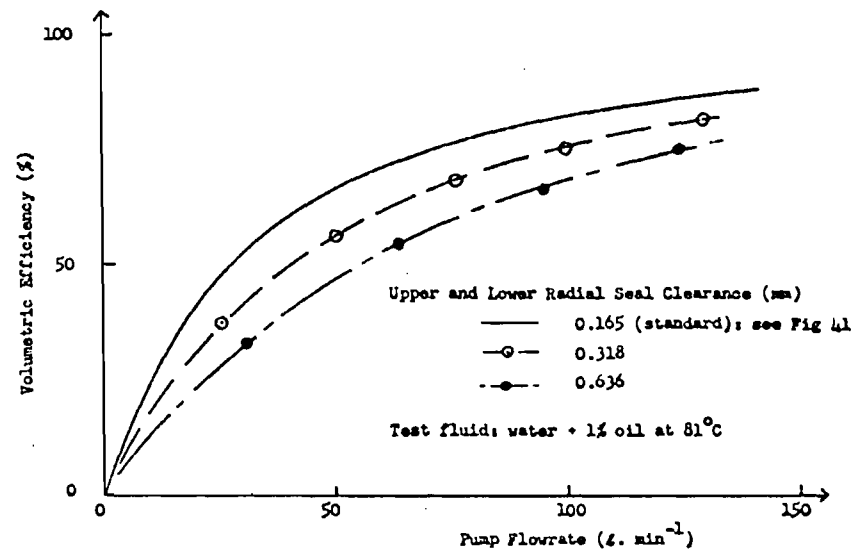
FIGURE 76. EFFECT OF INCREASED SEAL CLEARANCE ON VOLUMETRIC EFFICIENCY
AT 1500 RPM IN HOT WATER.
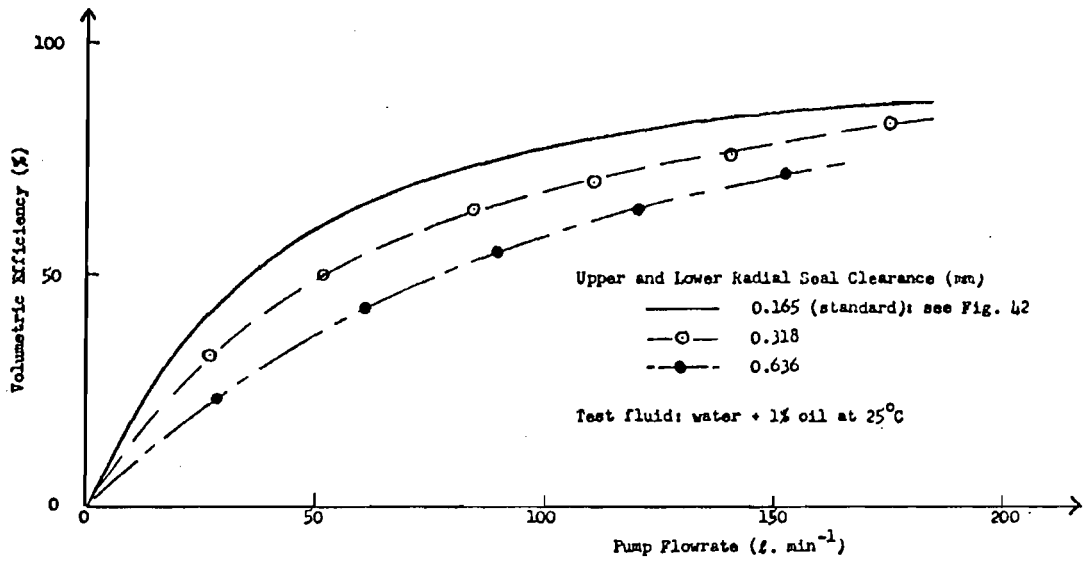
FIGURE 77. EFFECT OF INCREASED SEAL CLEARANCE ON VOLUMETRIC EFFICIENCY AT 2000 RPM IN COLD WATER.
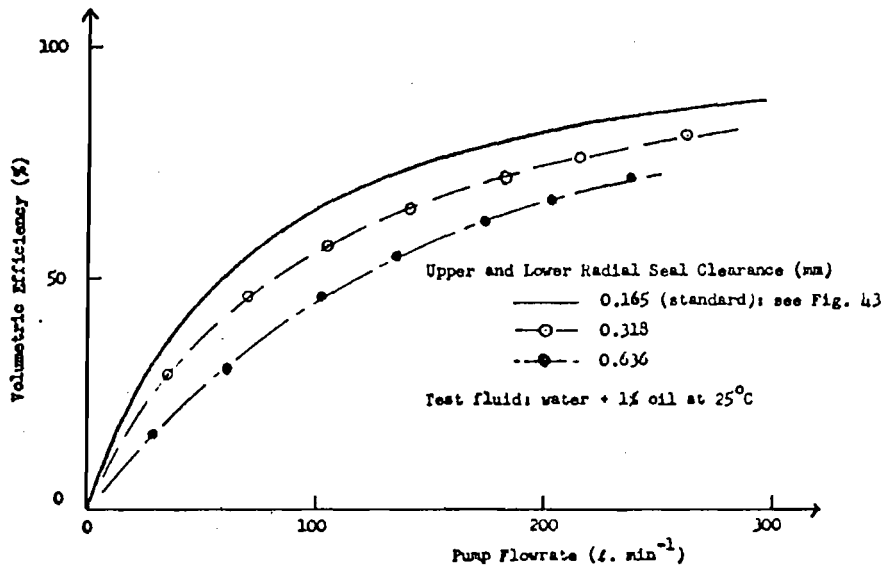
FIGURE 78. EFFECT OF INCREASED SEAL CLEARANCE ON VOLUMETRIC EFFICIENCY AT 3000 RPM IN COLD WATER.
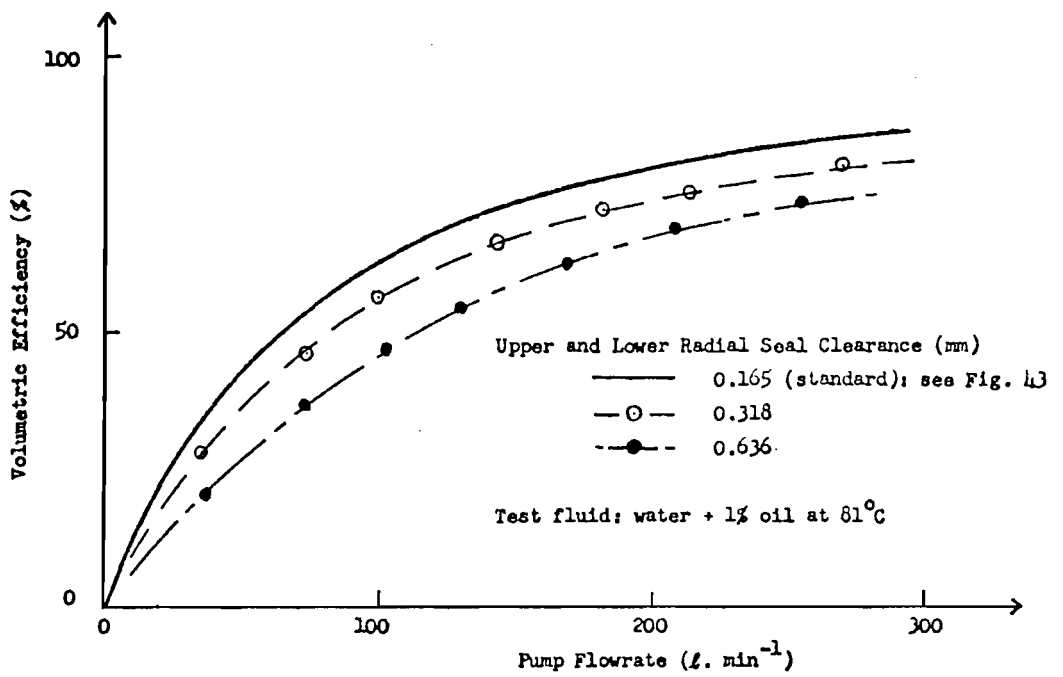
FIGURE 79.   EFFECT OF INCREASED SEAL CLEARANCE ON VOLUMETRIC EFFICIENCY AT 3000 RPM IN HOT WATER.
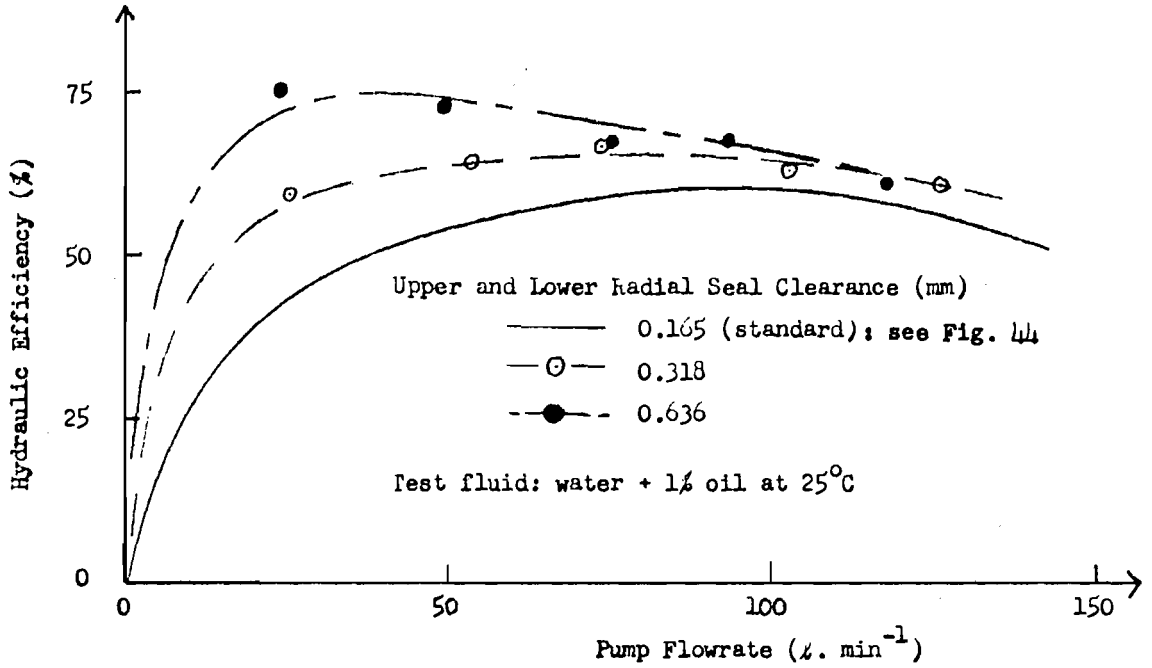
FIGURE 80. EFFECT OF INCREASED SEAL CLEARANCE ON HYDRAULIC EFFICIENCY
AT 1500 RPM IN COLD WATER.
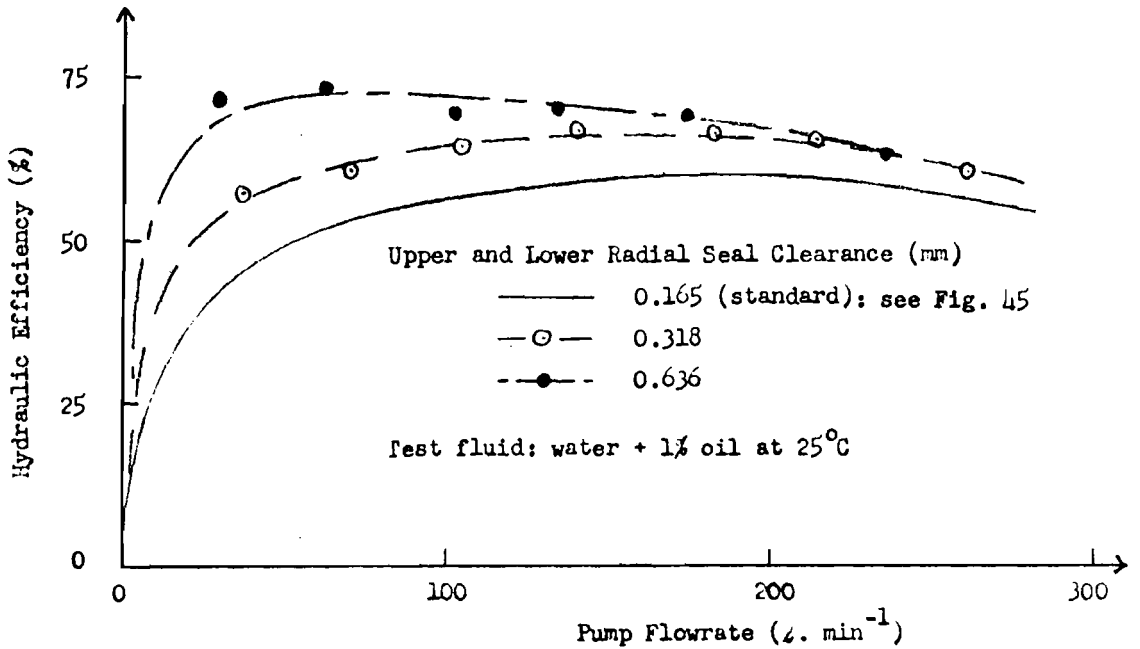
FIGURE 81. EFFECT OF INCREASED SEAL CLEARANCE ON HYDRAULIC EFFICIENCY
AT 3000 RPM IN COLD WATER.
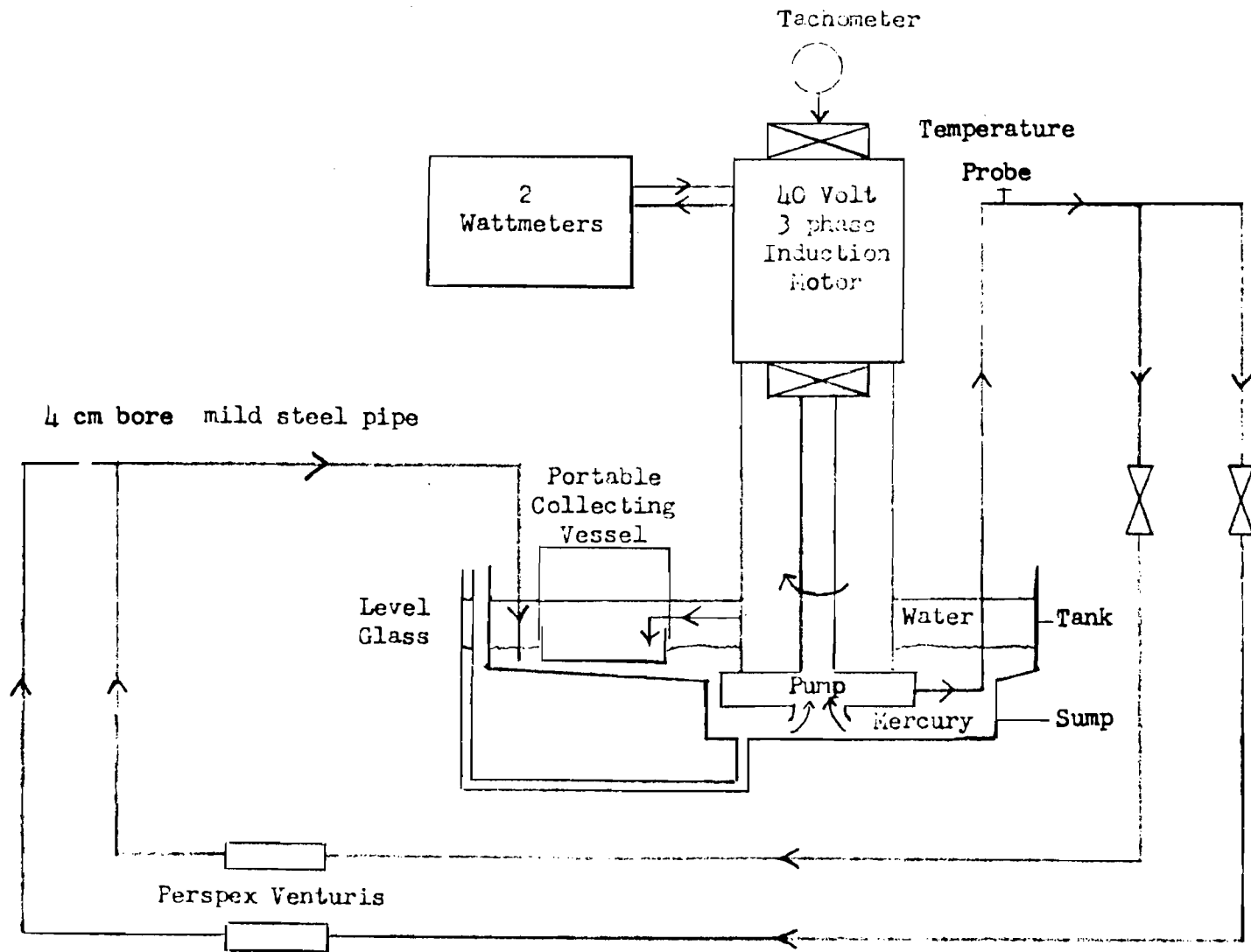
FIGURE 82. MERCURY TEST RIG.
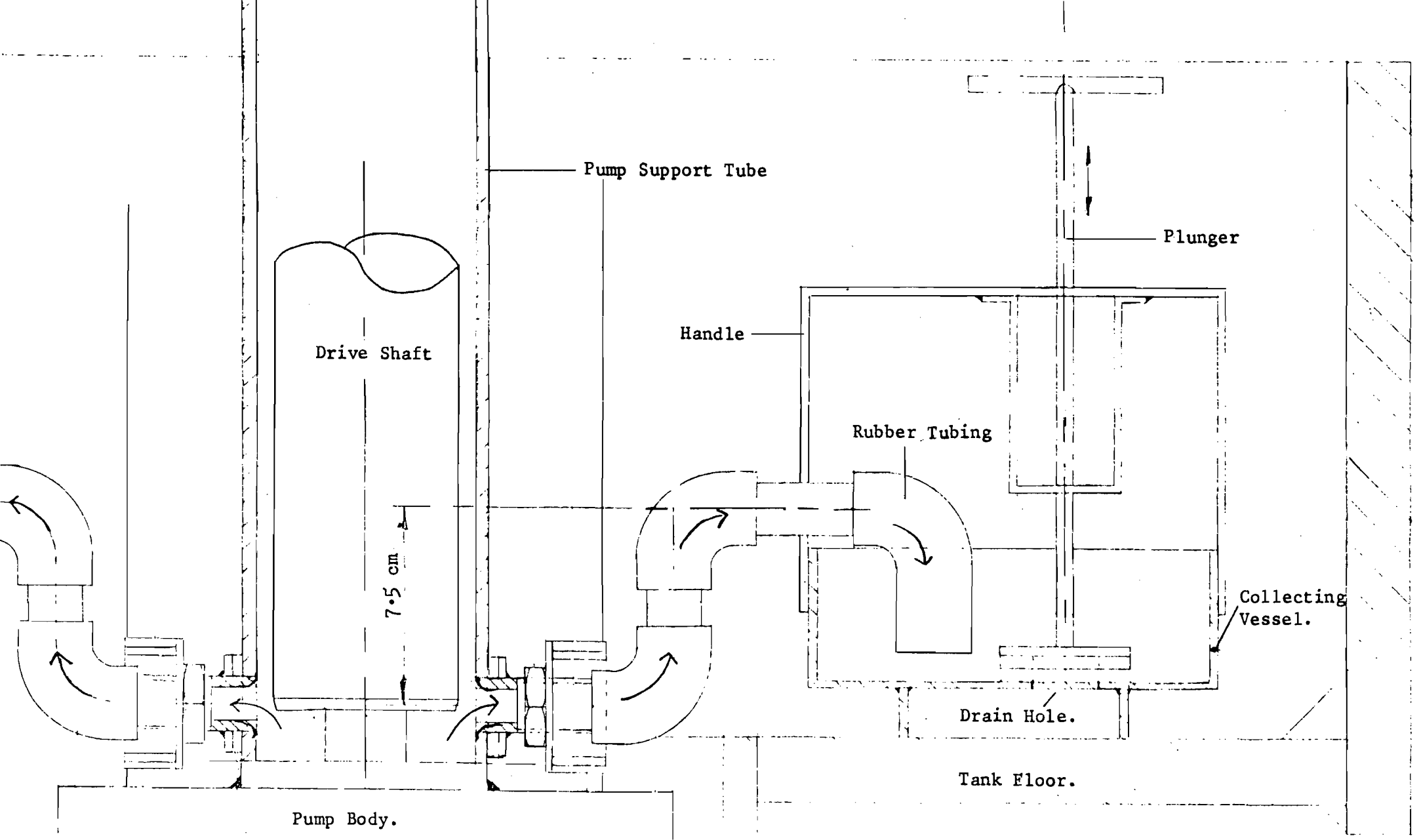
FIGURE 83.   DIAGRAM OF ARRANGEMENT FOR UPPER NECKRING LEAKAGE MEASUREMENT ON MERCURY TEST RIG.

Test fluid: clean mercury

Nominal pump speed: 1450 rpm ($\pm$ 1%)

Standard seal clearance

Mercury Temperature

▽	20°C	Trials on modified O.L.R.
▼	55°C	20.6.78
+	40°C	Increasing flowrate
×	40°C	Decreasing flowrate

Trials on original O.L.R. 11.5.77

⊙ Unknown   Data from chlorine plant maintenance manual.
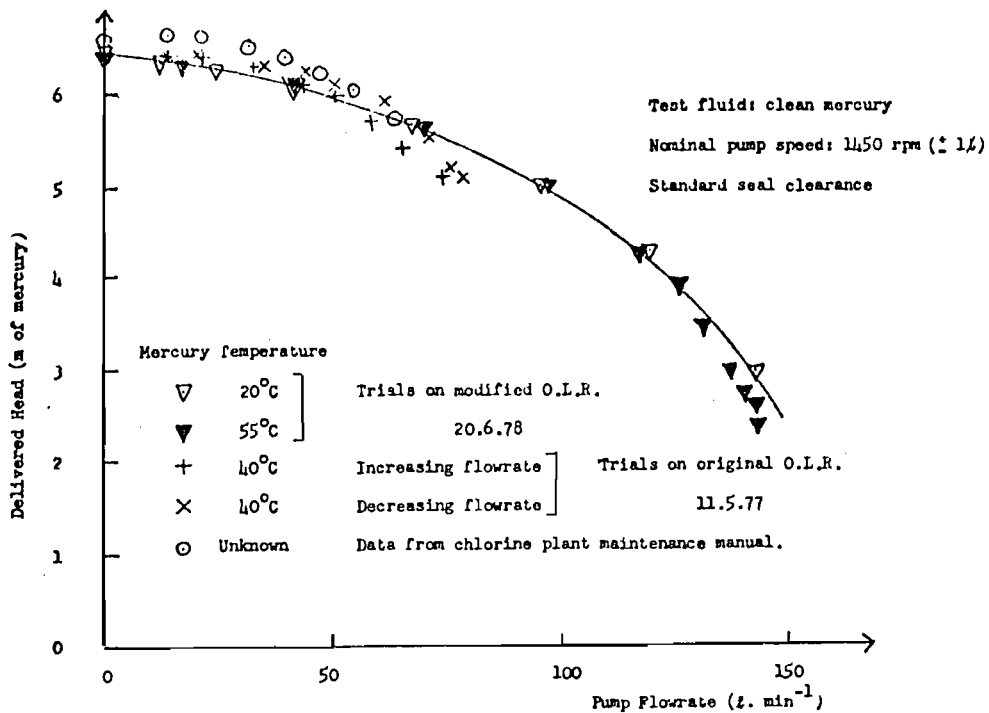
FIGURE 84.   PUMP HEAD CHARACTERISTIC AT 1450 RPM IN MERCURY.

Test fluid: clean mercury

Nominal pump speed: 1450 rpm ($\pm$ 1%)

Standard seal clearance

Mercury Temperature

+   ~ 20°C   Trials on modified O.L.R., 30.6.78

⊙   Unknown   Data from chlorine plant maintenance manual

▣   Unknown   As above, with correction for motor efficiency
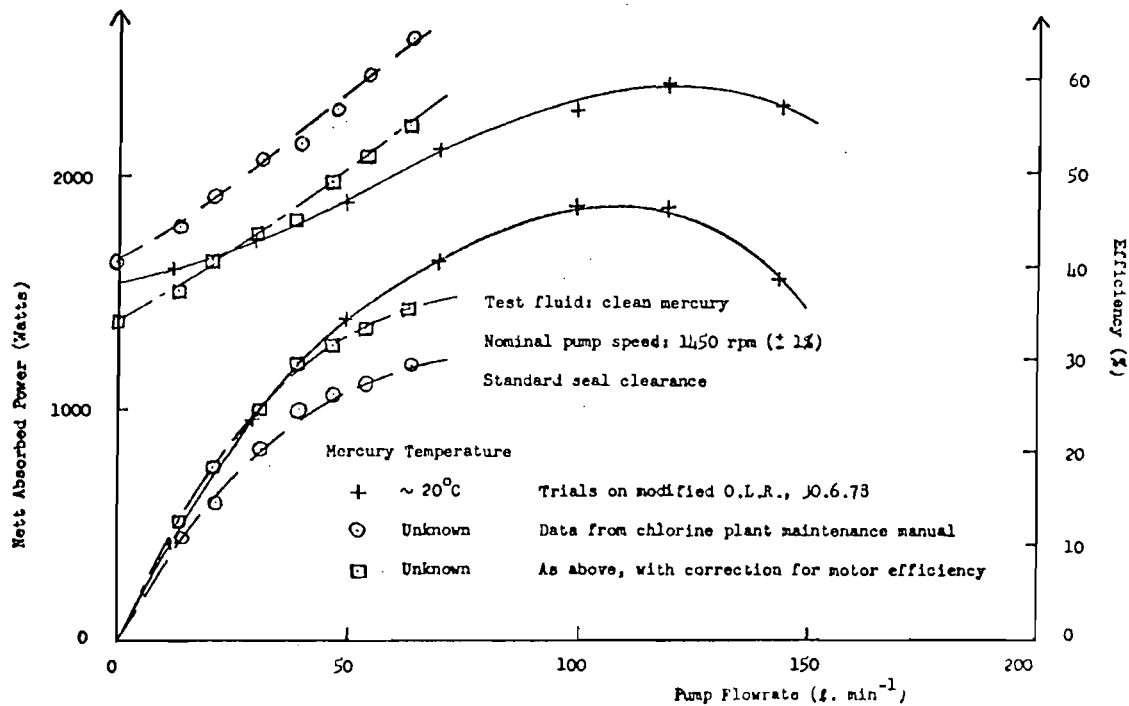
FIGURE 85.   PUMP ABSORBED POWER AND EFFICIENCY CHARACTERISTICS AT 1450 RPM IN MERCURY.
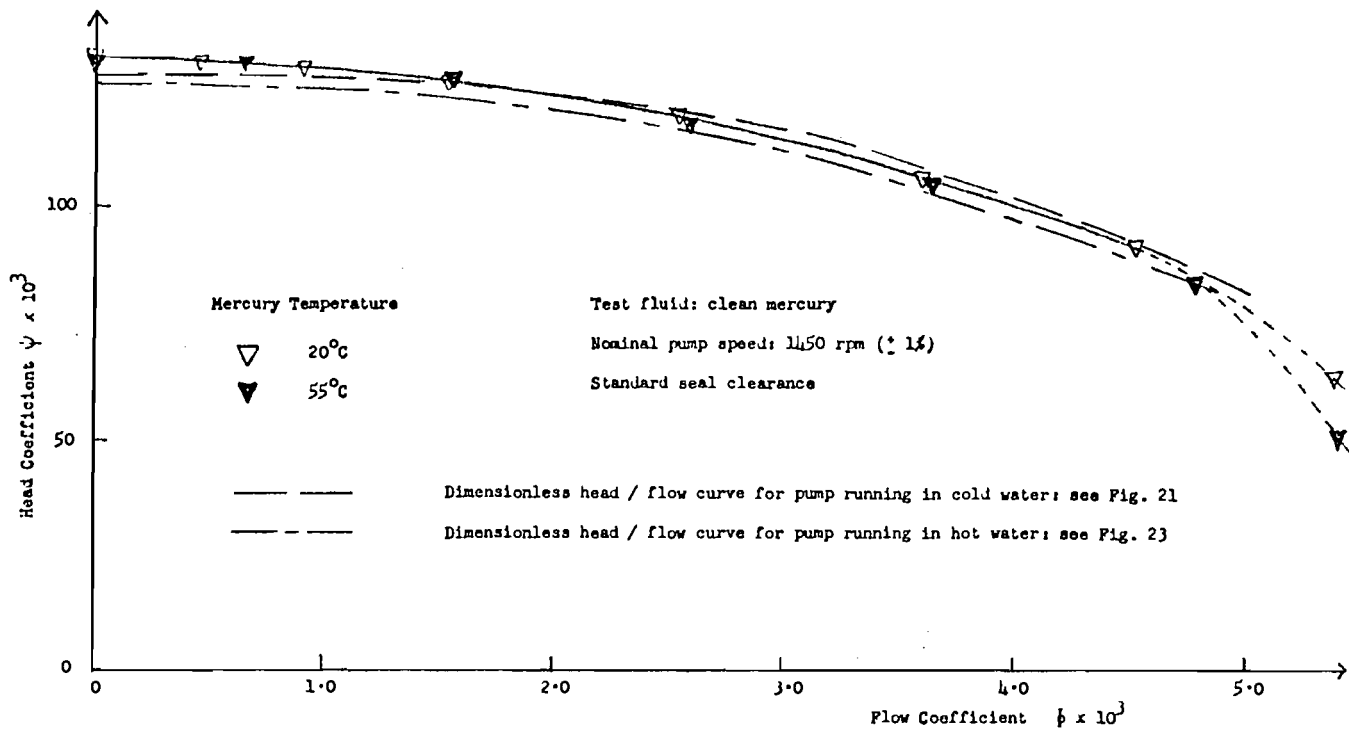
FIGURE 86.   DIMENSIONLESS HEAD / FLOW CHARACTERISTIC IN MERCURY.
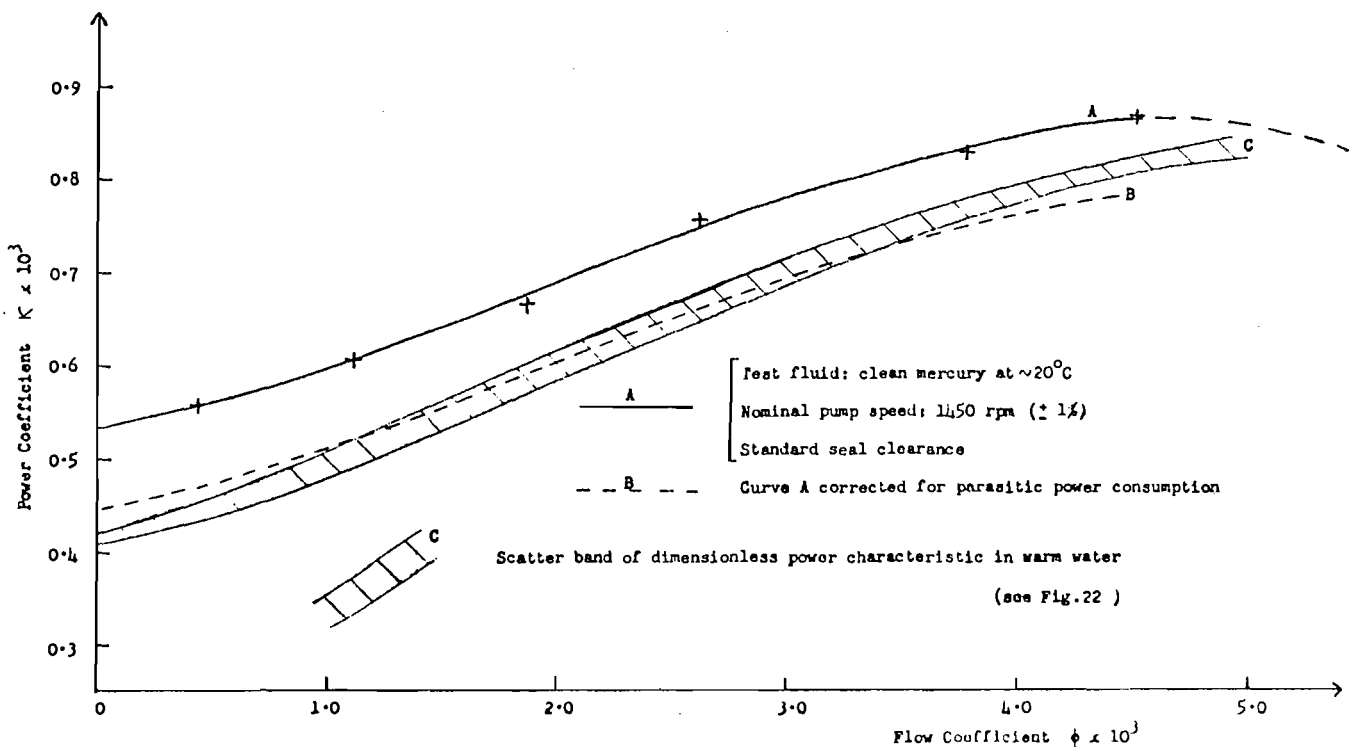
FIGURE 87.   DIMENSIONLESS POWER / FLOW CHARACTERISTIC IN MERCURY
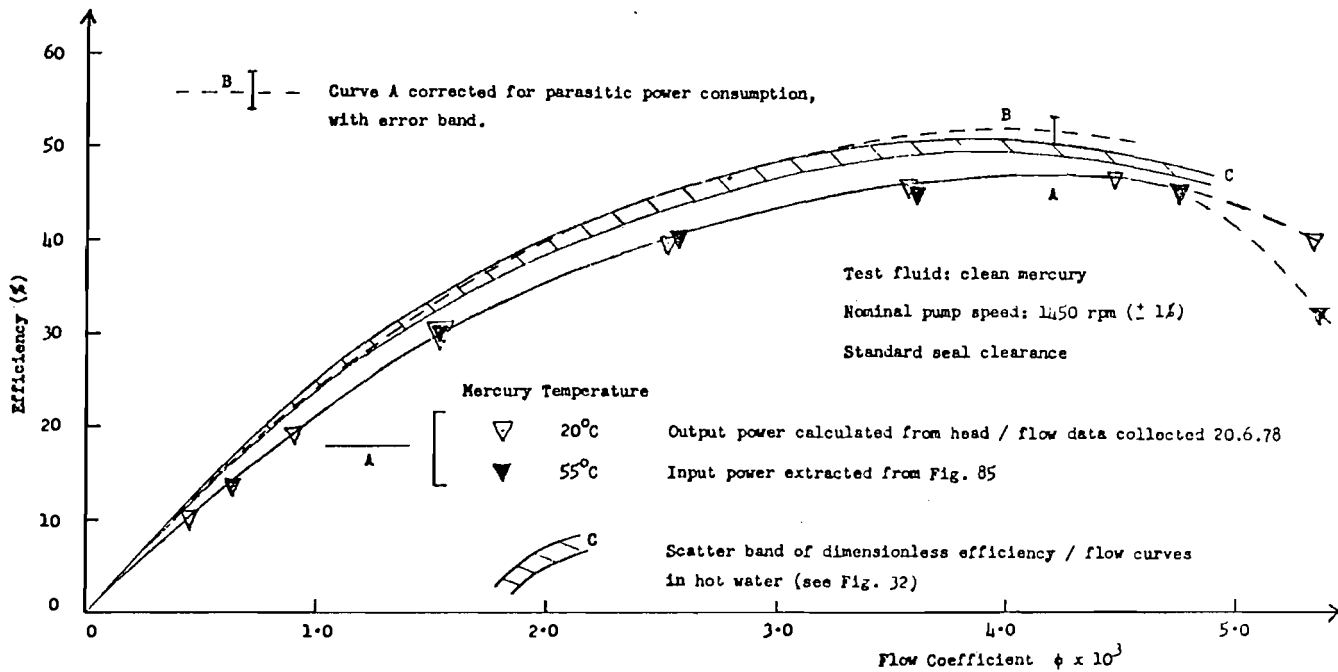
FIGURE 88. DIMENSIONLESS EFFICIENCY / FLOW CHARACTERISTIC IN MERCURY
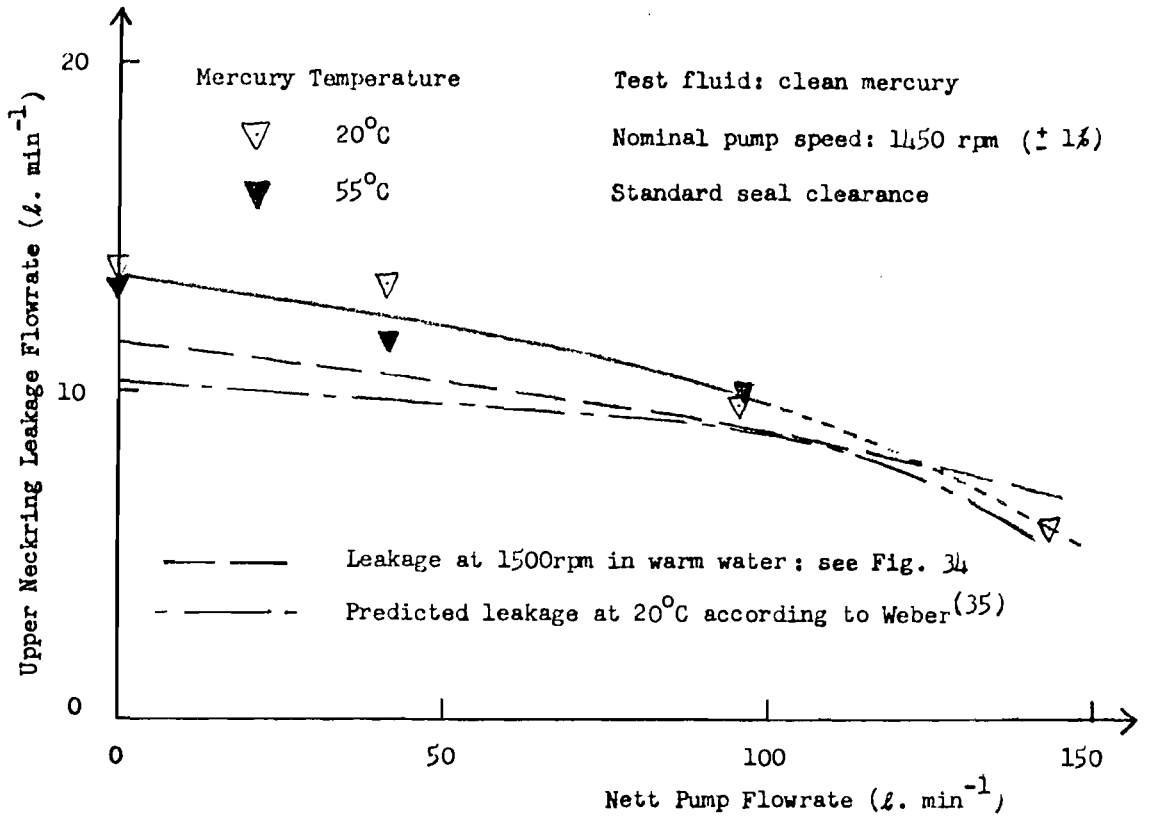
FIGURE 89. UPPER NECKRING LEAKAGE VERSUS NETT PUMP FLOWRATE IN MERCURY
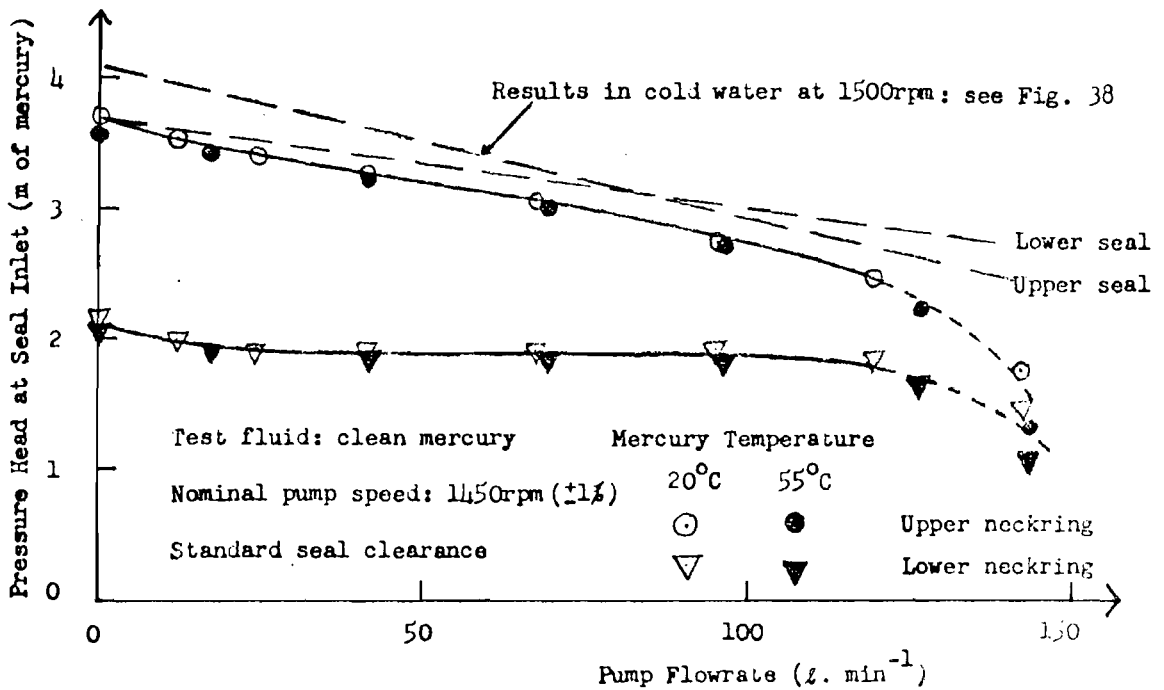
FIGURE 90. SEAL INLET PRESSURE VERSUS PUMP FLOWRATE IN MERCURY
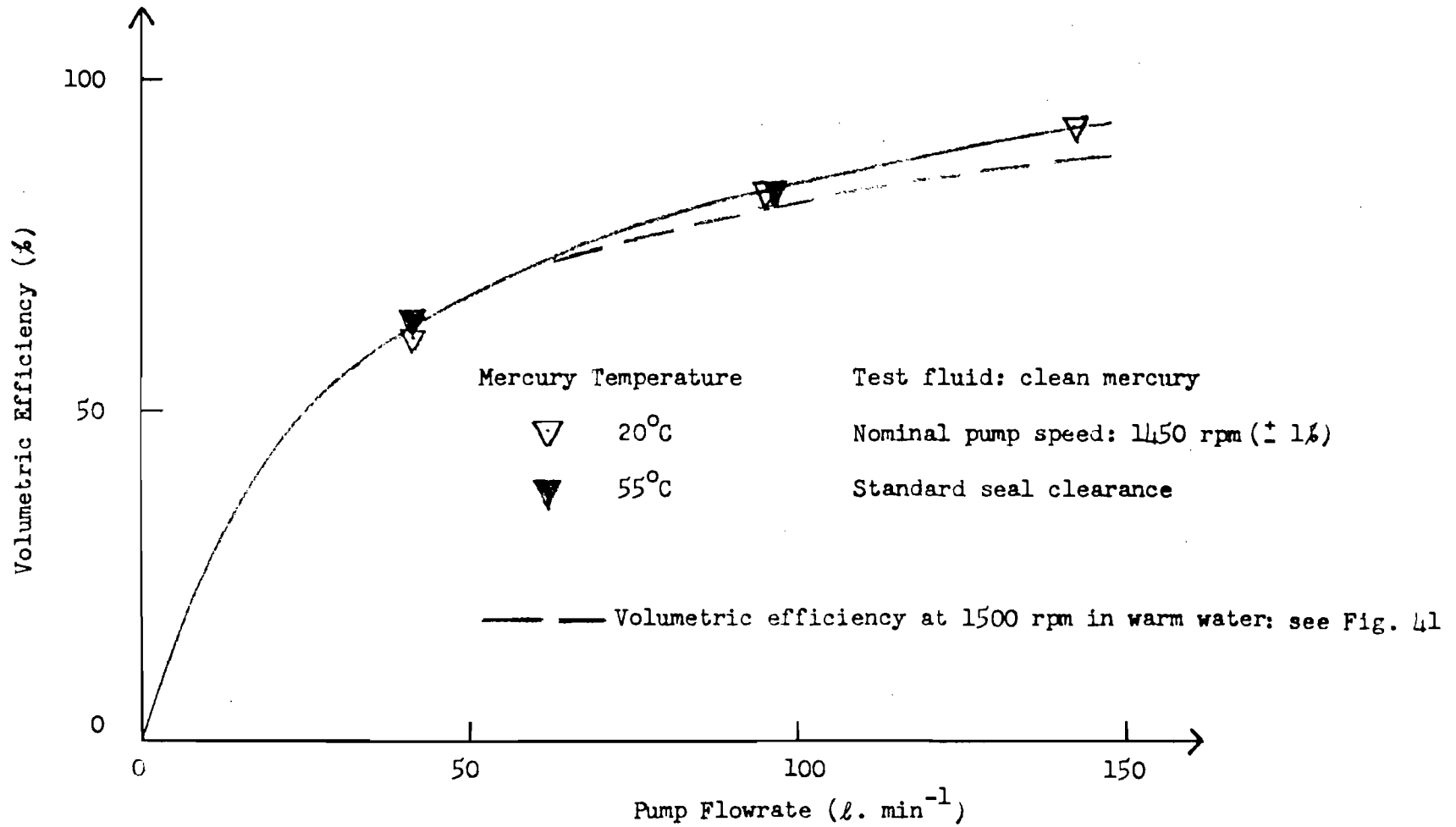
FIGURE 91.   VOLUMETRIC EFFICIENCY CURVE IN MERCURY

FIGURE 92.   WORN PUMP IMPELLER.

FIGURE 93. INNER SURFACE OF PUMP IMPELLER: UPPER SECTION $(x \frac{1}{2})$.

FIGURE 94. INNER SURFACE OF PUMP IMPELLER: LOWER SECTION $(x \frac{1}{2})$.
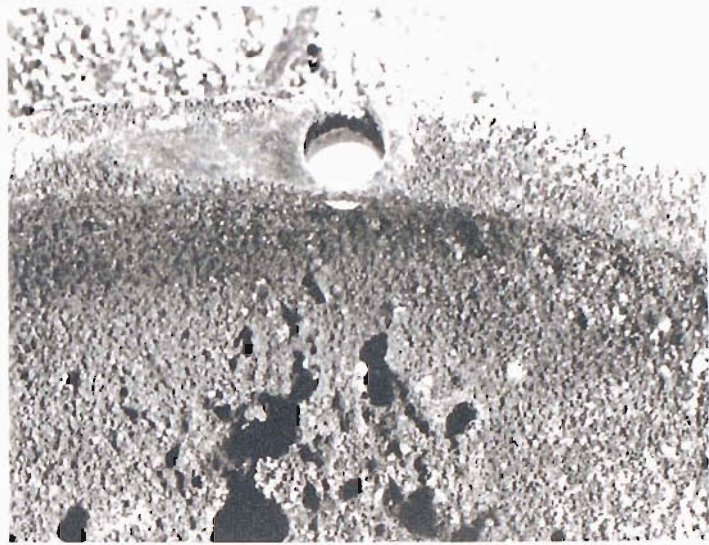
FIGURE 95.   PITTING OF PUMP IMPELLER SURFACE AND UNDERCUTTING OF VANES (x 5)

FIGURE 96.   ORIGINAL MACHINED SURFACE OF LOWER IMPELLER SECTION,
              PROTECTED FROM MERCURY FLOW BY CONTACT WITH VANES (x 10)

FIGURE 97.   MICROSTRUCTURE OF PUMP IMPELLER BODY: COARSE GRAPHITE
FLAKES IN FERRITE MATRIX (x 150).
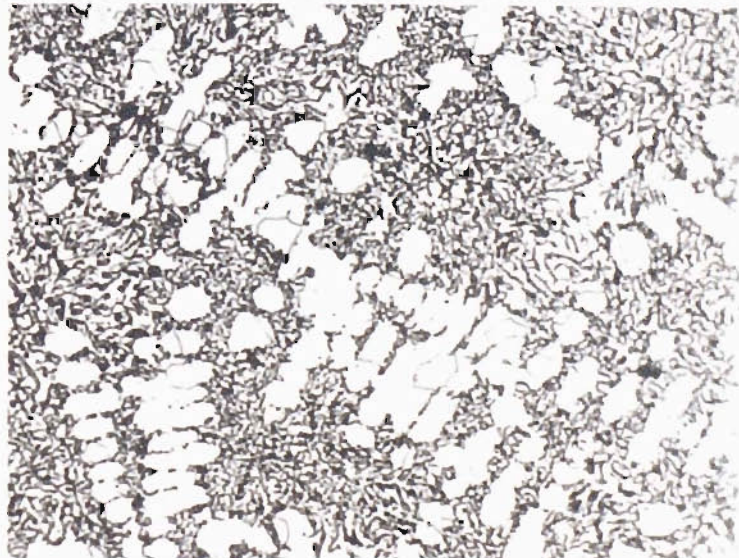
FIGURE 98.   MICROSTRUCTURE OF PUMP IMPELLER VANES: REFINED GRAPHITIC
STRUCTURE IN FERRITE MATRIX (x 150).
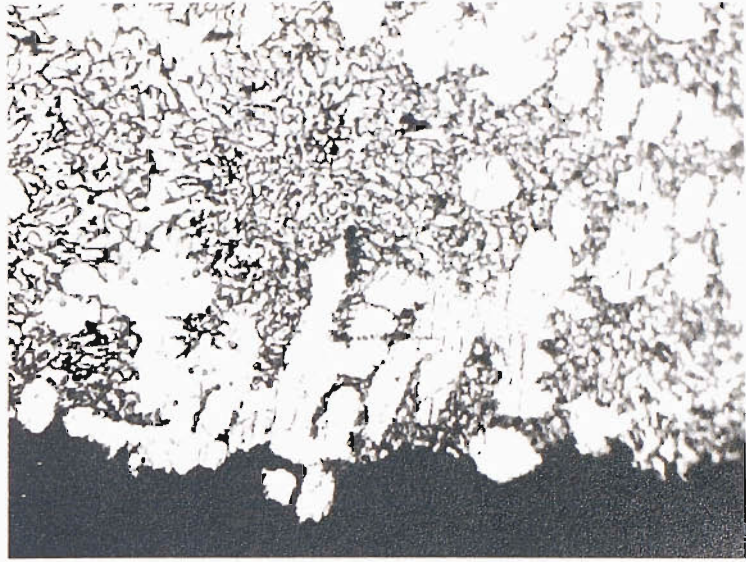
FIGURE 99.   ERODED SURFACE OF PUMP IMPELLER VANES (x 200).
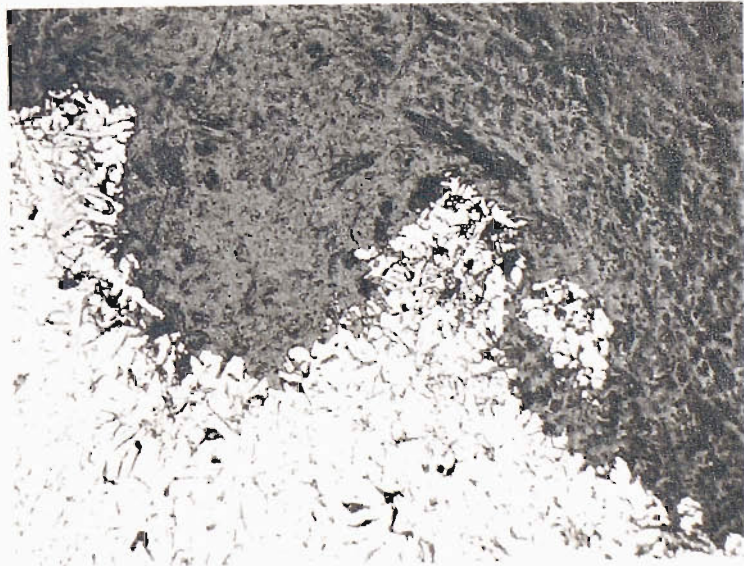
FIGURE 100.   PITTING ON PUMP IMPELLER SURFACE (x 20).
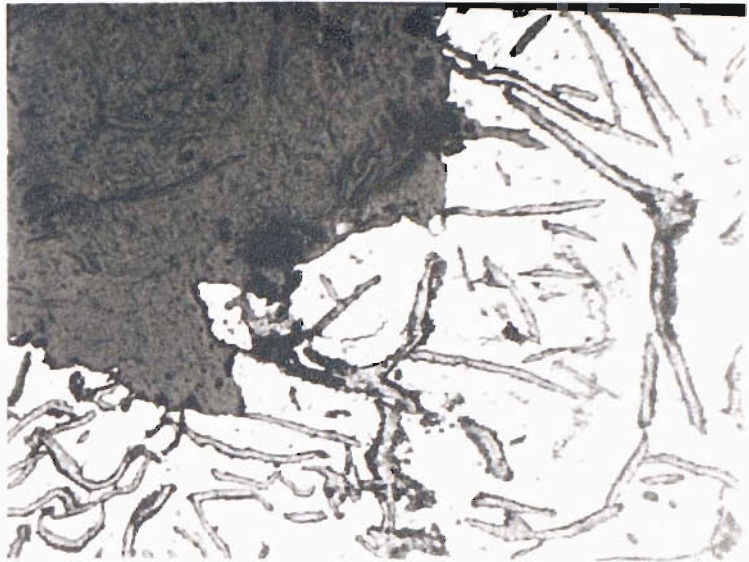
FIGURE 101.   PITTING ON PUMP IMPELLER SURFACE (x 150).

FIGURE 102.   ORIGINAL MACHINED SURFACE (LEFT) AND ERODED SURFACE
(RIGHT) OF LOWER SECTION OF PUMP IMPELLER (x 100).
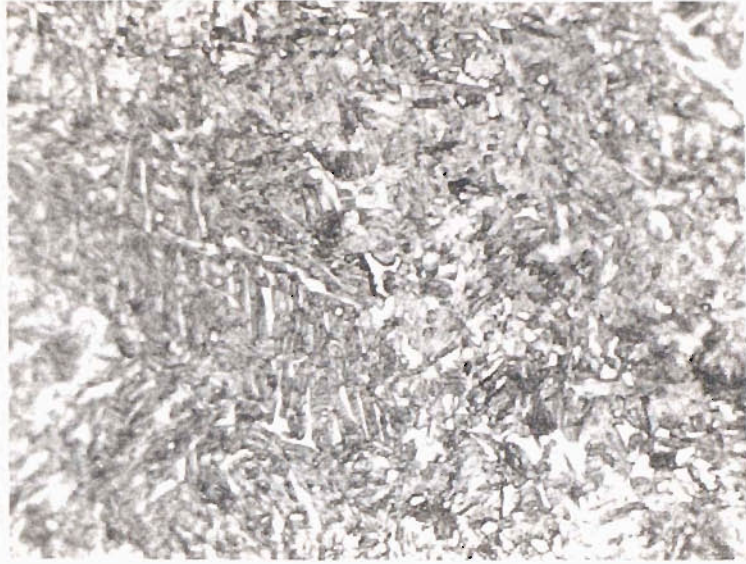
FIGURE 103.   GENERAL MICROSTRUCTURE OF THE CORE OF A NEW UPPER NECKRING (x 400/

FIGURE 104.   MICROSTRUCTURE OF THE WEARING SURFACE OF A NEW UPPER NECKRING
(x 225).
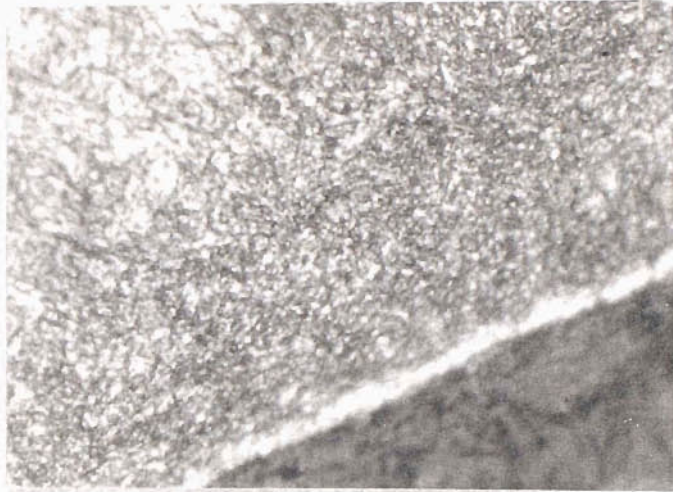
FIGURE 105.   MICROSTRUCTURE OF THE WEARING SURFACE OF A NEW UPPER NECKRING
               (x 670).

FIGURE 106.   GENERAL MICROSTRUCTURE OF THE CORE OF A WORN UPPER NECKRING
               (x 530).
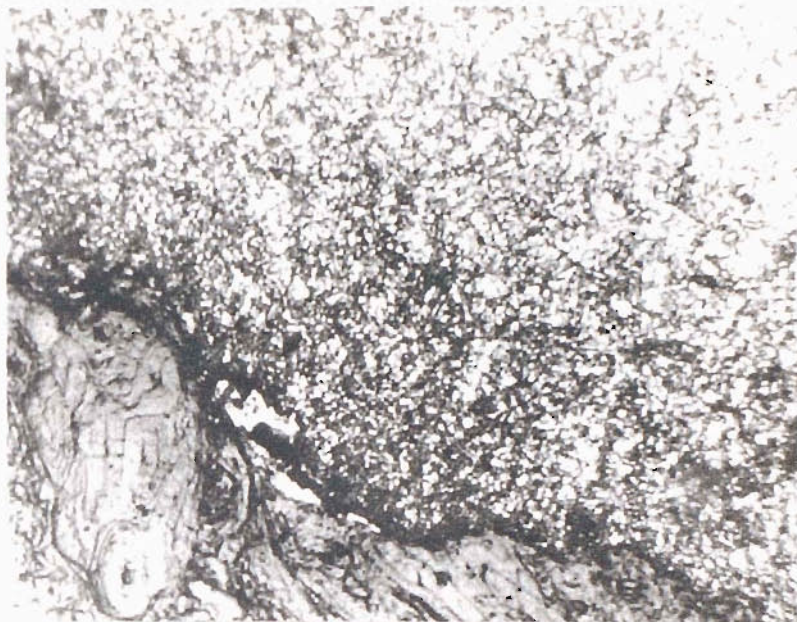
FIGURE 107. MICROSTRUCTURE OF THE WEARING SURFACE OF A WORN UPPER NECKRING (x 220).
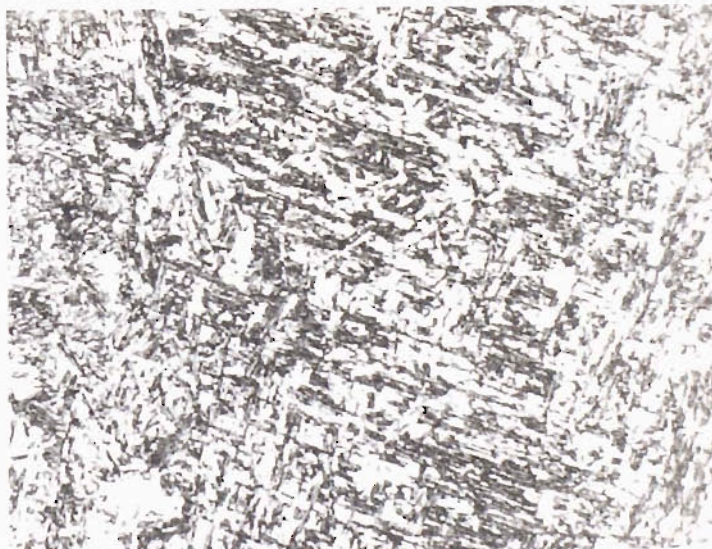
FIGURE 108. GENERAL MICROSTRUCTURE OF THE CORE OF A NEW LOWER NECKRING (x 200).
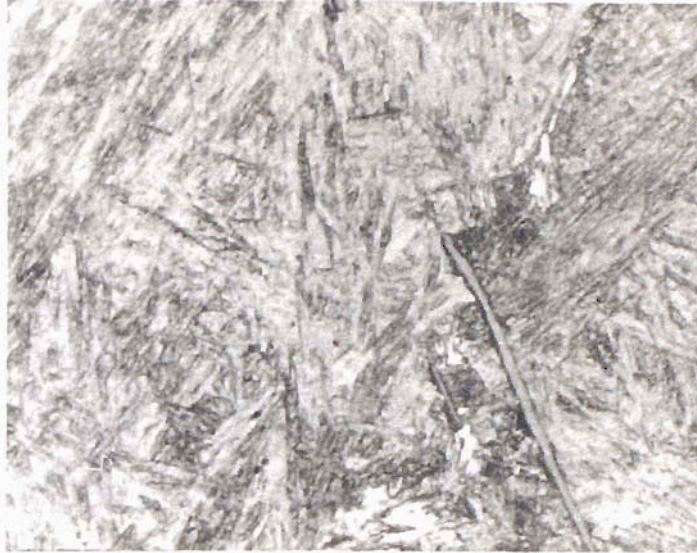
FIGURE 109.   GENERAL MICROSTRUCTURE OF THE CORE OF A NEW LOWER NECKRING (x 700).

FIGURE 110.   MICROSTRUCTURE OF THE WEARING SURFACE OF A NEW LOWER NECKRING (x 100).
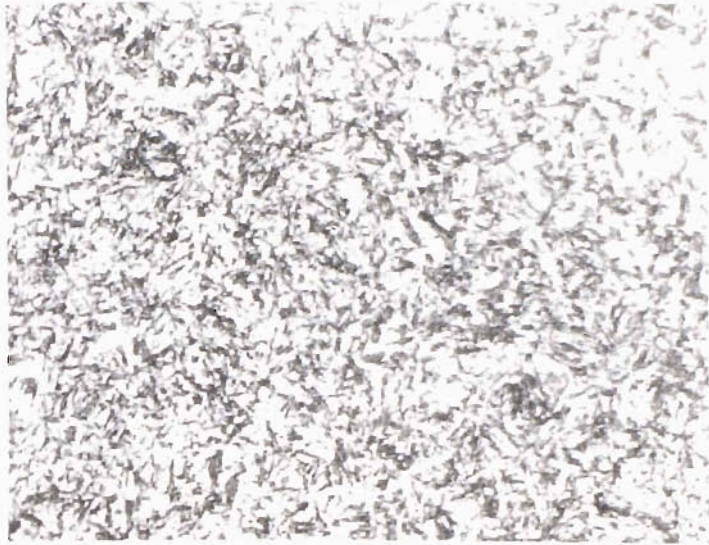
FIGURE 111.   MICROSTRUCTURE OF THE WEARING SURFACE OF A NEW LOWER NECKRING (x 500).
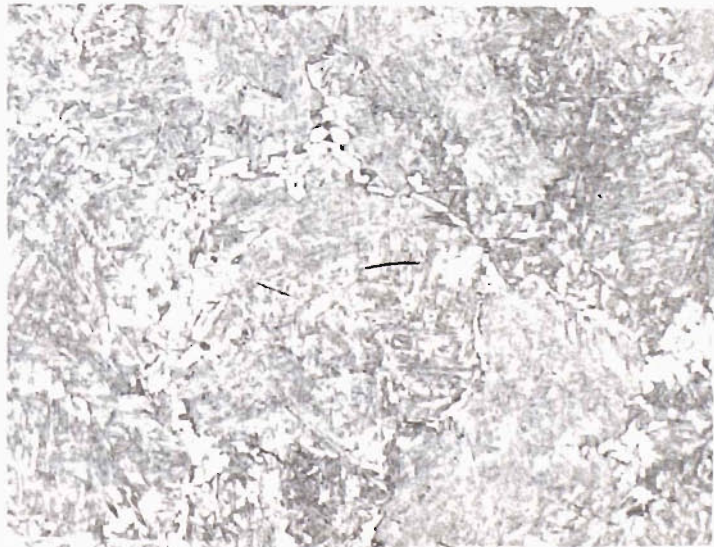
FIGURE 112.   GENERAL MICROSTRUCTURE OF THE CORE OF A WORN LOWER NECKRING (x 120).
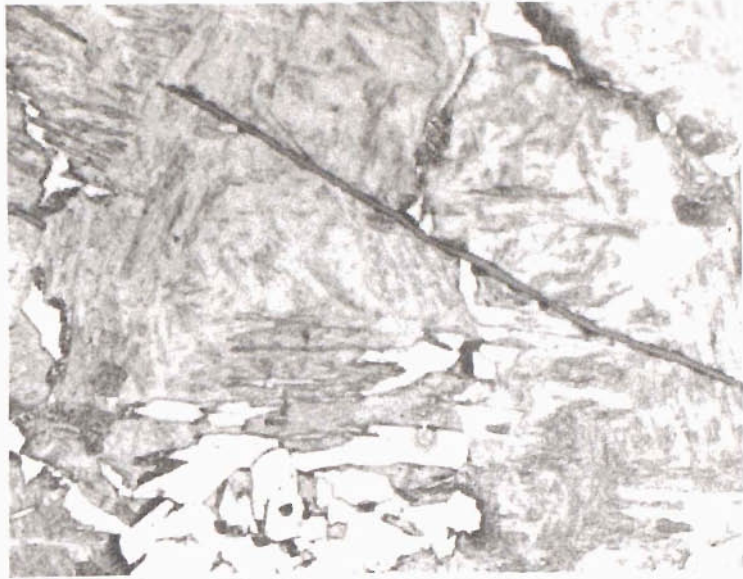
FIGURE 113.   GENERAL MICROSTRUCTURE OF THE CORE OF A WORN LOWER NECKRING (x 550)

FIGURE 114.   MICROSTRUCTURE OF THE WEARING SURFACE OF A WORN LOWER NECKRING (x 150).
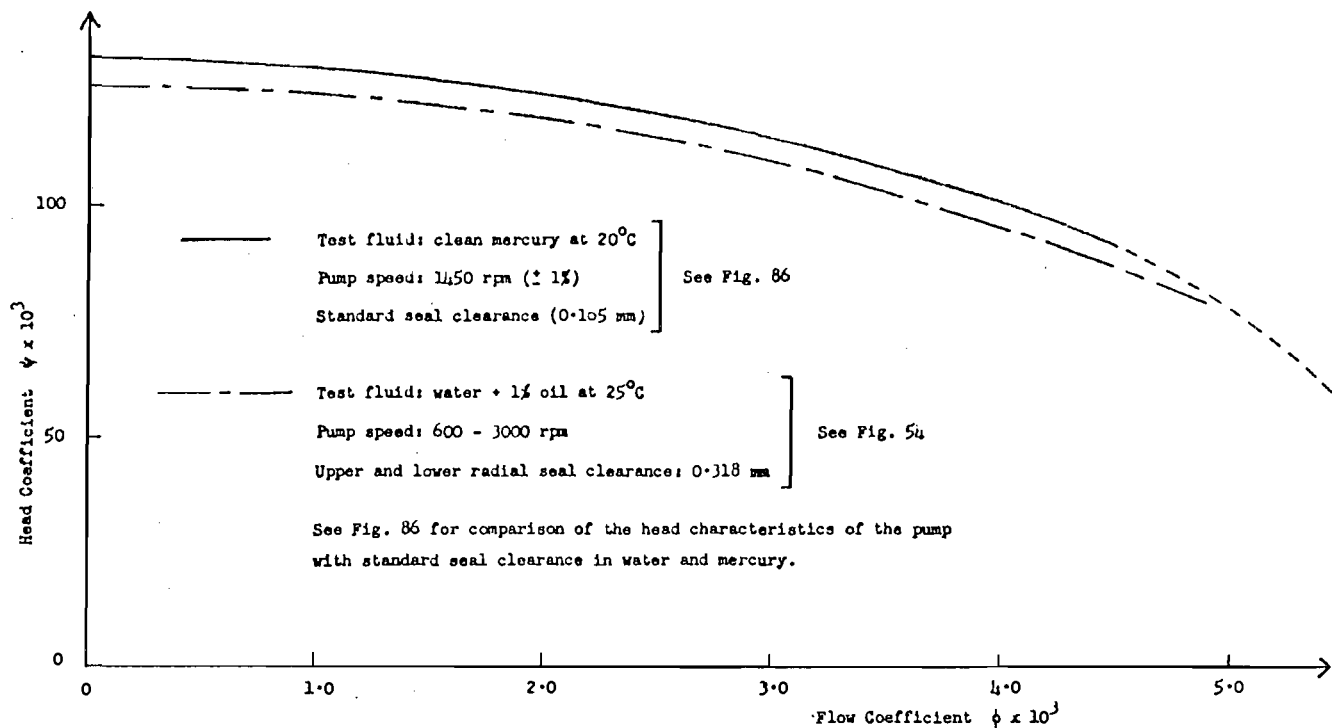
FIGURE 115   COMPARISON OF PUMP HEAD CHARACTERISTICS WITH DISSIMILAR SEAL CLEARANCES IN WATER AND MERCURY
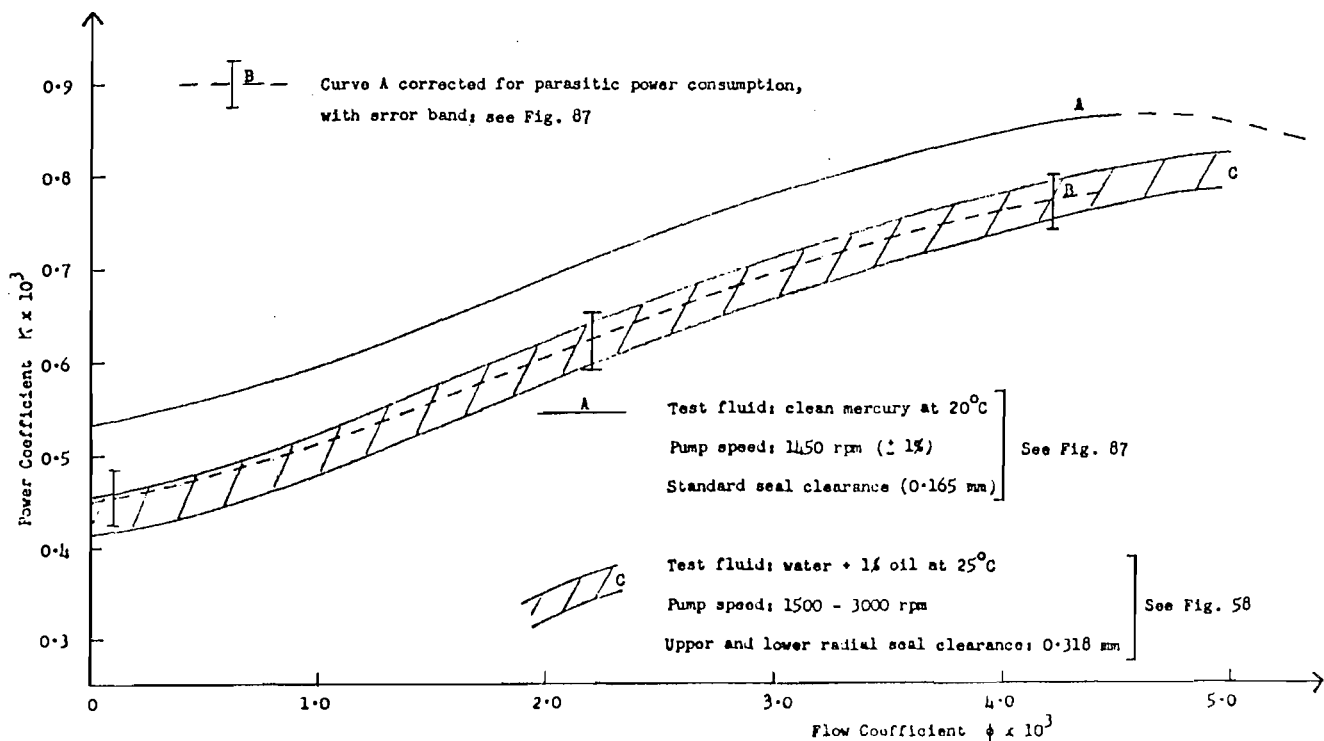
FIGURE 116.   COMPARISON OF PUMP POWER CHARACTERISTICS WITH DISSIMILAR SEAL CLEARANCES IN WATER AND MERCURY
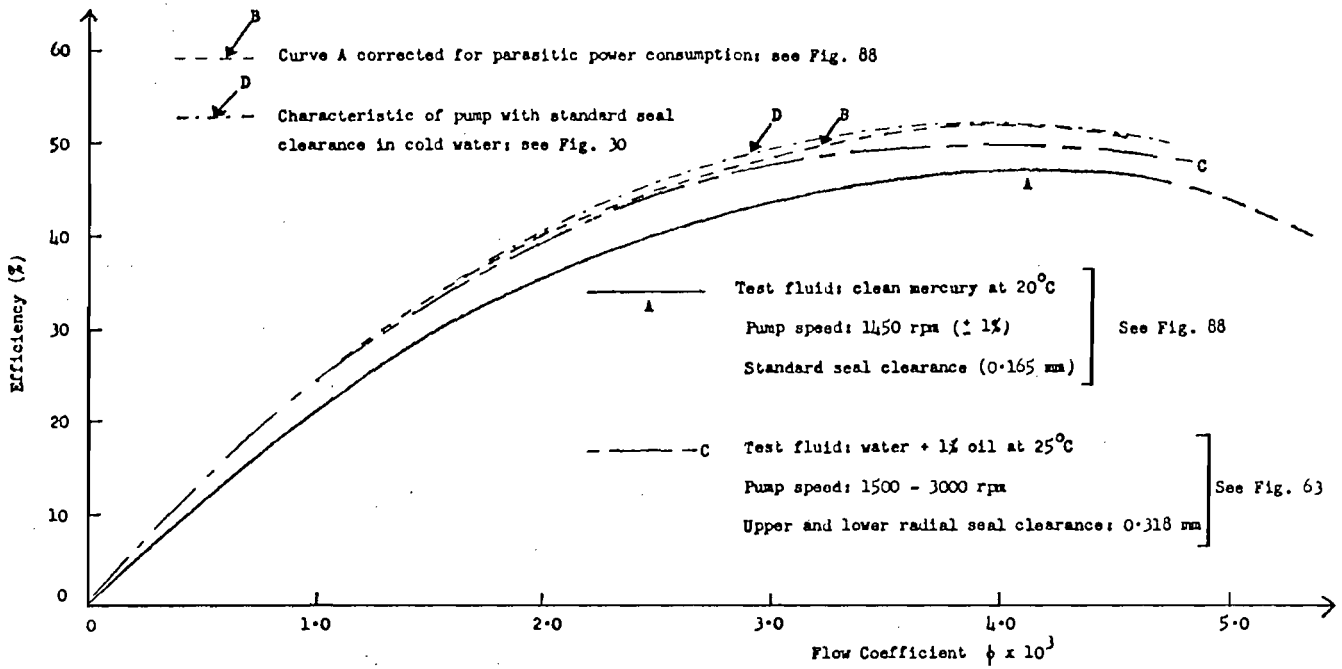
FIGURE 117. COMPARISON OF PUMP EFFICIENCY CHARACTERISTICS WITH DISSIMILAR SEAL CLEARANCE IN WATER AND MERCURY
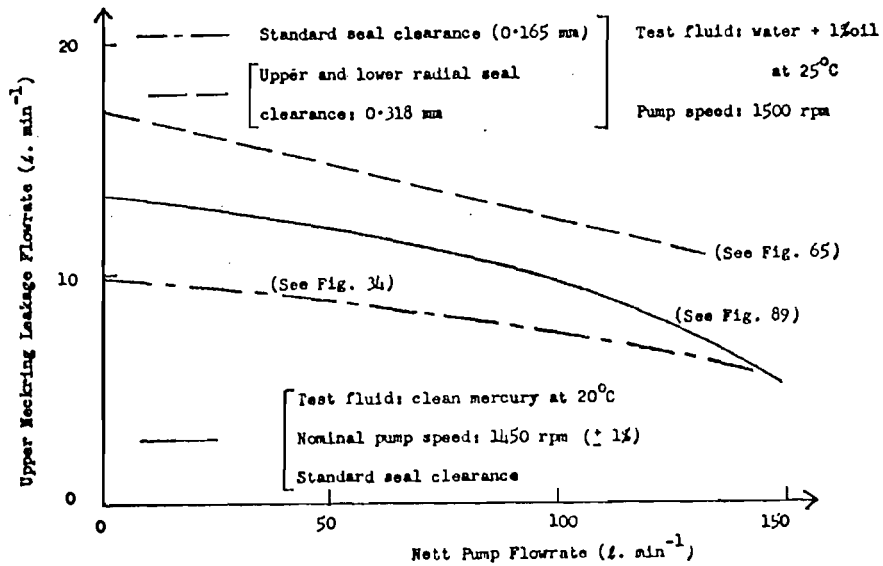
FIGURE 118. COMPARISON OF LEAKAGE WITH DISSIMILAR SEAL CLEARANCES IN WATER AND MERCURY.
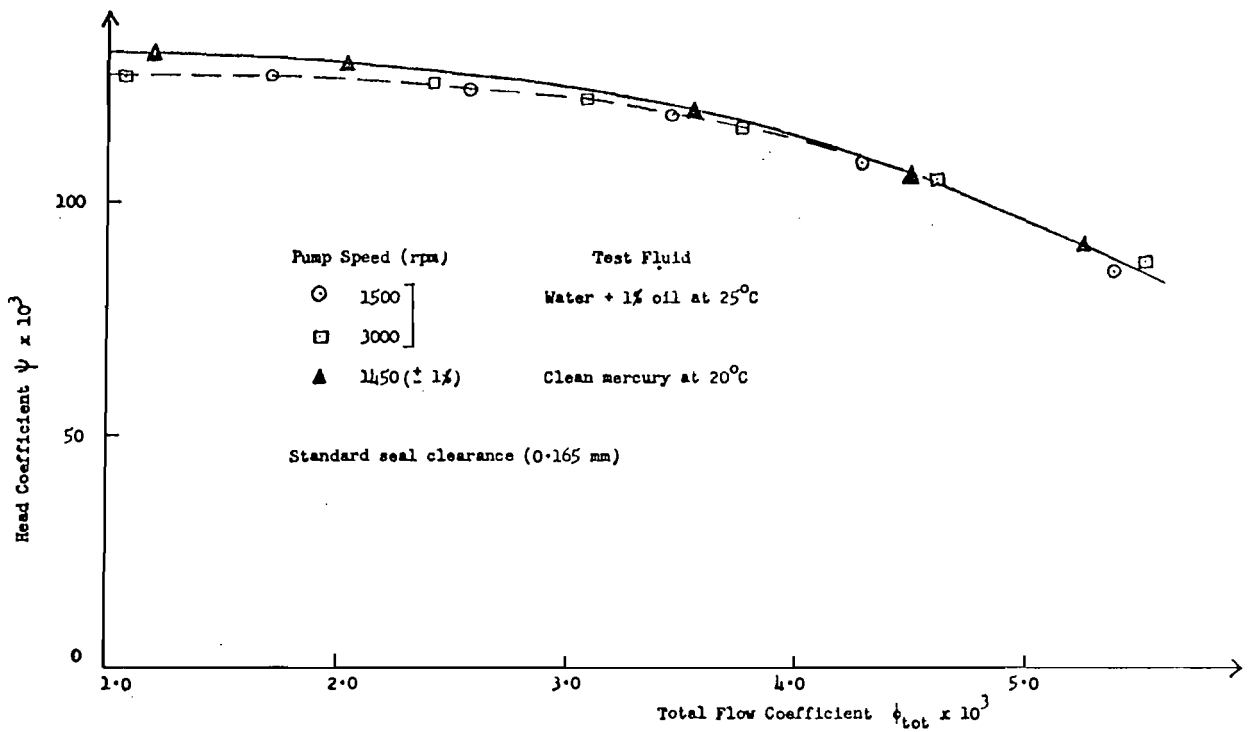
FIGURE 119. DIMENSIONLESS HEAD / TOTAL FLOW CHARACTERISTIC IN WATER AND MERCURY.
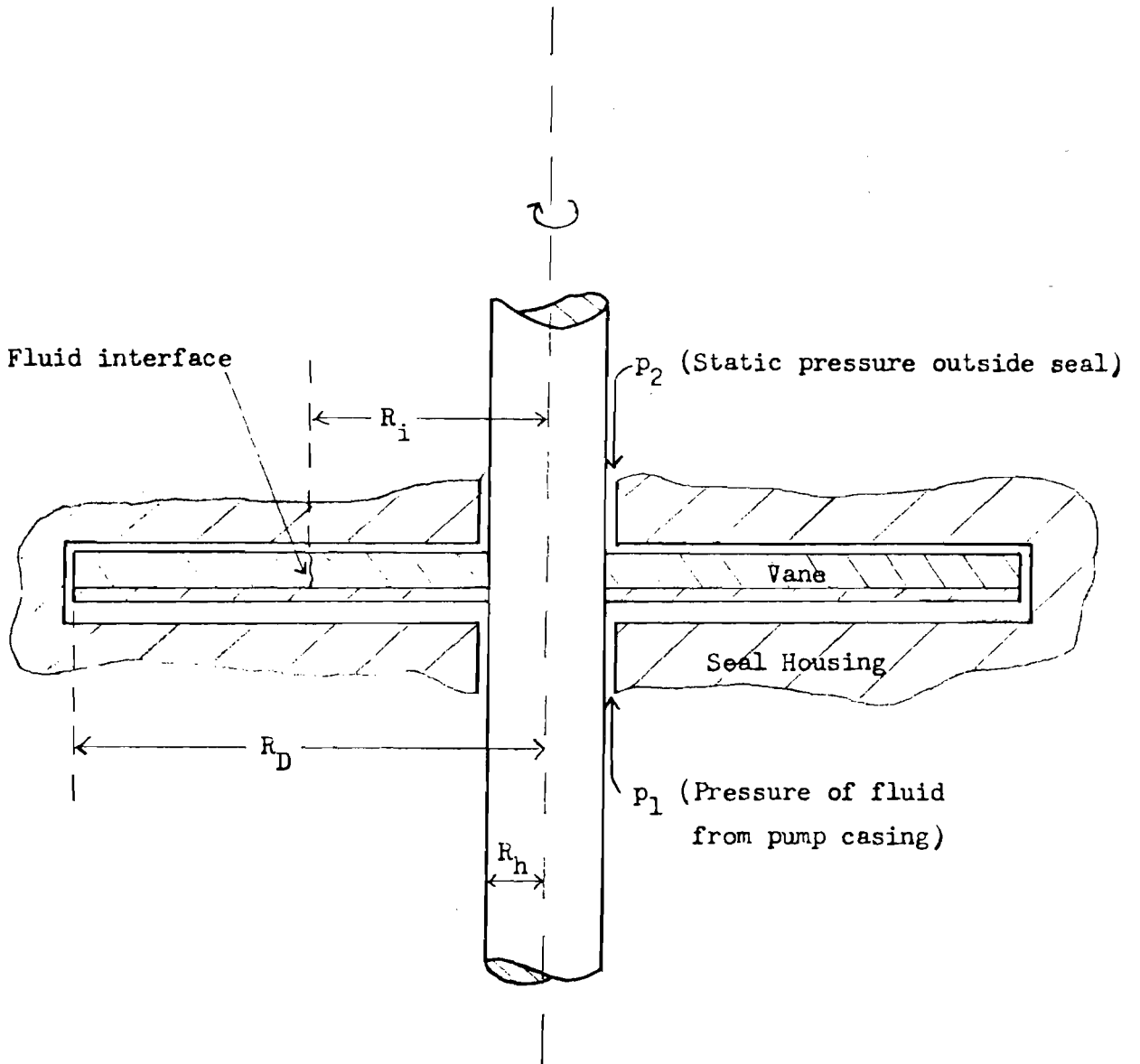
FIGURE 120. DIAGRAM OF A HYDRODYNAMIC DISC SEAL (HDS).

Tapping Radius (mm)
50 45 40 35

Tapping Radius (mm)
40 50 60 70

Seal Casing

TWO-STAGE HDS

Shaft

Seal Casing

SINGLE STAGE HDS

P

HDS Impeller

HDS Impeller

P

P

P

P

HDS Impeller

HDS Impeller

P

P

Pump Casing

P

P

Pump Impeller

Fluid Outlet

P

Lower Neckring

P

Fluid Inlet
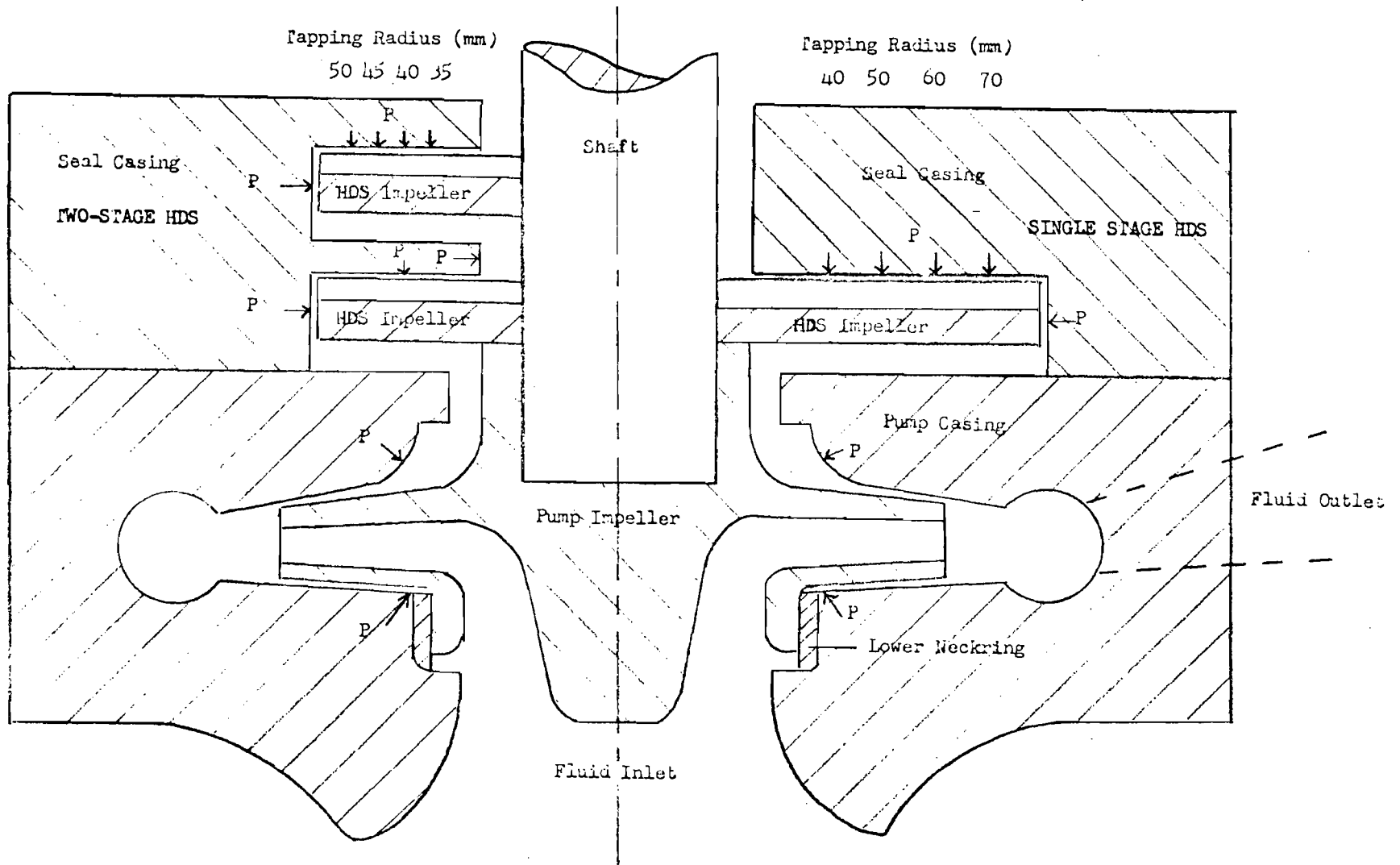
FIGURE 121. ASSEMBLY OF PUMP WITH SINGLE AND TWO-STAGE HDS.
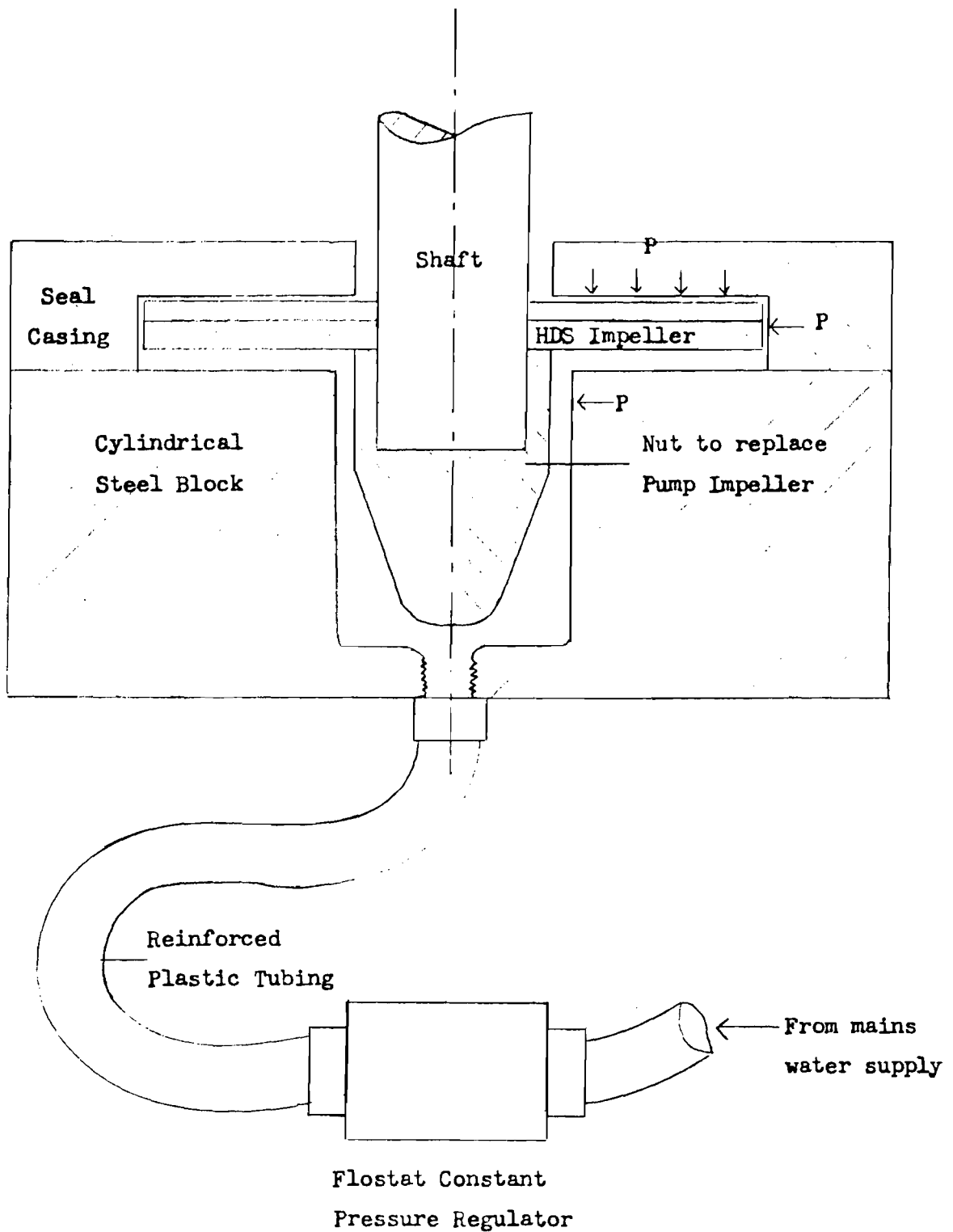
FIGURE 122. ARRANGEMENT FOR HDS TRIALS IN BARE CONFIGURATION.
(Single stage HDS illustrated)
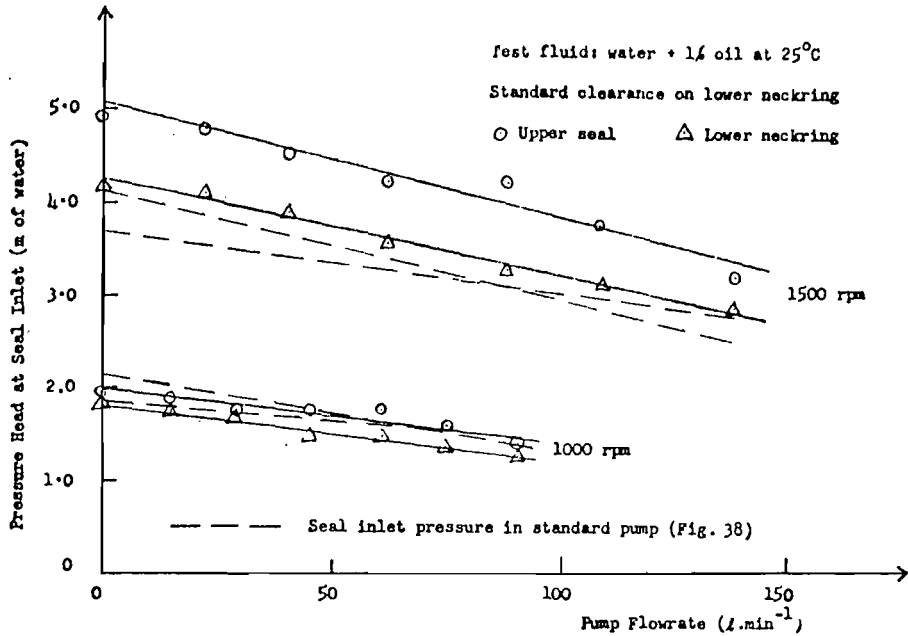
FIGURE 123. SEAL INLET PRESSURE V. PUMP FLOWRATE WITH SINGLE STAGE HDS IN WATER (1000 - 1500 RPM).
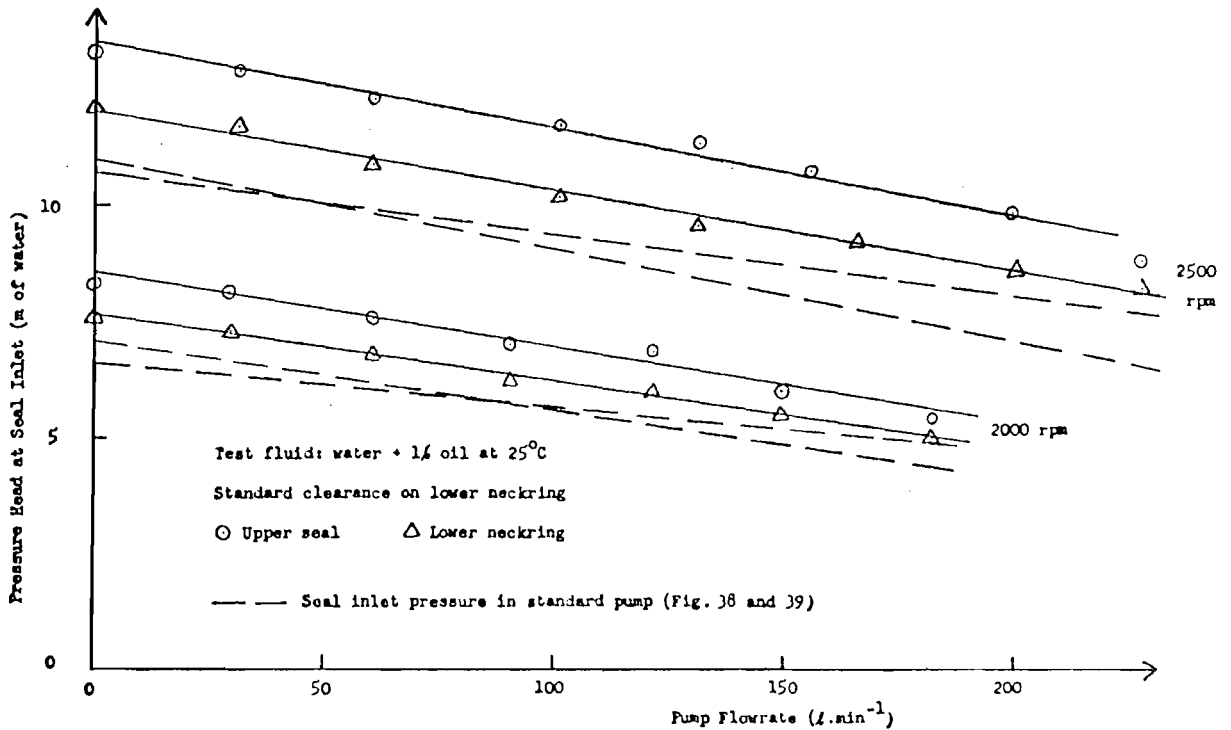
FIGURE 124. SEAL INLET PRESSURE V. PUMP FLOWRATE WITH SINGLE STAGE HDS IN WATER (2000 - 2500 RPM).
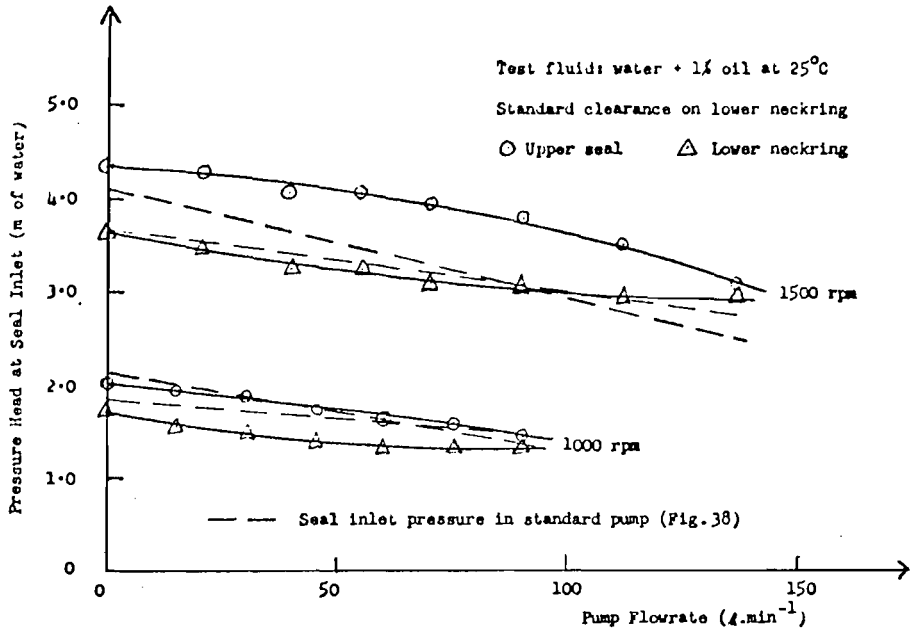
FIGURE 125. SEAL INLET PRESSURE V. PUMP FLOWRATE WITH TWO-STAGE (I) HDS IN WATER (1000 - 1500 RPM).
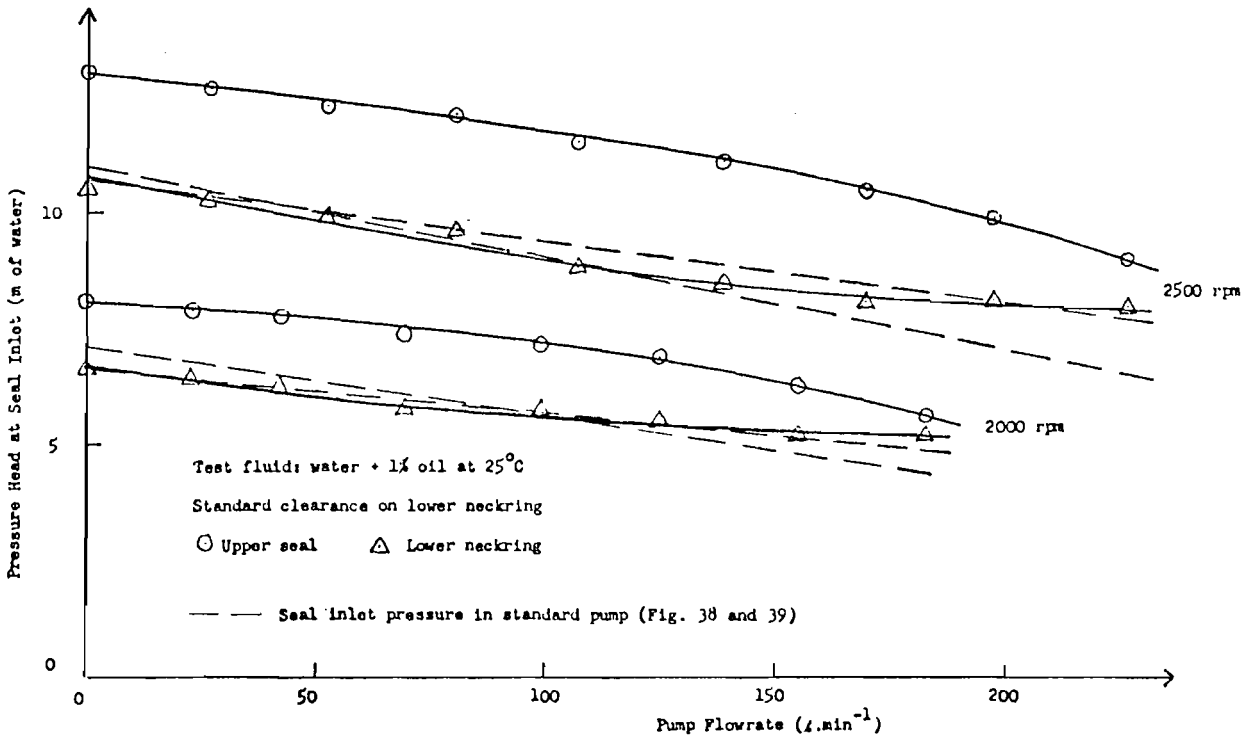
FIGURE 126. SEAL INLET PRESSURE V. PUMP FLOWRATE WITH TWO-STAGE (I) HDS IN WATER (2000 - 2500 RPM).
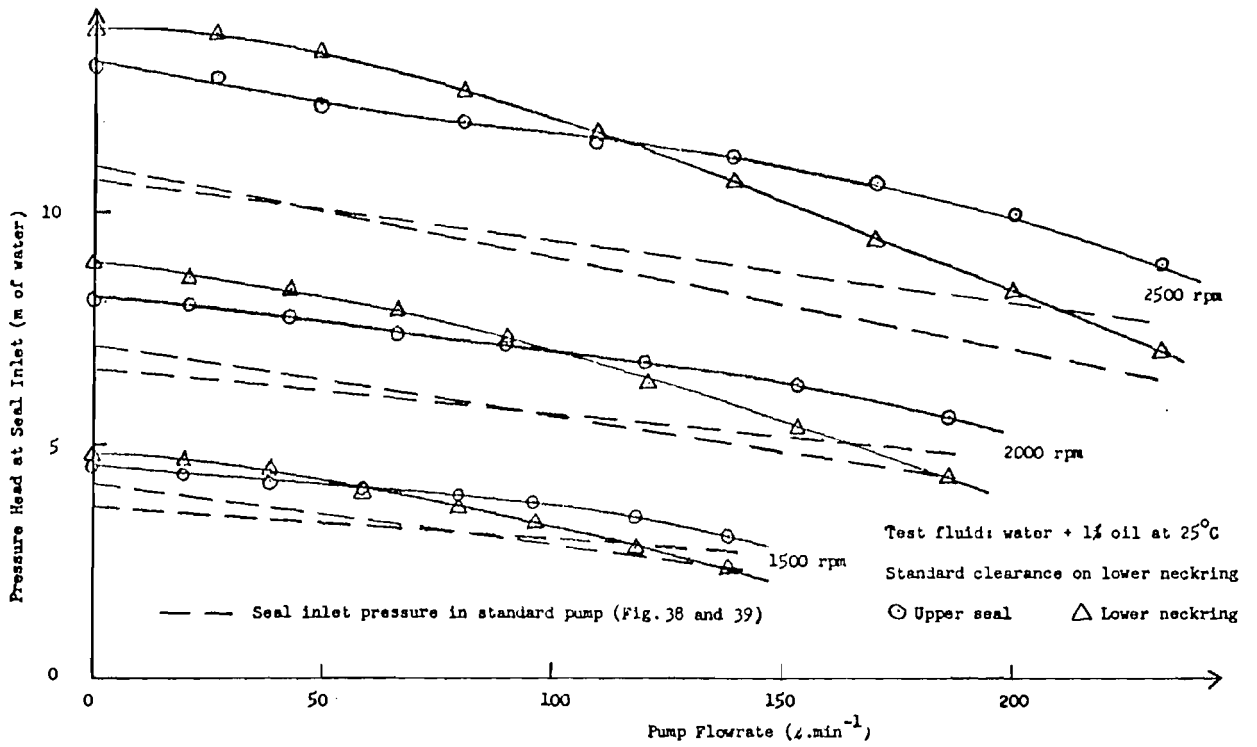
FIGURE 127. SEAL INLET PRESSURE V. PUMP FLORATE WITH TWO-STAGE (II) HDS IN WATER.
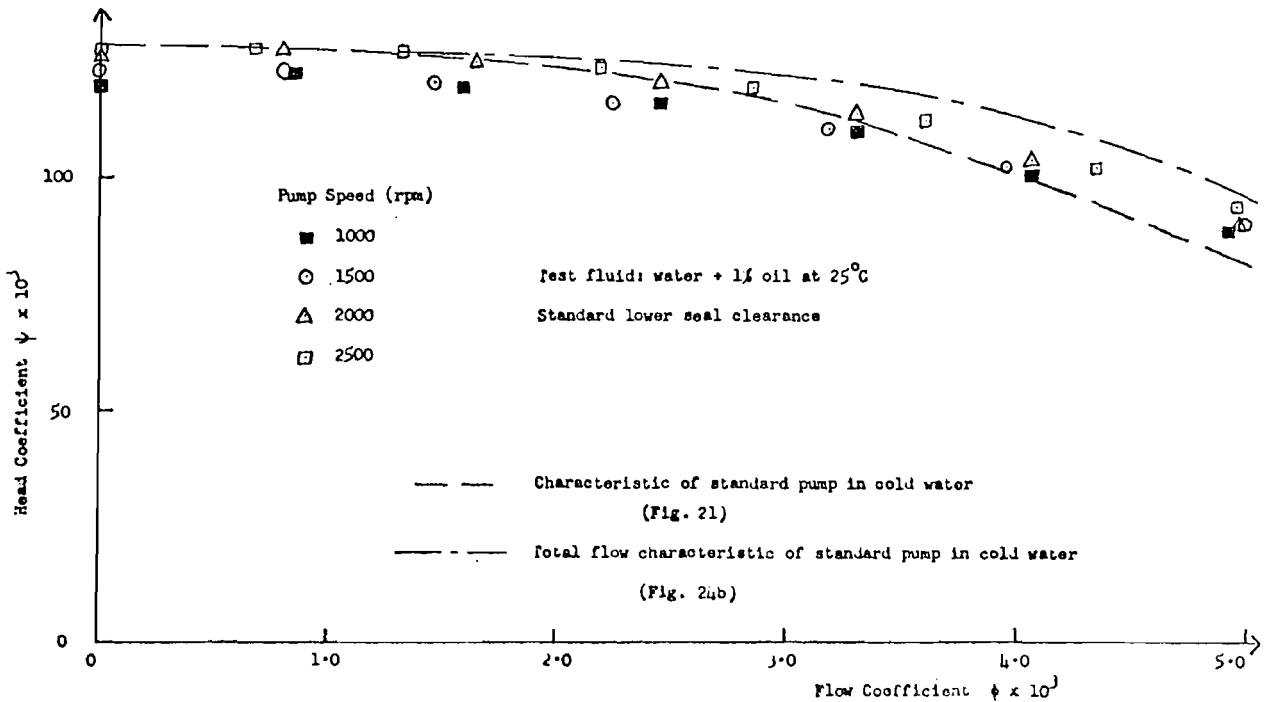
FIGURE 128. DIMENSIONLESS HEAD / FLOW CHARACTERISTIC WITH SINGLE STAGE HDS IN COLD WATER
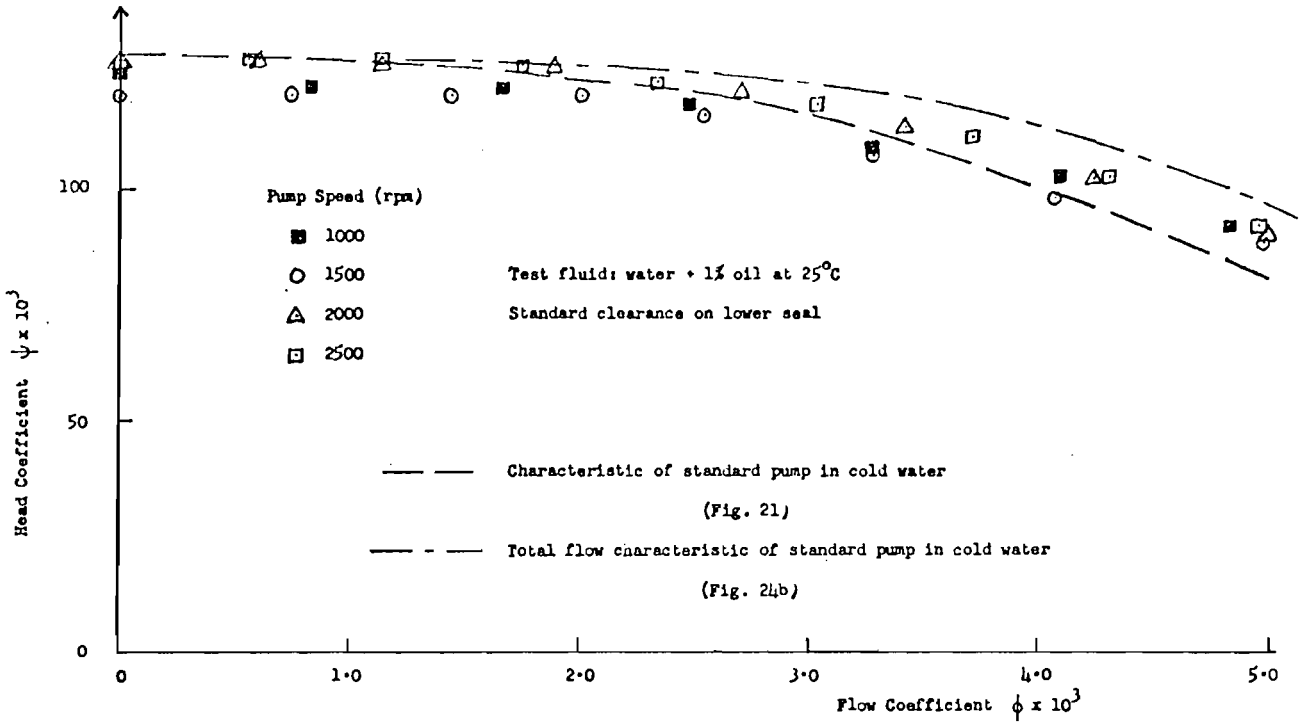
FIGURE 129.   DIMENSIONLESS HEAD / FLOW CHARACTERISTIC WITH TWO-STAGE (I) HDS IN COLD WATER.
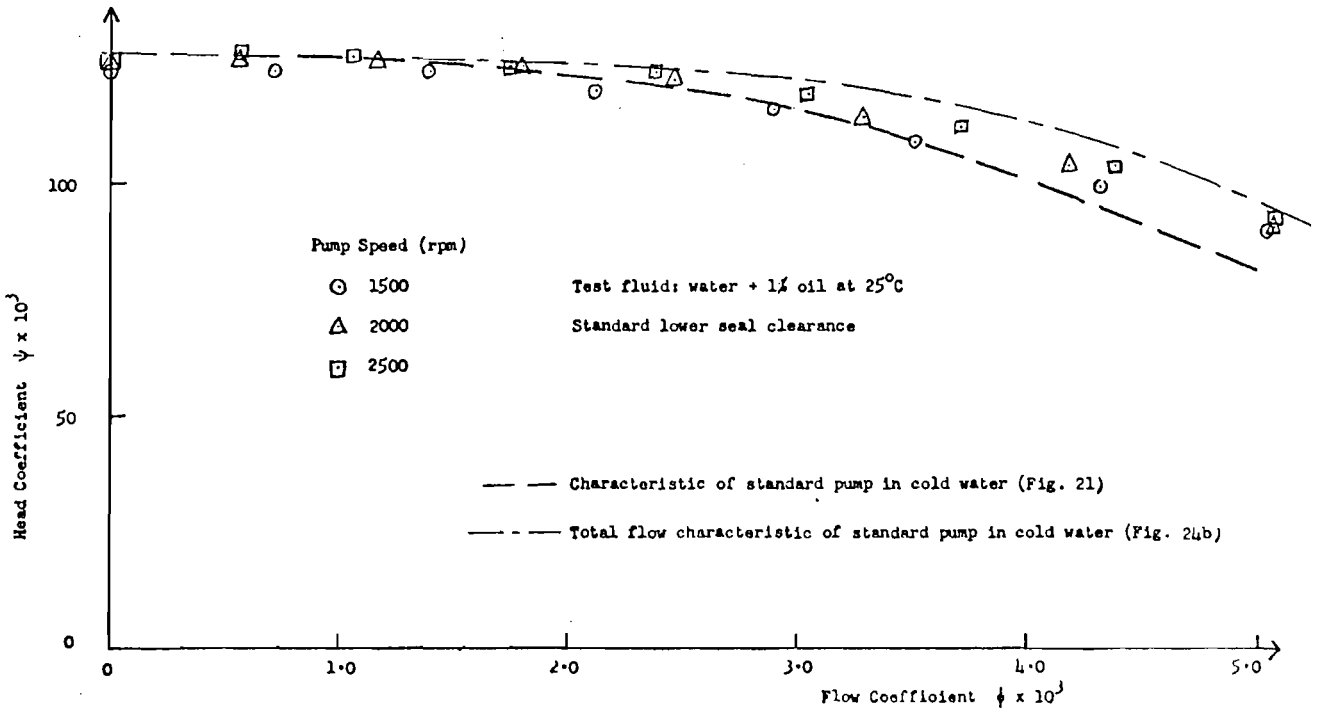
FIGURE 130.   DIMENSIONLESS HEAD / FLOW CHARACTERISTIC WITH TWO-STAGE (II) HDS IN COLD WATER.
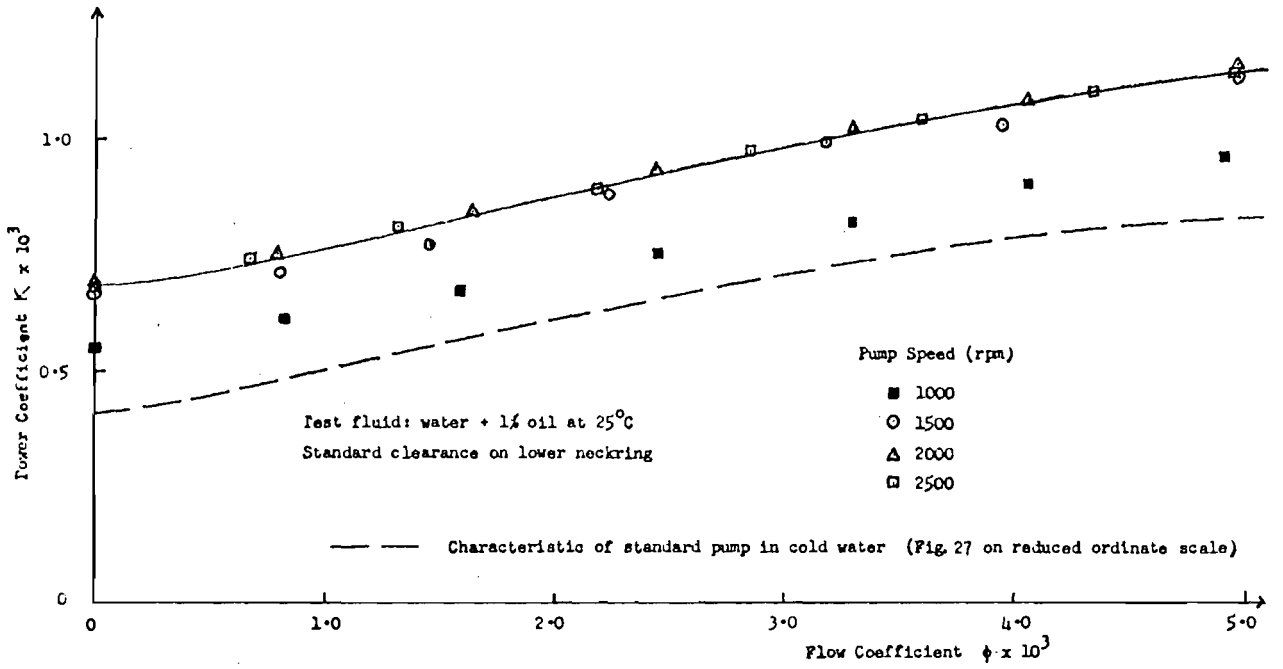
FIGURE 131.   DIMENSIONLESS ABSORBED POWER / FLOW CHARACTERISTIC WITH SINGLE STAGE HDS IN COLD WATER.
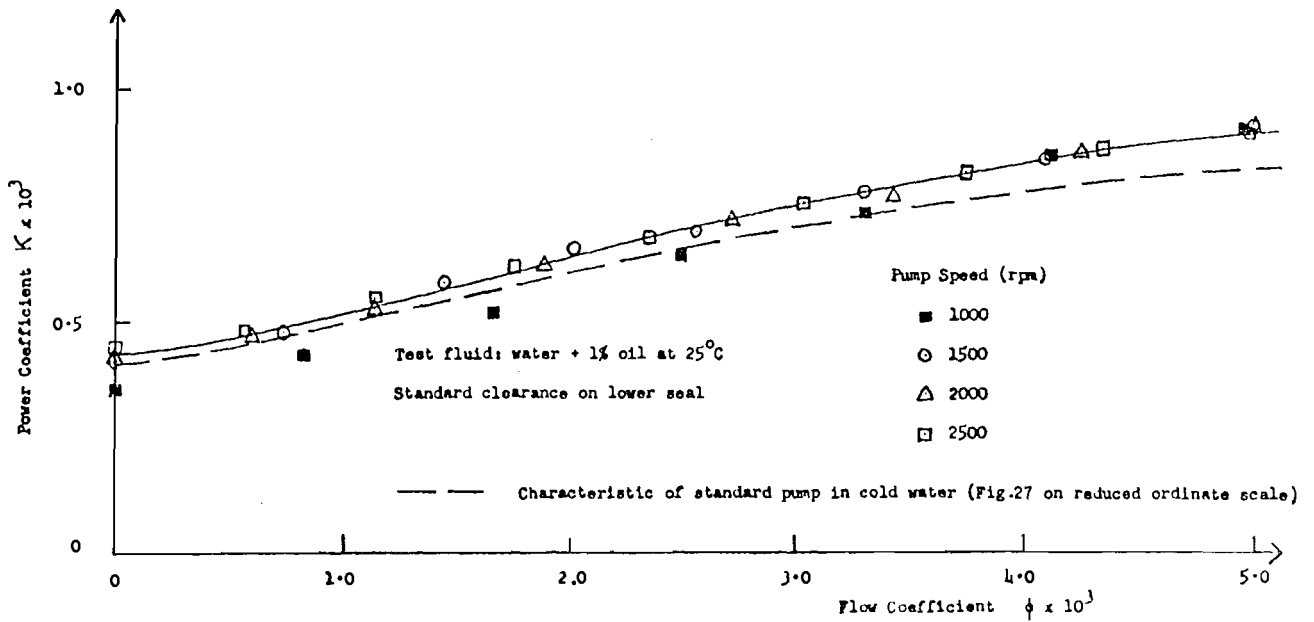
FIGURE 132.   DIMENSIONLESS ABSORBED POWER / FLOW CHARACTERISTIC WITH TWO-STAGE (I) HDS IN COLD WATER
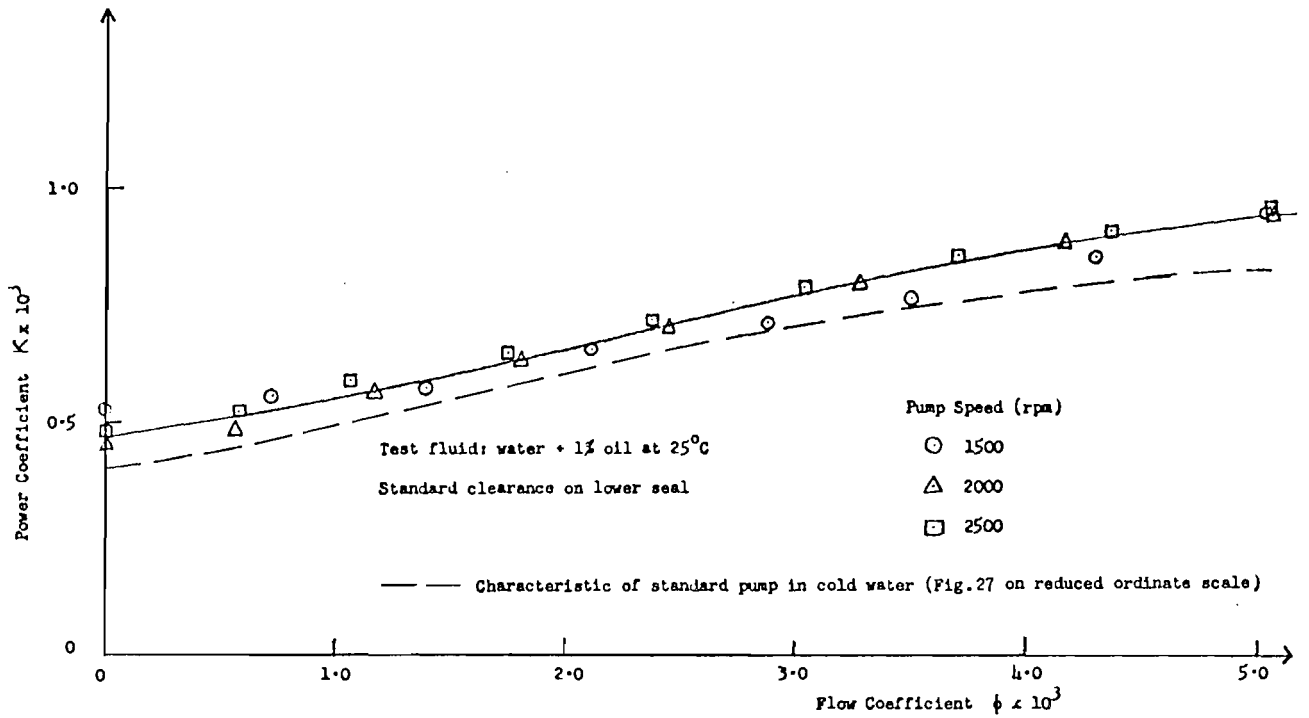
FIGURE 133.   DIMENSIONLESS ABSORBED POWER / FLOW CHARACTERISTIC WITH TWO-STAGE (II) HDS IN COLD WATER.
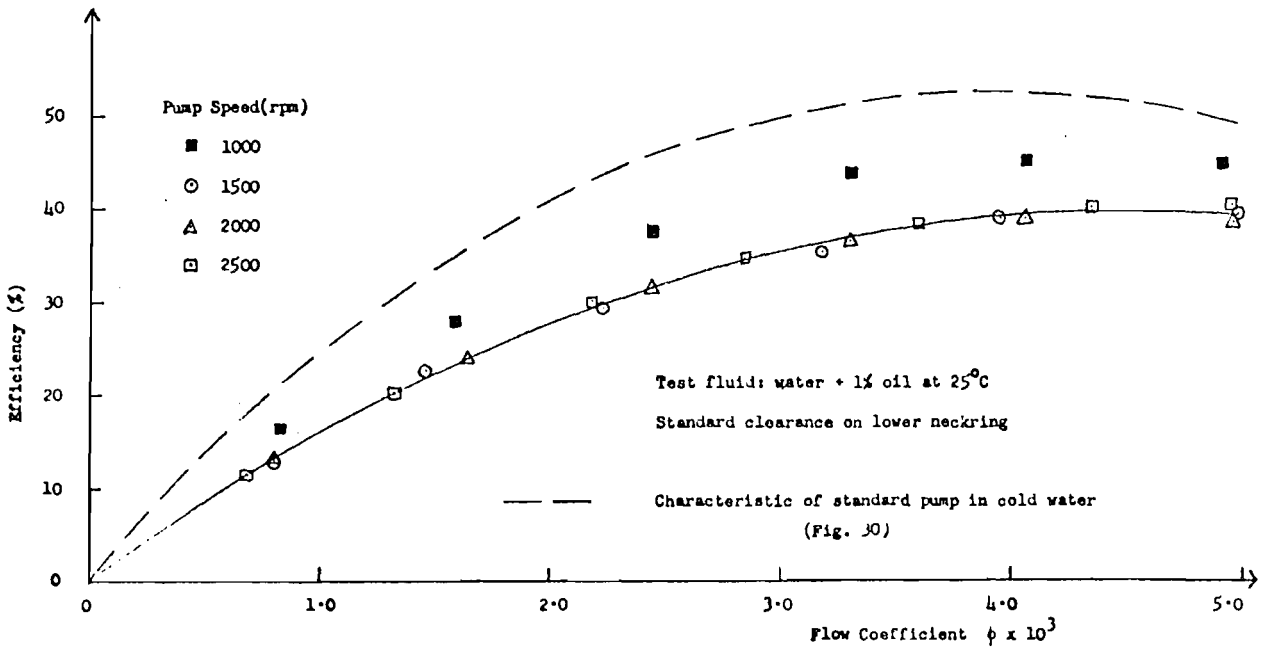
FIGURE 134.   DIMENSIONLESS EFFICIENCY / FLOW CHARACTERISTIC WITH SINGLE STAGE HDS IN COLD WATER.
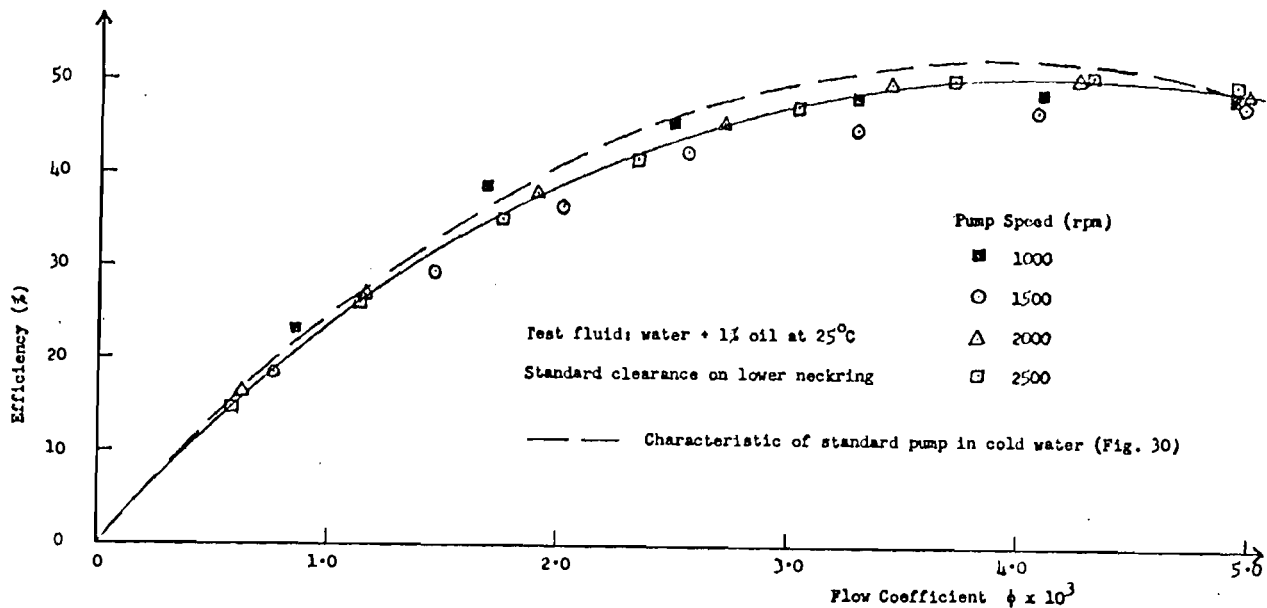
FIGURE 135.   DIMENSIONLESS EFFICIENCY / FLOW CHARACTERISTIC WITH TWO-STAGE HDS (I) IN COLD WATER
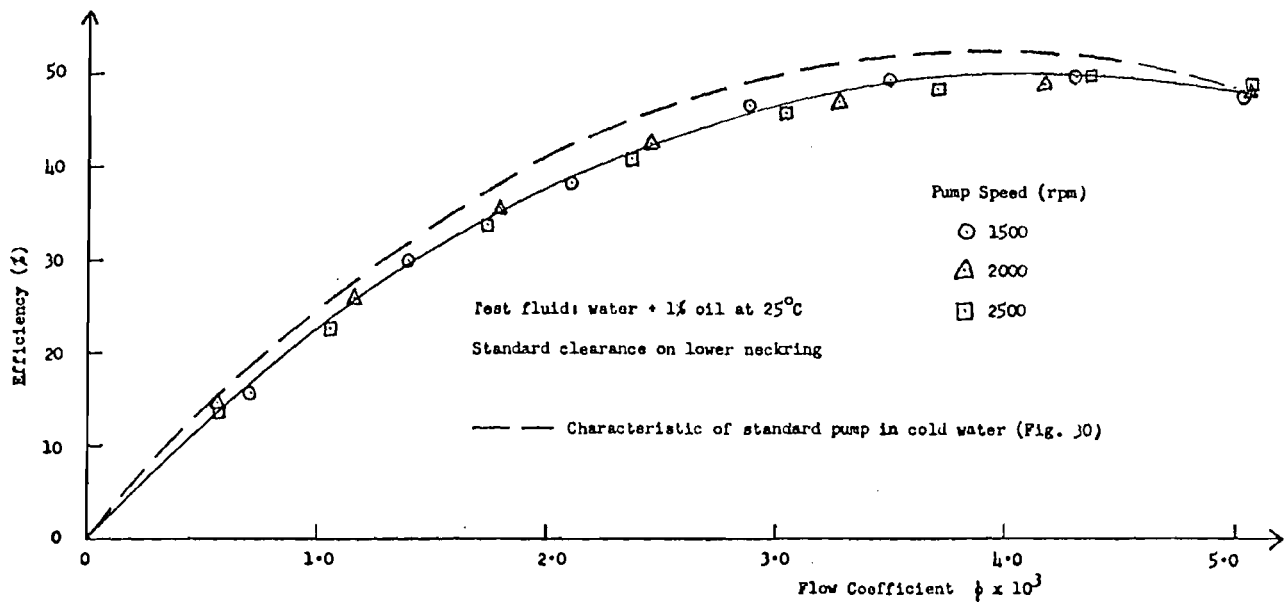
FIGURE 136.   DIMENSIONLESS EFFICIENCY / FLOW CHARACTERISTIC WITH TWO-STAGE HDS (II) IN COLD WATER.
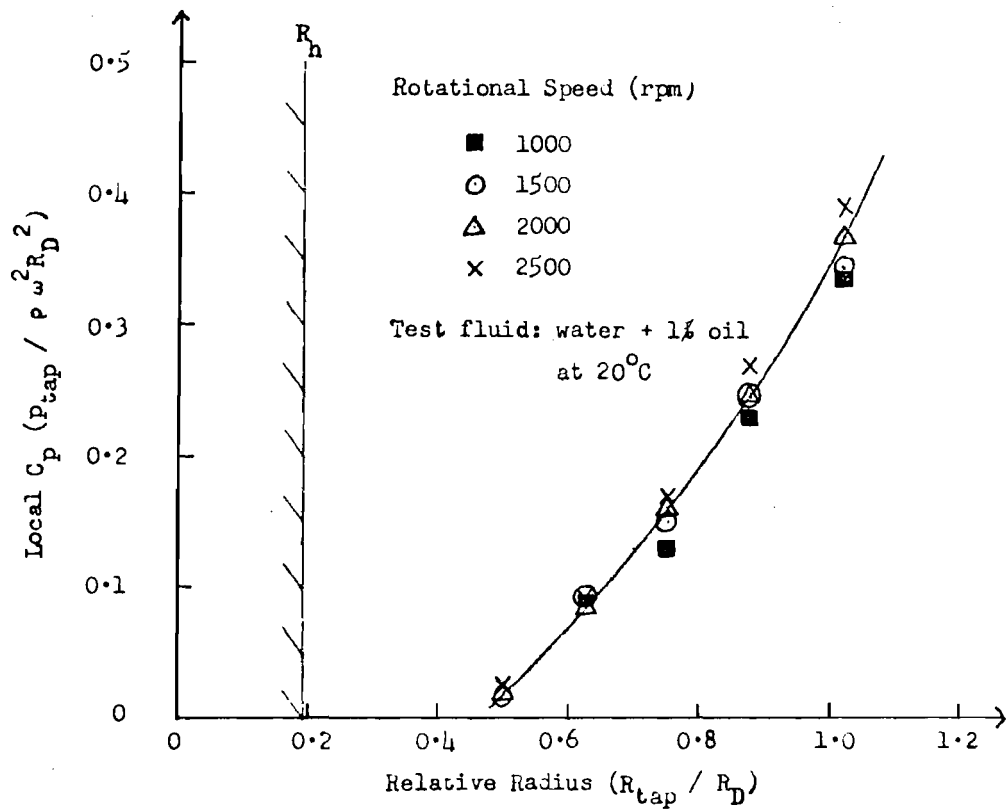
FIGURE 137. RADIAL PRESSURE DISTRIBUTION: SINGLE STAGE HDS FITTED ON PUMP IN WATER.

Test fluid: water at $20^{\circ}C$

Rotational Speed (rpm)

■ 1000
◯ 1500
△ 1800

Results from seal
tests in pump (Fig. 137)

Local C_p ($P_{tap} / \rho \omega^2 R_D^2$)

Relative Radius (R_{tap} / R_D)
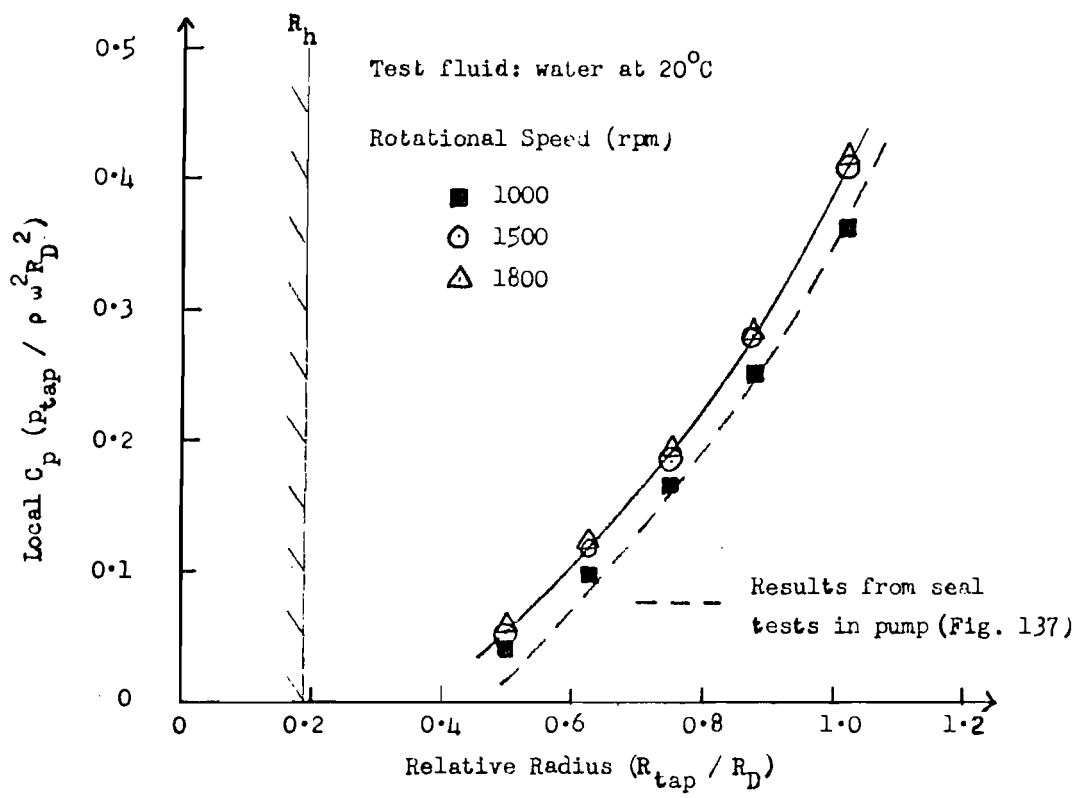
FIGURE 138. RADIAL PRESSURE DISTRIBUTION: SINGLE STAGE HDS ALONE IN WATER.
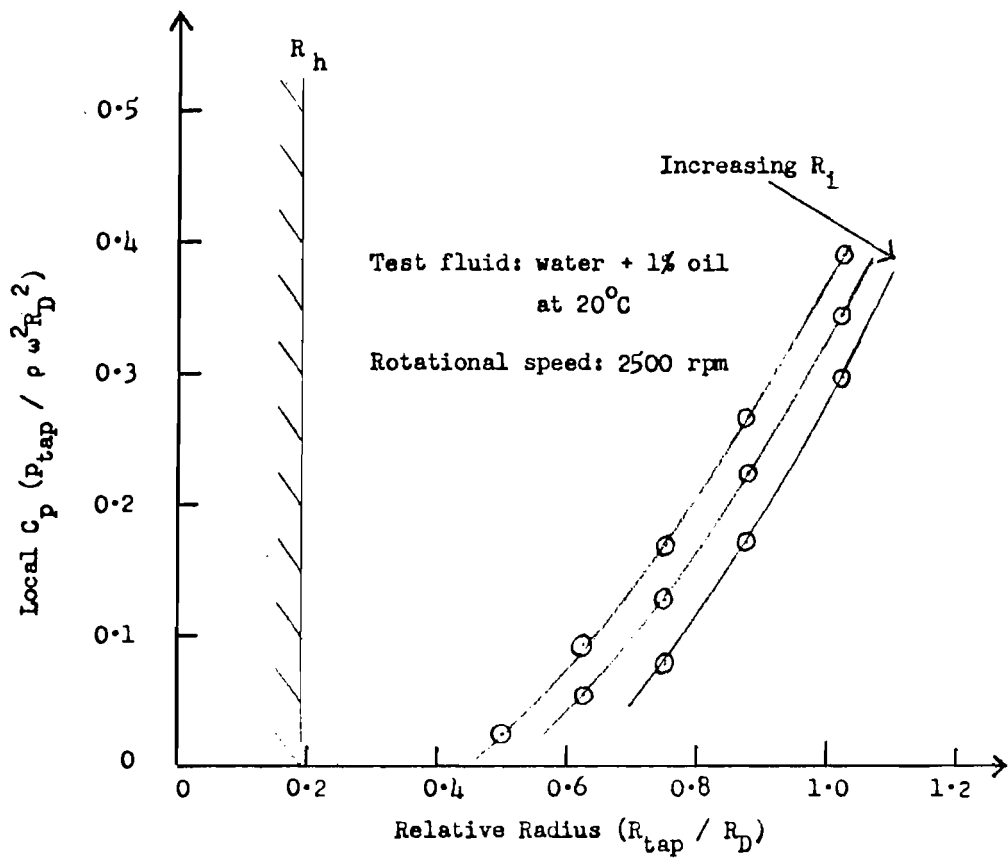
FIGURE 139. EFFECT OF INTERFACE POSITION ON RADIAL PRESSURE DISTRIBUTION:
SINGLE STAGE HDS FITTED ON PUMP IN WATER.

Test fluid: water + 1% oil at 20°C

$(k_v)^2$ calculated between $R_{tap}/R_D = 0\cdot75 - 0\cdot875$

Rotational speed: 2500 rpm

Rotational speed: 2000 rpm

Rotational speed: 1500 rpm

$X \ (= R_i/R_D)$
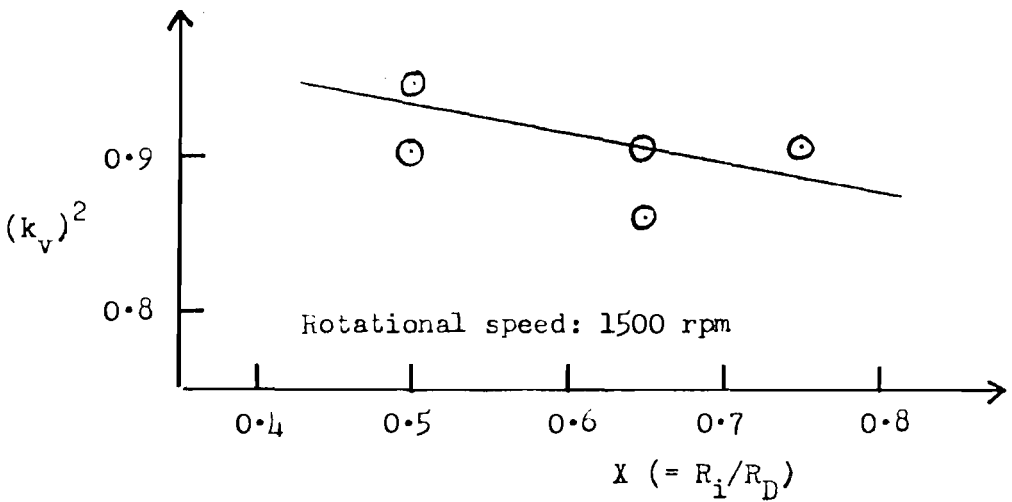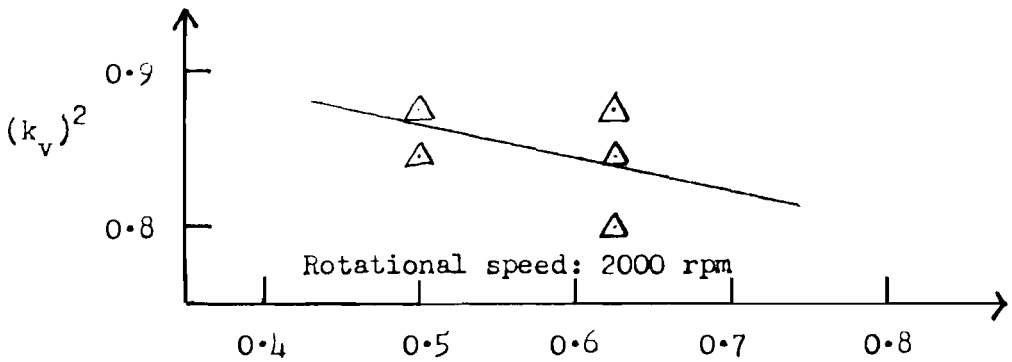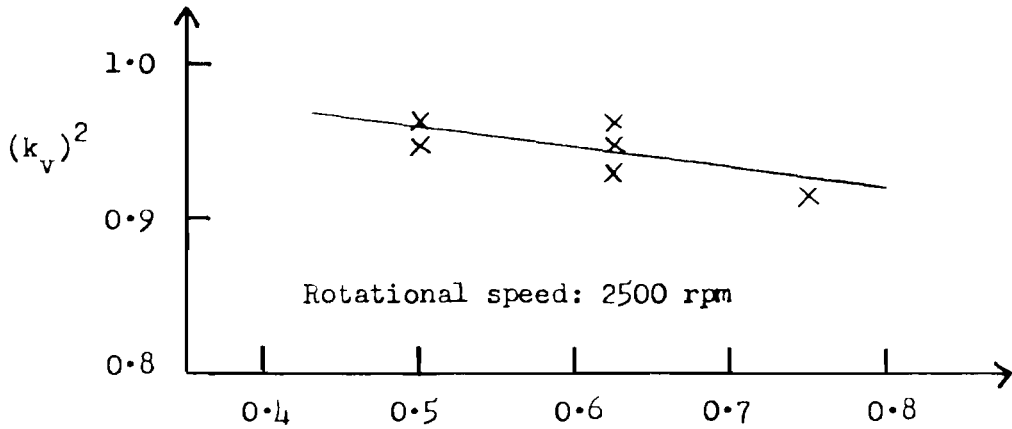
FIGURE 140. EFFECT OF INTERFACE POSITION ON TIP REGION K_V IN WATER (SINGLE STAGE HDS FITTED ON PUMP).

Test fluid: water + 1% oil at 20°C

$(k_s)^2$ calculated between $R_{tap}/R_D = 0.39 - 1.02$
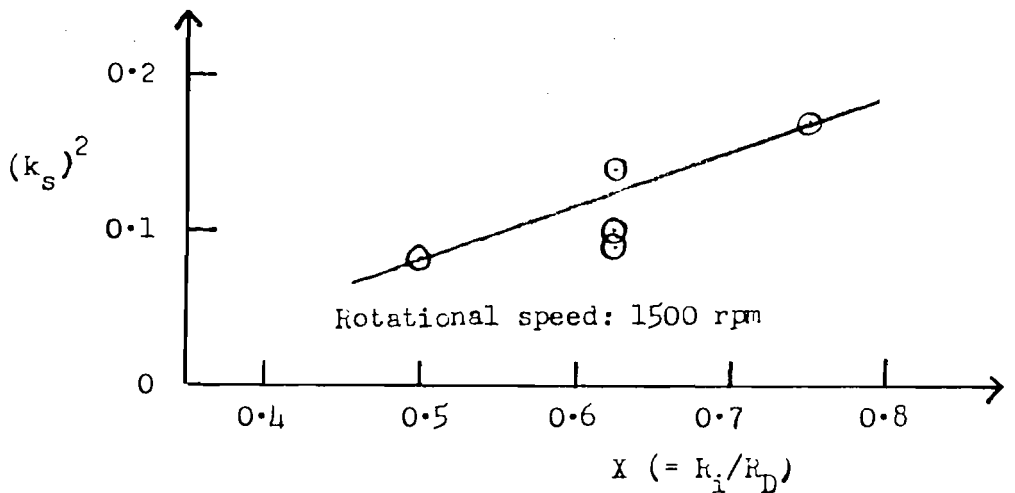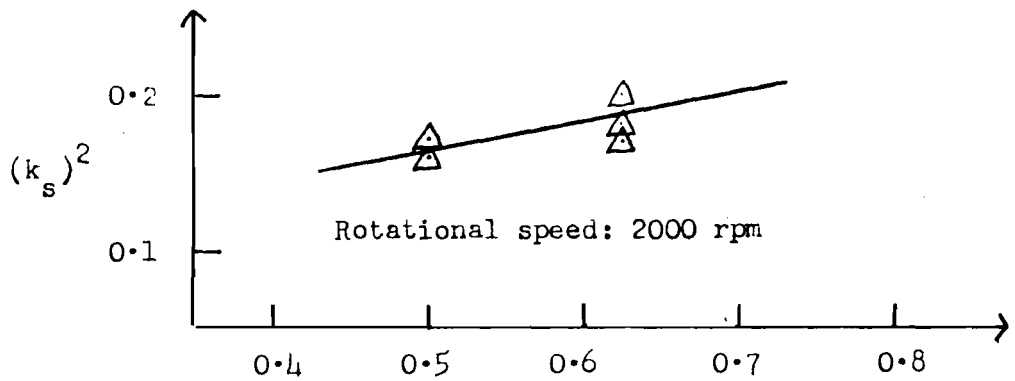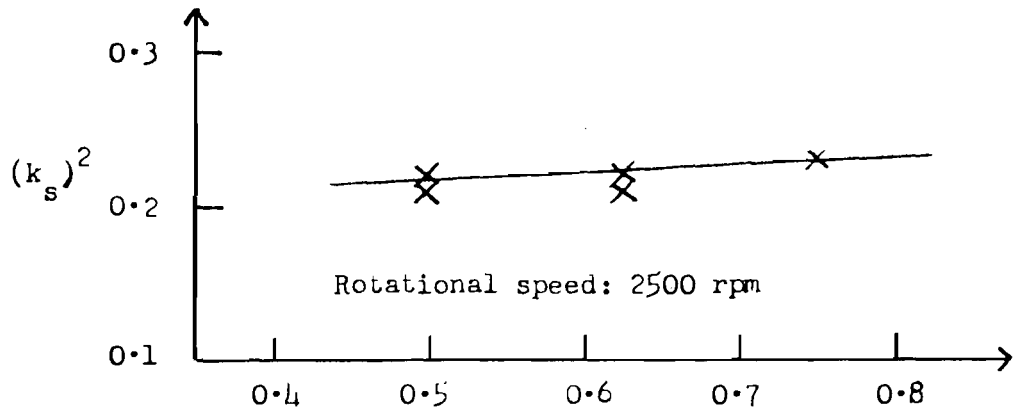
FIGURE 141. EFFECT OF INTERFACE POSITION ON AVERAGE k_s IN WATER
(SINGLE STAGE HDS FITTED ON PUMP).

Test fluid: water + 1% oil at 20°C

Rotational speed: 1500 rpm
$(k_v)^2$ calculated between R_{tap}/R_D = 0·75 - 0·875

Rotational speed: 1500 rpm
$(k_s)^2$ calculated between R_{tap}/R_D = 0·39 - 1·02

X (= R_i/R_D)
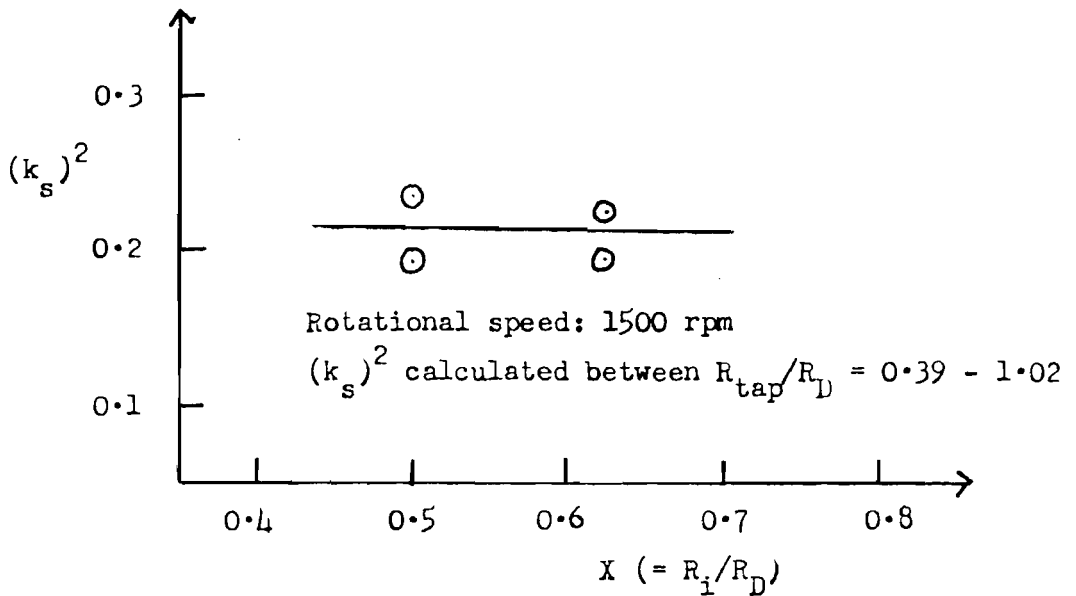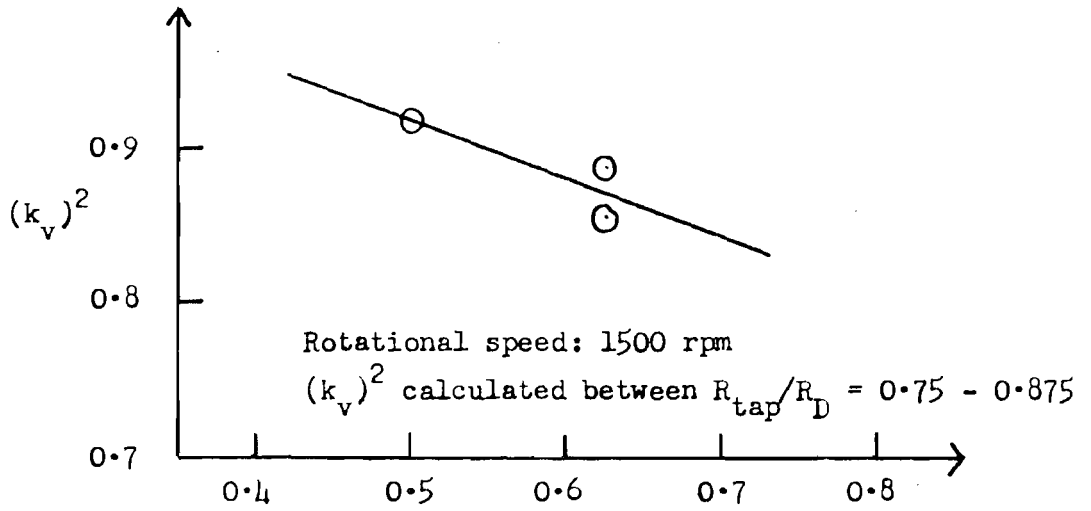
FIGURE 142. EFFECT OF INTERFACE POSITION ON TIP REGION K_v AND AVERAGE K_s
(SINGLE STAGE HDS ALONE IN WATER).
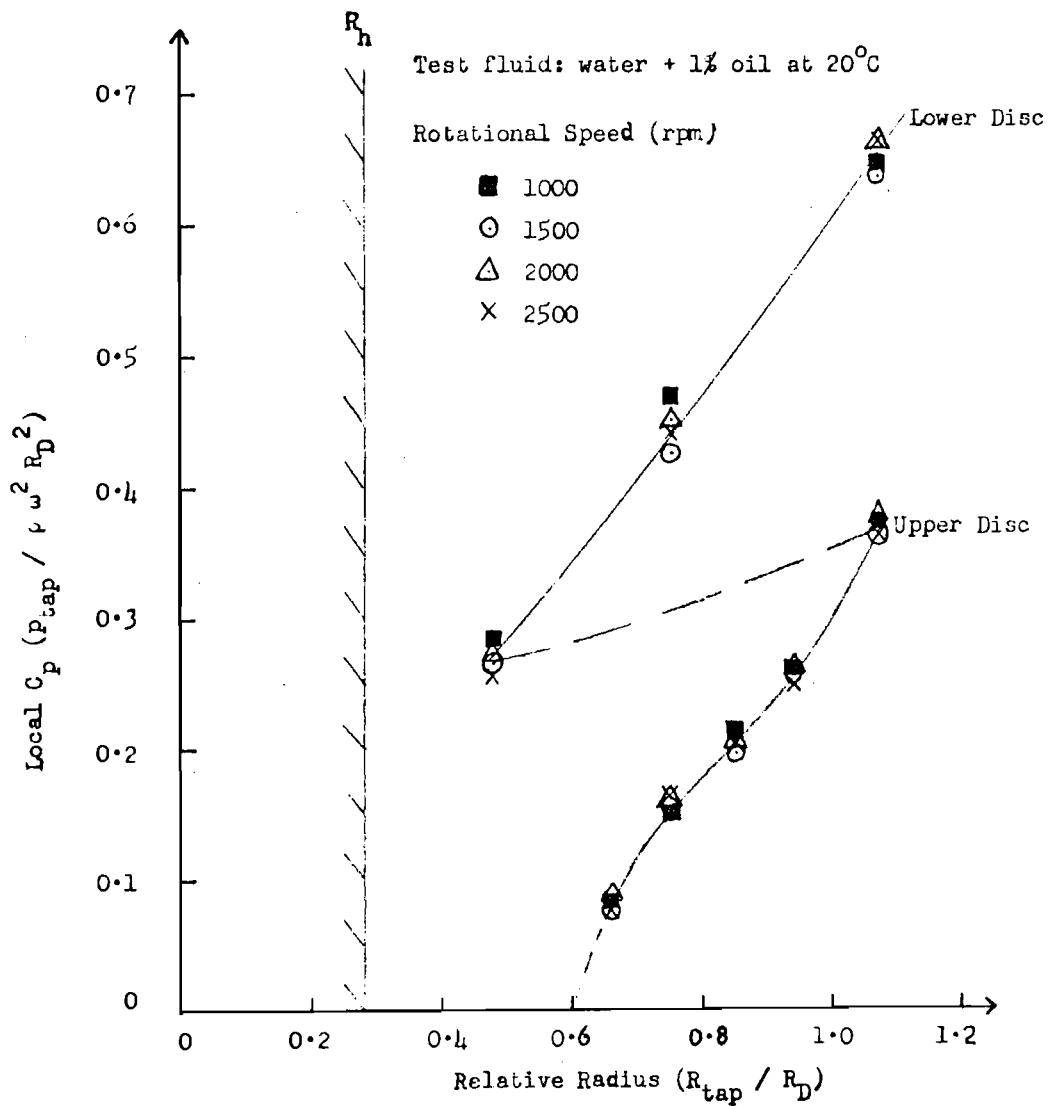
FIGURE 143. RADIAL PRESSURE DISTRIBUTION: TWO-STAGE (I) HDS FITTED ON PUMP IN WATER.
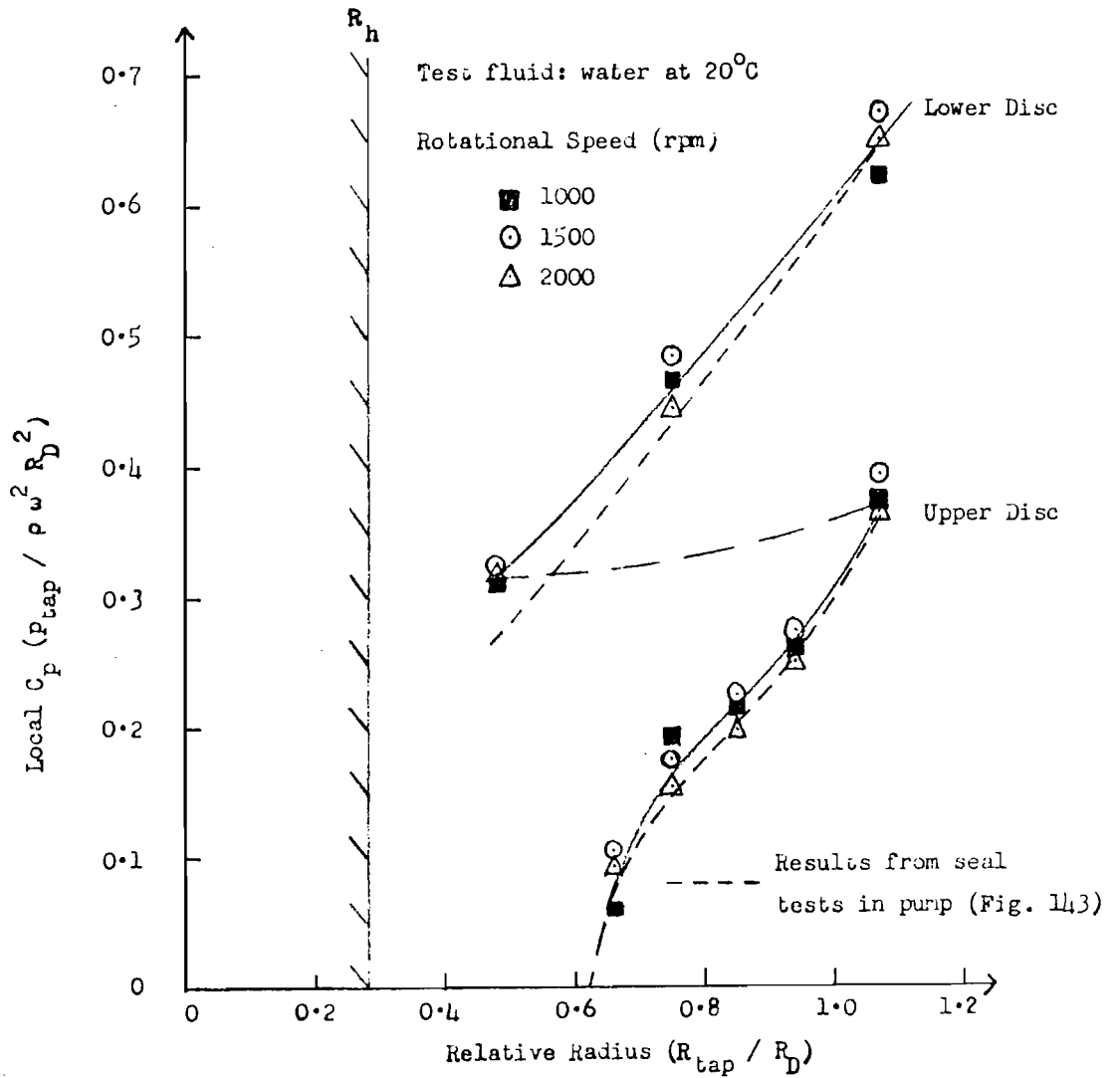
FIGURE 144. RADIAL PRESSURE DISTRIBUTION: TWO-STAGE HDS ALONE IN WATER.
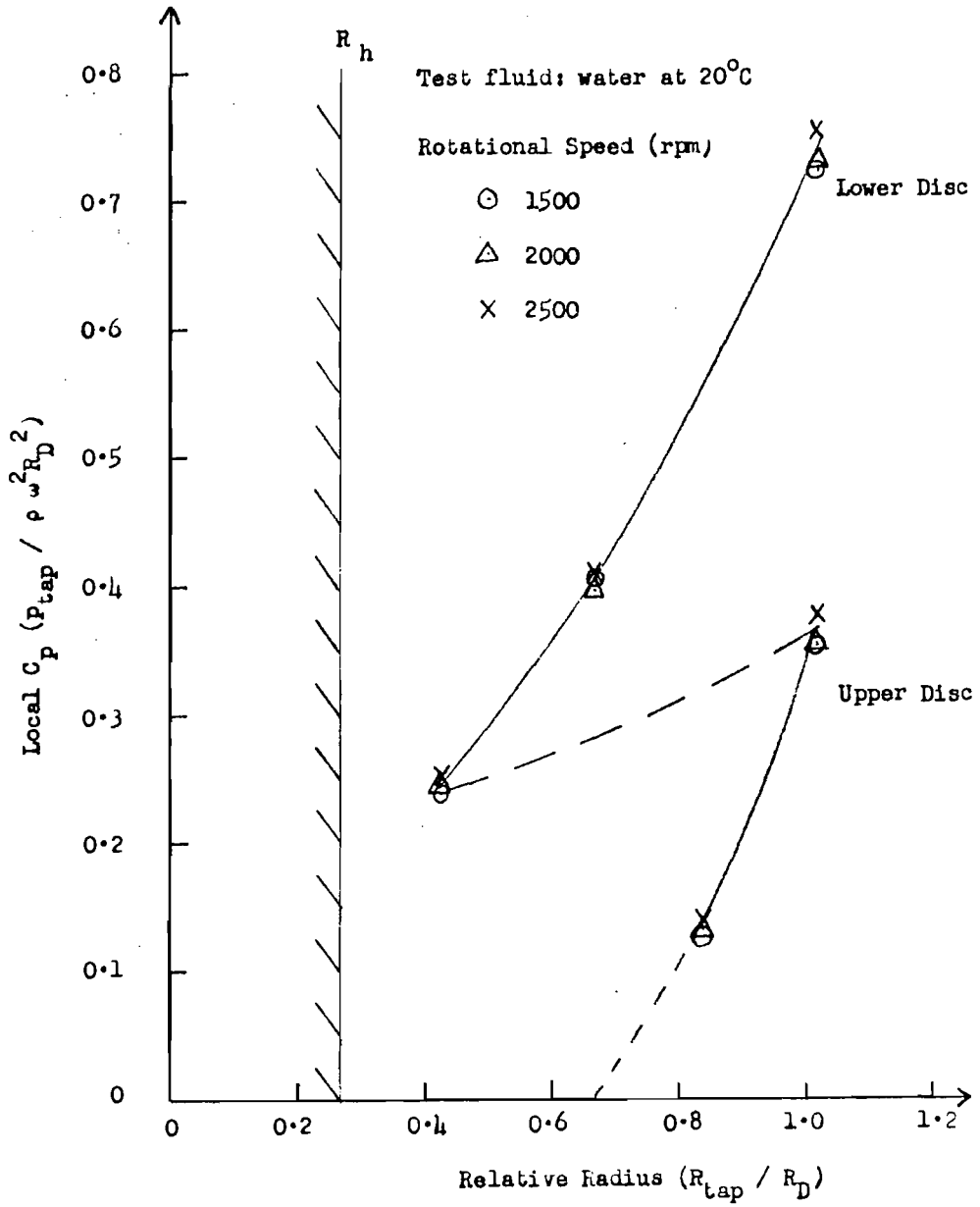
FIGURE 145.   RADIAL PRESSURE DISTRIBUTION: TWO-STAGE (II) HDS FITTED ON PUMP
IN WATER.

Pump with single stage HDS (Fig. 131)

Pump with two-stage (II) HDS (Fig. 133)

Pump with two-stage (I) HDS
(Fig. 132)

Standard pump corrected for power absorbed
by neckrings and by shaft rotating in water

Test fluid: water + 1% oil at 20°C
Standard clearance on neckrings

Power Coefficient $K \times 10^3$

Corrected Flow Coefficient $\phi' \times 10^3$
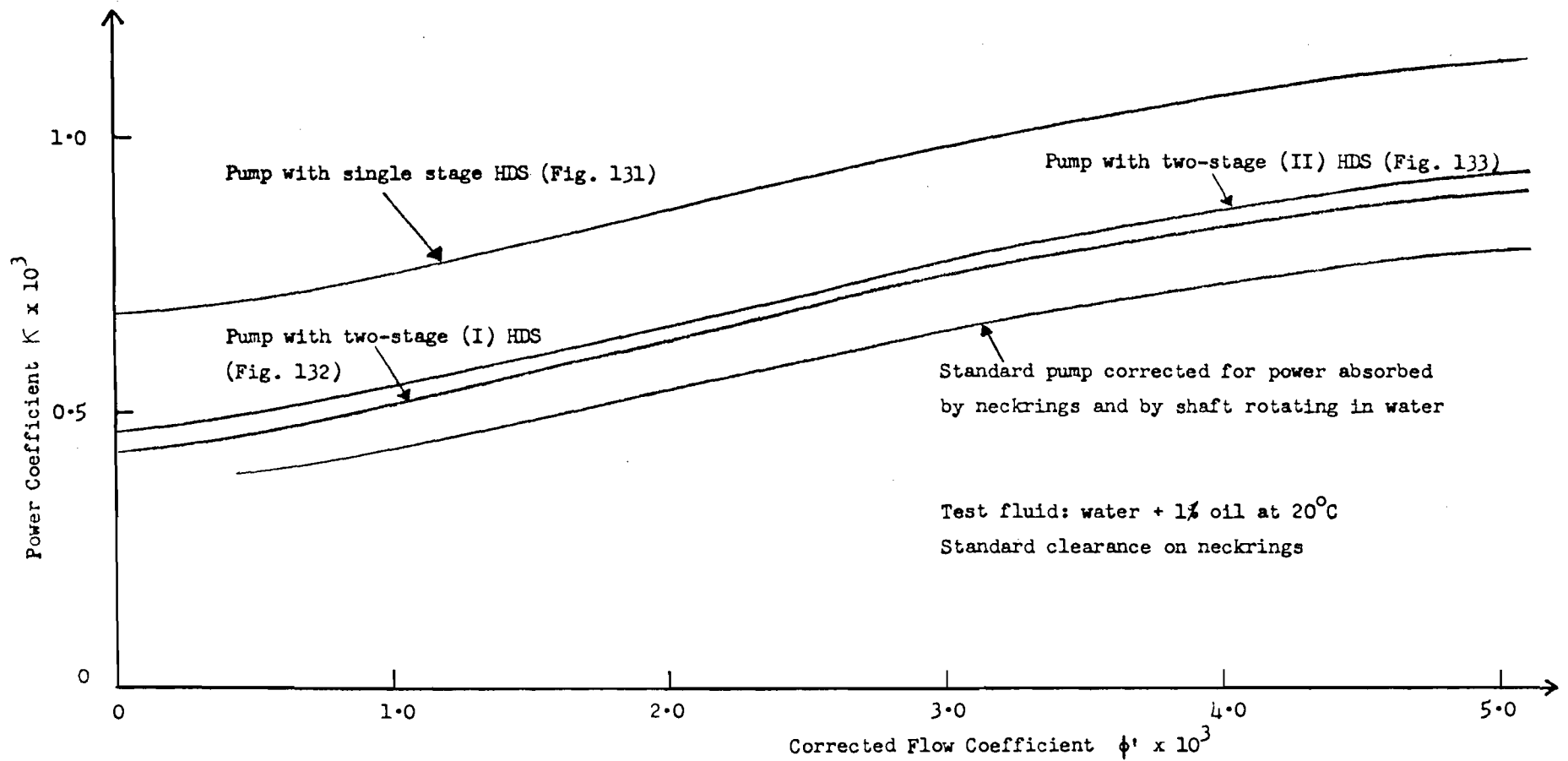
FIGURE 146.   POWER CHARACTERISTIC OF THE STANDARD PUMP, CORRECTED FOR THE EFFECTS OF UPPER NECKRING LEAKAGE,
COMPARED WITH THE CHARACTERISTICS OF THE PUMP FITTED WITH A HDS, ALL RUNNING IN WATER.
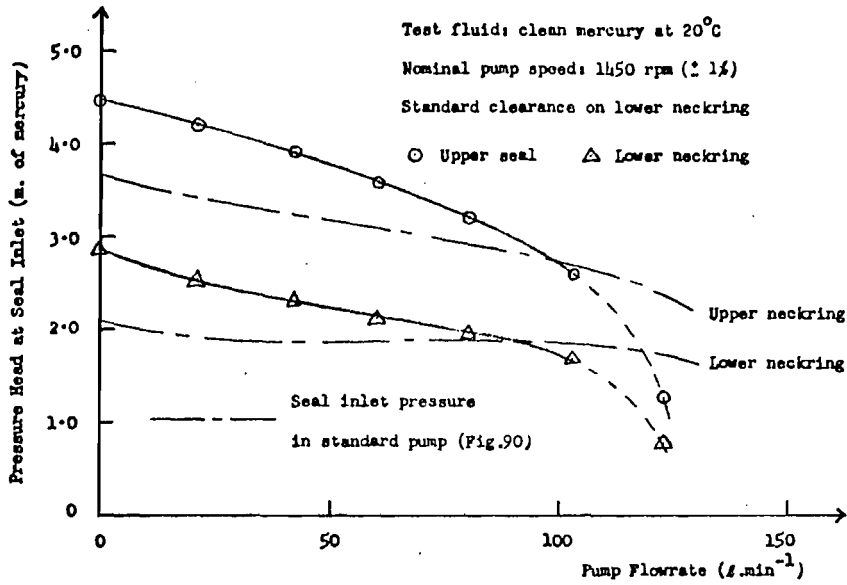
FIGURE 147. SEAL INLET PRESSURE V. PUMP FLOWRATE WITH SINGLE STAGE HDS IN MERCURY
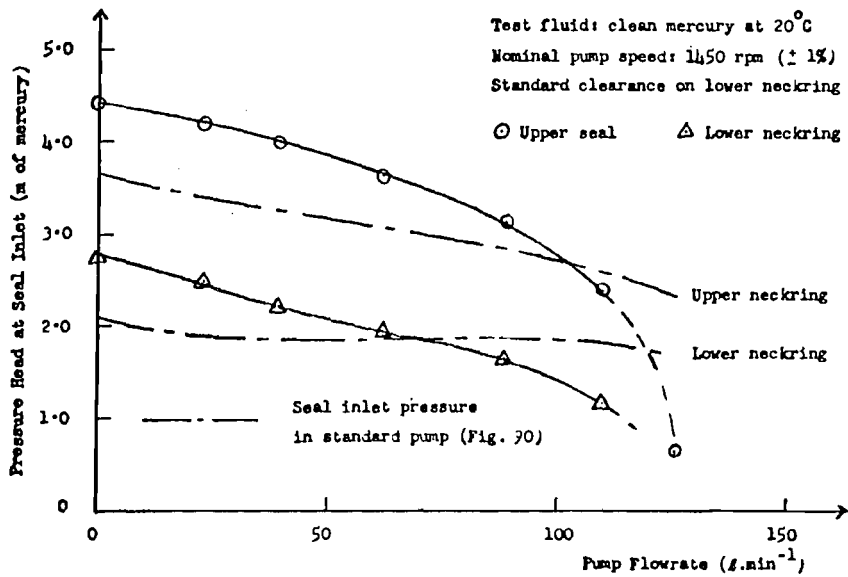
FIGURE 148. SEAL INLET PRESSURE V. PUMP FLOWRATE WITH TWO-STAGE (I) HDS IN MERCURY
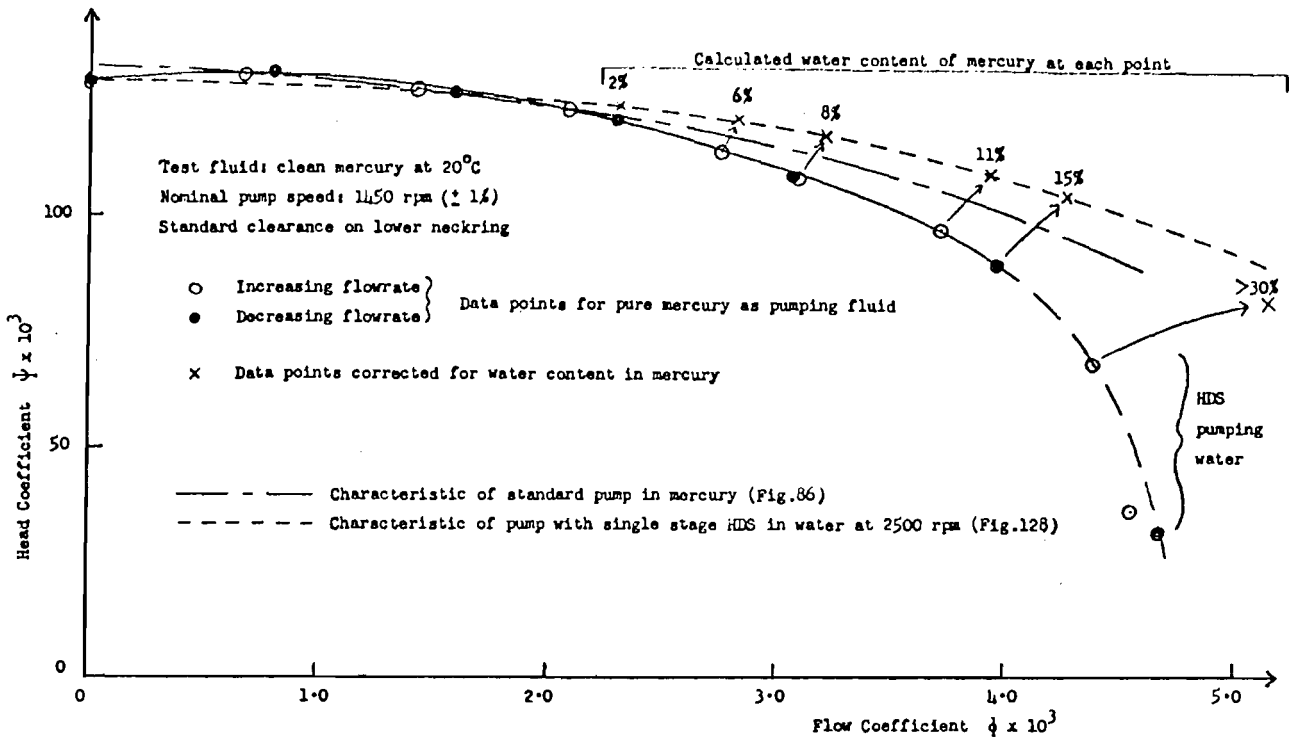
FIGURE 149. DIMENSIONLESS HEAD / FLOW CHARACTERISTIC WITH SINGLE STAGE HDS IN MERCURY.
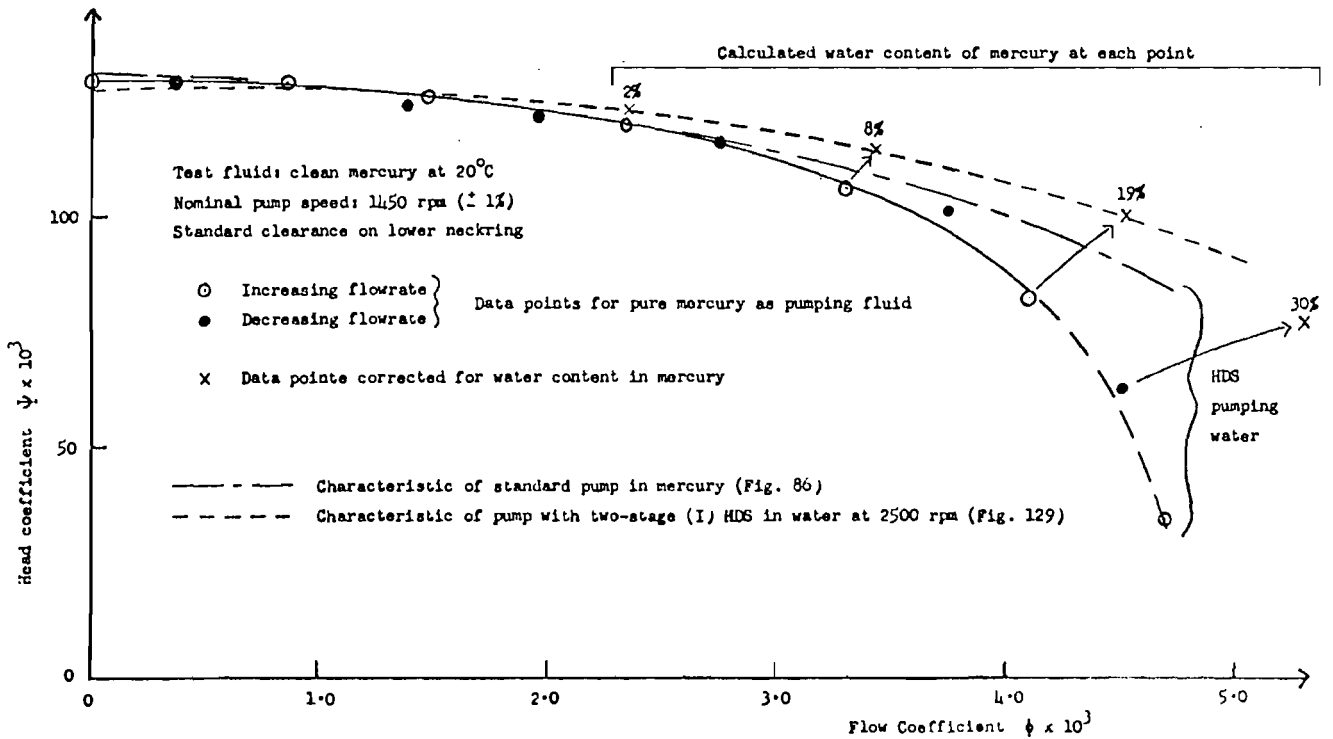
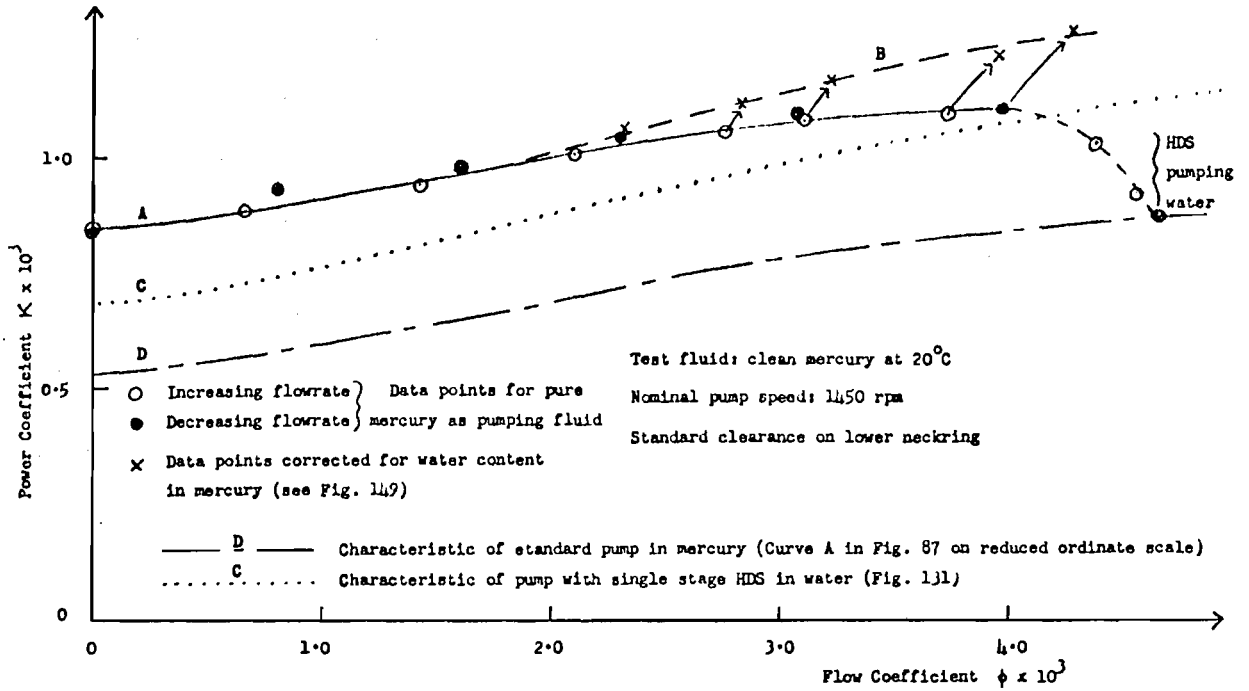FIGURE 150. DIMENSIONLESS HEAD / FLOW CHARACTERISTIC WITH TWO-STAGE (I) HDS IN MERCURY.

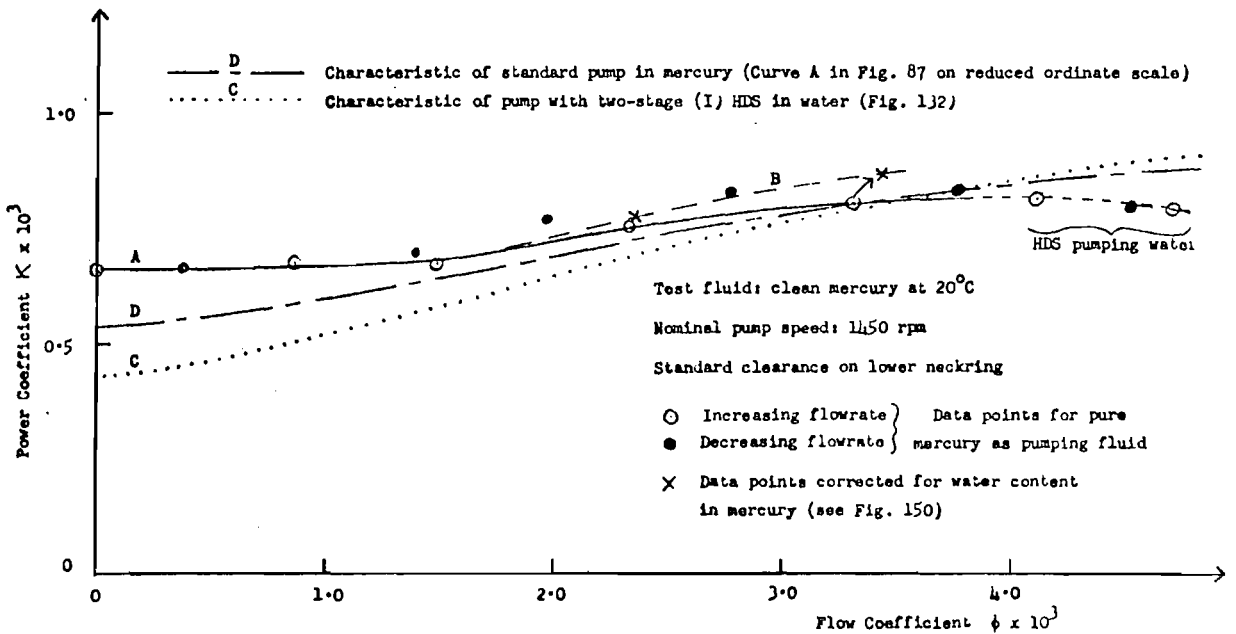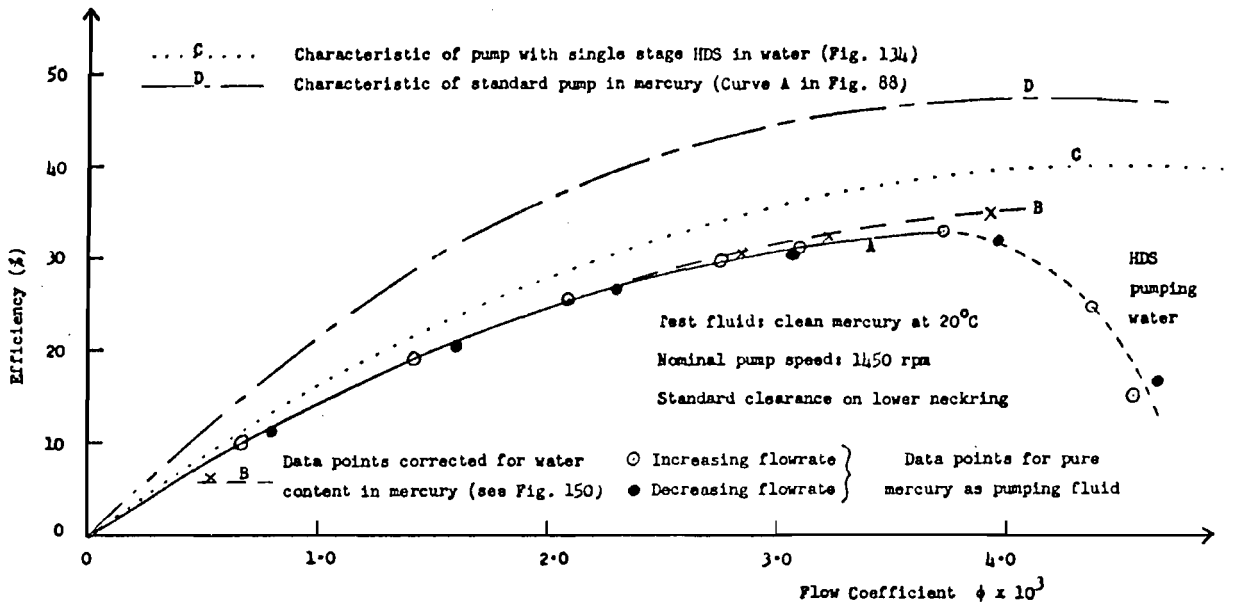FIGURE 151.   DIMENSIONLESS ABSORBED POWER / FLOW CHARACTERISTIC WITH SINGLE STAGE HDS IN MERCURY

FIGURE 152.   DIMENSIONLESS ABSORBED POWER / FLOW CHARACTERISTIC WITH TWO-STAGE (I) HDS IN MERCURY

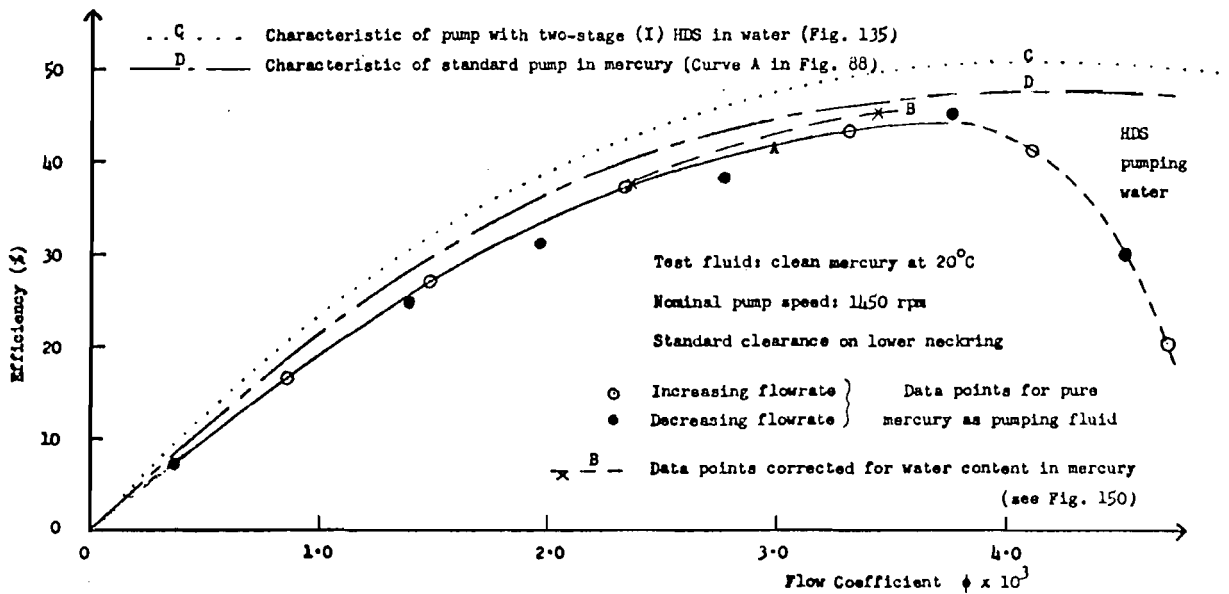**FIGURE 153.** DIMENSIONLESS EFFICIENCY / FLOW CHARACTERISTIC WITH SINGLE STAGE HDS IN MERCURY

FIGURE 154. DIMENSIONLESS EFFICIENCY / FLOW CHARACTERISTIC WITH TWO-STAGE HDS (I) IN MERCURY
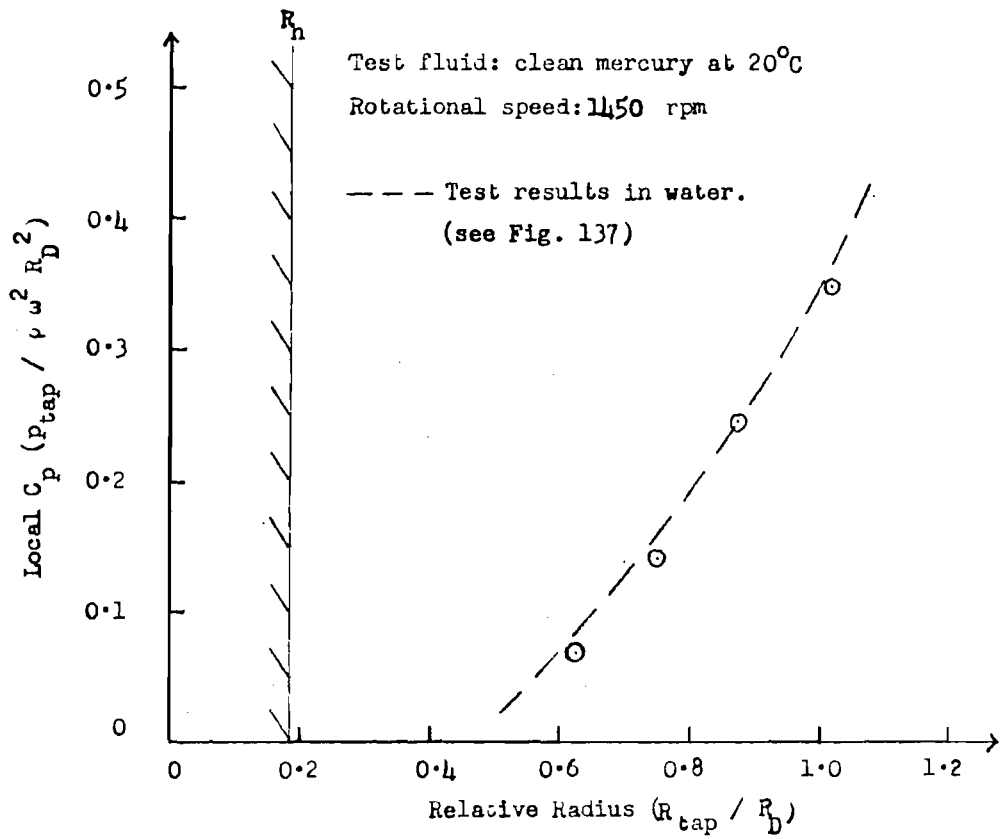
FIGURE 155. COMPARISON OF RADIAL PRESSURE DISTRIBUTION FOR SINGLE STAGE HIS IN PUMP FOR WATER AND MERCURY.
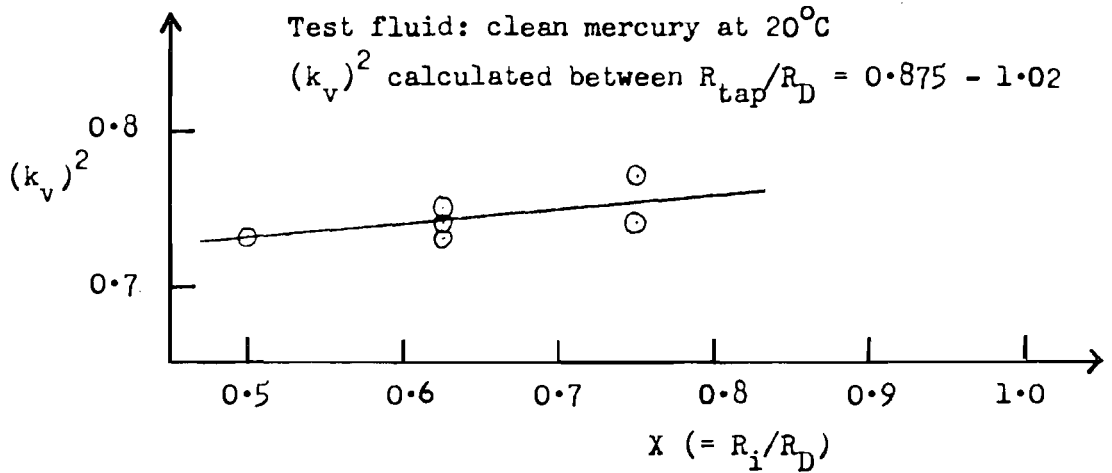
FIGURE 156(a). EFFECT OF INTERFACE POSITION ON TIP REGION K_V IN MERCURY
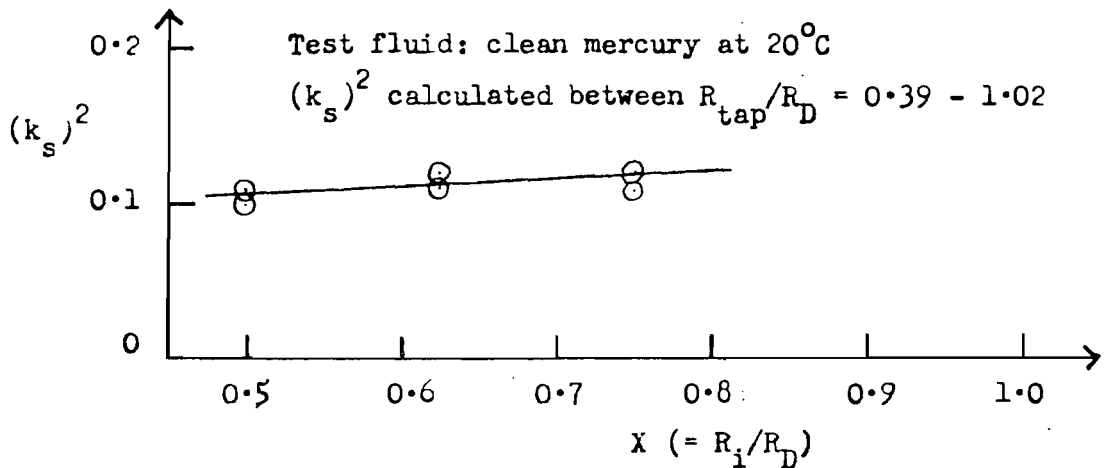(SINGLE STAGE HDS FITTED ON PUMP).

FIGURE 156(b). EFFECT OF INTERFACE POSITION ON AVERAGE K_S IN MERCURY
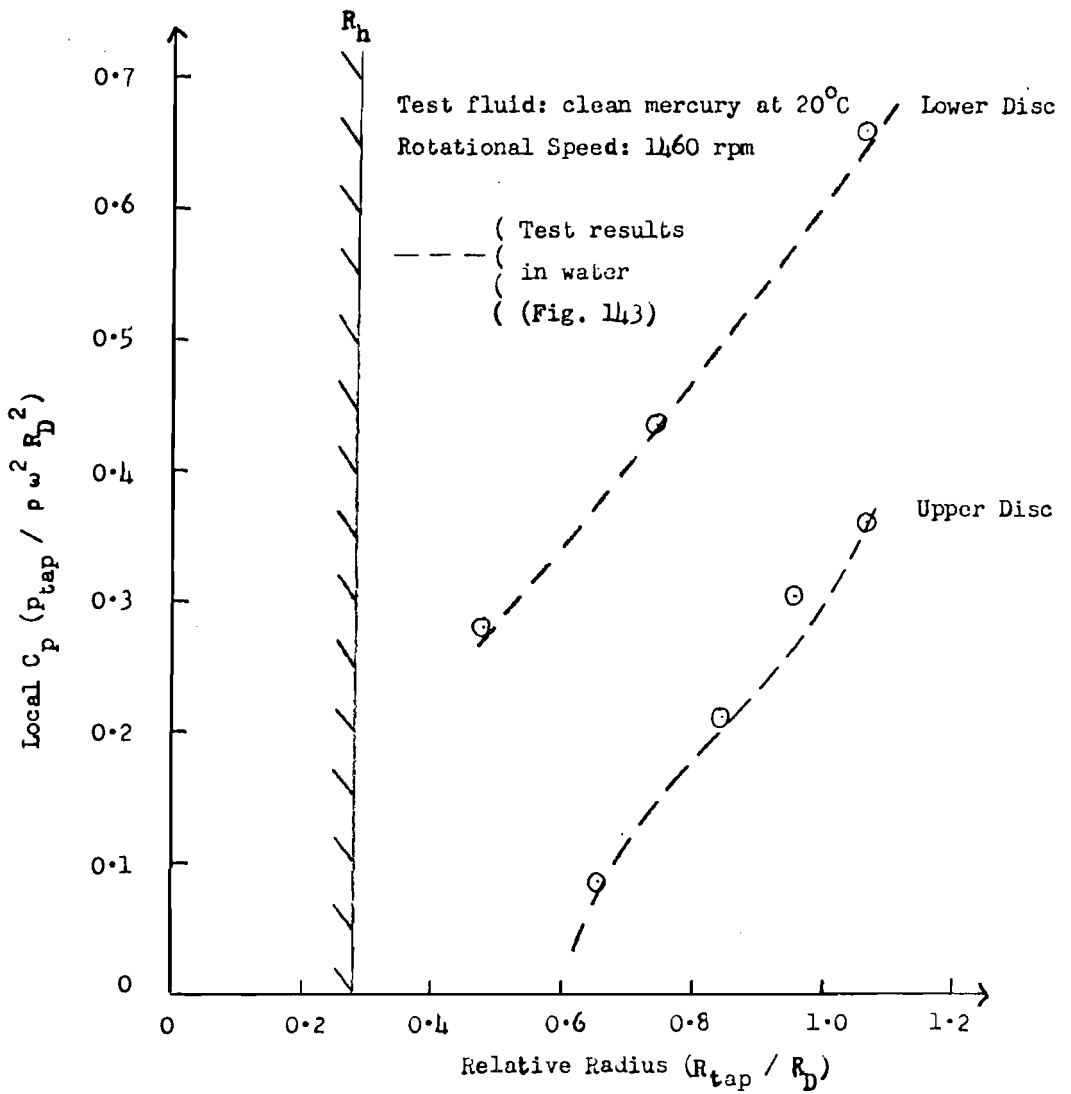(SINGLE STAGE HDS FITTED ON PUMP).

FIGURE 157. COMPARISON OF RADIAL PRESSURE DISTRIBUTION FOR TWO-STAGE (I) HDS IN PUMP FOR WATER AND MERCURY.

Pump + Single Stage HDS
(corrected for water content)

Pump + Two Stage (I) HDS (corrected for water content)

Standard Pump (corrected
for power absobed by
neckrings and shaft)

Test fluid: clean mercury at 20°C
Nominal pump speed: 1450 rpm
Standard clearance on neckrings (0·165mm)

Power Coefficient $K \times 10^3$

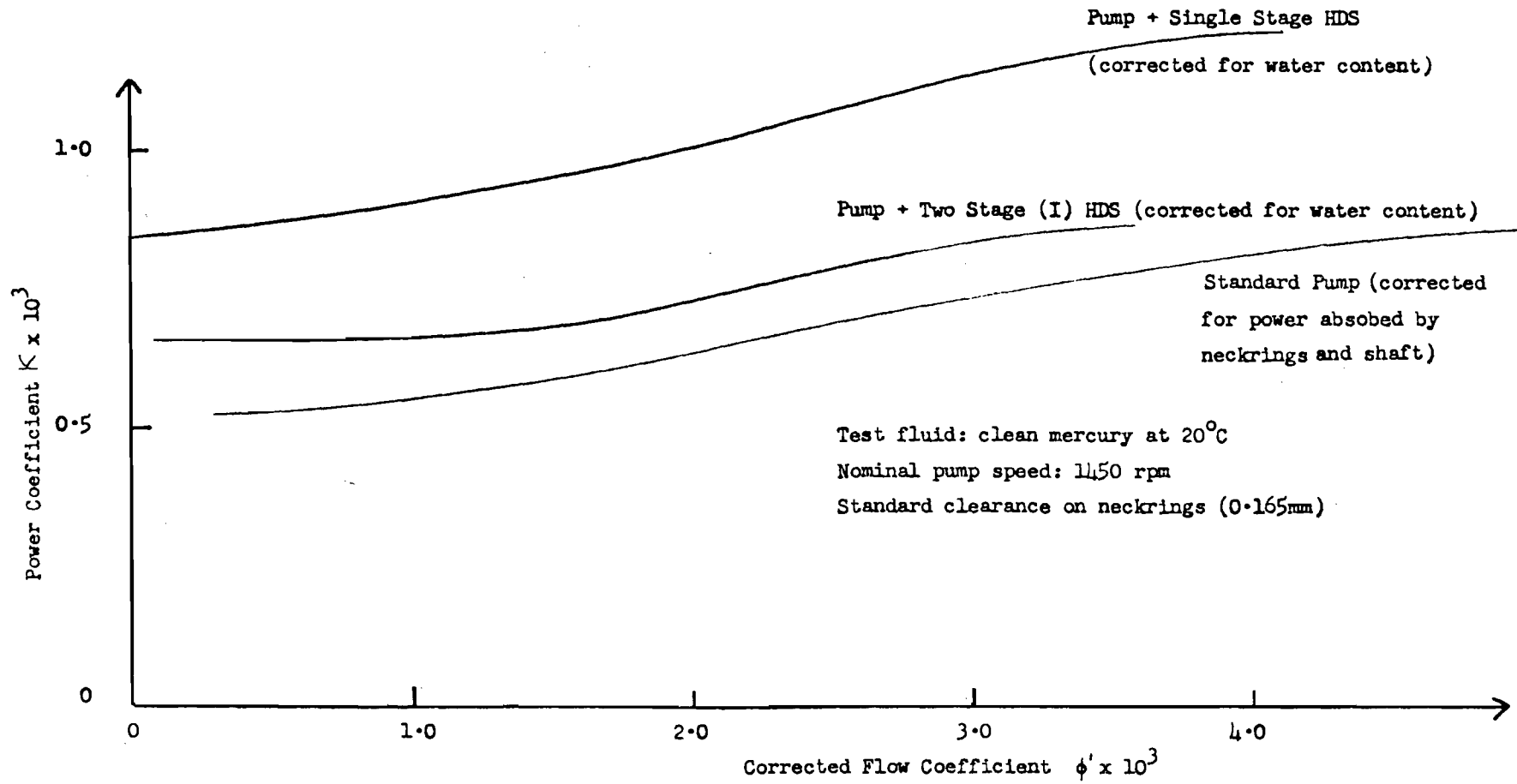Corrected Flow Coefficient $\phi' \times 10^3$

FIGURE 158.   POWER CHARACTERISTIC OF THE STANDARD PUMP, CORRECTED FOR THE EFFECTS OF UPPER NECKRING LEAKAGE, COMPARED WITH
THE CHARACTERISTICS OF THE PUMP FITTED WITH A HDS, ALL RUNNING IN MERCURY.
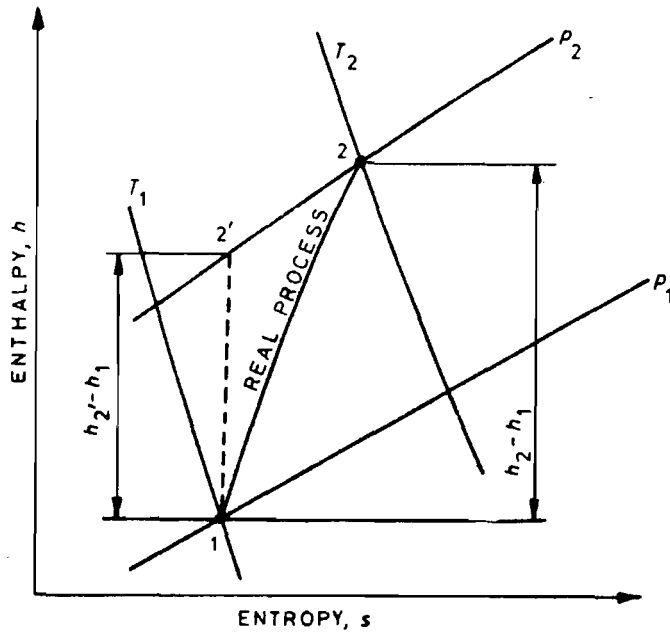
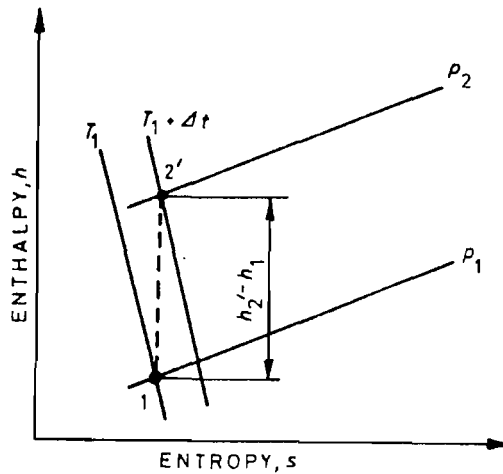FIGURE 159. DIAGRAM TO ILLUSTRATE ENERGY TRANSFER IN THE PUMPING
PROCESS.

FIGURE 160. DIAGRAM TO ILLUSTRATE ISENTROPIC ENTHALPY DIFFERENCE
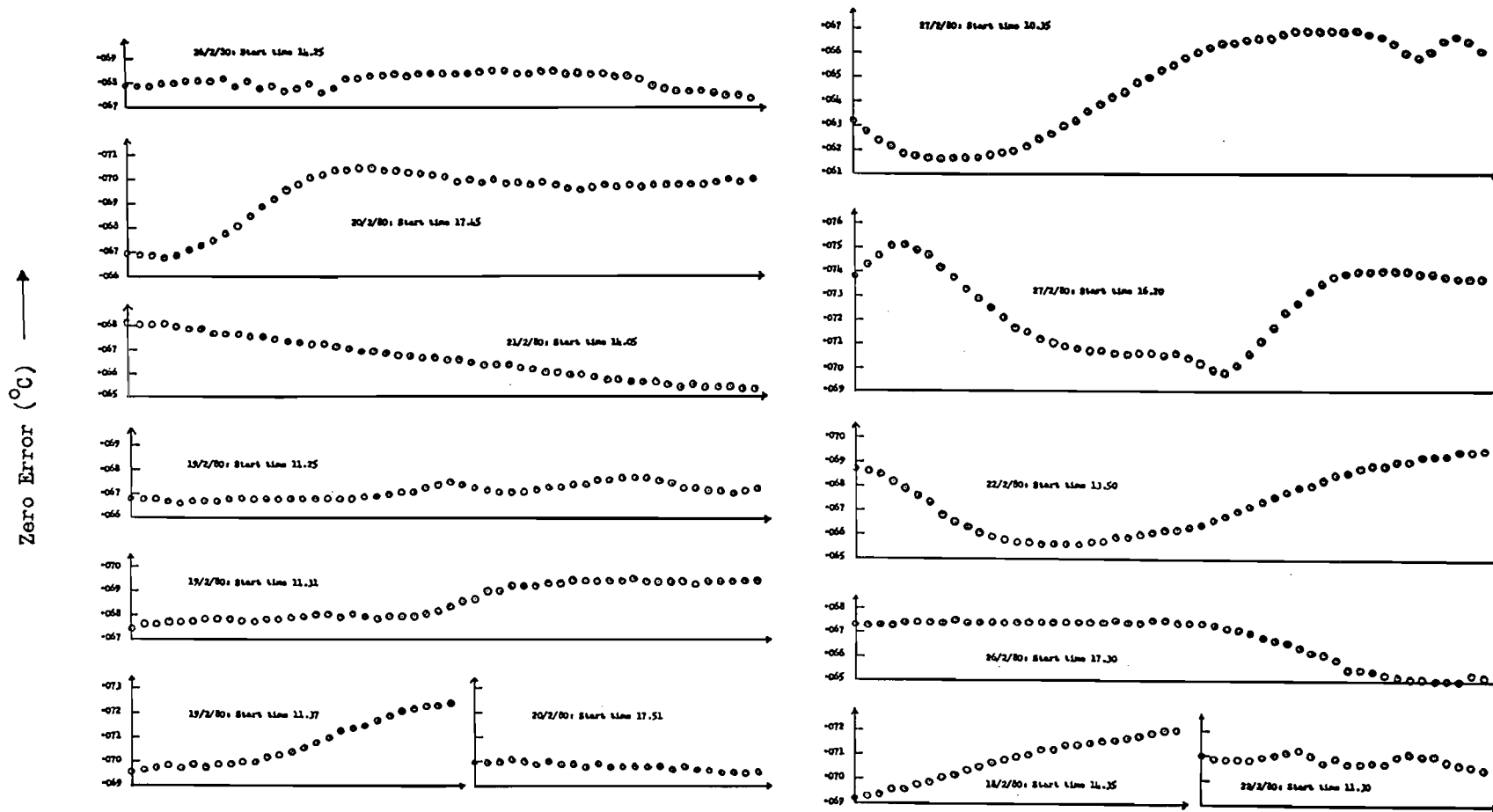IN THE PUMPING PROCESS.

Zero Error (°C) ⟶

Time: 3 second continuous sampling period ⟶

FIGURE 161.   GRAPHICAL PRESENTATION OF ZERO ERROR DATA FOR THE QUARTZ CRYSTAL THERMOMETER.

Pump speed: 2000 rpm

Test fluid: water + 1% oil at 20°C

Standard clearance on lower neckring

99% confidence interval from statistics

Efficiency characteristic of pump alone, computed from efficiency characteristic of pump fitted with two-stage (I) HDS (see Fig. 135) with allowance for power absorbed by the HDS.
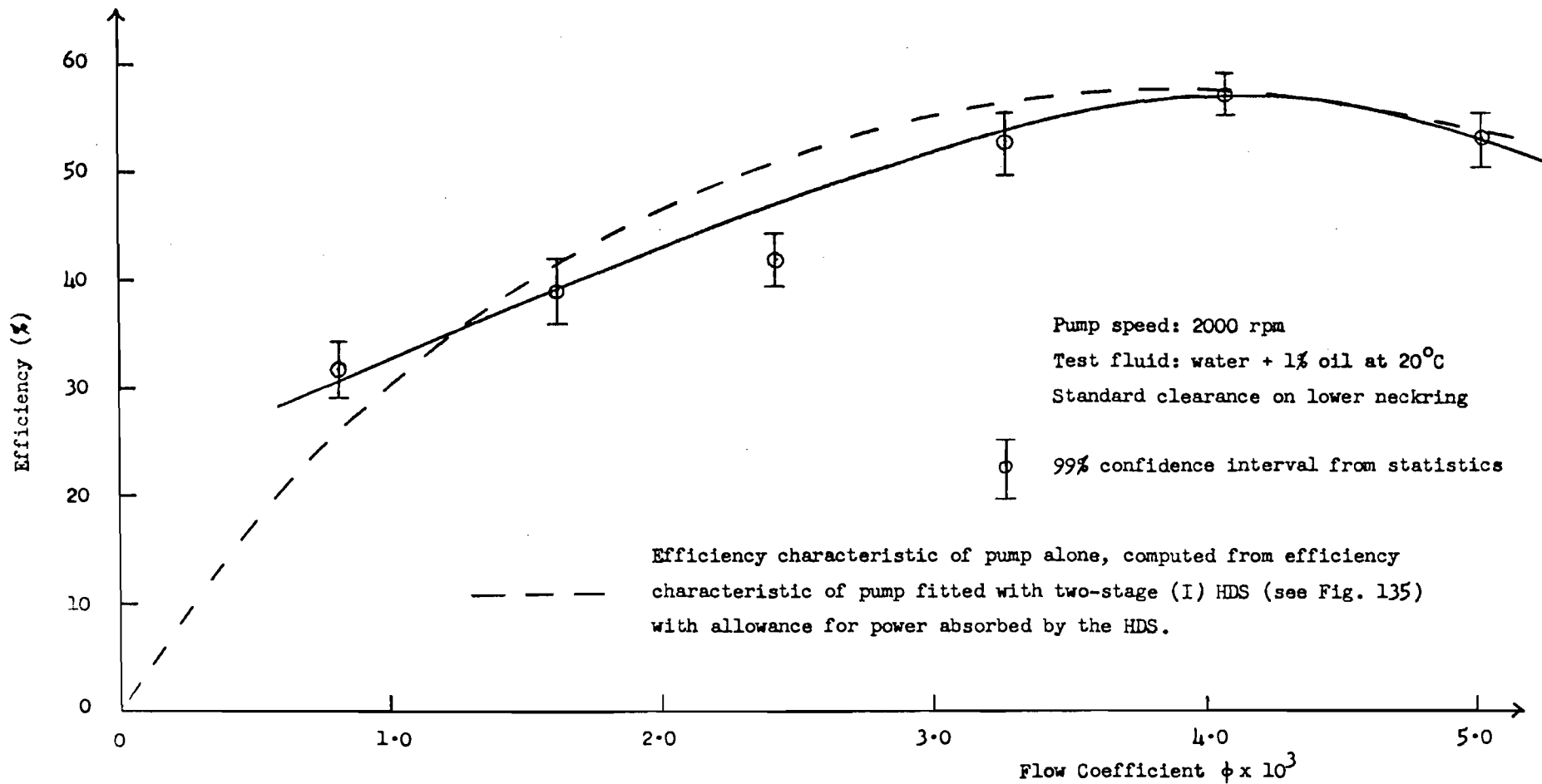
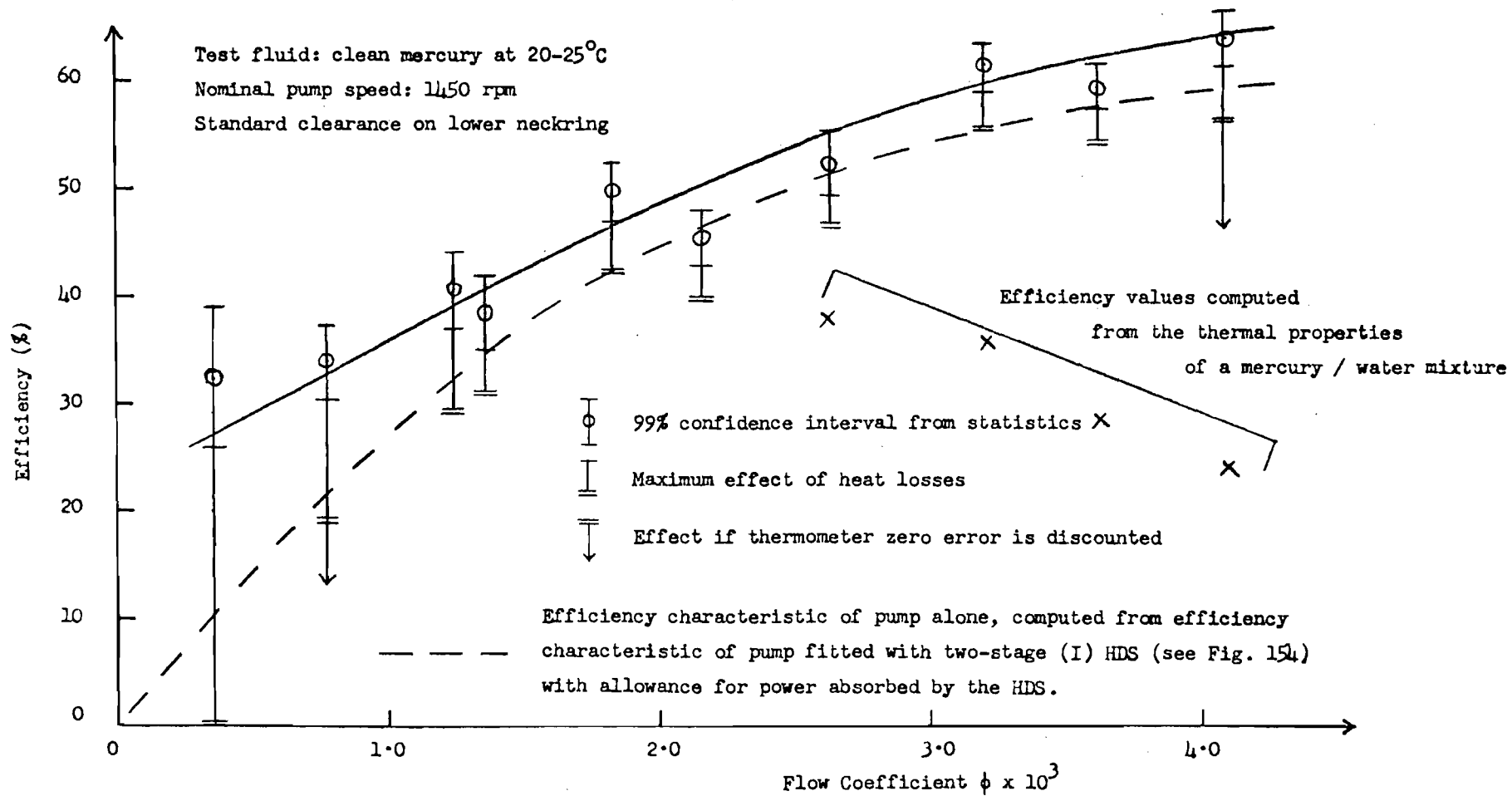FIGURE 162. EFFICIENCY CHARACTERISTIC FROM THERMOMETRIC MEASUREMENTS IN WATER: PUMP FITTED WITH TWO-STAGE (I) HDS.

FIGURE 163. EFFICIENCY CHARACTERISTIC FROM THERMOMETRIC MEASUREMENTS IN MERCURY: PUMP FITTED WITH TWO-STAGE (I) HDS.

Seal Casing

HPS Impeller

Proposed
Bleed
Flowpath

Shaft

HDS Impeller

Upper neckring

Back Vanes

Pump Casing
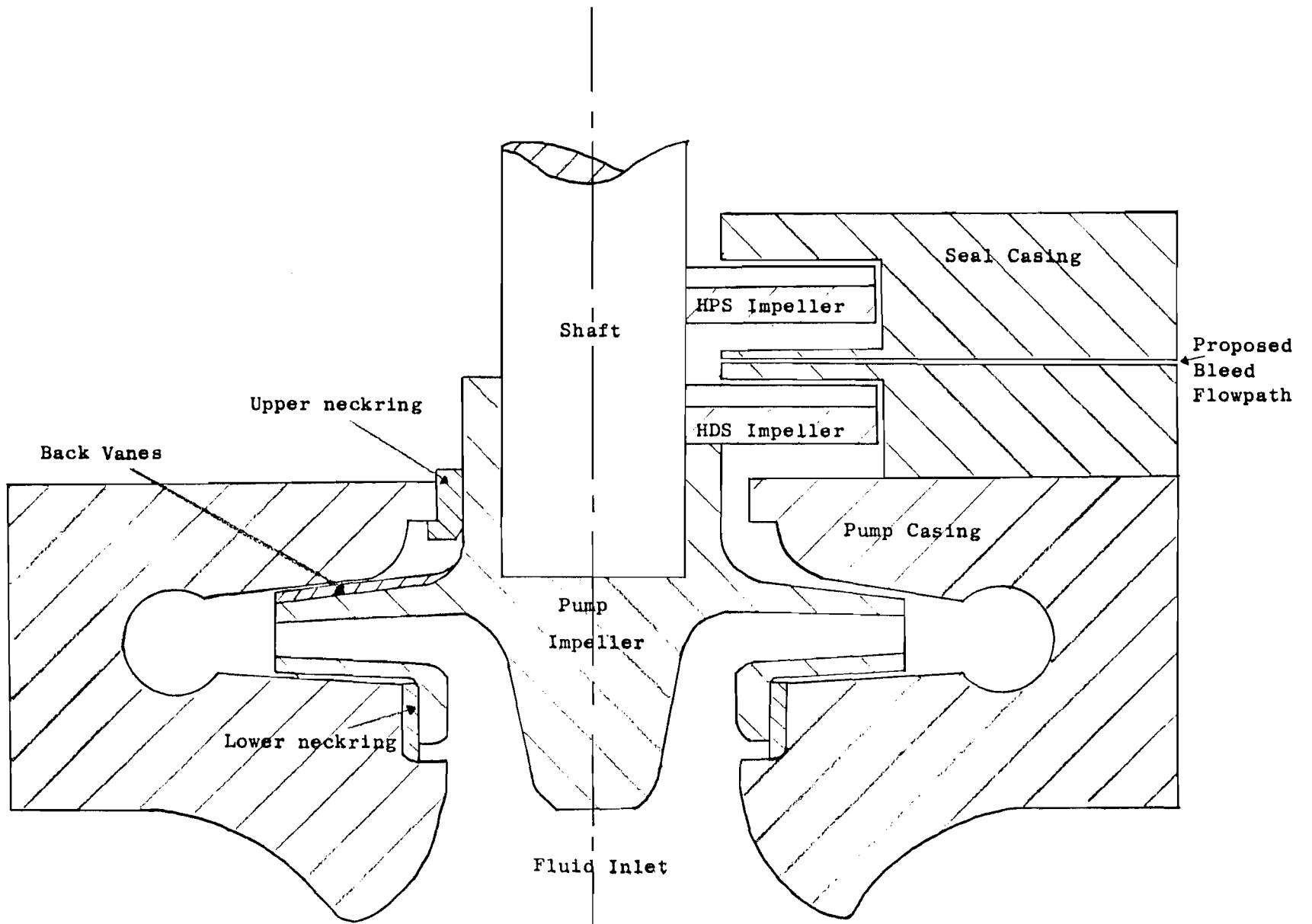
Lower neckring

Pump

Impeller

Fluid Inlet

Figure 164a Back-Vaned Impeller Design

Figure 164b Bleed Flowpath for Two-Stage HDS